UNIVERSITY OF OKLAHOMA

GRADUATE COLLEGE

DEVELOPMENT OF CONTRAST AGENTS FOR OPTOACOUSTIC IMAGING

A DISSERTATION

SUBMITTED TO THE GRADUATE FACULTY

in partial fulfillment of the requirements for the

Degree of

DOCTOR OF PHILOSOPHY

By

WILLIAM M MACCUAIG

Norman, Oklahoma

2023

DEVELOPMENT OF CONTRAST AGENTS FOR OPTOACOUSTIC IMAGING

A DISSERTATION APPROVED FOR THE
STEPHENSON SCHOOL OF BIOMEDICAL ENGINEERING

BY THE COMMITTEE CONSISTING OF

Dr. Lacey McNally, Chair

Dr. Edgar O'Rear

Dr. Roger Harrison

Dr. Sepideh Razavi

Acknowledgements

I would like to begin by thanking my Ph.D. adviser, Dr. McNally for her guidance, support, and confidence throughout my studies. In the McNally lab, I've been able to improve my skills in conducting science, writing, communication, among a myriad of others. Her aid throughout the length of my Ph.D. has allowed me to grow as a student, a scientist, a professional, and a person. Thank you for all the support over the years.

I would like to thank each of the members of my thesis committee: Dr. Edgar O'Rear, Dr. Roger Harrison, and Dr. Sepideh Razavi. Their help, support, and suggestions have been greatly appreciated and have helped lead me to this point. In addition, I'd like to thank the faculty and staff of the Stephenson School of Biomedical Engineering.

I would also like to thank my friends and lab mates at OU that I've had the pleasure of meeting over the years. I've been able to learn something from each of you and I sincerely appreciate it. Meredith Jones, B.F, M.M, A.S, A.F, B.R, J.H, Z.H, B.H, K.H, A.A, M.S, K.H, L.P, S.C, K.M, T.H, E.S, E.N, K.V, R.B, I.D, H.A, N.S. I'd also like to thank all collaborators of the McNally lab, both at the University of Oklahoma and outside, for their valuable input and help on various parts of this document.

Finally, I'd like to thank my family. To my partner Nicole, thank you for always being there for me. You provided inspiration, wisdom, and love when I found myself needing it the most; I can't thank you enough. To my parents, Bill and Shannon, and sister, Katie, thank you for the unwavering and unconditional support and confidence. I wouldn't be where I am today without your guiding presence. And to the rest of my extended family and friends; thank you for your constant love and support, I appreciate all of you.

Table of Contents

List of Figures

Chapter 1:

Chapter 2:

Chapter 3:

List of Tables

Chapter 1:

Chapter 3:

Chapter 4:

Abstract

Optoacoustic imaging is an emerging modality with inherent advantages relevant for clinical use. Following excitation of optoacoustic contrast agents with ultrashort (~10 ns) pulses of near-infrared light, thermoelastic contractions and expansions of the molecule are produced and detected as acoustic waves. As the pathlength of light is reduced by half, and since near-infrared light penetrates efficiently in biological tissue, the influence of the imaging depth/spatial resolution tradeoff is significantly diminished; an unavoidable phenomenon in traditional optical imaging. Multiwavelength illumination allows for understanding of optoacoustic signal as a function of excitation wavelength, which can be utilized in unmixing algorithms, a feature that is unavailable with conventional ultrasound. Such unmixing algorithms have the ability to separate and determine the location and concentration of multiple optoacoustic agents in an unknown sample. There is a need for developing improved optoacoustic contrast agents and delivery mechanisms to further increase the applications of optoacoustic imaging. In this dissertation, newly synthesized squaraine and cyanine compounds are extensively characterized to determine how molecular structure directly impacts the ability to generate optoacoustic signal. Specifically, which molecular features result in changes to optoacoustic intensity and spectral shape, e.g., optoacoustic signal vs. wavelength. These studies show that through heavy halogenation, addition of rotatable bonds, and functionalization with diethylamino groups positively impact the strength of the contrast agents and may result in bathochromic shifts. Further, mesoporous silica nanoparticles have shown potential for inert, high cargo, and tunable delivery agents, that will not impact optoacoustic imaging due to the silica base. However, silica nanoparticles have previously been linked to toxicity, along with commonly used silica gatekeeping coatings. After toxicity evaluation

of commonly used coatings on silica nanoparticles, chitosan was deemed nontoxic and shows potential as a pH-responsive coating on silica nanoparticles. Overall, nanoparticles have struggled in clinical settings such as cancer, due to poor understanding on how to improve tumor specificity. Optoacoustic imaging was utilized to visualize actively and passively targeted mesoporous silica nanoparticles of various size. Our results strongly suggest that 25-50 nm silica nanoparticles coated with chitosan and actively targeted with pH low insertion peptides significantly improve tumor specificity in an orthotopic model of pancreatic cancer. This data represents tools and guidelines to follow in the creation of optoacoustic contrast agents and delivery mechanisms to specifically target biological processes, such as pancreatic cancer. In addition, these results suggest future opportunities to improve optoacoustic imaging applications.

Chapter 1 – Introduction

Sections of this chapter have been published as review manuscripts in *Radiology: Imaging Cancer* and *ACS Bioconjugate Chemistry*:

William M MacCuaig*, Meredith A Jones*, Oshaani Abeyakoon, Lacey R McNally. "Development of Multispectral Optoacoustic Tomography as a Clinically Translatable Modality for Cancer Imaging" *Radiol Imaging Cancer* 2020 Nov 20; 2(6): e200066. doi: 10.1148/rycan.2020200066

Kristina Ilina*, **William M MacCuaig***, Matthew Laramie*, Jannatun N. Jeouty, Lacey R. McNally, Maged Henary. "Squaraine Dyes: Molecular Design for Different Applications and Remaining Challenges" *Bioconjugate Chem.* 2019 July 31; 31(2):194-213. doi: 10.1021/acs.bioconjchem.9b00482

The goal of the work detailed herein is to expand the relevance of optoacoustic tomography through improving optoacoustic signatures and the delivery of contrast agents. Optoacoustic imaging is an emerging modality that has recently gained popularity as a clinically translatable technique. Optoacoustic imaging exploits the photoacoustic effect, which is the generation of mechanical pressure waves as a result of light absorption of chromophores and subsequent thermoelastic contractions. Advantageous to conventional and optical imaging techniques, optoacoustic imaging uses near-infrared (NIR) light, which penetrates efficiently in biologic tissue. The high-transparency characteristics of NIR light in biological tissue mitigate the issue of photon scatter and therefore allow for increased depth penetration into tissue with reduced sacrifice to resolution[1,2]. In essence, high spatiotemporal and spectral resolution from light-based illumination imaging is merged with excellent depth penetration of ultrasound (US) imaging to result in a clinically relevant tool for noninvasive imaging[3,4].

While optoacoustic imaging techniques range from macroscopic purposes (optoacoustic computed tomography) to microscopic purposes (optoacoustic microscopy)[5], this work

will be focused on optoacoustic tomography. Optoacoustic tomography can image at depths up to 5 cm, allowing for noninvasive organ imaging in a clinical setting[2,6]. Typically, optoacoustic tomographic systems use large-field illumination and capture generated ultrasonic waves with a 2D (**Figure 1.1A-B**) or 3D array (**Figure 1.1C-D**) of transducers. When acquiring images, samples are placed perpendicular to the excitation laser bundle. In the case of preclinical imaging specifically, *in vitro* testing is performed using tissue mimicking phantoms. The phantoms, fabricated from polymerized agar and intralipid to simulate human tissue imaging properties, are loaded with contrast agents and rotated to be consistent with the geometry of the transducer (**Supporting Figure S1.1A-D)**. *In vivo* testing with small animal models is performed similarly to the *in vitro* evaluation; serial cross-section slices of animals are acquired by movement of the animals through the transducer array (**Supporting Figure S1.1E-F)**.

Improvements in optoacoustic detection systems have allowed for real-time image visualization, a valuable feature in the clinic. Addition of multiwavelength illumination and spectral processing to optoacoustic tomography creates the ability to separate individual optoacoustic agents from the total signal; a feature that is not possible with single wavelength illumination[5,7]. Together, optoacoustic tomography coupled with multispectral processing creates a powerful imaging tool that allows for a noninvasive and spectrally enhanced clinical method of tracking multiple agents within the body, known as multispectral optoacoustic tomography (MSOT)[5,7].

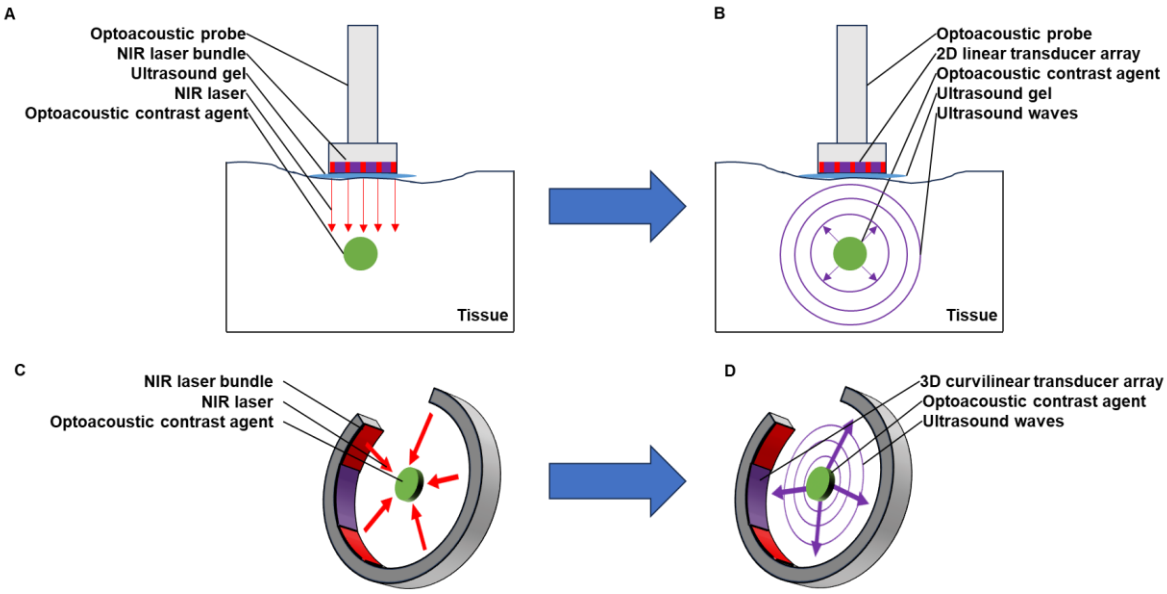

Figure 1.1: Common optoacoustic tomography imaging setups. A) Clinical probes emit pulsed NIR light to excite contrast agents and B) contains a 2D linear transducer array to acquire resultant ultrasonic waves. C) Preclinical system emits NIR light from a near-full ring inside of a water bath to excite contrast agents and D) acquire ultrasonic waves through the same 3D curvilinear transducer array.

MSOT uses multiple wavelengths to acquire optoacoustic images, allowing for the identification of multiple distinct chromophores based on unique spectral identifiers[5,7]. In particular, most MSOT setups are equipped with tunable (1 nm accuracy) lasers with working ranges from approximately 680 nm to 1200 nm. By utilization of nanosecond pulsed near-infrared light, instantaneous temperature increases are assumed, negating thermal diffusion effects.[8] This allows for the assumption that the amplitude of the generated optoacoustic waves is proportional to the incident light intensity and the absorption/thermoelastic properties of the absorber.[9] Following molecular contractions and expansions as a result of temperature increases, resultant ultrasonic waves are created with broadband frequency that can range from less than 1 MHz to several hundred MHz.[10] The ultrasonic frequency is largely a result of the size of the absorber;

larger absorbers generate lower frequency components.[9] For optoacoustic tomography, detection of the acoustic waves at each transducer element is required to merge data and formulate an image. Since high-frequency ultrasound waves are attenuated at a higher rate, central frequencies of transducers used in optoacoustic tomography are typically between 5 and 20 MHz to maximize imaging depth.[11]

Signal reconstruction follows image acquisition. If the image needs to be reconstructed in real time, a back projection reconstruction can be used. Although sufficient, back projection places a higher emphasis on high-frequency signals and may produce negative optical-absorption values in the images, of which have no physical interpretation[12]. MSOT software allows the user to modify the bandpass filter to adjust the low and high frequency cutoffs to remove the negative values and deconvolute with the electrical impulse response of the transducer before back projection reconstruction. A more accurate reconstruction algorithm is a model-based approach. This approach factors in the geometry of the transducer, yielding a more accurate image, but this is at the cost of computational performance time. Model-based reconstructions are favorable and frequently used to reconstruct offline[12].

After successful reconstruction, the spectral shapes of these chromophores must be unmixed from each other and the background to identify respective origins. The process of spectral unmixing requires subpixel detection in that the signal produced from each individual pixel can be a composite signal from one or more chromophores in different concentrations. High heterogeneity of human tissue also has a substantial effect on the acoustic properties of the tissue, resulting in wavelength and position dependent optical fluence problems that affect the spectral signature produced. This phenomenon is

commonly termed spectral coloring[7,13]. The nonuniformity of human tissue poses a challenge for characterizing the optical properties of tissues; however, complex nonlinear mathematic formulations can be used to account for the spectral coloring[7,14]. When using MSOT *in vivo*, a linear regression is used to unmix the spectral signatures in real time. To use a linear-regression unmixing method, the spectra of interest must be predefined, usually as oxyhemoglobin, deoxyhemoglobin, and other agents of interest. Although linear unmixing models are most commonly used, these models assume that wavelength- and depth-dependent fluence issues are uniform and therefore can be neglected[15]. Many different unmixing algorithms have been successfully developed to obtain information of interest, but there is no reference standard. The unmixing algorithms include statistical detection methods such as adaptive match filters, adaptive cosine estimators, principal component analysis, and independent component analysis. These statistical methods model the background as a multivariate distribution, in which statistical outliers are then defined as locations of positive targets[7,13]. Modeling the background as a statistical distribution handles spectral coloring by accounting for spectral fluctuations. Statistical methods are successful for small, spatially constrained targets, such as solid tumors or tissue metastases, but would fail in cancers in which the target is spread throughout the blood or background tissue. Principal and independent component analyses are unique in that they can be used blindly, with no prior knowledge of the target spectra. Although seemingly advantageous, these blind methods introduce uncertainty and are often not reproducible[7].

After successful unmixing, the image can be visualized where signal from each optoacoustic agent is layered on a grayscale background image. The wavelength of the

background image can be chosen on the basis of the experimental needs. Choosing a wavelength around 900 nm for the background image will highlight anatomic features while minimizing background contributions from the strongly emitting chromophores, oxyhemoglobin, and deoxyhemoglobin. The background image can be modified offline at any point in the image processing. Preclinically, it is possible to visualize multiple chromophores on the same background image in real time. However, clinical MSOT imaging in real time requires each agent of interest to be in a different panel. Offline, the different agents can be merged and layered to visualize their interactions[16] (**Figure 1.2**).

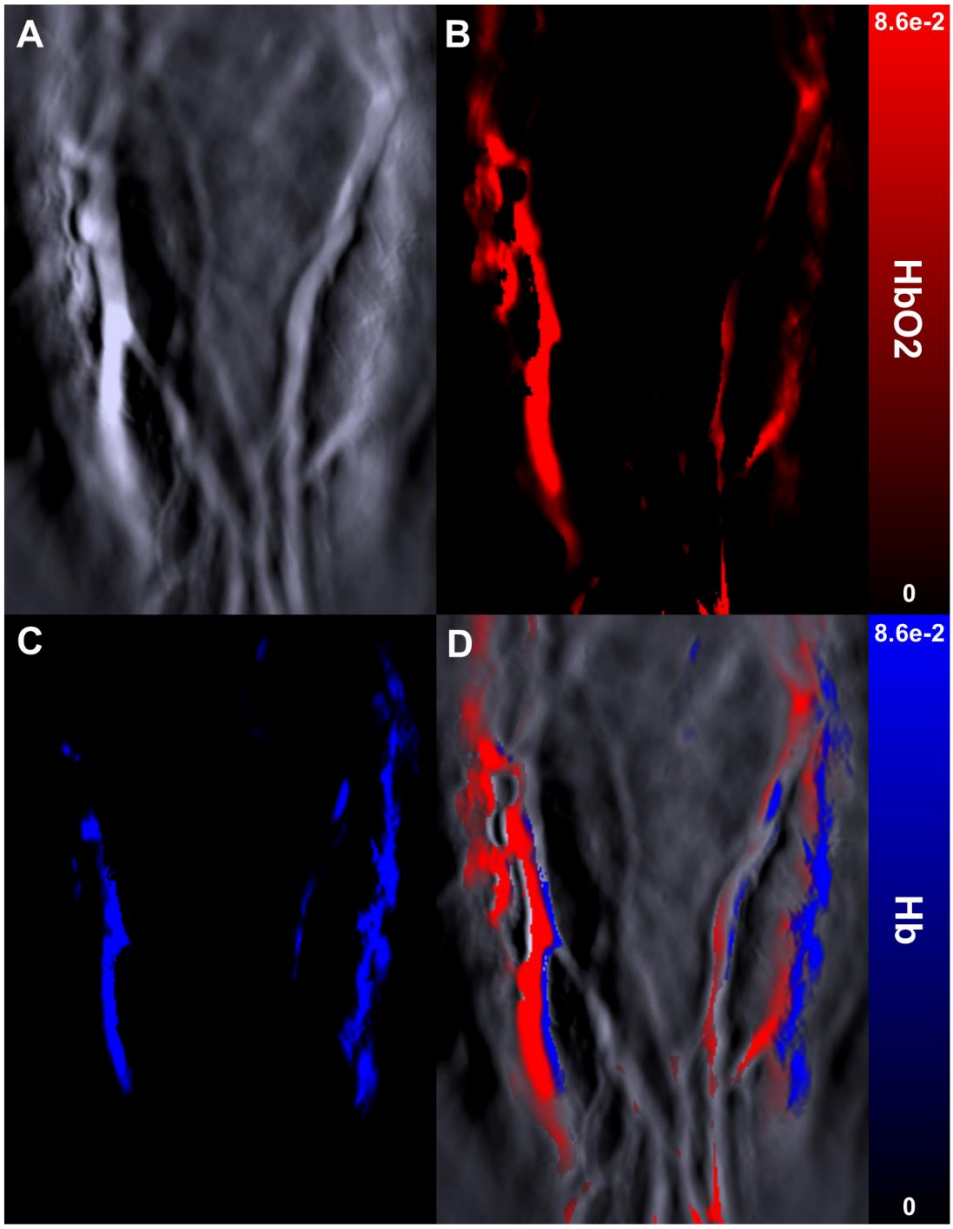

Figure 1.2: Multispectral optoacoustic tomography of a human finger. A) Backprojection reconstructed, mixed optoacoustic image B) Multispectral processed oxygenated hemoglobin map. C) Multispectral processed deoxygenated hemoglobin map. D) Oxygenated and deoxygenated hemoglobin maps overlaid on background image (900 nm signal) of a human finger.

The potential value of optoacoustic imaging, namely MSOT, in the clinic has been recognized, but successful clinical translation is currently in preliminary stages[17] (**Table**

1.1). Availability of optimized optoacoustic contrast agents is among the largest limiters of optoacoustic imaging currently. Similar to other imaging techniques, MSOT and other optoacoustic modalities employ reporter agents, whether endogenous to the body or exogenous, to enhance contrast for identification of disease. Most diseases tend to result in overexpression or alteration of various molecules in the body, some of which are optoacoustic by nature and are therefore detectable directly by using MSOT[6,16,18]. Oxygenated and deoxygenated hemoglobin are the two most popular contrast agents; due to differences in spectral signatures of the two molecules, applications that involve differences in oxygenated blood can be monitored with optoacoustic imaging (**Figure 1.2**). Such applications can include gastrointestinal disease and cancer as well as symptoms such as hypoxia and angiogenesis. The use of these endogenous agents eliminates the need for unnecessary risk associated with introduction of a drug into the body, while still providing structural and functional information. However, endogenous agents are often weak reporting agents in terms of specificity and intensity. In fact, the small group of optoacoustic agents represents a substantial bottleneck for optoacoustic imaging techniques. Although these agents have been under focus recently, the approval process is rather lengthy, hindering adoption of optoacoustic imaging in the clinic. To this end, a wide range of exogenous agents have been under development to mitigate this issue of sensitivity and be used in detection and tracking of the progression of various diseases. Some of these exogenous agents include NIR small organic dyes[19,20] and nanoparticles[21,22].

Table 1.1: Current clinical applications of optoacoustic imaging and multispectral optoacoustic imaging.

Application	Type	Laser	Detector	Patients	Study
Breast Imaging	Volumetric handheld probe	Q-switched OPO laser at 730, 760, 800, 850 nm	256 element, 4 MHz, spherical transducer array	2 women with dense fibro glandular breast tissue	Dean-Ben et al[23]
Breast Imaging	Optoacoustic microscopy	Q-switched alexandrite laser at 755 and 795 nm	512 element, 2 MHz, hemispherical transducer array	30 patients with known breast tumors	Toi et al[24]
Breast Imaging	MSOT	NIR laser at 28 wavelengths from 700 nm-970 nm	256 element, 5 MHz, arc transducer array	10 patients with breast cancer, 3 healthy volunteers	Diot et al[16]
Breast Imaging	MSOT+US	NIR laser at 800 nm	256 element, 4 MHz, arc transducer array	94 patients between the ages of 24-88	Abeyakoon et al[25]
Breast Imaging	Handheld OA/US transducer	NIR laser at wavelengths of 757 and 1064 nm	128 element, 4-16 MHz, linear array	2105 patients from 16 different sites	Neuschler et al[26]
Breast Imaging	Handheld OA/US transducer	NIR laser at wavelengths of 757 and 1064 nm	Four conventional US diagnostic transducers	209 patients from 5 different sites	Menezes et. al.[27]
Prostate Imaging	TRUSPA	Tunable pulsed laser 680nm – 950nm	64 element, 5 MHz, CMUT linear array	20 patients with prostate cancer (10 with ICG 10 without)	Kothapalli et al[28]

Gynecological Imaging	Optoacoustic imaging	Q-switch Nd: YAG 532nm laser	10 MHz focused transducer with 10mm focal distance	30 *ex vivo* cervical tissue samples	Peng et al[29]
Gynecological Imaging	Co-registered transvaginal OA Tomography/US	Pulsed Nd: YAG laser at 690-900 nm	128 element, 6MHz, endocavity US transducer	16 women	Nandy et al[30]
Gynecological Imaging	Fast scanning, optical resolution photoacoustic endoscopy	532 nm pulsed focused fiber laser	40 MHz custom focused ultrasound ring transducer	2 pregnant women	Qu et al[31]
Inflammatory Bowel Disease (Crohn's)	MSOT	Pulsed Nd: YAG laser at 680-980 nm	64 element, 4 MHz, and 256 element, 3 MHz, probes	108 patients	Knieling et al[3]
Inflammatory Bowel Disease (Colitis)	MSOT	Pulsed Nd: YAG laser at 680-980 nm	64 element, 4 MHz, and 256 element, 3 MHz, probes	44 patients	Knieling et al[32]
Dermatological Imaging	MSOM	flash-lamp pumped Nd: YAG OPO pulsed laser 460-650nm	54.2 MHz broadband spherically focused transducer	28-year-old healthy man	Schwarz et al[33]
Dermatological Imaging	Volumetric MSOT	690-900nm tunable OPO pulsed laser	256 element, 4MHz, spherical transducer array	3 patients with skin lesions	Chuah et al[34]
Lymph Node Imaging	Vevo LAZR optoacoustic imaging	Pulsed laser 680-970 nm	21 MHz, linear	12 lymph nodes *ex vivo*	Langhout et al[35]

			transducer array		
Lymph Node Imaging	Handheld MSOT	ND: YAG tunable OPO laser from 680-980nm	256 element, 4MHz, cylindrically focused array	20 patients with administered ICG	Stoffels et al[1]
Grave's Disease	Handheld MSOT	Pulsed laser 700-970 nm	256 element, 4MHz, arc orientation	8 volunteers and 10 patients	Kronke et al[36]
Grave's Disease and Thyroid Cancer	Handheld MSOT	9 ns pulsed laser from 700-950 nm	256 element, 3MHz, 40x40 mm field of view	18 patients	Roll et al[37]
Cardiovascular Disease Monitoring	Volumetric MSOT	Pulsed laser 730-1064 nm	256 element, spherical array	16 volunteers	Ivankovic et al[38]
Systemic Sclerosis	Handheld US/MSOT	Pulsed Nd: YAG laser at 680-980 nm	256 elements, 4MHz, linear array	8 volunteers and 7 patients	Masthoff et al[39]
Metabolic Disease in Adipose Tissue	MSOT	Pulsed laser at 680-950 nm	256 element, 5MHz, cylindrically focused array	13 volunteers	Reber et al[40]

Clinically approved organic dyes for angiography, including indocyanine green (ICG) and methylene blue, have been shown to generate optoacoustic signal in addition to the more common use of generating fluorescence signal[41]. Particularly, albumin binds ICG, creating an impermeable probe for detection with optoacoustic modalities. Isosulfane blue is another example of an organic dye used for photoacoustic imaging[19]. In addition, a variety of fluorescence molecules have shown the potential for generating optoacoustic signal detectable with modalities such as MSOT. These include cyanine dyes and NIR

proteins such as Cy-series[20] and the iRFP-series[42] of agents. An example of an NIR dye is IR800CW[43], which is currently in phase II trials for fluorescence imaging and has shown optoacoustic signal generation with associated imaging targets[44]. Recently, the potential for the use of squaraine dyes in optoacoustic applications has been summarized, with the summary including how structural characteristics are thought to affect absorption spectra[45]. Synthesized organic dyes are most often used for perfusion imaging when used as single-element contrast agents, but incorporation into other technologies provides improvements to photostability, clearance, and specificity by active targeting for use as a molecular probe[46]. Squaraine dyes are a class of organic dyes with an electron deficient central four-membered ring that have a resonance stabilized zwitterionic structure[47]. Squaraines have been used as contrast agent for fluorescence imaging due to their planar structures and zwitterionic properties[48,49]. Such properties result in squaraine dyes exhibiting strong absorption and emission in the NIR region, which also implicate squaraines as potential contrast agents for optoacoustic imaging. Squaraines have extremely intense and narrow absorption bands in the NIR range with a high molar absorption coefficient[50-53]. Squaraine dyes also demonstrate excellent photostability[54-56] and high quantum yield[50]. Additionally, they are prepared through a straight forward synthetic procedure[57].

Gold nanoparticles have been among the most-studied metal-based optoacoustic contrast agents, as the physical shape of these particles provides an opportunity to craft a highly distinguishable absorption spectrum[58]. Further, gold naturally provides high absorption of NIR light, resulting in a strong optoacoustic signal. Because of ease of synthesis and established methods, gold nanoparticles have been studied in their

conventional spherical geometry, as well as in the shape of rods, shells, and other unique structures, mostly in the context of tumor imaging[22,59]. However, the strong and distinguishable signal is accompanied by toxicity, namely induction of reactive oxygen species and accumulation in the liver and spleen[60]. Surface modifications of these particles, such as polymer coatings or peptide conjugates, are essential when considering the goal of clinical translation, as these modifications could partially mitigate issues of toxicity, but may come at the expense of reduced optoacoustic signals. Other types of metal-based nanoparticles have shown optoacoustic activity, such as silver and iron oxide[21,61]. Often, absorption profiles of nanoparticles are tunable according to structural characteristics. In addition to metal-based particles, carbon nanotubes are another form of specialized optoacoustic nanoparticle, with sizes less than 5 nm, that relies heavily on the aforementioned surface modifications[62,63]. With the core particle–synthesis procedure of metal-based nanoparticles having been well established, recent focus in this area has concerned the development of activatable optoacoustic agents and surface modifications. These modifications aim to relieve toxicity, incorporate active targeting for specificity, or enable inclusion of other contrast agents within the particles for controlled delivery[6,64].

The aim of this dissertation is to describe the work that has been performed to 1) develop a more advanced understanding of how to generate optoacoustic contrast agents (Chapters 2-3) and 2) apply optoacoustic imaging to specifically visualize targeted tissue, in this context, pancreatic ductal adenocarcinoma in a murine model (Chapters 4-5).

Chapter 2 – Influence of Structural Moieties in Squaraine Dyes on Optoacoustic Signal Shape and Intensity

This chapter has been accepted and is in press as a research manuscript in *Chem*:

William M MacCuaig, Carly Wickizer, Richard S. Van, Megan R. Lerner, William E. Grizzle, Yihan Shao, Maged Henary, Lacey R McNally. “Influence of Structural Moieties in Squaraine Dyes on Optoacoustic Signal Shape and Intensity”

2.1 Abstract:

Optoacoustic imaging has grown in clinical relevance due to inherent advantages in sensitivity, resolution, and imaging depth, but development of contrast agents is lacking. This study assesses the influence of structural features of squaraine dyes on optoacoustic activity, through computational models, *in vitro* testing, and *in vivo* experimentation. The squaraine scaffold was decorated with halogens and side chain extensions. Extension of side chains and heavy halogenation of squaraines both increased optoacoustic signals individually, although had a more significant effect in tandem. Density functional theory models suggest the origin of increased optoacoustic signal is due to increases in transition dipole moment and vibrational entropy, which manifested as increased absorbance in NIR wavelengths and decreased fluorescence quantum yield. This study provides insight into the structure-function relationships that will lead to guiding principles for optimizing optoacoustic contrast agents. Further developments of squaraines and other agents will further increase relevance of optoacoustic imaging in a clinical setting.

2.2 Introduction:

Optoacoustic imaging is an emerging imaging modality that utilizes the photoacoustic effect to achieve clinically significant resolution at depths beyond current techniques[6,65]. Following unique absorption of nanosecond pulsed near-infrared light by selected

optoacoustic agents, thermoelastic expansions generate detectable ultrasonic waves[66]. In contrast to optical imaging, optoacoustic imaging overcomes the restriction of depth due to photon scattering while maintaining high sensitivity and spatial resolution on the scale of 10 cells, or 200 microns in a clinical setting, and as low as 75 microns[65,67]. This advantage has established optoacoustic imaging as a powerful modality and supports ensuing clinical trials[65,68-71]. Multi-wavelength illumination with a tunable laser source and processing equipped with optoacoustic tomography, coined as multispectral optoacoustic tomography (MSOT) allows for separation of optoacoustically active chromophores. However, to successfully separate the chromophores, which include oxyhemoglobin and deoxyhemoglobin, absorption spectra need to be unique. With few distinct endogenous contrast agents[72,73], MSOT clinical trials have largely been limited to conditions involving differential oxygenation, such as breast cancer[4,16,26], inflammatory bowel diseases[74], or dermatologic conditions[39,75]. Utilization of exogenous contrast agents presents an opportunity for optoacoustic imaging to expand in relevancy in the clinic. Optoacoustic imaging has largely exploited commercially available near-infrared dyes, including IR-800-CW[43,76], indocyanine green (ICG)[41,77], or methylene blue (MB)[78,79]. IR-800-CW was specifically engineered for maximum fluorescent signal resulting in sub-optimal optoacoustic signals, or non-unique and non-separable spectral shapes. Interestingly, not all near-infrared dyes used for fluorescence present measurable optoacoustic signal, including Rhodamine 800[78].

While optoacoustic imaging often detects near infrared fluorescent dyes, the fundamental understanding of structural features that give rise to optoacoustic signal is limited[78]. Generally, the relationship between optoacoustic signal generation and structural features

is based upon knowledge from fluorescence, and therefore lacks guiding principles for the design of enhanced optoacoustic agents. For example, compounds with high ring density, electron-donating groups, and rigidity of the central ring tend to show fluorescent properties[80,81]. However, the generation of fluorescence and optoacoustic signal are different pathways of energy dissipation, and therefore, fluorescence quantum yield and optoacoustic activity are inversely related. As fluorescence is a result of radiative decay and optoacoustic activity is due to non-radiative decay, e.g., generation of heat, it is likely that there are moieties that result in increased optoacoustic activity at the expense of fluorescence. Rhodamine 800, as an opposite example, generates substantial fluorescent signal, but no measurable optoacoustic signal[78].

Squaraine dyes are relatively basic and stable molecules[45] that in turn may facilitate a greater understanding of specific influences of structural features on optoacoustic signal. Easily controllable molecules are critical for understanding the origin of complex energy transfer through a systematic approach. Ultrasonic waves originate from thermoelastic expansions, which are a direct result of molecular overtone transitions due to anharmonicity of chemical bond vibrations.[82] These thermoelastic expansions have been shown to increase through nonradiative heat generation by chemical reduction of reactive oxygen species. Introduction of heavy atoms and halogens can reduce reactive oxygen species generation[83], and therefore we hypothesize inclusion of heavy side chains conjugated to the central squaric acid may enhance non-radiative decay and thermoelastic potential of compounds, leading to increased optoacoustic activity. Thus, this study details a systematic approach to increasing side chain weight by: 1) various halogenation (fluorine, chlorine, bromine) at the 5th position of the heterocyclic ring; and

2) extended hydrocarbon chains. This study sought to elucidate the potential role of varying the side chain substitutions at the heterocyclic ring N-atoms in the generation of optoacoustic signals using an *in vivo* model as a first step in identifying the role for specific structural features in generating optoacoustic signals and greater intensities. Further, computational modeling approaches are utilized to develop an understanding of how to create primarily optoacoustic contrast agents and potentially provide predictions on the strength of optoacoustic molecules. In addition, a second class of molecules were synthesized and evaluated for increased optoacoustic signal due to halogenation of side chains.

2.3 Materials and Methods:

2.3.1 Materials

All chemicals and solvents were of American Chemical Society grade or high-performance liquid chromatography (HPLC) purity and were used as received. HPLC grade ethanol, MB dye (M9140), and tetrahydrofuran were purchased from Sigma-Aldrich (St. Louis, MO, USA). Milli-Q water-unit was purchased through Milli-Pore, Sigma. All other chemicals were purchased from Fisher Scientific (Pittsburgh, PA, USA) or Acros Organics (Pittsburgh, PA, USA). The reactions were monitored using ultraviolet-visible (UV−VIS) and near-infrared (NIR) absorption spectra and recorded on a Varian Cary 50 spectrophotometer.

2.3.2 Synthesis of Optoacoustic Dyes

The corresponding hydrazines (4.00 g, 22.3 mmol) were reacted with 3-methylbutanone (3.00 mL, 28.0 mmol) in acetic acid and heated to a 100°C for 24 h (**Figure 2.1**). The resulting mixture was diluted with dichloromethane followed by successive neutralization

with sodium bicarbonate. The extracts obtained were then concentrated under reduced pressure to afford the cyclized intermediates. Intermediates were furthered alkylated using 3-bromo-N, N, N-trimethylpropan-1-ammonium bromide, or methyl iodide in acetonitrile under reflux conditions for about 72 h to form heterocyclic salts. The ^{1}H nuclear magnetic resonance (NMR) and ^{13}C NMR spectra were obtained using high-quality Kontes NMR tubes (Kimble Chase, Vineland, NJ, USA) rated to 400 MHz and were recorded on an Avance II spectrometer (Bruker, Billerica, MA; 400 MHz for ^{1}H and 100 MHz for ^{13}C) in dimethylsulfoxide-d6, and D_2O. High-resolution mass spectra (HRMS) were obtained at the Georgia State University Mass Spectrometry Facility using a Q-TOF micro (ESI-Q-TOF) mass spectrometer (Waters, Milford, MA, USA). All compounds tested were >95% pure.

The various salts (1 molar eq.), squaric acid (0.5 molar equiv.), and quinoline (5 molar equiv.) were dissolved in a mixture of n-butanol and benzene (40 mL, 1:1 by volume). The resulting mixtures were refluxed under azeotropic distillation condition using a Dean Stark apparatus for 15 h. The reaction mixtures were continuously monitored using UV-VIS/NIR spectrophotometry until signals were observed. After successful completion of the reactions, the solvents were removed under reduced pressure. The crude products were precipitated using ethyl acetate and acetone and dried under vacuum. The desired optoacoustic probes were finally obtained following co-precipitation methods using methanol and ethyl acetate.

2.3.3 Dye Evaluation

Following synthesis of compounds, each was diluted for subsequent evaluation and analysis. Specific dilution methods are noted under the relevant type of analysis.

Squaraines were diluted in ethanol (50%) and water to a concentration of 1 mM and loaded into 3 mm cylindrical wells in solidified tissue mimicking phantoms consisting of 1.3% wt agar and 6% vol intralipid in distilled water. Samples were evaluated via MSOT at multiple wavelengths (680-900 nm in 5 nm steps) for NIR absorption and optoacoustic signal generation.

2.3.4 Computational Modeling

Density functional theory (DFT) and time-dependent density functional theory (TD-DFT) calculations were performed using the Q-Chem Software package[84]. For each molecule, the ground-state geometry was optimized in the gas-phase using DFT with the Perdew-Burke-Ernzerhof (PBE) functional[85] and 6-31+G* basis set[86]. At these optimized geometries, TD-DFT calculations were performed with the same combination of functional and basis set to obtain the vertical excitation peaks for each molecule. The lowest energy (highest wavelength) absorption was analyzed. The orbital plots were generated using the IQmol graphical user interface. The vibrational entropies were obtained from harmonic frequency analysis on the ground-state potential energy surfaces.

2.3.5 Cell Lines

293 human kidney cells, HEPG2 human liver cells, COLO205 human colon cells and human umbilical vein endothelial cells (HUVEC) (American Type Culture Collection, Manassas, VA, USA) were utilized in this study. Cells were grown in standard Dulbecco's Modified Eagle Medium (DMEM) equipped with 10% fetal bovine serum (FBS) and 1% L-glutamine. Cells were housed in an incubator at 37°C and 5% CO_2.

2.3.6 *In Vitro* Cell Viability

Kidney (293), liver (HEPG2), colon (COLO205), and umbilical vein (HUVEC) cell lines were plated at $5x10^3$ cells per well for 24 h in 96 well plates as indicated above. Squaraines were diluted in phosphate buffer saline (PBS) at concentrations of 200 µg/mL and 20 µg/mL. Cyanine dyes were diluted in PBS at concentrations of 100 µg/mL and 10 µg/mL. Cells received treatment with 2.5 µL of dyes at each concentration allowed to continue to incubate for 24 h. ATPlite™ (Perkin Elmer, Waltham, MA) was utilized with a Synergy HTX plate reader (BioTek, Winooski, VT) to measure adenosine triphosphate (ATP) levels for cellular viability assessment. To avoid potential interactions with other dye-based viability assays (MTT and MTS assays) ATPLite™ was utilized.

2.3.7 Western Blot Analysis

Colon (COLO205) cells were treated with 200 µg/mL of squaraines, or 600 nM of paclitaxel for 8 h. Protein lysates were harvested and quantified with standard techniques. 4-12% bis-tris gels were loaded with treated cell lysates and transferred to standard western blot membranes. Caspase 3 (pro+active) antibody was utilized to evaluate if treated cells were undergoing apoptosis. Paclitaxel (600 nM) enters cells through caveolae-mediated endocytosis[87] and causes mitotic halt and cellular death through microtubule stability and thus, served as a positive control in this study.[88] Vinculin antibody was used as a loading control. Membranes were visualized and quantified on a LI-COR Odyssey CLx near-infrared imaging system.

2.3.8 Thermal Stability

Photothermal stability studies were performed on compounds. Stock solutions (1 mM) were prepared in dimethyl sulfoxide, and the solutions were diluted to an optical

absorbance of 1. Solutions were placed 12 inches from a 15 W UV lamp. Absorbance values at maximum were measured as a function of time irradiated by the UV lamp.

2.3.9 Murine Model

4 wk old athymic female mice were used for this study. The hair of immunocompetent mice often obscures signal due to the lack of a smooth surface between skin and ultrasound gel/water/transducer. Utilization of athymic mice eliminates a potential confounding variable. Studies strictly adhered to the Oklahoma University Health Science Center Institutional Animal Care and Use Committee approved protocol (IACUC number 302166). Mice were set on a 2920X alfalfa free diet and ultrapure water to reduce background imaging signals.

2.3.10 *In Vivo* Evaluation of Dye Accumulation

All mice received oral administration with 100 μM squaraine dyes in water through standard, sterilized 20-gauge gavage needles. Oral administration was utilized for visualization of the colon lining and not the vasculature. Approximately five minutes following oral administration, mice were anesthetized and were imaged for up to 30 minutes, or 6 hours for longer term study in the supporting information, using InVision 512 TF MSOT (iThera Medical, Munich, Germany). Tomographic cross-section images were acquired prior and subsequent to the target cross-sections to ensure visualization of all signal from compounds. A custom designed animal holder (iThera Medical) was used in tandem with a nose cone for anesthesia (1.5% isoflurane in 0.8 L/min medical air and 0.2 L/min O_2) to allow for ventral imaging. 25 frames at each 0.2 mm imaging slices in the axial direction through the spleen and into the colon were captured at wavelengths 680, 710, 730, 740, 750, 760, 770, 780, 800, 850, and 900 nm for each position with a tunable,

pulsed NIR laser source. Acquisition time was limited to 10 μs per frame to reduce impact of animal movements. Mice were carefully monitored by video observation while imaging to ensure no distress throughout the procedure. Following completion of imaging, mice were evaluated with NIR fluorescence using an advanced molecular imager (AMI) (Spectral Imaging Instruments, Tucson, AZ). NIR fluorescence was used to corroborate results observed with MSOT imaging. Mice were euthanized by carbon dioxide overdose and cervical dislocation following completion of live-animal imaging.

2.3.11 *Ex Vivo* Organ Analysis

Upon completion of live-animal imaging, organs including the colon, liver, spleen, and kidney were excised using standard techniques. Organs were evaluated *ex vivo* using NIR fluorescence to confirm live-animal imaging results with MSOT and NIR fluorescence imaging. Liver, kidney, small intestine, and colon also were stained with hematoxylin and eosin (H&E) to assess morphological toxicity.

2.3.12 Statistics

Analysis of variance (ANOVA) with post hoc comparisons was utilized to evaluate differences in optoacoustic signal *in vivo* of squaraine compounds. Tukey and Bonferroni corrections were in agreement in the context of adjusting p-values due to multiple comparisons. Significance is defined as (* - $p<0.08$; ** - $p<0.01$; *** - $p<0.001$).

2.4 Results and Discussion:

2.4.1 Dye Synthesis and Characterization

The identification and development of small molecule dyes that are synthesized specifically for optoacoustic imaging is in its preliminary stages. This demands extensive work in designing and synthesizing biosensors with certain structural features that would

generate high intensity and unique optoacoustic spectral signals. Optoacoustic probes with tunable features such as absorption in the NIR region, high extinction coefficient, good photostability, sustained solubility under physiological pH, heavy atoms, and rotatable bonds requires in-depth design and synthetic approaches. Water soluble squaraine dyes, which were highly stable in serum have been synthesized previously[84]. Due to their improved water solubility and stability in serum, this class of compounds was chosen for further evaluation of optoacoustic properties. To achieve this goal, the synthesis procedure reported to synthesize the highly stable symmetrical squaraine dyes was followed, as shown in **Figure 2.1**. A second class of cyanine compounds (**Supporting Figure S2.1**) was synthesized subsequently to ensure universal increase of optoacoustic signal due to side chain halogenation.

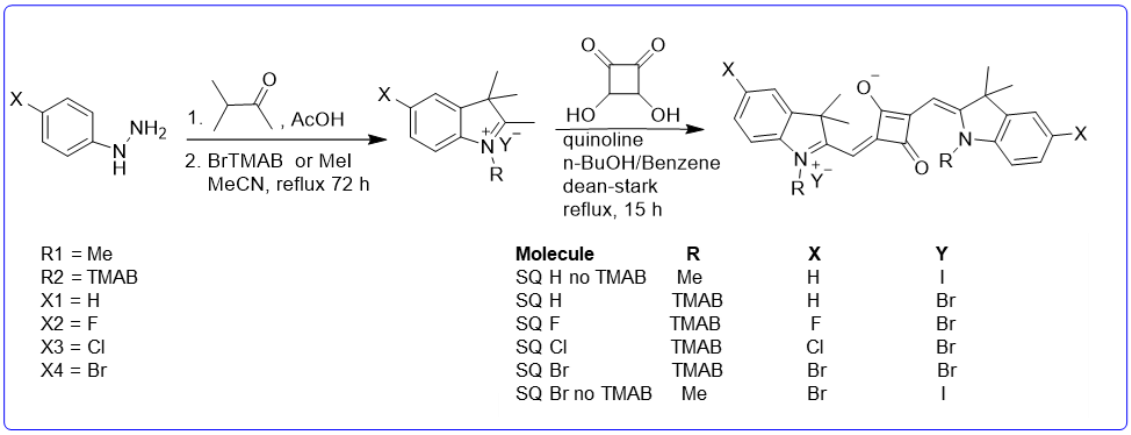

Figure 2.1: Synthetic steps for squaraine optoacoustic probes.

The synthesis begins by performing a Fischer indole cyclization reaction using derivatives of phenyl hydrazine. These nonhalogenated (X = hydrogen (H)) and halogenated (X = fluorine (F), chlorine (Cl), bromine (Br)) hydrazines were allowed to react with 3-methyl-2-butanone under acidic conditions. The intermediates formed after successfully cyclizing

the reactants were further treated with methyl iodide (no TMAB) or 3-bromo-N, N, N-trimethylpropan-1-ammonium bromide (TMAB) in acetonitrile under reflux conditions for 72 h to form salt derivatives, which are intermediates used for synthesis of final squaraines (SQ), and were not evaluated. The probe products obtained were cooled down to room temperature and then precipitated using either acetone or ethyl acetate. The final probes were obtained by reacting the respective indolium salts (2 mole), squaric acid (1 mole), and quinoline in a 50:50 mixture of n-butanol and benzene under reflux conditions for 15 h. To obtain maximum yields, the reactions were performed using a Dean Stark apparatus. The reaction mixtures were continuously monitored using UV-VIS/NIR spectrophotometry until dye signals were observed. After successful completion of the reactions, the solvents were removed under reduced pressure. The crude products were precipitated using ethyl acetate and acetone and dried under vacuum. The desired optoacoustic squaraine probes were finally obtained following a coprecipitation method using methanol and ethyl acetate. All NMR and mass spectra of the compounds are in the **Supporting Figures S2.2-2.16**. **SQ Br no TMAB** is structurally similar to **SQ H no TMAB** with the substitution of bromine at the X position in order to determine the effect of bromination without trimethylpropylammonium substitutions.

To determine the photostability of squaraine derivatives, each compound was incubated in FBS at 37°C. A stock solution of 1 mM of the squaraine dyes was first prepared in dimethyl sulfoxide and an aliquot of these stock solutions (10 µM) was diluted in 100% FBS supplemented with 50 mM HEPES buffer at pH = 7.4 and the absorbance was measured. The solution was continuously irradiated with a xenon lamp at 150 W for 72 h. The optical responsiveness, recognized by absorbance as a percentage of original

absorbance, was measured over 72 h (**Figure 2.2A**). Squaraine dyes with bromine and chlorine atoms (**SQ Br** and **SQ Cl**) retained absorption strength over time, which will result in consistent optoacoustic signal generation. The photothermal stability exhibited by these dyes indicate the absence of photodegradation for application-based timescales. A stable squaraine dye is less likely to undergo photodegradation or other chemical changes that could alter its thermal properties. Thus, **SQ Br** and **SQ Cl** possess adequate thermal stability, which is important for maintaining optoacoustic signal generation over time. In addition, photodegradable squaraine dyes can result in the release of byproducts or changes in the surrounding environment, potentially contributing to background noise in the optoacoustic signal. As a result, photostable squaraine dyes (**SQ Br** and **SQ Cl**) are less likely to introduce these sources of noise, enabling clearer and more accurate optoacoustic signal interpretation. Optical and molecular properties of synthesized squaraine are described (**Figure 2.2B-C**).

A

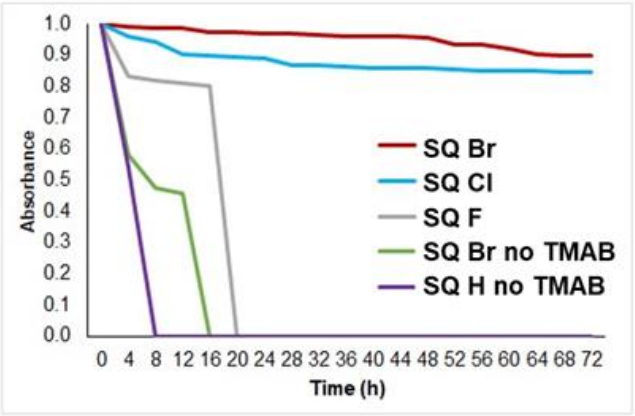

B

Molecule	Λ_{abs} (nm)	Λ_{ems} (nm)	Extinction Coefficient ($M^{-1}cm^{-1}$)	Quantum Yield (Φ, %)
SQ H no TMAB	624	629	129,777	37
SQ H	630	645	168,350	-
SQ F	637	646	193,950	40
SQ Cl	638	656	229,800	40
SQ Br	638	656	204,000	28
SQ Br no TMAB	634	639	109,324	30

C

Molecule	Rotatable Bonds	Surface Area ($Å^2$)	Volume ($Å^3$)	LogD
SQ H no TMAB	8	550	403	-1.2
SQ H	20	796	594	-5.1
SQ F	20	813	607	-4.8
SQ Cl	20	809	622	-3.9
SQ Br	20	818	635	-3.5
SQ Br no TMAB	8	569	443	0.1

Figure 2.2: A) Photothermal stability of squaraines. Compounds were diluted to an optical absorbance of 1 and re-measured after irradiation with a UV lamp. B) Optical properties for squaraines in FBS supplemented with HEPES buffer at pH 7.4 and warmed to physiological temperature (37°C). C) Molecular properties of squaraines. Rotatable bonds, surface area, and volume were computed with RDkit. LogD (lipophilicity) (pH 7.4) was computed with ChemAxon.

Following the synthesis of **SQ H no TMAB** and **SQ H**, initial evaluations via MSOT revealed that **SQ H** exhibited small changes in optoacoustic signal intensity when compared to **SQ H no TMAB** (**Figure 2.3B-C**). Optoacoustic signal has previously been correlated with number of rotatable bonds in the subject molecule[78], however few changes were observed here, likely due to lack of electron withdrawing moieties in the two compounds. This is supported by the increases in vibrational entropy and oscillator strength associated with the substitution of the methyl group (**SQ H no TMAB**) with trimethylpropylammonium (**SQ H**). In addition to optoacoustic data, **Figure 2.3D-I** shows the absorbance and fluorescence intensity of each squaraine and **Figure 2.2B** details the optical properties. Notably, the stark difference between fluorescence and absorbance in **SQ Br** (**Figure 2.3H**) suggests the possibility for high optoacoustic activity.

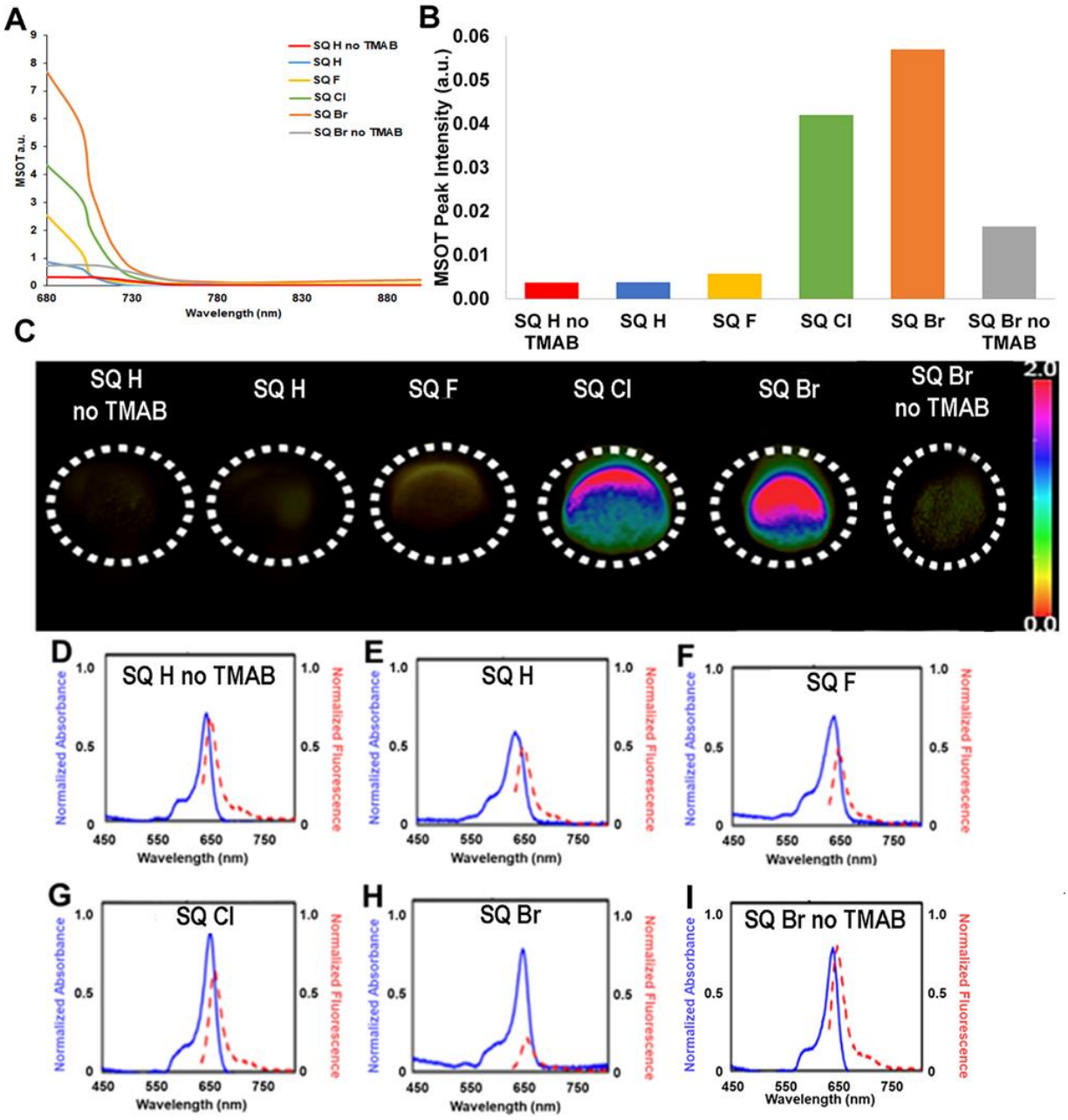

Figure 2.3: Optoacoustic evaluation of squaraines. A) Optoacoustic absorption spectra of squaraines, measured as a function of wavelength. B) Peak optoacoustic intensity of squaraines from optimal tomographic slices portrayed in C). C) Optoacoustic images of squaraines in tissue mimicking phantoms. After encapsulation within tissue mimicking phantoms, in a conical shape, cross section of phantoms rotated horizontally were acquired to yield 2D circular images. UV-VIS absorption (10 μM) and fluorescence spectra (2 μM) for: D) **SQ H no TMAB;** E) for **SQ H**; F) **SQ F**; G) **SQ Cl**; H) **SQ Br**; and I) **SQ Br**

no TMAB in 100% FBS supplemented with 50 mM HEPES buffer at pH = 7.4 and warmed to physiological temperature (37°C). No p-values to report.

Side chains attached to the heterocyclic terminals are hypothesized to impact vibrational entropy of the molecule and are further investigated here. Addition of various electron withdrawing or donating groups can be utilized to maximize photon absorption and provide the molecule with increased size and flexibility for enhanced optoacoustic activity. As the addition of electronegative atoms increases the electron withdrawing strength of the heterocyclic terminals, increasingly large halogens were used for side chains in **SQ F, SQ Cl,** and **SQ Br**. Similar evaluation *via* MSOT revealed significant increases in generated optoacoustic signal due to bromine, chlorine, and fluorine substituted side chains in squaraines **SQ Br**, **SQ Cl**, and **SQ F** respectively (**Figure 2.3A-C**). Following noted increases in **SQ Br**, **SQ H no TMAB** was additionally substituted with bromine at the X-position without trimethylpropylammonium substitution, resulting in **SQ Br no TMAB**, which showed increased optoacoustic signal generation. This data suggests that heavy halogen substitutions, combined with the addition of the trimethylpropylammonium group, may act in tandem to increase optoacoustic activity. The halogenated squaraine compounds are hypothesized to create suitable energy gaps beneficial for non-radiative energy transfer through dissipation, rather than photon emission. This results in quenching of fluorescence, and amplification of optoacoustic signal[85]. Increasing the weight of the halogen increases the probability of intersystem crossing, further amplifying optoacoustic signal, hypothetically at the expense of fluorescence signal[86]. Results also suggest that rotatable bonds from the trimethylpropylammonium group addition are critical for optoacoustic signal[78,89]. Compared to rigid agents such as Rhodamine-800,

which contains no rotatable bonds and displays no optoacoustic activity[78], squaraine compounds functionalized with trimethylpropylammonium groups to increase the number of rotatable bonds exhibit increased optoacoustic activity. Such structural modifications may be impactful for the future development of effective and unique optoacoustic contrast agents.

2.4.2 Quantum Mechanical Computational Modeling

To further understand and identify the variations in experimentally determined optoacoustic capabilities of the trimethylpropylammonium pendant group and halogen substitutions of squaraines, density functional theory (DFT) and time-dependent density functional theory (TD-DFT) were utilized. DFT and TD-DFT are advanced computational methods that have been used extensively to gain a deeper understanding of molecular structures and respective absorption and fluorescence properties[90-93]. DFT and TD-DFT calculations were performed using the Q-Chem Software package[94]. For each molecule, the ground-state geometry was optimized in the gas-phase using DFT with the Perdew-Burke-Ernzerhof (PBE) functional[95] and 6-31+G* basis set[96]. *Cis* isomers of squaraine compounds are assumed to be dominant in this context due to similarities in trends of experimental and computational measurements. Namely, calculated UV-VIS absorbance wavelengths of *cis* isomers were in agreeance with experimentally measured results. All computational data for *cis* isomers are included in the Supporting Information (**Supporting Figure S2.23**). Here, DFT results show a correlation between higher vibrational entropy and MSOT peak intensity between squaraines **SQ H no TMAB** and **SQ H**, the sole structural difference being the trimethylpropylammonium in place of the methyl group on **SQ H** (**Figure 2.4A**). Higher vibrational entropies indicate the molecules

may have the tendency to undergo interatomic stretching, bending, or rotation more readily. Increased tendency of interatomic movement could enhance non-radiative relaxation channels that generate thermal energy, leading to thermoelastic expansions of higher amplitude, and thus, optoacoustic signal generation[97]. DFT modeling confirms squaraines with intense optoacoustic signal have larger vibrational entropies in squaraines with TMAB and halogen substitutions, indicating maximizing vibrational entropy can enhance optoacoustic signal generating capabilities (**Figure 2.4A**).

In general, a greater magnitude of molecular expansion is possible as a result of the halogenated side chains. Maximizing *cis-trans* photoisomerization is anticipated to contribute to higher dynamics and larger expansion of the molecule, leading to higher optoacoustic intensity. (**Figure 2.4D-E**). This effect may be in part due to the halogens acting as electron withdrawing groups in the squaraines, although, the electron withdrawing strength, or halogen electronegativity, was found to be inversely correlated to optoacoustic signal intensity. In addition, electronic excitation probability, i.e., oscillator strength, which is directly related to molar absorptivity, of the synthesized molecules trends with optoacoustic signal strength. As shown in **Figure 2.4B**, the oscillator strengths of the relevant absorption peaks from TD-DFT calculations follows the order of Br > Cl > F > H squaraine substitutions, which is in excellent agreement with experimental MSOT observations of squaraines **SQ Br** > **SQ Cl** > **SQ F** > **SQ H**. Furthermore, **SQ H no TMAB** was predicted to have the weakest oscillator strength, again, consistent with the weak optoacoustic signal as observed through experimental results.

Computationally, the oscillator strength was obtained as $\frac{2}{3}\Delta E|\vec{\mu}|^2$, where ΔE is the absorption energy and $\vec{\mu}$ is the dipole moment. **Figure 2.4C** shows the variation in

transition dipole moments among the squaraine compounds, which directly influences the respective predicted oscillator strengths. Like the trend in **Figure 2.4B**, **SQ Br** holds the largest transition dipole moment, followed respectively by **SQ Cl**, **SQ F**, **SQ H**, **SQ BR no TMAB**, and **SQ H no TMAB**. Through these computational studies, we have identified that the trimethylpropylammonium pendant group and the halogen substituents located on the terminal heterocycles are important factors in optimizing optoacoustic signal generation of these compounds.

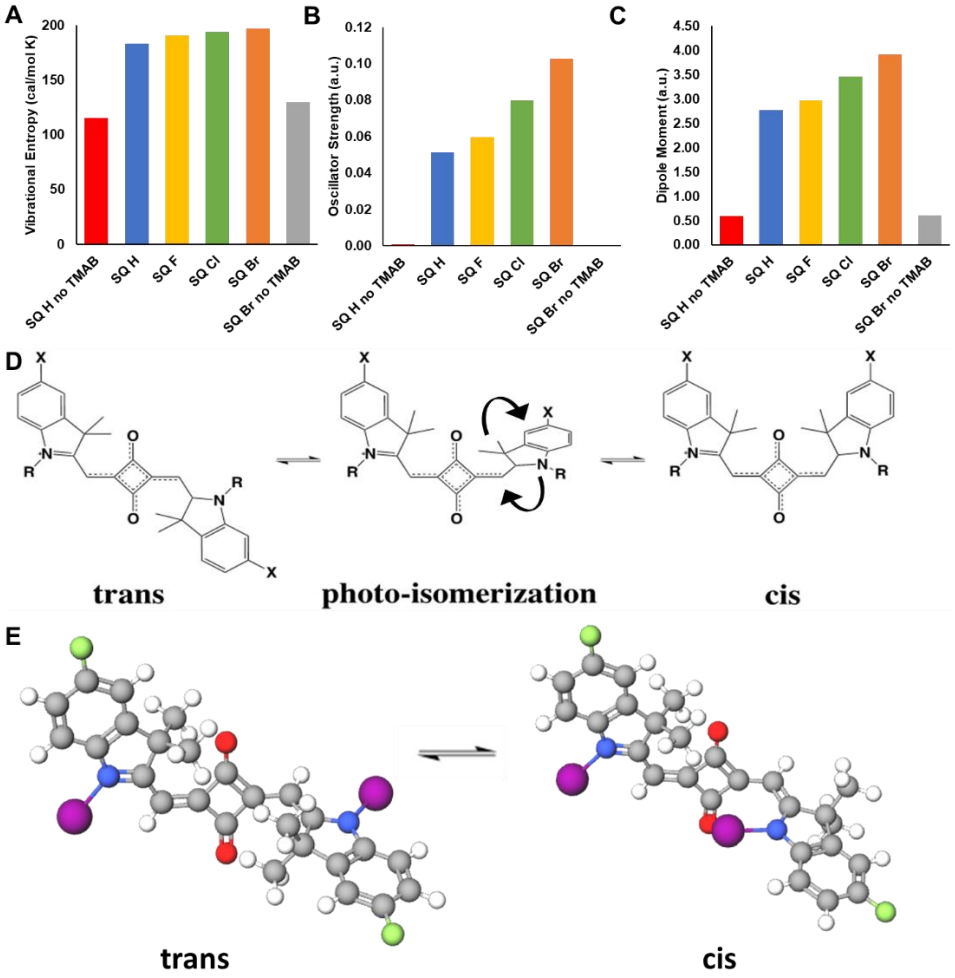

Figure 2.4: Computational modeling of squaraines. A) Vibrational entropy of squaraines from DFT frequency calculations. B) Oscillator strength of the lowest-energy absorptions of squaraines in *cis* conformations from TD-DFT calculations. C) Transition dipole

moment of the lowest-energy absorptions of squaraines in *cis* conformations from TD-DFT calculations. D) 2-D structure of squaraines in *trans* and *cis* conformations through photo-isomerization. E) 3-D structure of squaraines in *trans* and *cis* formations through photo-isomerization. PBE functional and 6-31+G* basis set were used in all DFT and TD-DFT calculations. No p-values to report.

Figure 2.5A-F indicate full computationally derived absorption spectra of squaraines. For MSOT, optoacoustic signal is generated because of the NIR absorption and thus, major and minor peaks at wavelengths below 680 nm do not contribute to optoacoustic signal in a significant fashion. Such peaks in **Figure 2.5** may be disregarded as each has no relation to optoacoustic signal. As expected from experimentally measured optoacoustic activity, a weak absorption peak is observed around 700 nm and 752nm of **SQ H no TMAB** and **SQ Br no TMAB**, respectively. In contrast, larger absorption peaks around 700 nm are noted for TMAB substituted squaraines, each correlating with measured optoacoustic signal (**SQ Br** > **SQ Cl** > **SQ F** > **SQ H** > **SQ H no TMAB**). This data suggests that TMAB functionalized squaraines generate optoacoustic signal after absorption of ~700 nm light, while **SQ H no TMAB** and **SQ Br no TMAB** weakly absorb ~700/750 nm light, and therefore generate minimal optoacoustic signal.

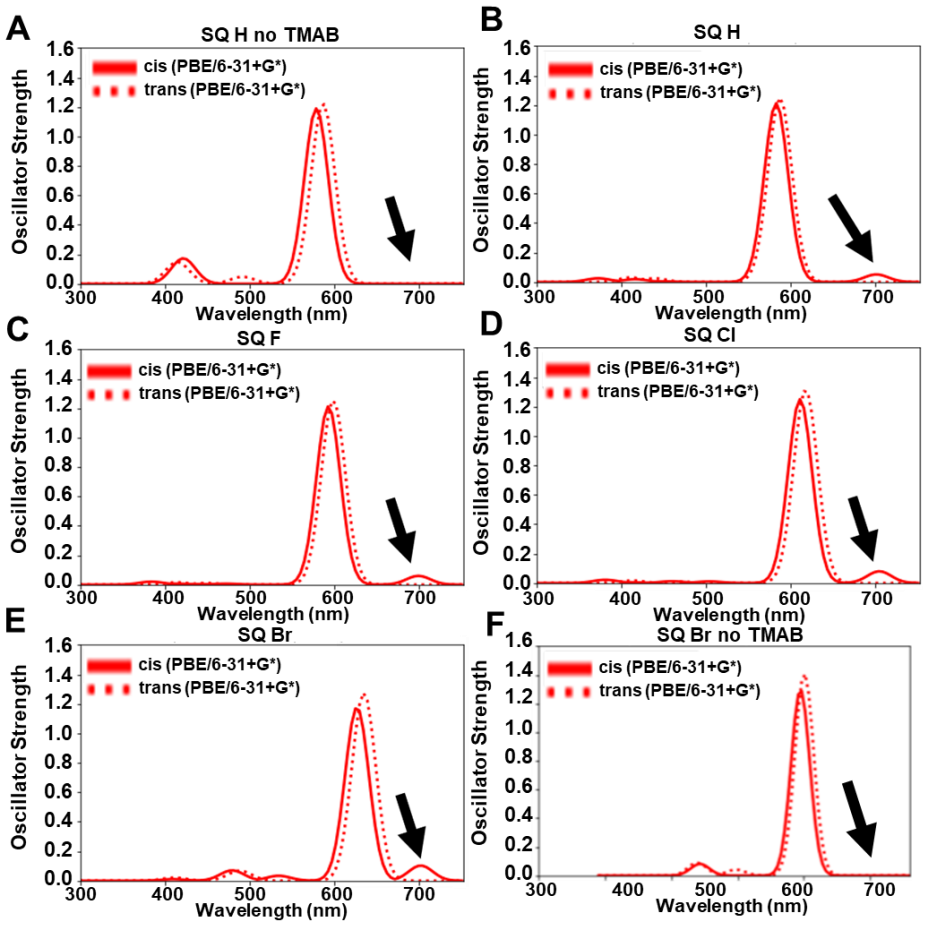

Figure 2.5: Full TD-DFT derived absorption peaks of *cis* and *trans* isomers of squaraine compounds, A) **SQ H no TMAB**, B) **SQ H**, C) **SQ F**, D) **SQ Cl**, E) **SQ Br**, F) **SQ Br no TMAB**. Arrows in panels A-F indicate the absorption peak that is responsible for optoacoustic signal generation. Lower wavelengths (<680 nm) are not available on optoacoustic measurement. No p-values to report.

The highest occupied molecular orbital (HOMO) and lowest unoccupied molecular orbital (LUMO) of a compound are regularly used to extract optical and chemical properties, including electron-donating, electron-accepting, stability, and absorbance[98]. Generally, the energy difference between HOMO and LUMO is used to predict strength and stability of the target compound[99]. In this context, frontier orbitals are utilized to explain the significant differences in transition dipole moment in these squaraine compounds with

identical conjugation cores. **Figure 2.6** shows the frontier molecular orbitals involved in the electronic excitations that contribute to the absorption peaks of interest where a higher amplitude indicates a larger contribution. **Figure 2.6A** shows that the relevant absorption peak for **SQ H no TMAB** and **SQ Br no TMAB** are mostly due to an excitation from HOMO-1 (the second highest occupied molecular orbital) to LUMO, with an amplitude of 0.9961 and 0.9967, respectively. However, HOMO-1 is localized on the center of the compound, while LUMO is fully delocalized over the entire molecule for **SQ H no TMAB** and **SQ Br no TMAB**. The resultant partial charge-transfer character, when combined with the symmetries of HOMO-1 and LUMO orbitals, leads to a near-zero transition dipole moment for **SQ H no TMAB** and **SQ Br no TMAB**. For TMAB substituted squaraines, the charge-transfer character of the first absorption peak was reduced in two ways: 1) contribution to HOMO-1 from trimethylpropylammonium pendant groups caused delocalization of HOMO-1, resulting in a larger degree of overlap between HOMO-1 and LUMO of TMAB substituted squaraines, and 2) amplitude reduction of HOMO-1 to LUMO excitation compared to **SQ H no TMAB** and **SQ Br no TMAB**. Additionally, non-charge-transfer HOMO to LUMO excitation contributed to the absorption peaks of these compounds with amplitudes of 0.4044 (**SQ H**), 0.4021 (**SQ F**), 0.4216 (**SQ Cl**), and 0.4383 (**SQ Br**), which explains the trend in the predicted transition dipole moments. From this analysis, we hypothesize that changes in electronic excitation character due to trimethylpropylammonium pendant group and halogen substitutions are responsible for varying degrees of photon absorption in the NIR wavelength range, which contributes to the variations in experimentally observed optoacoustic signal intensity (**Figure 2.3B**).

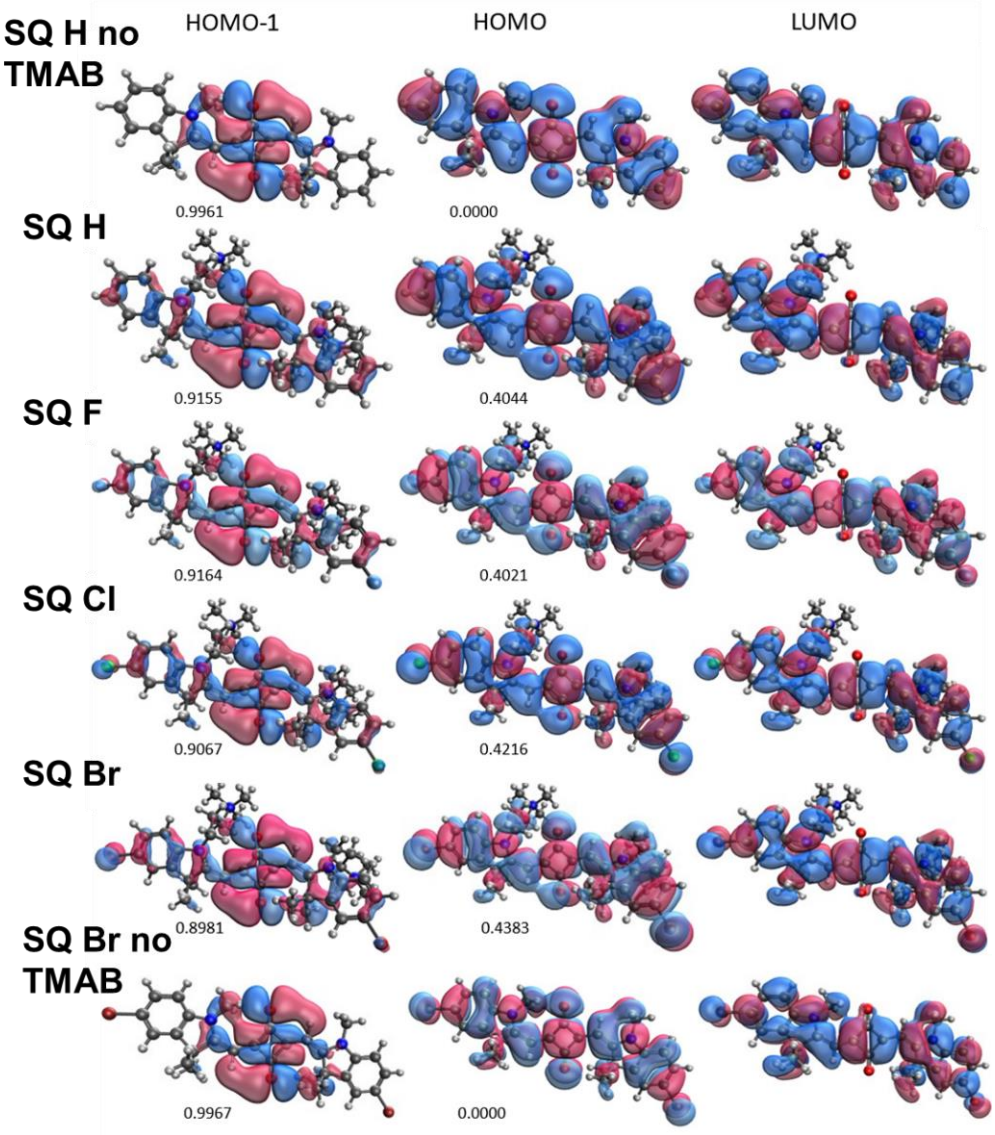

Figure 2.6: HOMO-1, HOMO, and LUMO of squaraines from DFT calculations using PBE functional and 6-31+G* basis set. Amplitudes for HOMO-1 to LUMO and HOMO to LUMO electronic transitions for the lowest energy absorption are listed below the respective orbitals. For a specific molecular orbital (HOMO-1, HOMO, or LUMO), isosurfaces are shown in blue (isovalue = 0.02) and red (isovalue = -0.02).

2.4.3 Cellular Viability

Cells were treated with squaraine dyes of multiple concentrations and evaluated for viability. While TMAB substituted squaraines show no toxicity following treatment with

cells at both concentrations evaluated, decreases in viability of cells following treatment with squaraines **SQ H no TMAB** and **SQ Br no TMAB** in kidney (**Figure 2.7A, E**), liver (**Figure 2.7B, F**), colon (**Figure 2.7C, G**), and umbilical vein (**Figure 2.7D, H**) cells. Kidney and liver cells were chosen due to being the major organs involved in clearance of drug injected intravenously[100]. Colon cells were included for consistency with *in vivo* oral gavage administration. Note that all squaraines were cleared through the gastrointestinal system following gavage (See below, **chapter 2.4.4**). Umbilical vein cells were included due to common use as an endothelial cell for *in vitro* studies, and as results are often transferable to other endothelial cell types[101]. 200 µg/mL treatment resulted in less viability of cells following the treatment period as compared to 20 µg/mL. Minor issues with solubility were observed with squaraines **SQ H no TMAB** and **SQ Br no TMAB**, which may have contributed to lower viability. However, no treatments imposed any tissue damage, as indicated through histological analysis (**Figure 2.9C**). In addition, western blot analysis revealed no changes in caspase 3 protein expression levels compared to untreated cells, indicating the absence of apoptosis as a result of treatment with squaraine dyes (**Supporting Figure S2.26**). These results indicate that varying alkyl chains can alter charge and salt bridge formation, which contributes to stability and cytotoxicity *in vitro* in addition to vibrational entropy and optoacoustic signal.

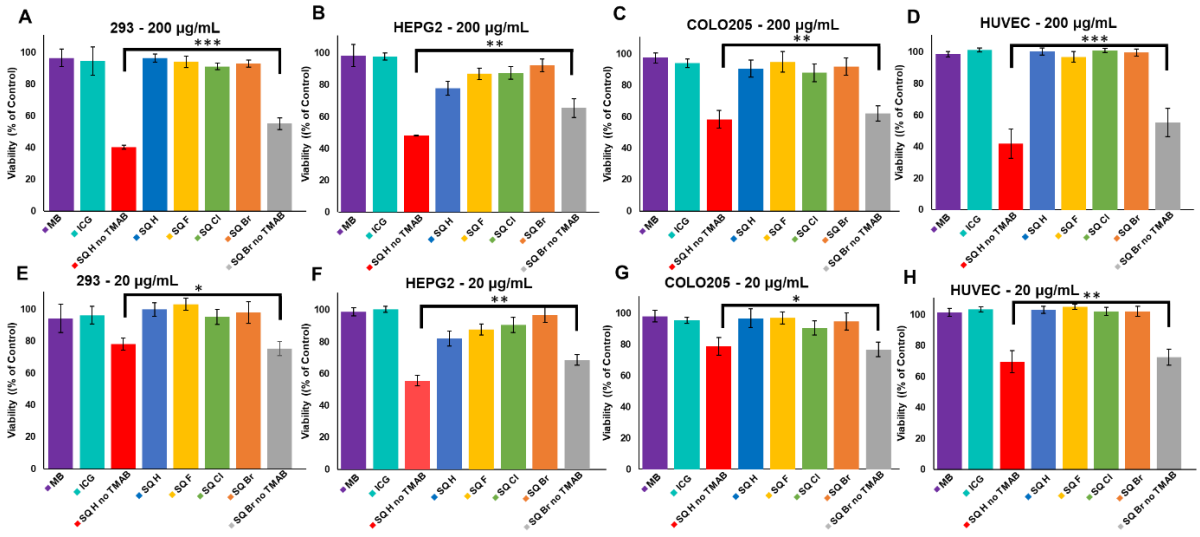

Figure 2.7: Cellular viability of cells following 24 h treatment with squaraines and standard infrared dyes indocyanine green and methylene blue. Viability is shown as a percentage of control (untreated) cells. A) 293 kidney cells at 200 µg/mL, B HEPG2 liver cells at 200 µg/mL, C) COLO205 colon cells at 200 µg/mL, D) HUVEC umbilical vein endothelial cells at 200 µg/mL, E) 293 kidney cells at 20 µg/mL, F) HEPG2 liver cells at 20 µg/mL, G) COLO205 colon cells at 20 µg/mL, H) HUVEC umbilical vein endothelial cells at 20 µg/mL. (*=p<0.08, **=p<0.01, ***=p<0.001) Error bars represent +/- 1 standard deviation of respective data.

2.4.4 *In Vivo* Detection of Squaraines

In vivo comparison of halogen substituted squaraine dyes was determined with MSOT following oral administrations of squaraine dyes into athymic mice. Athymic mice have no hair, which could often obscure signal due to a nonuniform surface between the skin and the transducer. Each animal received 200 µL of dye at 100 µM. Following administration of squaraine compounds, animals were imaged using MSOT. Results corroborate previous *in vitro* results, which indicate **SQ Br** as the strongest generator of optoacoustic signal (**Figure 2.8A-B**). Specifically, a mean optoacoustic signal value of 2.12 a.u. was significantly different from all squaraines **SQ Cl** (0.81 a.u.), **SQ F** (0.58 a.u.), **SQ H** (0.44

a.u.), **SQ Br no TMAB** (0.37 a.u.), and **SQ H no TMAB** (0.21 a.u.) ($p<0.001$, Tukey post-hoc). These data support the claim that heavy halogenated squaraine compounds functionalized with the dual TMAB pendant groups generate significantly more optoacoustic activity than counterparts. Evaluation of **SQ Br no TMAB** follows this trend by exhibiting higher signal than non-halogenated, non-TMAB functionalized squaraine dye (**SQ H no TMAB**), but less signal than the TMAB functionalized squaraine dye with the same bromine substitution (**SQ Br**). Following MSOT imaging, animals were imaged using NIR fluorescence in which similar trends were observed. (**Figure 2.8C-D)**. Notably, squaraine **SQ Cl** showed significantly more NIR fluorescence signal than other squaraines ($p<0.001$), albeit less optoacoustic signal than **SQ Br**. Due to maximum signal, **SQ Br** shows potential for future use as an optoacoustic contrast agent in a clinical setting, following further mutagenicity and teratogenicity studies. In the context of methods utilized herein, **SQ Br** could be used as a method to coat the inside of the colon, eliminating the requirement of a barium enema. This could aid in visualization of inflammatory bowel disease through use as a reporter agent specifically for ulcerative colitis or Crohn's disease. This study was designed to exhibit the intensity of a newly developed reporter dye for optoacoustic imaging. Expanding the collection of optoacoustic dyes will lead to simultaneous imaging of multiple reporter agents, an inherent advantage of MSOT, which has been previously exhibited[22]. Further studies could utilize optoacoustic compounds as a reporter agent through conjugation with a specific targeting molecule for visualization of specific biological processes. In addition, further studies could differ from oral administration of the dye. Oral gavage was chosen specifically to ensure a concentrated focal point *in vivo* for determination and comparison

of optoacoustic signal between each of the squaraine compounds. Other administration methods could potentially limit comparisons due to inconsistencies with concentrations in different areas of the animal.

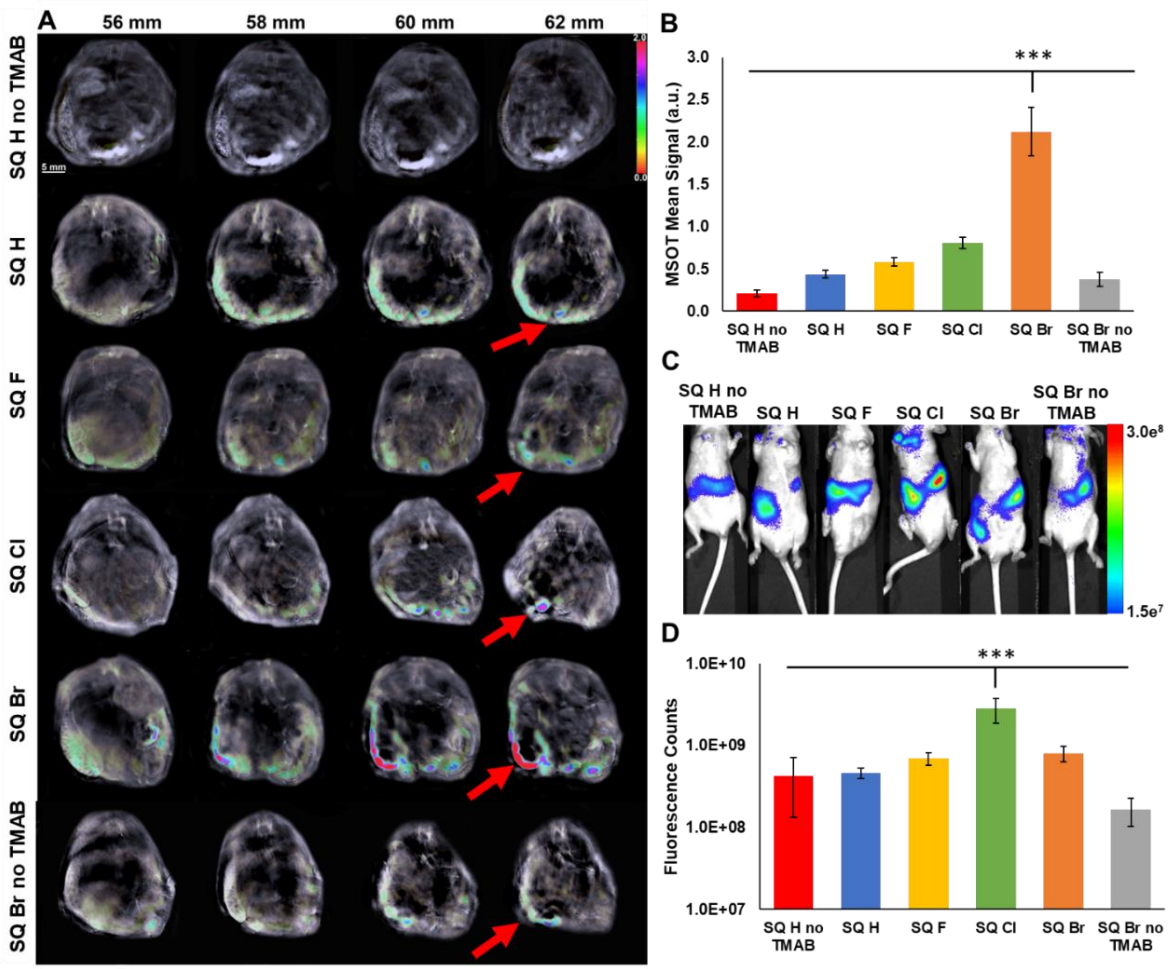

Figure 2.8: A) *In vivo* visualization of optoacoustic signal generated from squaraines subsequent to oral administration. Columns represent slightly different tomographic slices within the mouse. Red arrows show optoacoustic signal as a result of squaraine compounds in the colon. Higher slice numbers (top) indicate cross sections closer to the tail of mice. Refer to **Figure S1.1** for organ locations for tomographic cross sections. B) Quantification of optoacoustic signal observed in A) (n=3). C) *In vivo* visualization of NIR fluorescence signal generated from squaraines. D) Quantification of NIR fluorescence signal observed in C). (*=p<0.08, **=p<0.01, ***=p<0.001) Error bars represent +/- 1 standard deviation of respective data.

Following oral *in vivo* evaluation of squaraine compounds, organs were harvested for *ex vivo* confirmation with NIR fluorescence. Animal colons were imaged using NIR fluorescence to confirm squaraine presence in the colon (**Figure 2.9A-B**). Squaraine compounds were confirmed to be in the stool of the animal, and not the tissue of the colon, through NIR fluorescence imaging after washing of the colon with saline. (**Supporting Figure S2.27**). Squaraines were confirmed to be absent from the kidney, liver, and spleen (**Figure 2.9A-B**).

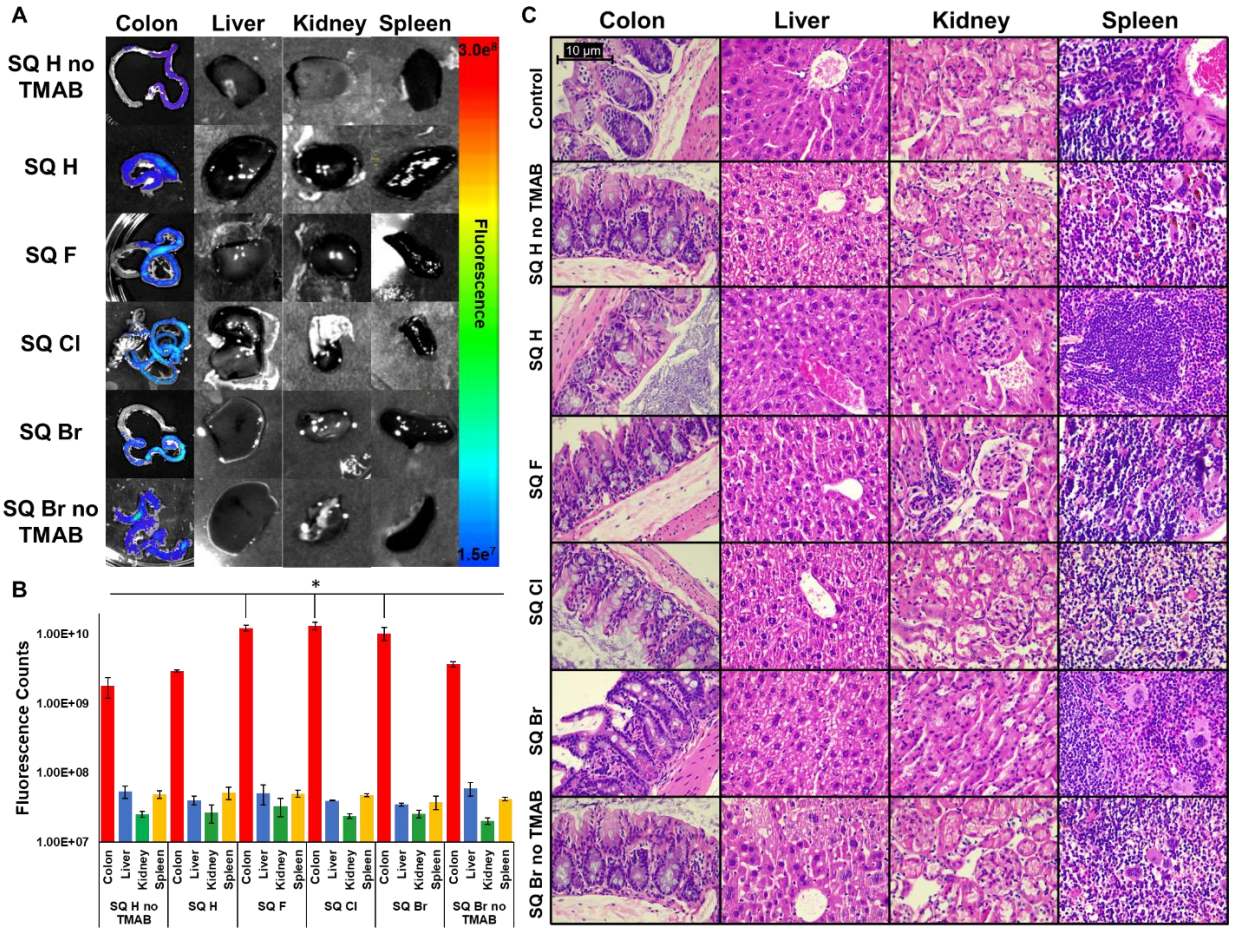

Figure 2.9: A) *Ex vivo* visualization of NIR fluorescence signal generated from squaraine compounds in animal colons, livers, spleens, and kidneys subsequent to oral administration. B) Quantification of NIR fluorescence signal observed in A). C) H&E histology images of colon, liver, kidney, and spleen of animals treated with squaraine

compounds. Images show no unusual morphology, indicating little risk of squaraine treatment on organs. (*=p<0.08, **=p<0.01, ***=p<0.001) Error bars represent +/- 1 standard deviation of respective data.

2.4.5 Histology

Histological evaluation of the colon, liver, kidney, and spleen by a board-certified pathologist following *in vivo* administration was performed to ensure that treatments with squaraine compounds were non-toxic to the evaluated animals. Assessment of histology showed little morphological changes outside the usual, indicating no treatment-imposed tissue damage (**Figure 2.9C**). In combination with lack of cellular toxicity (**Figure 2.7**), TMAB substituted halogenated squaraine dyes give no indication of toxicity.

2.4.6 Halogenated Cyanine Dyes

To ensure that changes in halogenation are not limited to squaraine molecules, an additional set of cyanine (CY) dyes were synthesized according to information derived from halogenated squaraines, coined as **CY H, CY Cl**, and **CY Br** (**Supporting Figures S2.1, S2.17-S2.22**). Notably, *in vitro* evaluation of CY dyes corroborated results from squaraine analogs; bromination (**CY Br**) resulting in the largest increase in optoacoustic activity, followed by chlorination (**CY Cl**), with non-halogenated counterpart (**CY H**) exhibiting the least optoacoustic signal (**Supporting Figure S2.31**). In addition, full DFT/TD-DFT calculations were performed to ensure trends in vibrational entropy, oscillator strength, and transition dipole moment were consistent with heavy halogenation (**Supporting Figures S2.32-2.35**). While CY dyes show significantly lower optoacoustic relevant oscillator strengths, the trends were constant with squaraine compounds, with the largest strengths observed in the bromine substituted **CY Br**, compared to chlorine substituted **CY Cl**, and non-halogenated **CY H**. Cell viability studies were performed

(**Supporting Figure S2.40**) prior to *in vivo* studies to ensure non-toxicity for oral administration. *In vivo* evaluation of CY dyes confirmed *in vitro* studies and corroborate information from squaraine compounds. **CY Br** showed the highest optoacoustic signal *in vivo* (1.12 a.u.), followed by **CY Cl** (0.70 a.u.), and the least signal from **CY H** (0.25 a.u.), indicating the trend of bromination > chlorination > non-halogenation. Fluorescence whole-body animal imaging and *ex vivo* imaging was performed consistent with previous squaraine studies (**Supporting Figure S2.41**). These data suggest that heavy halogenation for the purposes of increasing optoacoustic intensity is a universal property may be utilized in the development of optoacoustic contrast agents.

2.5 Conclusions:

This work had a focus on utilizing squaraine dyes modified with trimethylpropylammonium and halogen atoms for an emerging, clinically relevant optoacoustic imaging modality, MSOT. As previously mentioned, MSOT is a rapidly developing modality that has proven efficacy in clinical trials due to intrinsic advantages over traditional imaging techniques. With a current lack of guidelines for developing optimized optoacoustic contrast agents, the purpose of this study was to investigate how variations in squaraine dyes affect optoacoustic signal generation. Replacement of a methyl group with a trimethylpropylammonium pendant group resulted in significant increases in optoacoustic signal due to increased rotational bonds and vibrational entropy. Using DFT/TD-DFT, increases in the oscillatory strength was attributed to larger transition dipole moments arising from varied frontier orbital character. *In vivo* analysis of a mouse model corroborated observations that heavy halogen squaraine compounds with dual trimethylpropylammonium groups resulted in high resolution optoacoustic imaging. In

addition, a second compound class (CY) was synthesized to ensure utilization of heavy halogenation to boost optoacoustic signal is a universal property. While this study utilized oral gavage as the method of administration of contrast agent to ensure equally as strong concentrated areas of compounds *in vivo*, this is different than application in a clinical setting. Further developments of squaraines as well as other contrast agents will continue to increase the relevance and value of MSOT in a clinical setting; through spectral unmixing, several different contrast agents can be differentiated based on spectral signature[22].

2.6 Acknowledgements and Funding:

We acknowledge funding from the National Institutes of Health under grants F31CA261044, R01CA205941, R01CA212350, R01GM135392, and P30CA225520. Acknowledgements to Dr. Emmanuel Buabeng for collecting the thermal stability and some of the fluorescence data as well as participating in the project discussion.

Chapter 3 – Optimization of Optoacoustic Contrast Agents through Twisted Intramolecular Charge Transfer

This chapter is being prepared as a manuscript for submission.

3.1 Abstract:

Hemicyanine dyes have been regarded with great research interest due to diverse biomedical applications, including biomarkers and imaging detection in real-time. Such studies modify hemicyanines with functional groups for exploitation of properties for individual applications. This manuscript details synthesis of hemicyanine dyes with hydroxyl, amine, dimethylamino, and diethylamino functional groups on a xanthene donor moiety for use as optoacoustic contrast agents. Through utilization of polar solvents to stabilize a twisted intramolecular charge transfer state, unique optoacoustic contrast agents were synthesized. The hemicyanine compounds synthesized here provide a scaffold and baseline for future optoacoustic contrast agent development. As a majority of optoacoustic contrast agents exhibit peak signal generation at 650 – 700 nm, exploitation of the twisted intramolecular charge transfer state on compounds 13 and 14 allow optoacoustic signal to peak further into the near-infrared window; at 790 – 810 nm. These compounds were validated by *in vivo* optoacoustic imaging of compounds in the pancreas of a murine model. As the current library of optoacoustic contrast agents expands, the relevance and applications of optoacoustic imaging in a clinical setting will expand proportionately.

3.2 Introduction:

The optoacoustic effect was first reported by Alexander Graham Bell in the late 1800s[102]. This effect is the process by which a pulsed incident light source is used to excite a

material, thus increasing the temperature of the material, resulting in continuous thermal expansion and retraction. The thermal movement generates ultrasound waves, which may be recorded to measure and reveal material-specific properties related to absorbance and optoacoustic signal generation[65]. The optoacoustic effect may be exploited for the purpose of medical imaging, where the optoacoustic material is used as a reporter in the body. This technique rivals conventional imaging due to improved image quality by circumventing the unavoidable resolution and imaging depth tradeoff in optical imaging[4,68]. As thermal expansions are low-energy by comparison to fluorescence, near-infrared light is utilized in optoacoustic imaging, which passes through biological tissue with lower scatter and absorption rates than higher energy light[103]. In addition, generated ultrasound waves do not undergo scatter and attenuation similarly to optical imaging, thus protecting image resolution and allowing for increased imaging depth. Also, many optoacoustic imaging platforms are equipped with multispectral processing; the ability to separate the total signal of an optoacoustic image into distinct components based on the contrast agents in the signal[5,6,16,36]. As such, a variety of imaging platforms that rely on the optoacoustic effect have emerged and been used in a clinical setting to visualize differentials of oxy/deoxyhemoglobin, the most common endogenous optoacoustic agents. This allows for identification of ischemia, hypoxia, angiogenesis and the relationship to conditions such as irritable bowel syndrome, inflammatory diseases, and cancer[1,3,16,74]. However, with few exogenous agents, the clinical applications of optoacoustic imaging are limited to conditions with differential oxygenation, collagen, or melanin. As the library of optoacoustic contrast agents expands, the biomedical applications of optoacoustic imaging will proportionally expand.

Optoacoustic imaging has traditionally used near-infrared fluorescence agents that provide optoacoustic signal in addition to fluorescence. Since the two pathways are varying methods of energy dissipation, signal strength is hypothetically inversely related; maximization of optoacoustic signal will result by minimization of fluorescence. For example, IR780, indocyanine green (ICG), and methylene blue have been utilized as optoacoustic agents, but were primarily developed for near-infrared fluorescence. While the development of fluorescence agents is well-studied and detailed[104], there is less understanding of how to construct a strong optoacoustic contrast agent with a unique spectral signature. The addition of strong electron withdrawing groups has shown to increase the amplitude optoacoustic signal by reduction of charge-transfer character of relevant absorption peaks[78]. However, inciting bathochromic shifts in the optoacoustic spectra is critical for optimization of optoacoustic contrast agents and the creation of unique spectral signatures and has not been adequately studied.

Recently, hemicyanine dyes (HCs) have attracted attention for different applications, including non-invasive real-time sensing, biomarkers, and chemosensors[105,106]. The structure of HCs resembles a donor-π-acceptor scaffold where the indolium moiety is the acceptor and the xanthene group is the donor unit. The intramolecular charge transfer (ICT) within the system is from xanthene donor unit to the heterocyclic indolium acceptor moiety[107]. Modifications on the xanthene unit provide shifts in the absorbance wavelength maxima of the HC, which is often below 700 nm. However, with further modifications on the xanthene moiety, the absorbance maxima can be shifted to near-infrared (NIR) region (650-850 nm), which could further optimize HCs for optoacoustic imaging[6,107].

The presence of different functional groups (hydroxyl, amino, etc.) allows feasible modification with bio-conjugations to trigger analyte response[108]. The synthesis of the derivatives with different functional groups changed the optical properties of HCs and increased their versatility in various applications[107]. Optoacoustic imaging agents require high molar extinction coefficients to allow the maximal amount of light absorption, and thus, optoacoustic signal. In addition, strong optoacoustic contrast agents should exhibit low fluorescence quantum yield to enhance the energy dissipating through nonradiative pathways[109]. Based on previous research, the structural features, such as hydrophobicity, heavy atom effect, and rotatable bonds, may be utilized to increase amplitude of generated ultrasonic waves in contrast agents for optoacoustic imaging[89,110].

In this study, hemicyanine compounds with varying functional groups (hydroxy, amine, dimethyl amino, and diethyl amino groups) were synthesized in efforts to optimize optoacoustic signal, by bathochromic spectral shifts, through a twisted intramolecular charge transfer state (TICT). Twisting around a bond subsequent to absorption of light, i.e., molecular excitation, can lower the energy of the molecule, forming the TICT state[111,112] (**Figure 3.1**). For example, a phenoxazine/triphenyl-triazine molecule has been synthesized previously to result in red-shifted emission.[113] Electronic relaxation in the TICT state leads to a twisted ground state (TGS) and can result in fluorescence emission with large Stokes shifts[114,115], or interestingly in this context, thermoelastic expansions/contractions that correspond to bathochromic shifts. TICT states are relatively unique as high polarity donor and acceptor groups must be stabilized in a polar solvent to allow for efficient charge separation[111,114]. The compounds synthesized in this study include amino functional groups that allow for transition into a TICT state when

surrounded by solvents with sufficiently high dielectric constants[114]. Through exploitation of the TICT state, optoacoustic contrast agents may be red-shifted to show unique red-shifted spectral signatures, thus expanding the current library of optoacoustic dyes.

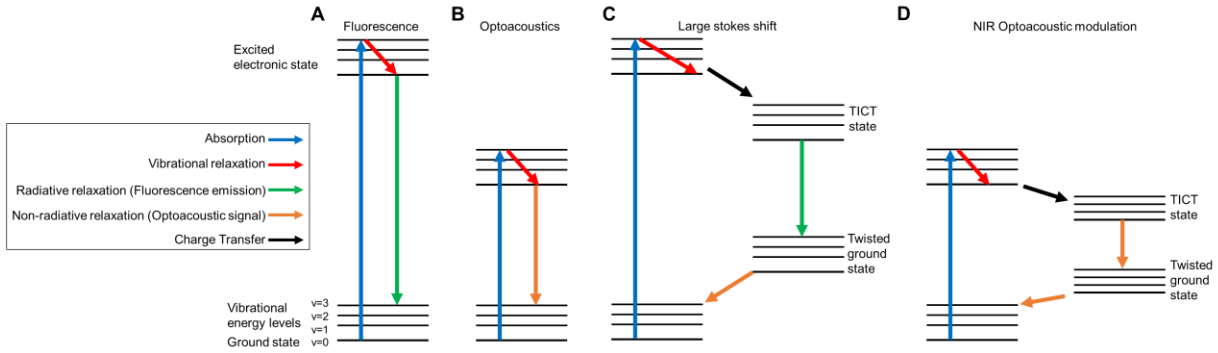

Figure 3.1: Diagrams of relevant energy systems for imaging. Following absorption of light and energy increase to an excited state, chromophores relax to ground state through radiative emission, or fluorescence (A), or non-radiative emission, or optoacoustic signal (B). In cases with high polarity donor/acceptor groups and a sufficiently polar solvent, intramolecular charge transfer may cause emission corresponding to wavelengths deeper into the near-infrared window for fluorescence (C) or optoacoustic signal (D).

3.3 Materials and Methods:

3.3.1 Chemicals

Chemicals used are American Chemical Society or high-performance liquid chromatography grade, purchased from Sigma Aldrich (Saint Louis, MO), Thermo Fisher Scientific and TCI America (Waltham, MA). ^{1}H- nuclear magnetic resonance (NMR) (400 MHz) and ^{13}C-NMR (100 MHz) spectra were recorded using a Bruker Avance spectrometer with dimethyl sulfoxide-d6 (Cambridge Isotope Laboratories, Andover, MA) and $CDCl_3$ (Sigma-Aldrich, Burlington, MA) containing tetramethylsilane (TMS) as a calibration standard. The melting points were measured with open capillary tubes and Thomas Hoover apparatus. The ultraviolet-visible (UV-VIS) absorptions and fluorescence emission were measured using a Varian Cary 50 spectrophotometer (Santa Clara, CA)

and Shimadzu RF-5301 PC spectrofluorometer, respectively. VWR disposable polystyrene cuvettes with path length 1 cm were utilized to dissolve the dye in solvents for measurement. The quantum yields of dyes were measured according to the reported method with reference to ICG.

3.3.2 Compound synthesis

3.3.2a Synthetic procedure of heptamethine cyanine dyes (9 and 10)

Heptamethine cyanine dyes 9 and 10 were synthesized according to the previously reported procedure.[116-118] As shown in **Figure 3.2**, the heptamethine cyanine dyes were formed by the condensation of substituted indolium salt (synthesis outlined in **Chapter 2.3.2**) and the Vilsmeier Haack linker.[118] The indolium salt (2 mol), substituted linker 3 (2 mol), and sodium acetate (3 mol) were added into a round bottomed flask and dissolved with 5 mL of acetic anhydride. The reaction was refluxed for 2-4 h at 70 °C. The reaction was monitored by UV spectrophotometer. After completion, the mixture was cooled down and precipitated with ether to crystallize. The solid was filtered and recrystallized with methanol and ethyl acetate (10:100). The products 9 and 10 yielded green solids.

3.3.2b Synthetic procedure for hemicyanine dyes 11A and 11B

The addition of resorcinol to heptamethine dye under basic conditions allowed the retro-Knoevenagel to occur. The resorcinol (2.5 mmol) was dissolved in acetonitrile (3 mL) under nitrogen atmosphere. Triethylamine (2.5 mmol) was added to the mixture and stirred for 15 min. Heptamethine cyanine dye (9 or 10, 1 mol) was added to the mixture. The reaction was refluxed at 80 ℃ for 2-4 h. The reaction was monitored with UV. After completion, the mixture was reduced and purify with silica gel column chromatography

using DCM-MeOH (90:10). The fractions were collected and dried with the vacuum. The solid was recrystallized and filtered. The product yielded dark blue solids.

3.3.2c Synthetic procedure for hemicyanine dyes 12A and 12B

3-nitro phenol (3 mmol) and potassium carbonate (3 mmol) were dissolved in acetonitrile (3 mL) by stirring for 15 mins at room temperature under nitrogen atmosphere. Then, the heptamethine cyanine dyes (9 or 10, 1 mmol) dissolved in acetonitrile were added to the reaction flask and refluxed at 80 °C for 12 hours. The reaction monitored by UV-VIS spectroscopy and upon completion, the solvent was evaporated. To reduce the dye, it was dissolved in 20 mL methanol and $SnCl_2$ (10 mmol) in diluted HCl solution (2 mL) was added. The mixture refluxed at 80 °C overnight. The solution was neutralized by NaCO3 and filtered. The filtrate was collected by washing several times with DCM and solvent evaporated. The solid was purified by silica gel column chromatography using DCM: MeOH (95:5) and recrystallized with MeOH: EtOAc (5:95) to yield green solids.

3.3.2d Synthetic procedure for hemicyanine dyes 13A, 13B, 14A, and 14B

The 3-(dimethylamino) phenol for 13a and 13b, and 3-(dimethylamino) phenol for 14a an 14b, (2.5 mmol) was dissolved in acetonitrile (3 mL). Triethylamine (2.5 mol) was added to the mixture and stirred for 15 min. Heptamethine cyanine dye (1 mmol) was also added to the mixture. The reaction was refluxed at 80℃ for 4 h. The reaction was monitored with UV. After completion, the mixture was reduced and purified with silica gel column chromatography using DCM-MeOH (90:10). The fractions were collected and dried under vacuum. The solid was recrystallized and filtered. The product yielded dark blue solids.

3.3.3 Compound characterization

3.3.3a Molecular properties

Molecular properties of hemicyanine compounds were calculated with ChemDoodle Web Components.

3.3.3b Absorbance

Following compound synthesis, each were diluted in ethanol (50%) to a dilution of 1 mM. Compounds were further diluted to lesser concentrations of 100 μM, 10 μM, and 1 μM. The absorbance of each of the dilutions were measured and recorded using a UV-VIS Varian Cary 50 spectrophotometer.

3.3.3c Optoacoustic spectra acquisition

Dilutions that were utilized in absorbance measurements were similarly used for optoacoustic signal quantification. 200 μL of solutions noted above were loaded into 0.5 mL microcentrifuge tubes and encapsulation within agar-based tissue mimicking phantoms. Samples were quantified using an iThera Medical InVision 512 TF MSOT. Samples were irradiated with a pulsed, tunable laser source at wavelengths at 10 nm intervals between 680 nm and 900 nm to measure optoacoustic signal as a function of wavelength of irradiated light. Single-wavelength measurements at 710, 730, 740, 810, and 830 nm were also acquired.

3.3.4 Evaluation of solvent effects

To evaluate the effects of solvent polarity on the stabilization of the TICT state, multiple solvents with varying polarities were used to solvate compounds prior to absorbance and optoacoustic signal quantification. Solvents used and respective dielectric constants include: diethyl ether – 4.3; acetic acid – 6; dichloromethane – 9.1; acetone – 18; ethanol (50%) – 45. As compounds varied in solubility depending on solvents, spectra were normalized to allow for comparison of spectral shape rather than magnitude. In addition,

diethyl ether, dichloromethane, and acetone were unable to produce stable absorbance measurements, and therefore were included only in optoacoustic measurements.

3.3.5 Evaluation of metal sensitivity

To evaluate if amino lone pairs results in varied optoacoustic/absorbance spectra, multiple concentrations (1:1, 10:1) of copper, zinc, iron, and sodium were added to 1 mM solutions of compounds. Absorbance and optoacoustic spectra were recorded with each sample (Supporting Information)

3.3.6 Cell lines

Human kidney cells (293), human liver cells (HEP3B), human lung cells (A427), and human umbilical vein cells (HUVEC) were acquired from American Type Culture Collection. All cells were grown in standard Dulbecco's Modified Eagle Medium (DMEM) supplemented with 10% fetal bovine serum (FBS) and 1% L-glutamine and incubated at 37 °C with 5% CO_2.

3.3.7 Cellular viability

Cell lines were plated at 5000 cells per well in a 96 well plate and incubated for 24 h to allow for adherence. Cells were treated with 2.5 µL compounds, as well as methylene blue and ICG controls at 200 µg/mL and 20 µg/mL. 24 h post treatment adenosine triphosphate (ATP) levels were measured via ATPlite™ to evaluate cellular viability. To avoid potential interactions with other dye-based viability assays (MTT and MTS assays) ATPLite™ was utilized.

3.3.8 Murine model

Female athymic nude mice aged 4 weeks were used for this study. Without hair, athymic mice are preferred for optoacoustic imaging due to a smooth connection between skin

and ultrasonic transducers. Immunocompetent mice with hair would require shaving/hair removal to eliminate the possibility of obscured signal. All experiments outlined herein are in strict adherence to the Oklahoma University Health Science Center Animal Care and Use Committee approved protocol (IACUC 302166). Mice were fed a special diet (2920 X alfalfa free feed and ultrapure water) to reduce background *in vivo* signal.

3.3.9 *In vivo* compound characterization

Mice were anesthetized with isoflurane and the abdomen was cleaned with betadine. An incision of 1 cm was made in the upper left quadrant of the abdomen. Using forceps, the spleen was retracted to expose the pancreas. 1 mM of the hemicyanine compounds were diluted to 100 μM in sterilized ultrasound gel, and 100 μL of diluted compounds were injected into a secluded region of the pancreas with a 25-gauge needle. Injected compounds were deemed successful if the injection site and compounds within could be visually identified. The organs were returned to the abdomen and the incisions were closed using 5-0 prolene sutures.

Mice were placed into the InVision 512 TF MSOT (iThera Medical, Munich, Germany) ventral side up and delivered constant anesthesia (1.5% isoflurane in 0.8 L/min medical air and 0.2 L/min oxygen). Serial slices of the abdomen were acquired at axial slices of 0.1 mm at intervals of 10 nm from 700 nm to 900 nm. 20 acquisitions (10 μs each) of each wavelength were recorded at each axial slice to minimize breathing artifacts. In addition, single wavelength signals were acquired at 710, 730, 740, 810, and 830 nm at a single slice with maximum compound presence. Through direct video feed of the animal, and through observation of breathing according to optoacoustic imaging, signs of distress were constantly monitored throughout optoacoustic imaging.

Following optoacoustic imaging, mice were imaged using NIR fluorescence with an advanced molecular imager (AMI) (Spectral Imaging Instruments, Tucson, AZ, USA). Mice were anesthetized as previously mentioned and imaged using multiple excitation and emission filters between 640 nm and 850 nm at 5 s of exposure for each image to confirm the presence of compounds.

3.3.10 *Ex vivo* organ analysis

Following *in vivo* imaging, mice were euthanized by isoflurane overdose and cervical dislocation. Vital organs including the pancreas, liver, kidney, spleen, heart, and lung were excised and evaluated using NIR fluorescence to confirm the presence or absence of compounds in relationship to *in vivo* NIR fluorescence and optoacoustic imaging. Organs were also fixed in formalin and hematoxylin and eosin (H&E) stained to assess toxicity.

3.3.11 Statistics

Differences in optoacoustic signal of compounds were evaluated with analysis of variance (ANOVA) and post hoc comparisons. Tukey and Bonferroni corrections were utilized to adjust p-values due to multiple comparisons. Significance in this context: (* - $p<0.08$, ** - $p<0.01$, *** - $p<0.001$).

3.4 Results and Discussion:

3.4.1 Dye synthesis

The development of unique optoacoustic contrast agents is a necessity for advancement of optoacoustic imaging as a clinically relevant imaging modality. Hemicyanine dyes have shown favorable features an both fluorescence and optoacoustic imaging agents due to strong absorbance in the near-infrared window, and ease of tunability. Therefore, a hemicyanine scaffold was chosen as the base of this study and equipped with high

polarity functional groups for the purposes of causing a twisted intramolecular charge transfer state. The synthesis for these compounds is outlined in **Figure 3.2**.

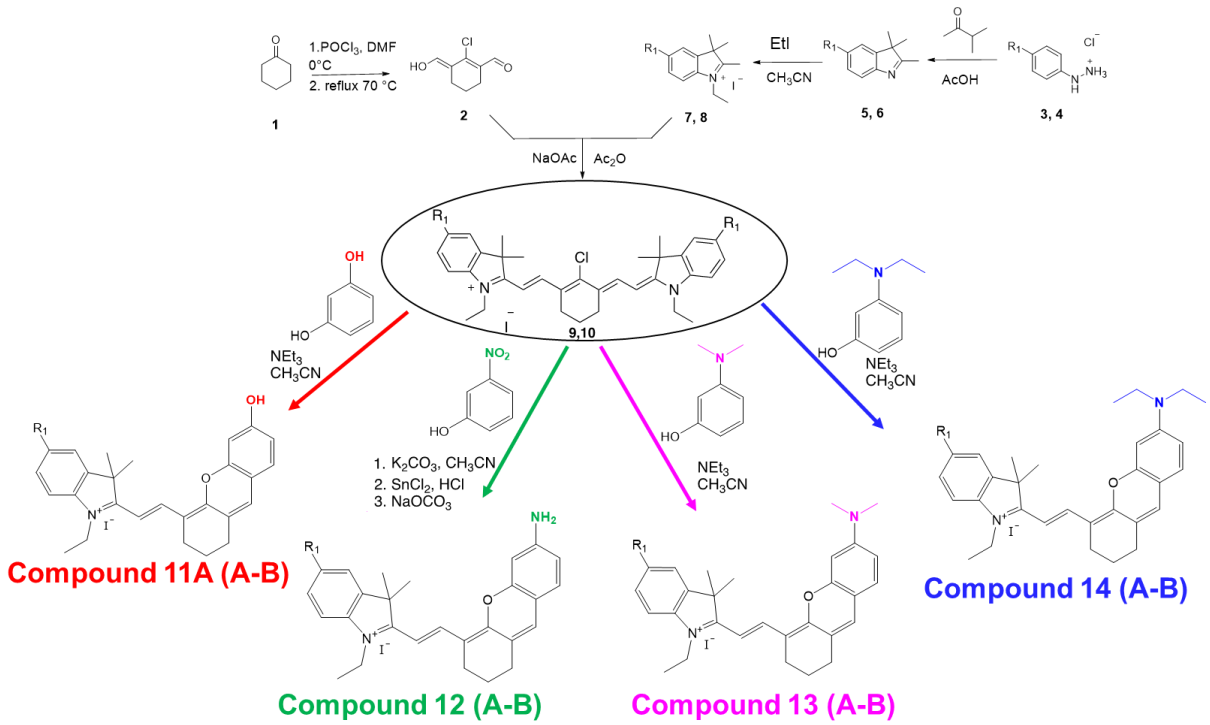

Figure 3.2: Synthesis of hemicyanine compounds with modified xanthene donor units.

Heptamethine compounds 9 and 10 were synthesized by condensation of substituted indolium salt and the Vilsmeier Haack linker. Indolium salt, linker 3, and sodium acetate were dissolved with acetic anhydride, and refluxed, cooled, and filtered. From compounds 9 and 10, compounds 11A-14B had slightly different synthesis procedures. For compounds 11A and 11B, resorcinol was added to triethylamine and compound 9 or 10. Compounds 11A and 11B were yielded following reflux and purification. 3-nitro phenol and potassium carbonate were added to compound 9 and 10 to yield compounds 12A

and 12B. Dimethylamino phenol or diethylamino phenol were added with triethylamine and compounds 9 and 10 to yield compound 13A and compound 13B or compound 14A and compound 14B. ^{1}H NMR and ^{13}C NMR spectra of final compounds can be found in the supporting information (**Supporting Figure S3.1-3.18**).

3.4.2 Compound characterization

Molecular properties are outlined in **Table 3.1.** Following compound synthesis and purification, each molecule was characterized in terms of molecular properties.

Table 3.1: Molecular properties of hemicyanine compounds 11A-14B

Molecule	Rotatable Bonds	Polarizability ($Å^3$)	Refractivity (cm^3/mol)	Polar Surface Area ($Å^2$)	Volume ($Å^3$)	LogP
11A	3	47.28	124.39	32.47	348.93	4.89
11B	3	49.75	132.16	32.47	369.88	5.69
12A	3	47.82	126.54	38.26	349.48	4.48
12B	3	50.26	134.31	38.26	370.42	5.27
13A	4	51.51	135.82	15.48	377.42	5.50
13B	4	53.94	143.59	15.48	398.36	6.30
14A	6	55.20	145.09	15.48	405.36	6.90
14B	6	57.61	152.86	15.48	426.30	7.69

Absorbance measurements of compounds 11A-14B reveal dual absorbance peaks for each molecule, which are relatively consistent between the A and B versions of each compound (**Figure 3.3**). Compound 11A-B show absorbance peaks at approximately 610 nm and 660 nm, 12A-B at about 632 nm and 691 nm, 13A-B at about 665 nm and 725 nm, and 14A-B at approximately 666 nm and 718 nm. Overall, dimethyl amino and diethyl amino functionalized hemicyanines (Compounds 13 and 14) exhibit very similar dual absorbance peaks, while compounds 11 and 12 are less red-shifted.

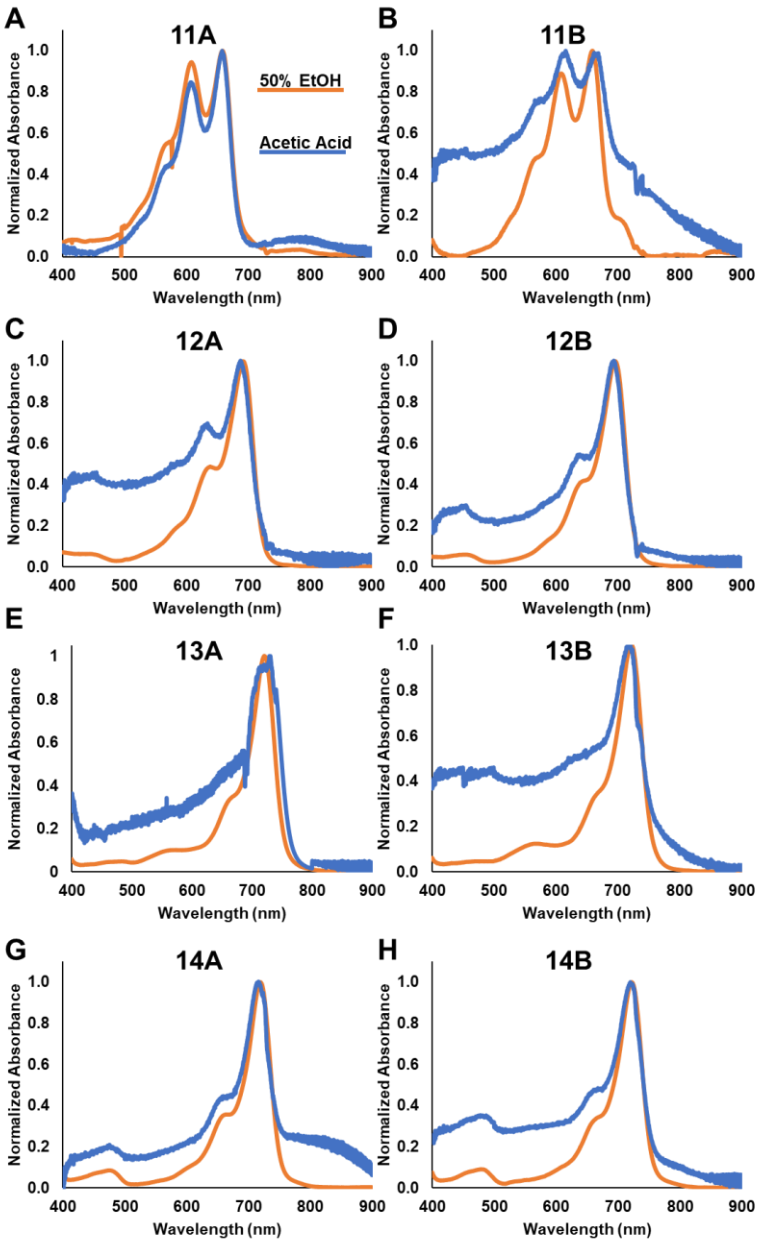

Figure 3.3: UV-VIS absorbance spectra of compounds 11A-14B in 50% ethanol in water (orange) and acetic acid (blue). A) Compound 11A, B) Compound 11B, C) Compound 12A, D) Compound 12B, E) Compound 13A, F) Compound 13B, G) Compound 14A, H) Compound 14B. Solvent polarity did not alter absorbance spectra of compounds evaluated. No p-values to report.

Subsequent to absorbance measurements, optoacoustic signal was measured (**Figure 3.4**). Optoacoustic spectra often correspond to absorbance measurements, due to

immediate relaxation of excited molecules, and thus, generation of ultrasonic waves through non-radiative decay. However, several compounds exhibit red-shifted optoacoustic signal compared to absorbance. To ensure the phenomenon was not occurring due to aggregation, multiple wavelengths were used to confirm. Largely, concentration of HCs resulted in only optoacoustic intensity differences, and not spectral shifts. Compound 13A was the sole exception to this observation, and shows a maximum peak shift due to formations of J-aggregates.[119]

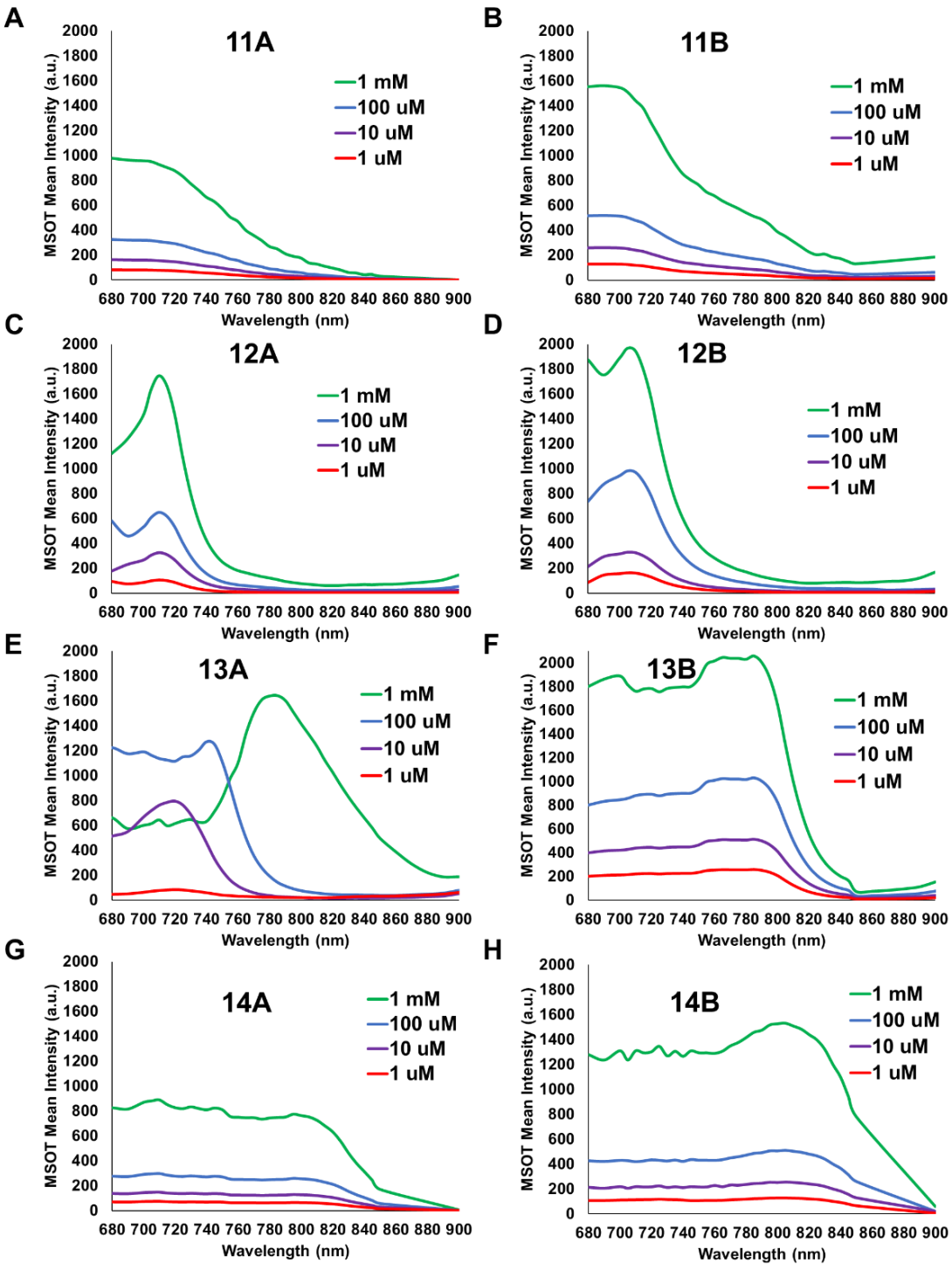

Figure 3.4: Optoacoustic spectra for compounds 11A-14B at a variety of concentrations between 1 mM and 1 μM to evaluate aggregation-based spectral shifts. A) Compound 11A, B) Compound 11B, C) Compound 12A, D) Compound 12B, E) Compound 13A, F) Compound 13B, G) Compound 14A, H) Compound 14B. No p-values to report.

Stabilization by polar solvent is required to observe molecule effects while in a TICT state[111,114]. In addition to ensuring metal sensing through nitrogen lone pair interactions (**Supporting Figure S3.19**) was not responsible for red-shifted optoacoustic signal, compounds 11A-14B were measured in solvents of varying dielectric constants, thus, polarity (**Figure 3.5**). Compounds 11 and 12 had insignificant changes in terms of spectral shifts dependent on solvent polarity. However, compounds 13 and 14 exhibited large differences in spectral signature. Notably, high polarity solvents (50% ethanol, 45 dielectric constant) in compound 14 result in red-shifted optoacoustic signal in which a maximum peak of approximately 810 nm was observed. As polarity of solvents were lowered, optoacoustic spectral signatures became blue-shifted; acetone (18 dielectric constant) peaked at 785 nm and dichloromethane (9.1 dielectric constant), acetic acid (6 dielectric constant), and diethyl ether (4.3 dielectric constant) each peaked at 735 nm. **Figure 3.3** indicated no changes in absorbance were observed between 50% ethanol and acetic acid, indicating the shift in optoacoustic signal was unable to be explained by solvent-driven absorbance shifts. Further, single-wavelength measurements were acquired for each compound and solvent to eliminate the possibility of delayed non-radiative responses from previous irradiation (**Supporting Figures S3.20-3.23**). Through stabilization of the twisted intramolecular charge transfer state with a high polarity solvent, non-radiative decay of compounds 13 and 14 result in large red-shifted shifts in optoacoustic signal; potentially establishing each of the compounds as a relevant contrast agent for optoacoustic imaging *in vivo*.

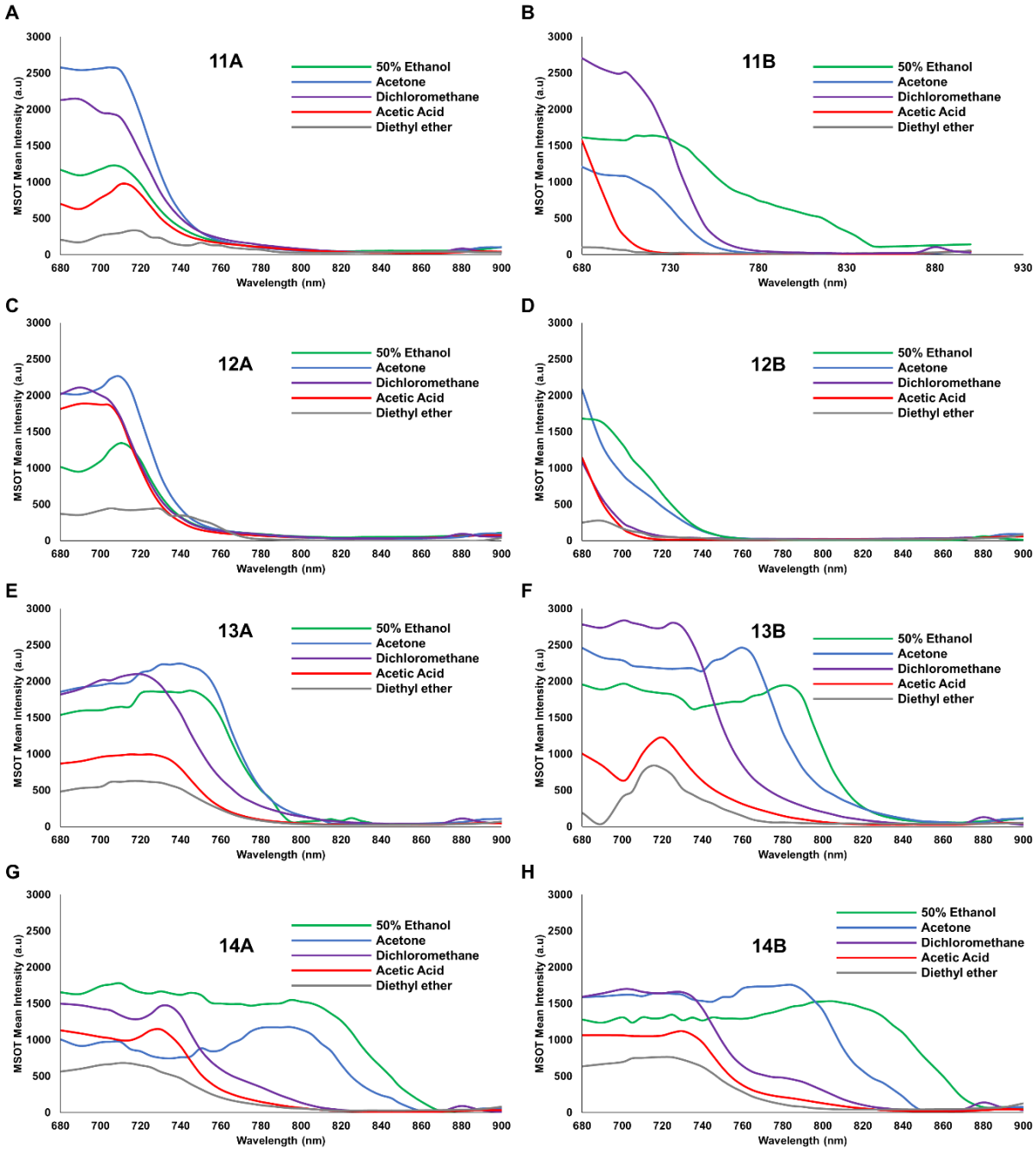

Figure 3.5: Optoacoustic signal as a function of wavelength in solvents of varying polarity, including 50% ethanol (45), acetone (18), dichloromethane (9.1), acetic acid (6), and diethyl ether (4.3). A) Compound 11A, B) Compound 11B, C) Compound 12A, D) Compound 12B, E) Compound 13A, F) Compound 13B, G) Compound 14A, H) Compound 14B. No p-values to report.

3.4.3 Cellular viability

Prior to evaluation of synthesized hemicyanine dyes *in vivo,* cellular viability was evaluated *in vitro* using human cell lines from kidney, liver, lung, and umbilical vein. Cells were treated with each hemicyanine compound (11A-14B) in addition to standard, commercial control dyes, methylene blue and ICG. 24 h post-treatment, cells were evaluated for viability using ATPLite. **Figure 3.6** shows that at both 200 µg/mL and 20 µg/mL, compounds 11A-14B had little impact of the viability of cell lines utilized. While umbilical vein cells are often utilized in viability assays due to results being transferable to other endothelial cell types[101], kidney, liver, and lung cells are major locations of drug accumulation following intravenous injection[100]. The results of the viability assay depicted in **Figure 3.6** support the hemicyanine dyes as potential *in vivo* contrast agents for optoacoustic imaging.

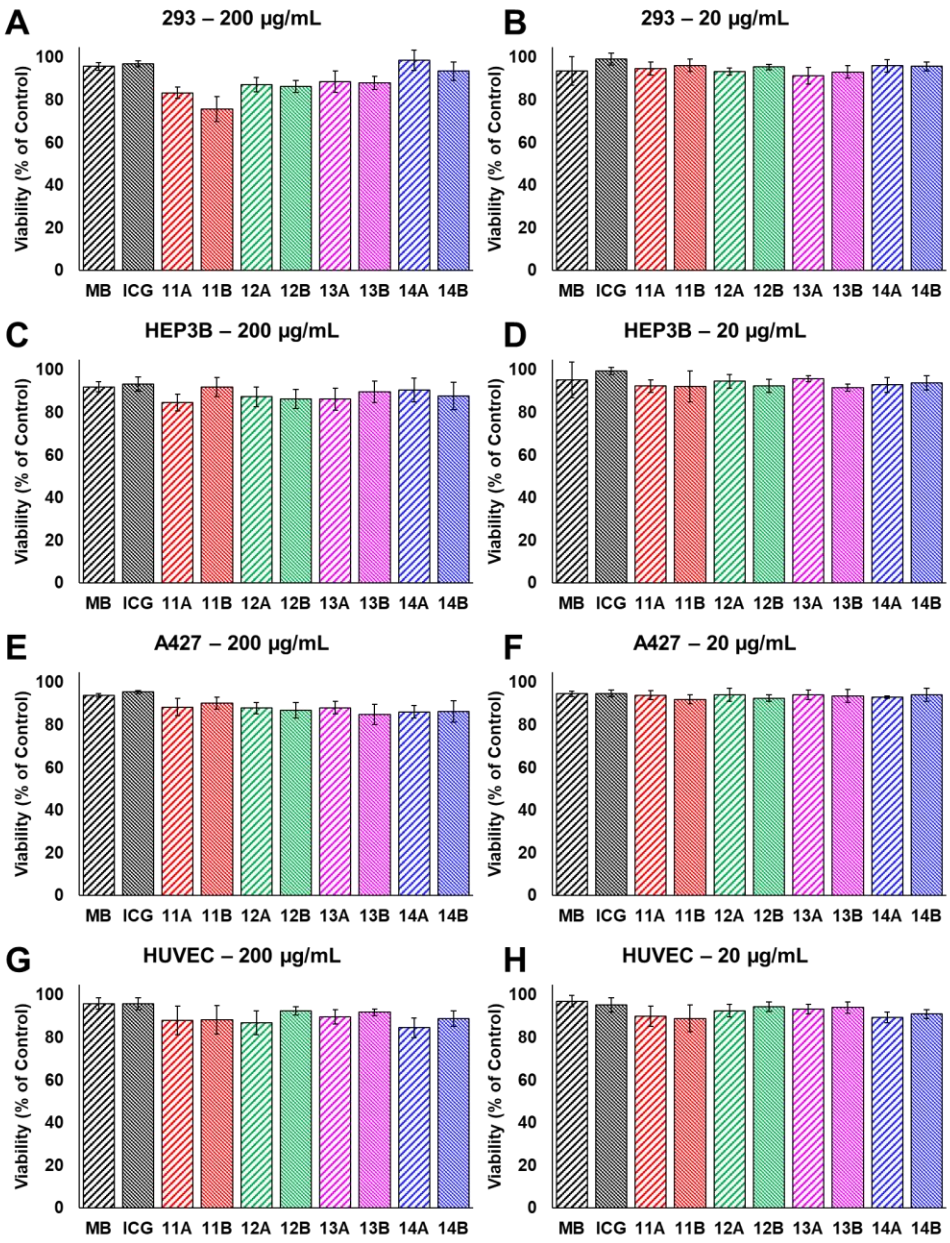

Figure 3.6: ATPLite cellular viability assays of hemicyanines 11A-14B and standard infrared dyes indocyanine green and methylene blue compared to positive (untreated) controls. Cell lines used include A, B) human kidney cells (293), C, D) human liver cells (HEP3B), E, F) human lung cells (A427), and G, H) Human umbilical vein endothelial cells. Cells were treated at 200 µg/mL (column 1 – A, C, E, G) and 20 µg/mL (Column 2 – B, D, F, H). No significance was observed ($p>0.05$).

3.4.4 *In vivo* imaging

In vivo evaluation of hemicyanine compounds were determined with multispectral optoacoustic tomography (MSOT) following injection of each compound into the pancreas of the mouse. Each animal received approximately 100 µL of 100 µM compounds that were mixed with sterilized ultrasound gel to increase structural stability and reduce chance of leakage. Results were consistent with prior findings; as compound 14B exhibited increased signal at aforementioned, red-shifted wavelengths as signals were spectrally unmixed utilizing the reference spectra corresponding to each compound (**Figure 3.7A-B**). With an average signal of 0.737 a.u., compound 11A showed significantly more signal than each other the other compounds (11B – 0.307 a.u., $p<0.01$; 12A – 0.187 a.u., $p<0.001$; 12B – 0.095 a.u., $p<0.001$; 13A – 0.078 a.u., $p<0.001$; 13B – 0.097 a.u., $p<0.001$; 14A – 0.061, $p<0.001$; and 14B – 0.410, $p<0.08$). In addition, compound 14B showed significantly more signal than compounds 12B, 13A, 13B, and 14A (all $p<0.05$). Of note, *in vivo* data inherently compares signal amplitude, rather than emphasizing red-shifted signal observed with diethyl and dimethyl amino groups. While not a perfect comparison, all compounds were also quantified using the spectra of compound 14B to specifically evaluate red-shifted signal portrayed in compounds 13 and 14 (**Supporting Figure S3.24**). This data confirms that compound 14B provides the most optoacoustic signal generation at wavelengths deeper into the NIR window. This may be due in part to compounds 13 and 14 being capable of reaching the TICT state, thus occluding typical optoacoustic signal generation at absorbance wavelengths.

Following optoacoustic imaging, whole-body near-infrared fluorescence was used to confirm presence of compounds in the pancreas of the animals (**Figure 3.7C-D**). Differences in fluorescence signal were revealed, however, such differences were

inconsistent compared to optoacoustic signal. For example, compounds 12A and 12B, which were among the lowest optoacoustic signal, were significantly higher in terms of fluorescence signal than other compounds. Specifically, compound 12A ($1.61x10^9$ counts) was significantly higher than all other compounds excluding compound 12B ($1.41x10^9$ counts) ($p<0.001$). Further, compound 12B is also significantly higher than all other compounds excluding 12A and 14B ($8.96x10^8$ counts) ($p<0.001$). Direct comparison between optoacoustic and fluorescence values may be nuanced and difficult, however, there appears to be an inverse trend, which is consistent with TICT state theory and potential pathways of energy dissipation following excitation[111,112,114,115]. Data exhibited herein supports and encouraging the use of TICT state to increase optoacoustic signal generation at higher wavelength for creation and optimization of unique optoacoustic contrast agents.

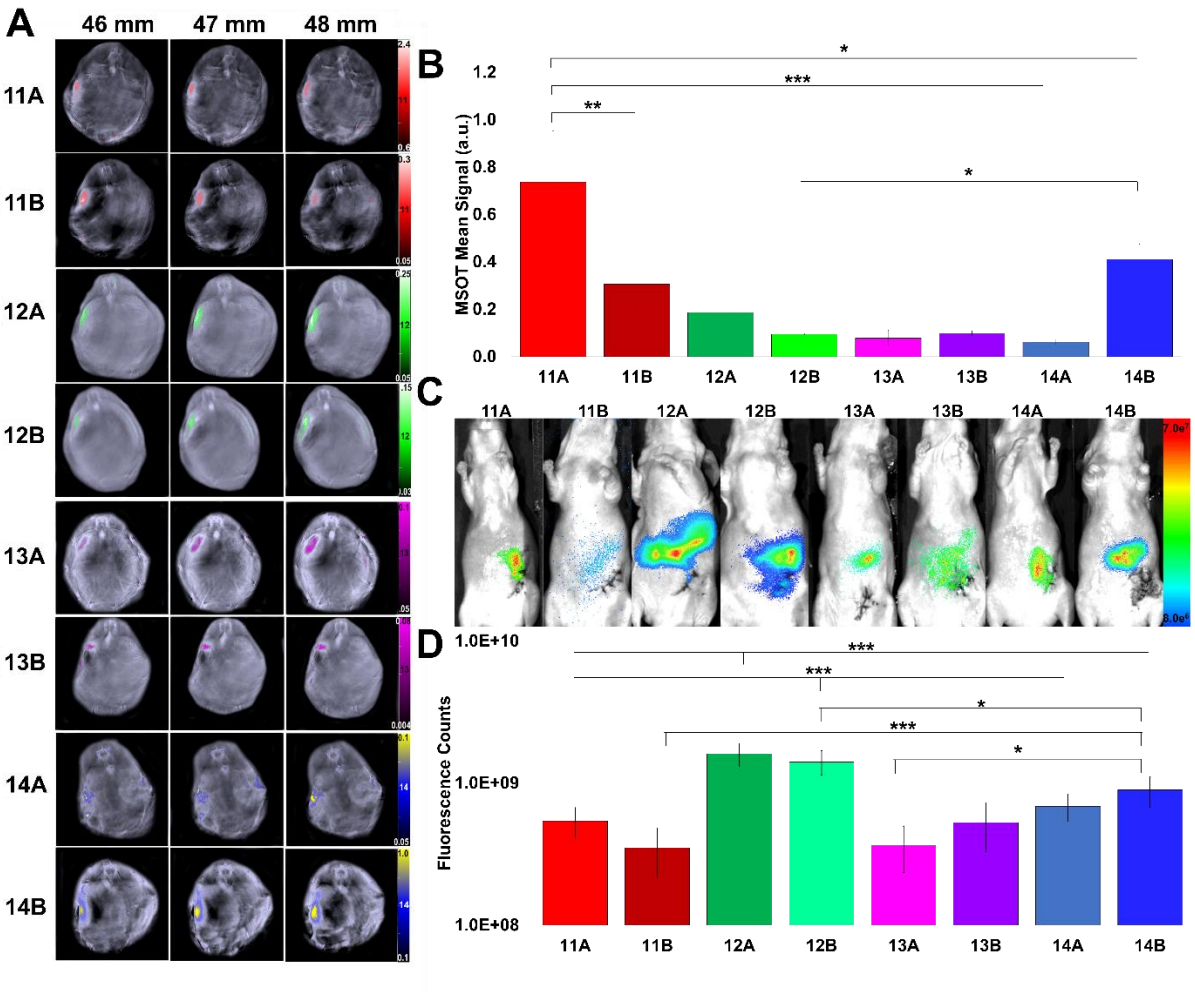

Figure 3.7: *In vivo* visualization of compounds 11A-14B. A) Optoacoustic tomographic slices within treated animals. Higher slice numbers (top) indicate cross sections closer to the tail of mice. Refer to **Figure S1.1** for organ locations for tomographic cross sections. B) Quantification of signal from A. C) Near-infrared fluorescence whole-body images of treated animal. D) Quantification of signal from B. * = $p<0.05$, ** = $p<0.01$, *** = $p<0.001$.

3.4.5 *Ex vivo* confirmation

Subsequent to *in vivo* evaluation of hemicyanine compounds, organs were excised and imaged with NIR fluorescence to further confirm presence of compounds in the pancreas exclusively. As expected, fluorescence signal from the pancreas of animals treated with

compounds 11A-14B were significantly higher than all other organs tested (kidney, liver, spleen, lung, heart) ($p<0.001$) (**Figure 3.8**).

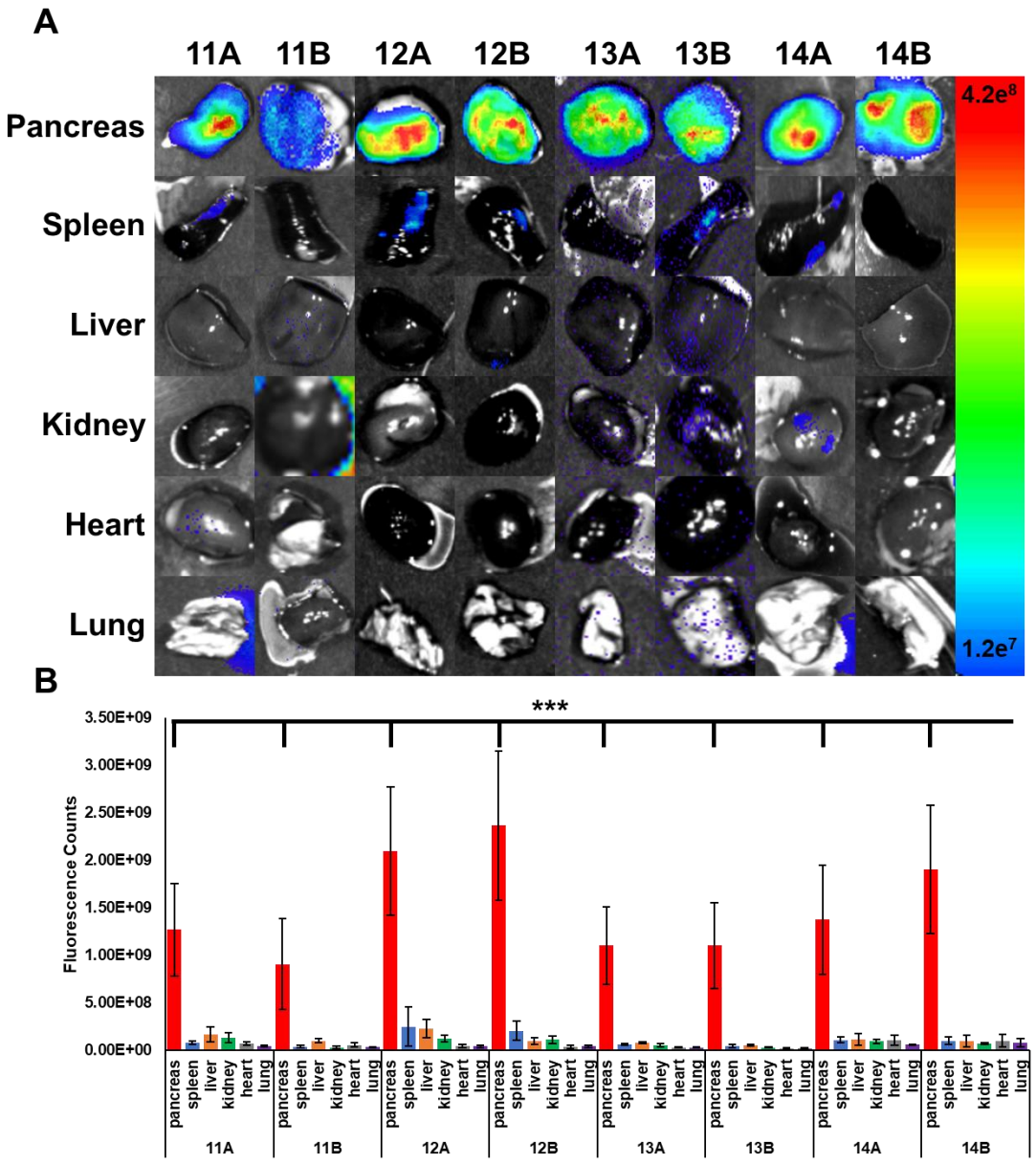

Figure 3.8: *Ex vivo* evaluation of animals treated with compounds 11A-14B. A) Visualization of NIR fluorescence signal in the pancreas, spleen, liver, kidney, heart, and lung. B) Quantification of NIR fluorescence from A. * = $p<0.05$, ** = $p<0.01$, *** = $p<0.001$.

Following full *in vivo* and *ex vivo* experimentation, portions of excised organs (pancreas, spleen, liver, kidney, heart, and lung) were fixed in formalin and standard H&E stained. Histological evaluation showed that hemicyanine compounds were non-toxic to all animals. No morphological changes were observed, indicating no tissue damage.

3.5 Conclusions:

This manuscript focused on developing functionalized hemicyanine compounds for use as unique optoacoustic contrast agents. MSOT is a developing optoacoustic modality that has shown high potential in a clinical setting due to intrinsic advantages over many optical-based imaging modality such as increased imaging depth. However, a lack of unique contrast agents has limited MSOT. The hemicyanine dyes evaluated herein exploit twisted intramolecular charge transfer to shift optoacoustic signal generation to a unique wavelength range, given an appropriate solvent polarity. Data was validated *in vivo* in the pancreas of a murine model. Utilization of the TICT state can be incorporated into future optoacoustic contrast agent development to progress optoacoustic imaging applications in a clinical setting.

3.6 Acknowledgement and Funding:

This manuscript was supported by NIH grants F31CA261044, R01CA205941, R01CA212350, R01GM135392, and P30CA225520.

Chapter 4 – Toxicity Assessment of Mesoporous Silica Nanoparticles upon Intravenous Injection in Mice: Implications for Drug Delivery

This chapter has been published as a research manuscript in *Pharmaceutics*:

William M MacCuaig, Abhilash Samykutty, Jeremy Foote, Wenyi Luo, Alexander Filatenkov, Min Li, Courtney Houchen, William E Grizzle, Lacey R McNally. “Toxicity Assessment of Mesoporous Silica Nanoparticles upon Intravenous Injection in Mice: Implications for Drug Delivery” *Pharmaceutics* 2022 Apr 30; 14(5):969. doi: 10.3390/pharmaceutics14050969

4.1 Abstract:

Nanoparticles are popular tools utilized to selectively deliver drugs and contrast agents for identification and treatment of disease. To determine the translational potential of mesoporous silica nanoparticles (MSNs), further evaluations of toxicity are required. MSNs are among the most utilized nano-delivery systems due to ease of synthesis, pore structure, and functionalization. This study aims to elucidate toxicity as a result of intravenous injection of 25 nm MSNs coated with chitosan (C) or polyethylene glycol (PEG) in mice. Following acute and chronic injections, blood was evaluated for standard blood chemistry and complete blood count analyses. Blood chemistry results primarily indicated that no abnormalities were present following acute or chronic injections of MSNs, or C/PEG-coated MSNs. After four weekly administered treatments, vital organs showed minor exacerbation of pre-existing lesions in the 35KPEG-MSN and moderate exacerbation of pre-existing lesions in uncoated MSN and 2KPEG-MSN treatment groups. In contrast, C-MSN treatment groups had minimal changes compared to controls. This study suggests 25 nm MSNs coated with chitosan should elicit minimal toxicity when administered as either single or multiple intravenous injections, but MSNs coated with PEG, especially 2KPEG may exacerbate pre-existing vascular conditions. Further studies

should evaluate varying sizes and types of nanoparticles to provide a better overall understanding on the relation between nanoparticles and *in vivo* toxicity.

4.2 Introduction:

In disease treatment, nanomedicine is a potential solution that provides theranostic capabilities for a variety of applications. Of the wide diversity of nanomaterial formulations, mesoporous silica nanoparticles (MSNs) have emerged as a popular option due to the ability to facilitate specific cargo delivery for imaging, and/or therapeutics[120]. The increase in popularity of MSNs as nano-delivery vehicles owes to uniformity in synthesis, tunability, and facile functionalization[121,122]. MSNs can be synthesized in a uniform size range and the mesoporous structure can encapsulate a drug for treatment or medical imaging using clinically relevant modalities including magnetic resonance imaging (MRI) or fluorescence[123,124]. Surface modifications of MSNs permit targeting to disease-specific features within the body, such as unique extracellular receptors[125-127]. With such advantages, MSNs are intriguing for potential translation to a clinical setting.

Despite the potential for theranostic application of MSNs, concerns of toxicity have been partially responsible for impeded clinical translation. Historically, toxicity as a result of silica was associated with utilization of micro-scale particles, resulting in the development of autoimmune diseases[128]. Studies using silica nanoparticles have resulted in fibrosis and liver/kidney injury due to rapid renal clearance or sequestration to the liver[129,130]. In contrast, several *in vivo* studies indicate that silica nanoparticles are not toxic[131,132]. Inconsistent results in the evaluation of MSNs, and many types of nanoparticles, often occur due to multiple confounding factors in the nanoparticle system. That is, the nanoparticle type, cargo, functionalization, conjugation linkers, etc., all contribute to the

toxicity response, or lack thereof. With the increasing popularity and opportunity for clinical translation, head-to-head comparisons of MSNs with commonly used functionalization are required.

As mentioned, evaluation of the toxicity of functionalized MSNs is crucial for translational studies. MSNs are rarely used without being functionalized via external coating; cargo would rapidly exit from the porous silica into the surrounding environment without inclusion of an external coating. In addition, such coatings are often utilized to provide stealth in the body and/or specificity for application, therefore absence would greatly diminish efficacy[133-135]. While studies have observed that the use of an external coating on MSNs can mitigate toxicity and fibrosis[136], there are few head-to-head comparisons that carry clinical implications.

Polyethylene glycol (PEG) is a popular biocompatible polymer. When functionalized to nanoparticles such as MSNs, PEG adds stealth/targeting to permit nanoparticles to escape phagocytosis, leading to longer circulation in the bloodstream[137]. PEG can degrade *in vivo*, permitting cargo release, while maintaining minimal non-specific interactions[138]. However, PEG has been found to decrease uptake and interactions with target cells through too much of “stealth effect”, leading to decreased theranostic efficacy[139,140]. PEGylated nanomaterials have also been associated with renal toxicity and anaphylactic shock *in vivo*[141,142].

Chitosan is another commonly used biomaterial and nanoparticle coating *in vivo*. Chitosan is a deacylated form of naturally occurring polysaccharide chitin, and often is used as a nanomaterial due to pH-responsivity in biological relevant levels[22,143-145]. Protonation of an amine results in charge-based molecular swelling, allowing cargo

release specifically in acidic environments, including malignancies[146]. Chitosan also provides a “stealth effect” like PEG, since chitosan is naturally occurring, although positive surface potential often leads to non-specific interactions in the body[145]. While studies have successfully used chitosan as a non-toxic nanomaterial[145,147], some studies report toxicity as a result of agglomeration[148,149], warranting further investigation. PEG and chitosan are proper examples of nanomaterials that should be evaluated in head-to-head toxicity studies as MSN external coatings.

This study sought to isolate, assess, and compare the relative toxicity elicited as a result of MSNs coating. Such a study to isolate the base silica nanoparticle and external coating, without cargo and further functionalization, has thus far been absent from the literature, particularly when evaluating toxicity with both single and multiple injections. Most often, nanoparticle formulations are complex with numerous components preventing specific assessment of an individual component, i.e., coating, and overall leading to inconsistent toxicity results. Determination of the toxicity elicited by various aspects of a single nanoparticle system, e.g., nanoparticle base material, shape, size, conjugation, coating, drug, etc., is near impossible. To maintain clinical similarity to treatments such as chemotherapy, MSNs of each type would be intravenously injected once for acute assessment, and once a week for a month for chronic assessment. Following treatment with MSNs or coated MSNs, blood can be measured for complete blood count and blood chemistry, both in the short term, and longer term following multiple injections. Utilization of an immunocompetent mouse model provides key information relating to the toxicity as a result of MSN treatment. CD-1 female mice were the subject of this study due to extensive history of utilization for toxicology and pharmacology experimentation[150-152].

Large size, tail vein access, and low aggressiveness contribute to popularity of CD-1 mouse utilization in such studies. Following blood tests, mouse organs were harvested to evaluate if treatments caused toxicity through histopathology.

4.3 Materials and Methods:

4.3.1 Materials

Reagents from Sigma Aldrich (St. Louis, MO, USA): CTAB (hexadecyltrimethylammonium bromide) (molecular biology, ≥99%, H6269), low molecular weight chitosan (448,869), 2KPEG (poly (ethylene glycol)) (MW: 2000, 84,797), 35KPEG (poly (ethylene glycol)) (MW: 35,000, 81,310), GPTMS (3-glycidyloxypropyl) trimethoxysilane (≥98%, 440,167), TMOS tetramethyl orthosilicate (≥99%, 341,436), benzoylated dialysis tubing (D7884), TEA triethanolamine (gas chromatography, ≥99.0%, 90,279). Other materials and reagents: Milli-Q water dispensed through Milli-Pore Sigma (Sigma-Aldrich, St. Louis, MO, USA); glacial acetic acid (certified American Chemical Society, ≥99.7%, A38C-212) (Waltham, MA, USA); ethyl alcohol (anhydrous, 200 proof) (Warner Graham Company, Cockeysville, MD, USA); Dulbecco's modified Eagle medium (DMEM) (ThermoFisher Scientific, Waltham, MA, USA); fetal bovine serum (FBS) (R&D Systems, Minneapolis, MN, USA).

4.3.2 Nanoparticle Synthesis

Mesoporous silica nanoparticles (MSNs) were prepared by modified Stober synthesis (**Figure 4.1**). A total of 2.00 g of CTAB was added to 240 mL of purified Milli-Q (MilliPore) water at 80 °C. After allowing the solution to reach 80 °C again, 0.42 g of TEA was added to the solution with moderate (400 rpm) stirring. Once heated to 80 °C, 11.0 mmol of TMOS was added and stirred on heat for 16 h. At completion, the reaction bottle was

removed from heating/stirring and allowed to cool to room temperature. To remove the CTAB surfactant scaffold from the MSNs, a 1:1 (v/v) solution of 2 M glacial acetic acid and ethanol was used to clean the MSNs. About 50 mL of MSNs were added to 2000 molecular weight cut off dialysis tubing and placed into a 1 L solution of aforementioned acid and ethanol mix with a stir bar (100 rpm). External solution was replaced every 2 h for the first three cycles, and then every 12 h for the next five cycles. MSNs were then dialyzed similarly in MQ water for four cycles, each cycle lasting 12 h. MSNs were removed from dialysis bags and stored in a glass bottle.

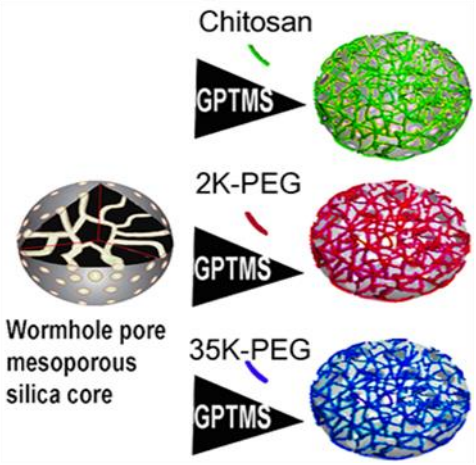

Figure 4.1: Schematic illustration of coated MSN preparation. Following synthesis of base MSNs, GPTMS linker is attached for subsequent chitosan, 2KPEG, or 35KPEG conjugation.

4.3.3 Nanoparticle Characterization

A Malvern Zetasizer Nano ZS (Malvern Panalytical, Malvern, UK) was used to analyze MSN diameter, polydispersity index (PDI), concentration, and zeta potential following synthesis, and throughout dialysis. Size parameter measurements were collected in triplicate using dynamic light scattering (DLS) and multi-angle dynamic light scattering

(MADLS) at three angles (173°, 90°, 7°). Particle concentration was determined using MADLS with an input of 145 kcps for dispersant mean count rate. An Eppendorf Vacufuge 5301 was used to lyophilize MSNs at a rate of 0.2 mL/h. A TriStar analyzer was utilized to vacuum dry the powders at 120 °C overnight. A seven-point Brauner, Emmett, Teller (BET) isotherm and a 50-point adsorption/desorption isotherm were collected. Specific surface area and pore volume calculations were acquired through BET and Barrett–Joyner–Halenda (BJH) methodology[153].

4.3.4 Nanoparticle Functionalization

Dialyzed MSNs were diluted in ethanol (4:1) and ultrasonicated for 1 min at room temperature to ensure dispersion. MSNs were functionalized for subsequent attachment of polymer gatekeeper. Before coating, GPTMS (0.45 mmol, 0.1 mL) was added to 5 mL of 100% ethanol, and 20 mL of dialyzed MSN. The solution was gently stirred at room temperature for 3 h for grafting to MSNs. MSNs with silane linker were acidified to pH 3.5 via dropwise addition of 100 mM HCl for conjugation of chitosan. MSNs with silane linker were basified to pH 10 by addition of 100 mM NaOH for conjugation of PEG. 1% w/v chitosan, 2KPEG, or 35KPEG was added at a ratio of 6:5. Conjugation of chitosan/PEG occurred through epoxy ring opening of GPTMS. Solutions were shaken at 1000 rpm for 12 h at room temperature. Coated MSNs were isolated by centrifuging solutions at 15,000 rpm for 30 m at room temperature.

4.3.5 Functionalized Nanoparticle Characterization

Following synthesis of C-MSNs, 2KPEG-MSNs, and 35KPEG-MSNs, size, zeta potential, and PDI were reacquired to survey for differences from uncoated MSNs. MSNs, 0.5 mL of C-MSNs, 2KPEG-MSNs, and 35KPEG-MSNs (10^{10} particles/mL) were exposed to 10%

FBS in standard DMEM cell growth media (1.5 mL) to simulate protein corona formation. After 24 h, each MSN group was revaluated using MADLS for differences in size and zeta potential as a result of protein corona formation. Prior to coating conjugation, fluorescence contrast agent IR780 was encapsulated within C-MSNs, 2KPEG-MSNs, and 35KPEG-MSNs to observe mechanism of agent release in hypoxia and biological conditions **(Supporting Figure S4.1**). IR780-loaded samples were pH adjusted to 6.6 or 7.4 diluted to an optical density of 1 OD/mL (V-730 ultraviolet-visible light spectrophotometer, JASCO, Easton, PA, USA). Samples were shaken moderately until repeated measures at distinct time points. Peak absorbance of the supernatant was measured (780 nm) to determine release of contrast agent.

4.3.6 *In Vivo* Nanoparticle Toxicity

Female CD-1 immunocompetent mice aged 4 weeks were used in strict adherence to the University of Oklahoma Institutional Animal Care and Use Committee approved protocol. CD-1 mice are a popular subject for pharmacology and toxicology applications. Immunocompetent CD-1 mice were specifically used in this study opposed to other chapters of this dissertation in order to evaluate the potential immune response elicited by administered particles. One week following receipt from Charles River Laboratories (Wilmington, NC, USA), mice were randomly divided into the following five groups:

1) Controls (C) n = 3.
2) Mesoporous silica nanoparticles with no coating (MSNs) n = 6.
3) Mesoporous silica nanoparticles coated with chitosan (C-MSNs) n = 6.
4) Mesoporous silica nanoparticles coated with 2 kDa polypropylene glycol (2KPEG-MSNs) n = 6.

5) Mesoporous silica nanoparticles coated with 35 kDa polypropylene glycol (35KPEG-MSNs) n = 6.

Except for controls, which received no injections, each animal received an intravenous tail injection of 10^{10} particles in 100 µL of treatments as noted in groups 2–5. Two points in time were studied; acute (24 h post-injection) and chronic (1 injection per week for 4 weeks) (**Figure 4.2**). The control animal samples were collected at the same time point as the chronic samples. About 24 h following treatment, blood samples were taken via retroorbital withdrawal from acute mice and analyzed by complete blood count (CBC) and blood chemistry (BC) tests. Chronic timepoint blood collection occurred after treatments 2 and 4, to minimize animal stress through overly frequent blood collection. Blood samples were analyzed using CBC and BC. Following completion of treatment, mice were euthanized via carbon dioxide overdose and cervical dislocation. Organs of interest (liver, spleen, kidney, pancreas, heart, and lung) were rapidly extracted from the euthanized mice and placed in neutral buffered formalin. After 16 h of fixation, tissues were processed to paraffin and embedded in paraffin blocks. Four micrometer tissue sections were cut from each tissue and stained with hematoxylin and eosin (H&E). Slides were analyzed blindly by both a board-certified veterinary pathologist (Foote) and a board certified diagnostic human pathologist with extensive experience in murine pathology (Grizzle, Luo, and Filatenkov).

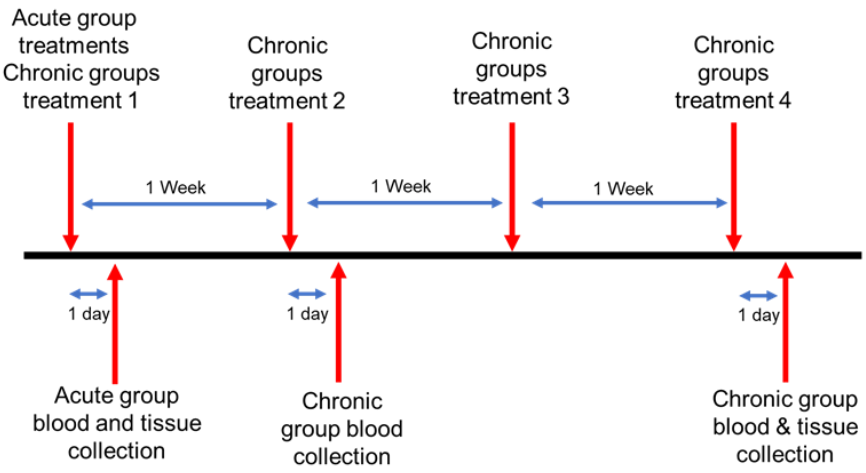

Figure 4.2: Timing schematic of *in vivo* toxicity studies with coated MSNs. Acute and chronic treatments began concurrently. Blood collections were held 24 h following select treatments. Tissue collections were held 2 4h following the final treatment for respective treatment groups.

4.3.7 Complete Blood Count and Chemistry Panels

Following retroorbital blood extraction from mice, complete blood counts were run using a Idexx Procyte DX Hematology Analyze (Idexx Laboratories, Westbrook, ME, USA) using ethylenediaminetetraacetic acid (EDTA) whole blood with 50 µL. Samples take 2 m to run. The Abaxis VetScan VS 2 (Zoetis, Parsippany, NJ, USA) was used for the blood chemistry panel with the Comprehensive Plus rotor. About 100 µL of lithium heparin (LH) whole blood was used to run samples in approximately 13 m.

4.3.8 Statistics

Statistical evaluation of the BC/CBC blood tests was performed using analysis of variance (ANOVA) and Tukey multiple comparison test with significance defined at $p<0.05$.

4.4 Results and Discussion:

4.4.1 Nanoparticle Synthesis and Characterization

MSNs were prepared through modified Stober synthesis. An emulsion of surfactant scaffold was formed under high temperature. Silica precursor coats the scaffold to create uniform MSNs of approximately 25 nm, measured with dynamic light scattering (DLS). While many sized MSNs are utilized, 25 nm has been identified as an intriguing size; large enough to avoid rapid glomerular filtration, but small enough to avoid sequestration by Kupffer cells in the liver[154]. Following preparation, MSNs are dialyzed to remove surfactant, preventing the possibility for surfactant-based toxicity. Prior to conjugation of coatings, nitrogen adsorption/desorption isotherms were analyzed with BET/BJH methodology to estimate MSN pore volume of 0.23 cm^3/g, and MSN specific surface area of 750 m^2/kg. Chitosan solution (1% weight by volume) was prepared in acetic acid and water. Due to controversy in toxicity as a result of PEG, PEG solutions with different molecular weights were utilized. PEG2000 and PEG35000 were selected due to a tradeoff between rapid clearance and extended circulation time that is relevant to drug delivery[155]. About 2% weight by volume solutions were prepared in water for molecular weights of 2 kDa (PEG2000) and 35 kDa (PEG35000). Following surfactant removal, MSNs were diluted in ethanol and functionalized using an organosilane-epoxy linker for external coating attachment. PEG2000, PEG35000, and chitosan solutions were added to the MSN solution for attachment of coating. Average diameters were as follows: MSNs - 25.8 (±2.1) nm; C-MSNs - 31.8 (±3.1) nm; 2KPEG-MSNs - 29.7 (±3.6) nm; and 35KPEG-MSNs - 30.1 (±2.3) nm (**Figure 4.3A-B**). Full size distributions are included (**Figure 4.3E–H**). All polydispersity indexes were around or below 0.15, indicating monodisperse samples (**Figure 4.3D**). After synthesis, surfactant surrounding MSNs result in zeta potential measurements of 46 mV, which is reduced to −5.6 mV after surfactant removal,

and increased to 11.3 mV following GPTMS addition (**Figure 4.3C**). Conjugation of chitosan was confirmed through increased zeta potential (44.1 mV) due to amine functional groups in physiological pH (7.4)[145,147]. Similarly, zeta potential for 2KPEG-MSNs (−0.6 mV) and 35KPEG-MSNs (−0.9 mV) increased slightly due to coating of silanol groups and decreasing external hydroxyl groups on MSNs, but not as dramatically as C-MSNs due to lack of amine functionality[156].

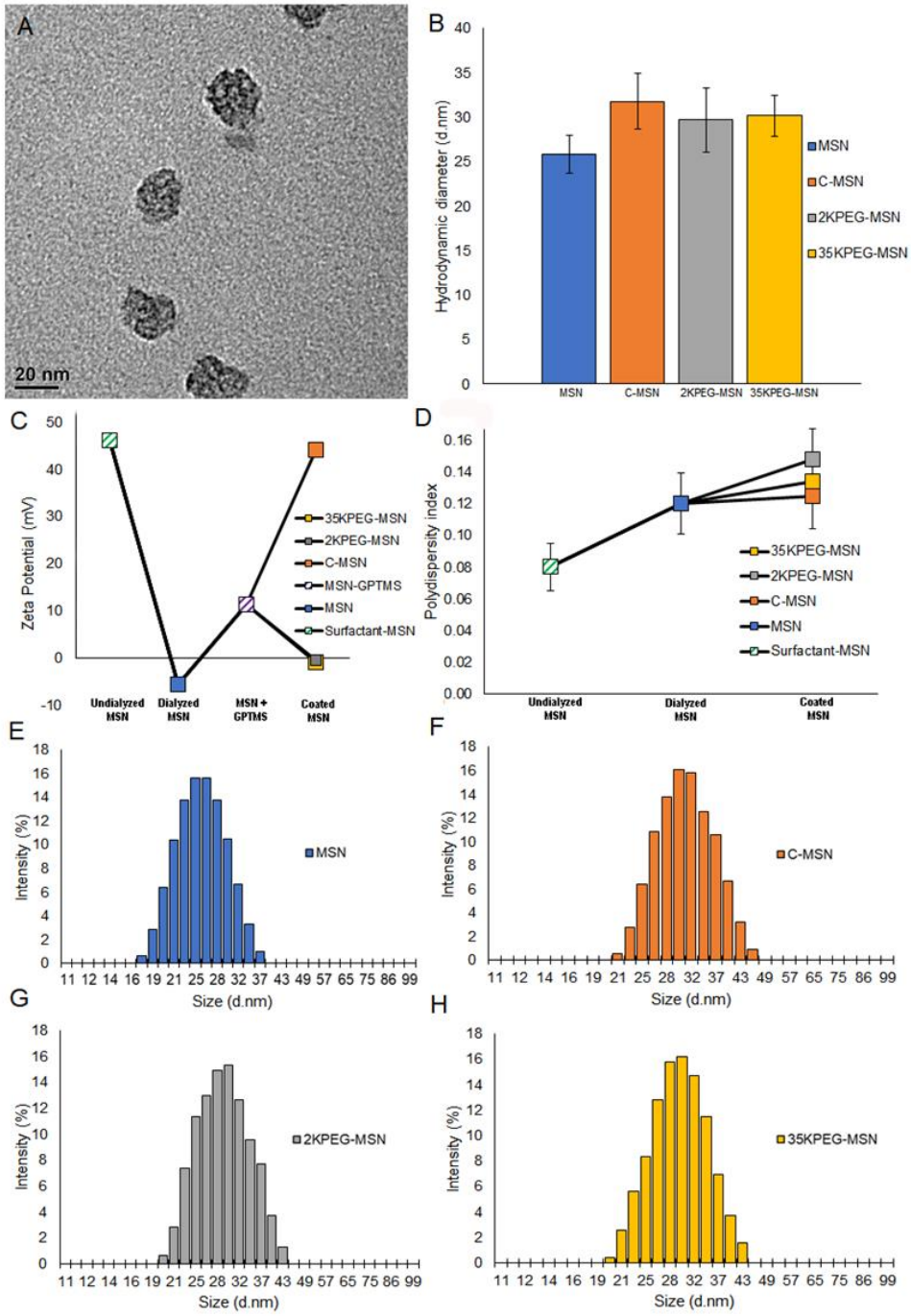

Figure 4.3: Characterization of coated MSN size and charge. A) Transmission electron microscopy image of synthesized MSNs. B) Diameters of nanoparticles utilized. Hydrodynamic diameters measured as 25.8 nm, 31.8 nm, 29.7 nm, and 30.1 nm for MSNs, C-MSNs, 2KPEG-MSNs, and 35KPEGMSNs, respectively. C) Zeta potential measurements of surfactant-MSNs, MSNs, C-MSNs, 2KPEG-MSNs, and 35KPEG-MSNs to ensure proper conjugation. D) Polydispersity index of samples throughout synthesis.

E) Full MSN size distribution as determined by DLS measurements. F) Full C-MSN size distribution as determined by DLS measurements. G) Full 2KPEG-MSN size distribution as determined by DLS measurements. H) Full 35KPEG-MSN size distribution as determined by DLS measurements. Error bars represent +/- one standard deviation of the mean. No p-values to report.

Addition of 10^5 MSNs into a 1.5 mL solution of 10% FBS in cell growth media resulted in minor increases in coated MSN size and shifts in surface charge (**Table 4.1**). Small increases in size and slight alterations surface charge were observed in MSNs, 2KPEG-MSNs, and 35KPEG-MSNs. C-MSNs were observed to significantly increase in size by 17.1 nm to 48.9 nm following exposure to FBS. Chitosan has a relatively strong positive surface charge, which interacts with proteins in the FBS solution to form a protein corona. Formation of negatively charged proteins around C-MSNs results in a large drop in zeta potential, from +44.1 mV to 12.6 mV. These results suggest that C-MSNs will likely form a protein corona upon introduction into the body.

Table 4.1: Size and charge characteristics of MSNs and coated MSNs following 24 h exposure to 10% FBS in cell growth media.

FBS treatment characterizations	Diameter by DLS (nm)			Zeta Potential (mV)		
MSN coating	As-prepared	FBS-treated	Change	As-prepared	FBS-treated	Change
MSN	25.8	28	+2.2	-5.59	-2.84	+2.75
C-MSN	31.8	48.9	+17.1	44.07	12.62	-31.45
2KPEG-MSN	29.7	29.9	+0.2	-0.58	-1.35	-0.77
35KPEG-MSN	30.1	30.3	+0.2	-0.91	-1.72	-0.81

4.4.2 *In Vivo* Nanoparticle Toxicity

CD-1 immunocompetent mice were utilized for testing *in vivo* toxicity. Mice were split into acute and chronic experiments, characterized by number of repeat treatments, toxicity evaluations, and time between treatments and measurements. Acute mice were intravenously injected with 10^{10} MSNs in 100 µL; C-MSNs, 2KPEG-MSNs, and 35KPEG-MSNs. About 24 h following treatment, blood samples were taken via retro-orbital withdrawal and analyzed by CBC and BC tests (**Table 4.2**). In addition to short-term evaluations, toxicity concerns over time are of great importance and clinical relevance when considering multiple injections. To elucidate chronic toxicity, CD-1 immunocompetent mice were intravenously injected with treatments consistent with the short-term studies (MSNs, C-MSNs, 2KPEG-MSNs, 35KPEG-MSNs), once a week for a total of four treatments. Blood samples were taken via retro-orbital withdrawal 24 h following treatment 2 and 24 h following the final treatment. Blood was not collected after treatment 3 to avoid stress on mice due to frequent collection. Subsequent to final blood collection for both acute and chronic treatment groups, mice were euthanized via CO_2 overdose and cervical dislocation. Organs were collected (liver, kidney, spleen, lung, pancreas, heart) for histopathologic evaluation (**Figure 4.4** and **Figure 4.5**).

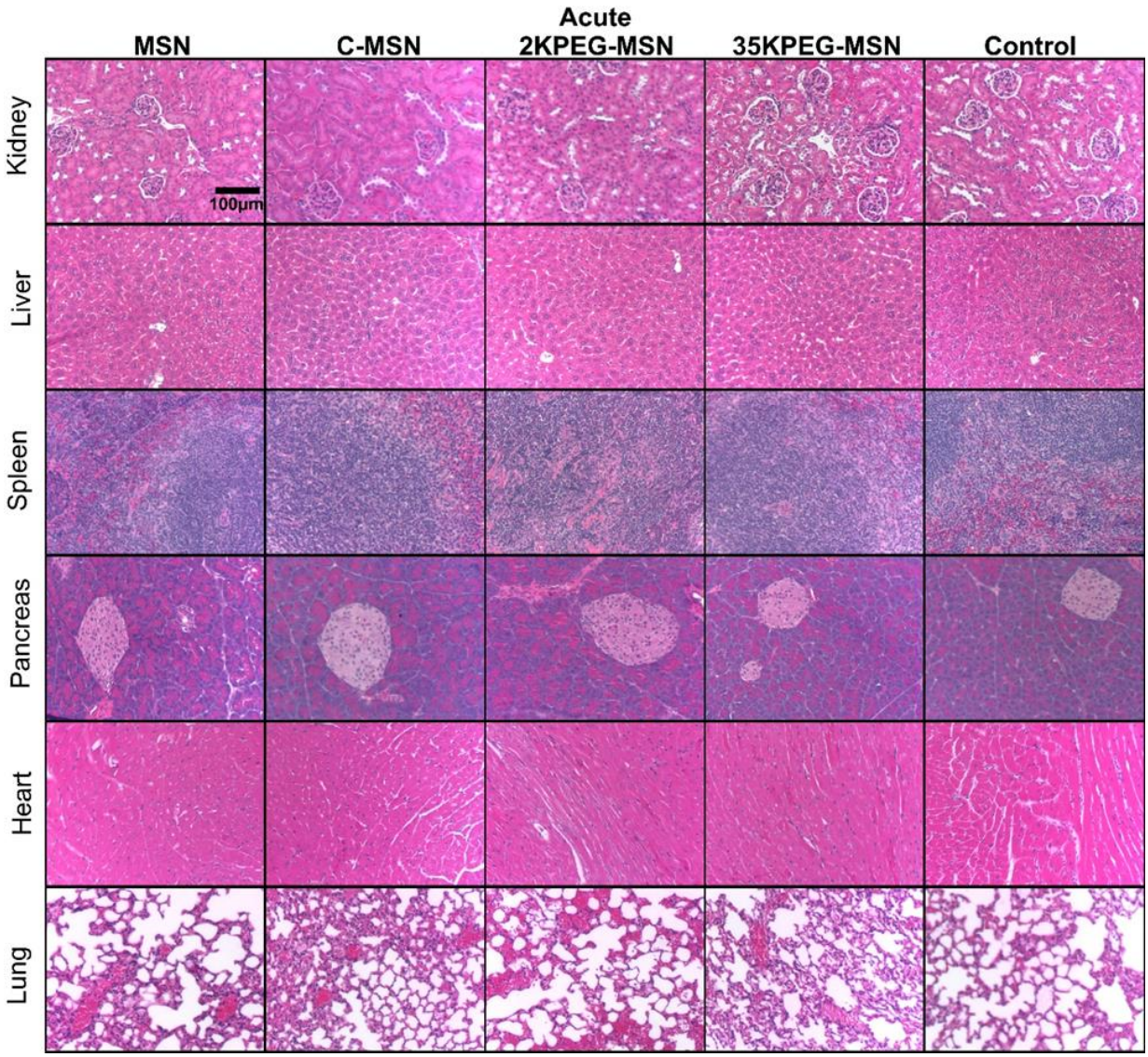

Figure 4.4: H&E-stained histological evaluation of vital organs following acute treatment with coated MSNs. Images were acquired at 10 X magnification.

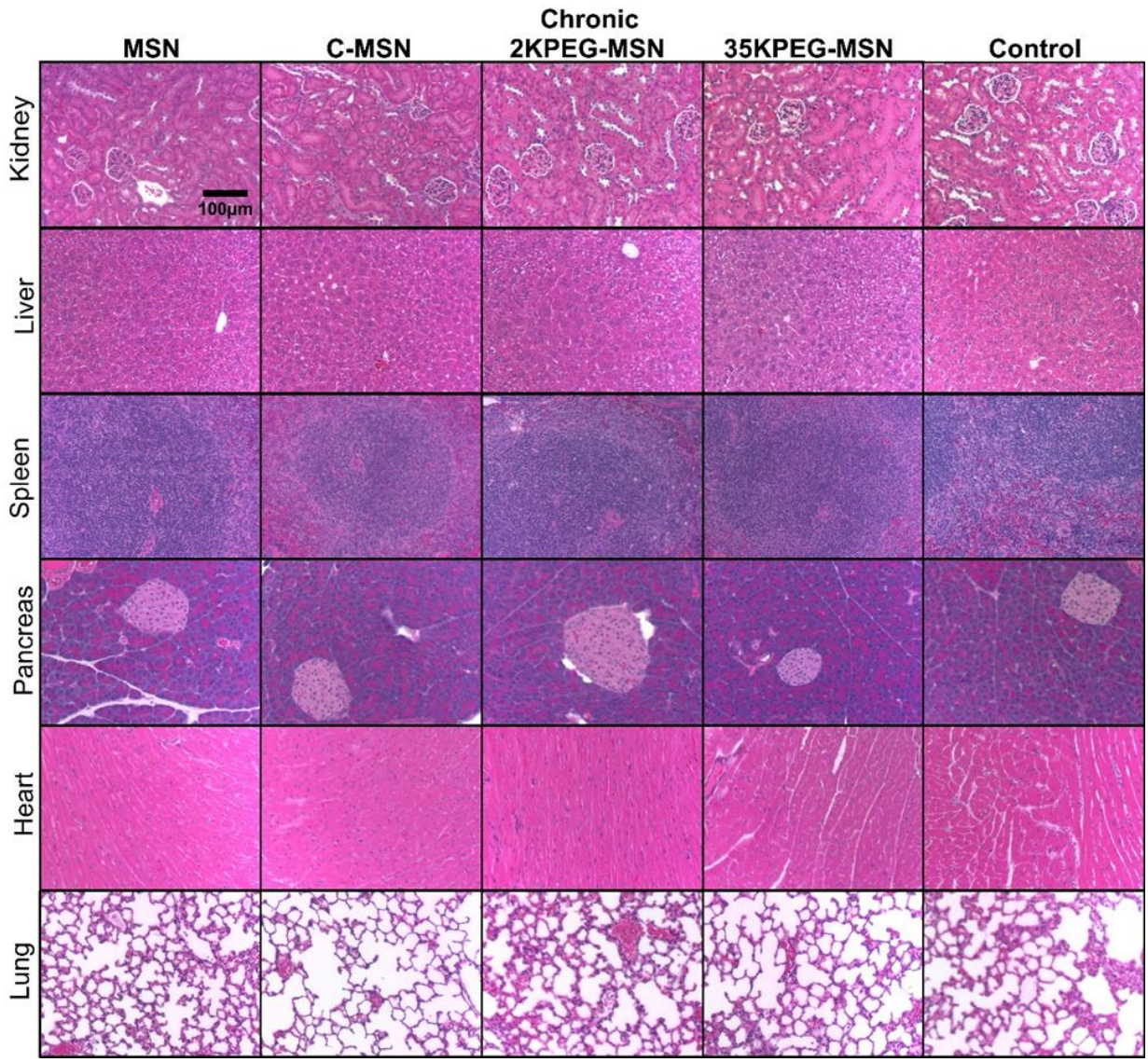

Figure 4.5: H&E-stained histological evaluation of vital organs following chronic treatment with coated MSNs. Images were acquired at 10X magnification.

In general, the histopathology of acute and chronic time points for the C-MSN group was similar to controls and the mice had no areas of fibrosis in any organ or other signs of organ damage. The histological and blood chemistry findings from mice acutely or chronically injected with C-MSN were consistent with control mice. While it would be unlikely to utilize uncoated MSNs as either a drug or contrast agent delivery system, we

found that uncoated MSN resulted in extensive right atrial right ventricle thrombus in one mouse.

In contrast, our study indicates that PEG may be a risk factor for increases in interstitial fibrin thrombi. Our findings show that 35KPEG-MSN had extensive interstitial fibrin thrombi in the alveoli, sinusoidal immature thrombi/hemorrhages, and had immature thrombi in the left atrium in one mouse. One mouse receiving 35KPEG-MSNs also had some areas of hepatic necrosis. The lower molecular weight PEG, 2KPEG-MSN, had greater and more extensive immature thrombi in the pulmonary arteries and veins estimated to occupy 50% of vessels. There also was an extensive thrombus in the left ventricle. While the 35KPEG-MSN treatment group contained one animal with interstitial fibrin thrombi, all animals in the 2KPEG-MSN group were observed with extensive thrombi in 50% of vessels. This suggests that PEG may be a culprit in increased interstitial fibrin leading to immature thrombi and even mature thrombi as well as pulmonary aggregation. While lower molecular weight PEG has increased propensity for aggregation[157], this is the first study to report PEG, specifically 2KPEG, and also 35KPEG to a much lesser extent, as a risk factor of increased interstitial fibrin, immature thrombi, fully mature thrombi (in the 2KPEG-MSN group), and pulmonary aggregations following acute and chronic treatments of intravenously injected nanoparticles without extensive complexity, i.e., targeting peptides, drugs, etc.

Observed tissue changes varied among individual mice in each group and among groups. Of note, tissue changes did not affect organ function per blood analysis, animal weights, or animal behavior. There is concern for an interstitial fibrin and thrombi in the vasculature, alveoli, and large thrombi as all mice receiving 2KPEG-MSNs had similar vascular

pathologies to a great extent and one animal out of six injected with or 35KPEG-MSNs to a much lesser extent. Tissues of mice receiving C-MSNs did not indicate a danger to the mice secondary to receiving these injections. Due to existing lesions in control mice, it is unlikely that these lesions would be induced de novo in cases receiving C- or 35KPEG-MSNs. At worst, the C-MSN or 35KPEG-MSN exacerbate existing conditions or because of these existing lesions may confuse comparisons. Because of preexisting vascular injury in arteries[158], our results may also suggest a more extensive healing process of injury for mice treated with MSNs and 2KPEG-MSNs compared to C-MSNs and 35KPEG-MSNs.

For the CD-1 mouse, the histopathology of mice is unusual. Specifically, hepatocytes have cytoplasm which are clear in the morning due to increased glycogen storage[159,160]. However, this may change in a few hours due to the fed-fasting cycle during the sleep cycle of the mouse, deeming it important to sacrifice the mice during the same temporal period[159,160]. This change has been described, but sometimes has led to incorrect interpretations that this change is instead a result of therapies. Control mice demonstrated no areas of fibrosis or acute inflammation. Two control mice had immature thrombi in heart, with one having immature thrombi and hemorrhage in the lung. Two of the control mice had multifocal areas of hepatic necrosis, and one was observed to have hepatic atrophy and areas of renal edema and hemorrhage. The control mice demonstrate three major potential pathologies, (1) areas of multifocal hepatocyte necrosis/atrophy; (2) multifocal areas of renal necrosis, edema, and hemorrhage; and (3) multifocal immature thrombi in the vasculature of the lungs, cardiac ventricles, atria, and pulmonary arteries. These lesions may be considered as secondary to existing pathologies as each was

observed in control mice that received no intravenous injections throughout the experimentation period. Notably, thrombosis has been reported as an occasional change consistent with the aging of CD-1 mice[161-163]. Thrombi often occur secondary to spontaneous/induced vasculitis rather than a toxicologically induced legion, possibly explaining thrombi presence in control mice[164]. In this study, while no organ failure is observed, extensive areas of thrombi were present in the lungs of pre-disposed CD-1 mice. Following treatments, PEG-coated MSNs appeared to exacerbate such injuries, where 2KPEG-MSNs treatment groups had larger areas of extensive thrombosis, suggesting increased aggregation propensity of lower molecular weight PEG.

Table 4.2: Blood chemistry and complete blood count values as reported from acute and chronic coated MSN treatment groups.

A	Blood Chemistry-Acute				
	Untreated	MSN	C-MSN	2KPEG-MSN	35KPEG-MSN
ALB	4.50	4.37	4.57	4.57	4.40
ALP	110.3	88.7	104.3	118.0	110.3
ALT	38.0	34.0	49.0	51.3	28.3
AMY	1189	1163	1067	986	1083
TBIL	0.33	0.40	0.40	0.40	0.30
BUN	20.0	21.7	21.3	18.7	19.3
CA	11.8	11.3	11.0	11.8	11.1
PHOS	8.17	7.70	7.97	9.60	7.70
CRE	0.27	0.33	0.27	0.30	0.33
GLU	128.7	103.7	108.3	117.7	119.7
NA+	154.7	154.3	153.7	159.0	154.0
K+	6.90	6.43	6.87	6.67	5.97
TP	6.03	5.80	6.00	6.07	5.90
GLOB	1.53	1.43	1.43	1.50	1.53

B	Blood-Chemistry-Chronic				
	Untreated	MSN	C-MSN	2KPEG-MSN	35KPEG-MSN
ALB	4.53	4.53	4.67	4.63	4.57
ALP	82.3	95.7	91.7	92.7	80.0
ALT	38.0	30.7	36.7	23.7	35.0
AMY	1095	1066	1085	1174	1067
TBIL	0.47	0.23	0.30	0.27	0.30
BUN	20.3	23.7	22.3	18.7	20.7
CA	11.3	11.0	11.1	11.3	11.2
PHOS	7.63	7.43	7.10	7.30	6.20
CRE	0.27	0.27	0.20	0.23	0.37
GLU	117.3	116.3	96.3	98.7	99.0
NA+	155.7	156.0	154.7	155.3	155.7
K+	6.93	7.00	7.05	7.13	6.10
TP	6.07	5.90	6.17	6.13	6.27
GLOB	1.57	1.37	1.50	1.50	1.67

C	Complete Blood Count-Acute				
	Untreated	MSN	C-MSN	2KPEG-MSN	35KPEG-MSN
RBC	10.2	10.5	10.3	10.3	10.5
HGB	16.6	17.2	16.4	16.2	16.7
HCT	56.9	58.4	55.4	55.1	58.3
MCV	56.0	55.5	54.0	53.6	55.4
MCH	16.3	16.3	16.0	15.7	15.8
MCHC	29.1	29.4	29.5	29.3	28.6
RDW-SD	28.9	29.7	28.8	29.0	29.5
RDW-CV	20.7	21.7	21.6	21.8	21.6
RET	409	396	440	367	541
RET %	4.05	3.78	4.32	3.57	5.18
PLT	904	776	979	878	1086
PDW	9.10	9.37	8.50	10.10	9.13
MPV	8.10	7.97	8.23	8.47	8.30
P-LCR	12.0	10.9	9.4	12.9	10.1
PCT	0.73	0.62	0.80	0.74	0.92
WBC	4.44	5.67	6.70	6.70	6.02
NEUT	0.52	0.78	1.46	0.80	0.67
LYMPH	3.79	4.72	5.03	5.74	5.19
MONO	0.02	0.03	0.01	0.03	0.04
EO	0.09	0.14	0.19	0.13	0.11
BASO	0.01	0.00	0.01	0.01	0.01

D	Complete Blood Count-Chronic				
	Untreated	MSN	C-MSN	2KPEG-MSN	35KPEG-MSN
RBC	10.4	10.2	11.4	10.7	10.8
HGB	16.7	15.8	17.1	16.4	16.3
HCT	56.8	54.5	57.6	56.2	56.1
MCV	54.6	53.4	50.6	52.6	51.9
MCH	16.0	15.5	15.0	15.3	15.1
MCHC	29.3	29.0	29.7	29.2	29.0
RDW-SD	30.1	30.1	29.1	29.3	29.7
RDW-CV	22.1	22.6	24.1	22.9	23.4
RET	282	380	562	477	564
RET %	2.69	3.77	4.96	4.40	5.22
PLT	1173	1113	1548	1338	1360
PDW	9.53	7.67	9.83	8.13	7.73
MPV	8.43	8.00	9.30	8.23	8.17
P-LCR	12.5	6.5	10.7	7.1	6.7
PCT	0.99	0.90	1.41	1.10	1.10
WBC	4.41	5.32	4.74	3.81	6.09
NEUT	0.46	0.79	0.85	0.45	0.79
LYMPH	3.81	4.37	3.77	3.23	5.10
MONO	0.01	0.03	0.02	0.03	0.05
EO	0.12	0.13	0.10	0.09	0.15
BASO	0.01	0.01	0.01	0.01	0.01

Blood tests revealed small, transient differences in 2KPEG-MSNs as compared to the other groups tested acutely. Specifically, phosphorous levels in the blood were elevated in the 2KPEG-MSN treatment group. High amounts of phosphorous in blood can be indicative of kidney disease, as kidneys are responsible for filtering and removing excess phosphorous from the blood[165]. Consistent with previous reports of kidney ailments, low molecular weight PEG may have negative impact on kidney function[141,142,166]. Specifically, PEG has shown to result in calcium phosphate crystal deposition in renal tubules[167]. The crystal deposition can lead to subsequent nephrocalcinosis and acute renal failure[167]. In addition, sodium levels in 2KPEG-MSN acute treatment groups were slightly elevated, suggesting possible dehydration, which could arise from many variables, including kidney dysfunction[168]. However, while transient differences were observed in the 2KPEG-MSNs acute treatment group, no differences were observed in the chronic treatment groups. No other biomarkers for kidney dysfunction (blood urea nitrogen, creatinine) were significantly different in the 2KPEG-MSN groups, suggesting only minor calcium phosphate crystal deposition[167]. Apart from these deviations in 2KPEG-MSN acute treatment groups, there were no other significant changes in acute or chronic levels as measured with blood chemistry and complete blood counts. Notably, white blood cells, neutrophils, lymphocytes, monocytes and other related immune system markers were not significantly different in MSN treated groups compared to controls. This indicates that none of the treatment groups elicited an immune response. PEG has a propensity to undergo cellular vacuolation[169,170] and these results suggest nanoparticles that utilize lower molecular weight PEG may be more at-risk for vacuolation.

4.5 Conclusions:

Increased potential of nanomedicine in a clinical setting has raised significant concern in regards to toxicity. Nanoparticles can be difficult to evaluate for toxicity due to inconsistencies with administration routes and a wide variety of nanoparticle base materials, modifications of the surface of nanoparticles, gatekeepers, and even drugs. With typical multifactorial nanoparticles, the toxicity is often assessed with only a single injection, without proper isolation of each factor of the nanoparticle system such as external coatings, conjugated ligands, or encapsulated drugs. MSNs are a specialized set of nanomedicines that contain: (1) A wide range of size from 3 nm to >100 nm in diameter[171-173]; (2) adaptable gatekeeper mechanisms to allow for stimuli-responsive cargo release or stealthing[133,174,175]; and (3) may have additional disease specific-targeting[154,176,177]. However, there is controversy in assessment of MSN toxicity and accumulation due to the numerous and variable features within MSNs. For example, simultaneous determination of elicited toxicity as a result of the nanoparticle core, shape, size, conjugation, drug, etc., is nearly impossible.

This suggests that PEG can exacerbate pre-existing vascular conditions, but that 2KPEG causes greater toxic impact than 35KPEG. This study evaluated MSN toxicity using uncoated MSNs, chitosan, low molecular weight PEG, and high molecular weight PEG administered intravenously in mice. Treatment groups were split into acute (1 injection) and chronic (1 injection per week over 4 weeks) for maintaining clinical relevance, i.e., single vs. multiple rounds of chemotherapy. The chitosan coating on MSNs (C-MSN) did not result in changes in histopathology of acute and chronic time points for the C-MSN group was similar to controls and the mice had no areas of fibrosis in any organ or other

signs of organ damage. The histological and blood chemistry findings from mice acutely or chronically injected with C-MSN were consistent with control mice. In 100% mice receiving 2KPEG-MSNs, the mice had increased interstitial fibrin, immature thrombi, and even fully mature thrombi in up to 50% of the pulmonary arteries and veins. Additionally, one mouse receiving multiple injections 35KPEG-MSN also had increased interstitial fibrin and immature thrombi. Thus, a main finding of this study suggests chitosan coating was safe, but that PEG coating can exacerbate pre-existing vascular conditions with 2KPEG causing much greater toxic impact than 35KPEG.

Efficacious drug delivery has been observed in each of the chosen gatekeepers, chitosan[154], 2KPEG[178], and 35KPEG[179]. While 2KPEG shows rapid clearance from the body, 35KPEG benefits from a longer circulation time[155]. Histological evaluation of the tissue suggests exacerbation of pre-existing thrombotic lesions of mice treated with uncoated MSNs and PEG-coated MSNs. These results suggest that PEG may negatively impact and worsen mice that have pre-existing vascular risk. In addition, low molecular weight PEG results in increased exacerbation of vascular injury. Small differences were observed in the blood chemistry (phosphorous, sodium) of acute low molecular weight PEG treatment group that indicated kidney dysfunction, but these results were not supported by other kidney-related biomarkers (blood urea nitrogen, creatinine). Such differences may be a result of increased calcium phosphate depositions as a result of PEG coating[167], where lower molecular weight PEG may have a higher propensity for cellular vacuolation[169,170]. Additional investigations of many molecular weights of PEG and chitosan may provide more valuable information concerning how external coatings affect MSN toxicity. Further studies to accurately define the limits of toxicity depending on

particle size, type, and application will improve translatability of MSNs and general nanomedicine from high potential to clinical translation.

4.6 Acknowledgements and Funding:

This research was funded by National Cancer Institute Grants R01CA212350, F31CA261044, and P30CA225520 and National Institute for Biomedical imaging and Bioengineering R01EB020125. The pathology samples were prepared with support from the SCC Tissue Pathology Core.

Chapter 5 – Active Targeting Significantly Outperforms Nanoparticle Size in Facilitating Tumor-Specific Uptake in Orthotopic Pancreatic Cancer

This chapter has been published as a research manuscript in *ACS Applied Materials & Interfaces*:

William M MacCuaig, Benjamin L Fouts, Molly W McNally, William E Grizzle, Phillip Chuong, Abhilash Samykutty, Priyabrata Mukherjee, Min Li, Jacek B Jasinski, Bahareh Behkam, Lacey R McNally. “Active Targeting Significantly Outperforms Nanoparticle Size in Facilitating Tumor-Specific Uptake in Orthotopic Pancreatic Cancer” *ACS Applied Materials & Interfaces* 2021 Oct 15; 13 (42):19614-49630. doi: 10.1021/acsami.1c09379

5.1 Abstract:

Nanoparticles are widely studied as theranostic vehicles for cancer; however, clinical translation has been limited due to poor tumor specificity. Features that maximize tumor uptake remain controversial, particularly when using clinically relevant models. We report a systematic study that assesses two major features for the impact on tumor specificity, i.e., active vs passive targeting and nanoparticle size, to evaluate relative influences *in vivo*. Active targeting via the V7 peptide is superior to passive targeting for uptake by pancreatic tumors, irrespective of nanoparticle size, observed through *in vivo* imaging. Size has a secondary effect on uptake for actively targeted nanoparticles in which 26 nm nanoparticles outperform larger 45 and 73 nm nanoparticles. Nanoparticle size had no significant effect on uptake for passively targeted nanoparticles. Results highlight the superiority of active targeting over nanoparticle size for tumor uptake. These findings suggest a framework for optimizing similar nonaggregate nanoparticles for theranostic treatment of recalcitrant cancers.

5.2 Introduction:

While many nanoparticles have been evaluated, both preclinically and clinically, for cancer, there are many barriers and few guiding principles leading to an overall particle

design that has been validated in a clinically relevant *in vivo* setting[180]. In terms of tumor specificity and uptake, nanoparticles consistently underperform in a clinical setting, leading to inadequate agent delivery to the lesion, thus reducing diagnostic and therapeutic efficacy. Prior studies examining the tumor specific features of nanoparticles are largely limited to computational and *in vitro* models. The failure to use clinically relevant *in vivo* models has led to controversy in the context of improving tumor specificity of nanoparticles. *In vitro* and computational models do not fully recapitulate the *in vivo* situation due to the complexities of the cancer microenvironment[181-184]. While active targeting and nanoparticle size, two of the most critical features known to affect tumor uptake[181,183], have been assessed individually[183,184], the irrelative influences on tumor specificity have not been rigorously studied together using *in vivo* models. Determination of relative influences of critical nanoparticle features on tumor specificity will accelerate the translation of nanoparticles into clinically viable theranostic tools for cancer.

Active targeting options, such as using antibodies (e.g., Her2[185]) or peptides (e.g., RGD[186] and folate targeting[187]), represent techniques to target cancers specifically through extracellular expression of receptors or other proteins. However, many cancers, including pancreatic cancer, have few, if any, identified receptors to facilitate active targeting of the tumor cells. The heterogeneity of pancreatic cancer hinders the development of specific and efficacious extracellular protein targeting[188]. However, acidosis resulting from tissue hypoxia and the Warburg effect is a microenvironmental hallmark of aggressive cancers, which can be exploited for active targeting[189,190]. Utilization of the pH-low insertion peptide V7 through a sulfhydryl reaction to a succinimidyl 4-(N-maleimidomethyl) cyclohexane-1-carboxylate (SMCC) linker (**Figure 5.1B**) allows for tumor cell-specific targeting in acidic

pH (6.8−6.6)[189,191,192]. 3D modeling of V7 using AMBER software has revealed an approximate length of 2.6 nm (**Supporting Figure S5.1**). The amino acid sequence and physical properties of V7 cause the peptide to undergo a conformational change into an active alpha helix state under acidic conditions, i.e., pH 6.8−6.6, potentiating its insertion into the target cell membrane[191] (**Figure 5.1C**). With an approximate pKa of 6.0, V7 exhibits a dynamic shifting range, in which more acidic environments promote a higher percentage of active state V7 peptides[193,194]. Specifically, V7 responsiveness to the transformation and internalization is facilitated directly by acidity in the pancreatic cancer microenvironment[189,194]. In addition to the ability of V7 to actively target the acidic microenvironment of pancreatic cancer, the extended chain conformation and high density of V7 reduce protein corona formation[195,196], similarly to poly (ethylene glycol) (PEG) but without the deleterious PEG-associated toxicity concerns[197]. Limiting protein corona formation is beneficial since the protein corona is associated with reduced tumor specificity and accumulation[195-197].

Core nanovehicle size is an additional critically important feature of nanoparticles for tumor uptake. Previous *in vitro* and computational modeling studies suggest that a nanovehicle size range centered on 50 nm is optimal for enhanced drug delivery and tumor specificity[181,198,199]. However, these studies failed to incorporate either active targeting or appropriate *in vivo* models. For pancreatic cancer specifically, a nanoparticle size range centered on 30 nm has been suggested, based on the vasculature collapse that in turn reduces the importance of the enhanced permeability and retention (EPR) effect[200]. These studies suggest that nanoparticle uptake would be optimal with nanovehicles in a size range centered near 30−50 nm. However, there are currently too

few studies evaluating this idea using viable translational nanoparticles in a clinically relevant model, especially when evaluated in combination with active targeting, a necessity for maximum delivery efficacy[182]. A rigorous examination of the relative influences of active targeting vs passive targeting and nanoparticle size on tumor uptake in a clinically relevant pancreatic cancer model is critically needed.

Mesoporous silica nanoparticles (MSNs) are tailorable nanoparticles that can enhance delivery of therapeutic drugs or diagnostic contrast agents and have been used with preclinical and clinical imaging platforms[201,202]. Applications include anticancer therapies[203-205] as well as noncancer treatments such as antibiotic delivery[206], where each application exploits the enhanced delivery capabilities of MSNs. Changes in the core physical parameters of MSNs such as size[207], shape[208], pore topology[209], and surface chemistry[210] affect the properties of the MSNs, including payload retention, targeted delivery, off-target delivery, and toxicity[125,211-213]. Facile alterations in MSN synthesis allow for fine-tuning of physical properties, which determine clinical potential (**Figure 5.1A**). MSNs generally have a longer circulation time in blood, have a higher capacity of cargo per unit volume, and have more favorable cargo release kinetics than other types of nanoparticles such as metal nanoparticles[214]. The tunability of MSNs makes agent encapsulation, retention, and release highly controllable, resulting in suitable theranostic tools for cancer.

Nanoparticle translation is often hindered by an inability to accurately track *in vivo* biodistribution. A newly emerging imaging modality, multispectral optoacoustic tomography (MSOT), has demonstrated potential to track nanoparticle tumor specificity and uptake *in vivo* and in real time[1,3,6,65]. MSOT uses multi wavelengths of pulsed near-

infrared (NIR) laser light to excite thermoelastic expansion of specific chromophores. Synchronized high-energy lasers allow for resolving power on the order of less than 10 cells for detection of small tumor masses, exceeding current resolution limits of 0.1−1 mm with conventional modalities such as positron emission tomography (PET) and magnetic resonance imaging (MRI)[215,216]. Select chromophores can be endogenous (e.g., deoxy- or oxy-hemoglobin) or exogenous contrast agents (e.g., indocyanine green (ICG)) and can be imaged simultaneously for multi-variable biodistribution analysis[22,189,217]. This allows for high- resolution and high-sensitivity detection of cancer with contrast levels unachieved with ultrasound or computed tomography[65]. The multimodal NIR and optoacoustic approach allows for imaging depths of up to 5 cm^1 for examination of tumors positioned orthotopically, such as pancreatic tumors within mice, which far bypasses the penetration limit of optical imaging methods[218]. The high concordance of MSOT with existing gold-standard imaging (such as radiography), the rapid speed and efficiency of MSOT, and increasing usage all suggest that MSOT is a reliable and clinically relevant metric of biodistribution[219]. MSOT has the potential to synergize well with nanoparticles equipped with high contrast per particle[6]. MSOT has shown capabilities for submillimeter detection of contrast agents previously[2], far more sensitive than current gold-standard imaging modalities, which are largely limited to a minimum of 1 cm detection.

Inspired by previous research on the critical individual effects of nanoparticle size and targeting using *in vitro* and computational models[220,221], our study uses MSOT to investigate active targeting and nanoparticle size to assess optimal characteristics for *in vivo* theranostic applications in a clinically relevant model. While previous studies have investigated nanoparticle size and targeting moieties in the past[181,183,184,198], a systematic

study using analogous nanoparticles for targeting versus size comparisons has not been reported. Active targeting, through V7, was evaluated against passive targeting in three analogously prepared MSNs, varying only in diameter (26, 45, and 73 nm). The range of sizes was chosen in this study to avoid potential glomerular filtration by the kidney but also to test the limits of sequestration by Kupffer cells in the liver[222-224] as well as utilize the effective range of the EPR effect in a poorly vascularized cancer model[200,225]. MSNs are specifically referred to by the silica precursor and resulting size as follows: 26 nm, tetramethyl orthosilicate (TMOS); 45 nm, tetraethyl orthosilicate (TEOS); and 73 nm, tetrapropyl orthosilicate (TPOS). Collectively, the MSNs will be referred to as TROS, where “R” corresponds to the length of the four hydrocarbon chains extending from the silicate core. MSNs were loaded with the optoacoustic contrast agent IR780, coated with a pH-sensitive polysaccharide gatekeeper, and actively targeted for the acidity of pancreatic cancer with V7 prior to *in vitro* and *in vivo* detection using fluorescence and MSOT. Specifically, chitosan is responsible for charge-based swelling in acidic environments, allowing release of optoacoustic contrast agents. Further, V7 becomes an active cellular membrane anchoring peptide in acidic environments, facilitating cellular uptake and subsequent optoacoustic agent release via chitosan.

Results show that active targeting is the primary influencer on tumor-specific nanoparticle uptake with size as a secondary factor. The greatest tumor-specific nanoparticle uptake was realized with V7-TMOS. Uniquely, the largest actively targeted particle, V7-TPOS, had greater tumor-specific uptake than the smallest passively targeted particle (TMOS), underlining active targeting via V7 as the predominant determinant of tumor-specific uptake. V7-TROS showed decreasing uptake with increasing particle size, i.e., specificity

was the greatest in V7-TMOS and the lowest in V7-TPOS. Passively targeted TROS did not exhibit significant changes in uptake as a result of size. The data clearly supports active targeting over size as the major factor in promoting tumor-specific uptake. In addition, V7-TMOS coupled with MSOT was able to achieve submillimeter detection of the small tumor presence *in vivo* in contrast to NIR fluorescence. In pursuit of nanoparticle translation to the clinic, it is imperative to incorporate active targeting to achieve high-specificity uptake in pancreatic and other recalcitrant cancers. Results are expected to readily translate to similar nonaggregate nanoparticle systems for relevant tumor types.

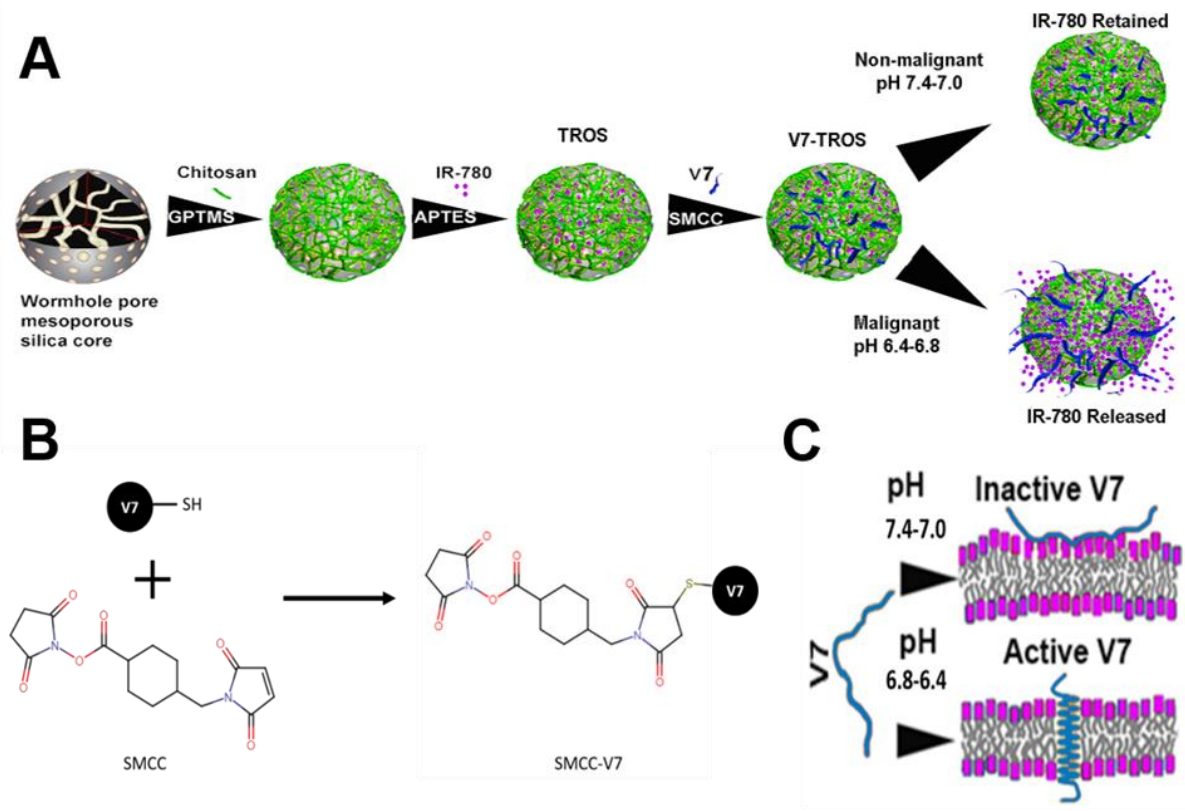

Figure 5.1: Schematic illustration of V7-TROS formation. A) Preparation of coating MSNs with pH-sensitive chitosan, encapsulation of optoacoustic cargo in MSNs, and pH low-insertion peptide V7 conjugation to MSNs. B) Conjugation chemistry of SMCC to the cysteine residue on V7 peptide. C) Activation mechanism of V7 peptide in acidic environments.

5.3 Materials and Methods:

5.3.1 Materials

Reagents purchased from Sigma Aldrich include: methanol (American Chemical Society reagent, ≥99.8%, 179337), CTAB hexadecyltrimethylammonium bromide (molecular biology, ≥99%, H6269), ammonium nitrate (≥99.0%, A9642), low molecular weight chitosan (448869), 1-propanol (anhydrous, ≥99.7%, 279544), GPTMS (3-glycidyloxypropyl) trimethoxysilane (≥98%, 440167), TEOS tetraethyl orthosilicate (gas chromatography, ≥99.0%, 86578), TMOS tetramethyl orthosilicate (≥99%, 341436), TPOS tetrapropyl orthosilicate (deposition grade, ≥98%, 679240), benzoylated dialysis tubing (D7884), TEA triethanolamine (gas chromatography, ≥99.0%, 90279), IR780 dye (≥98%, 425311), SMCC (succinimidyl 4-(N-maleimidomethyl)cuclohexane-1-carboxylate) (Powder, ≥98%, M5525), propidium iodide (PI) solution (1mg/mL, P4864). Milli-Q ultrapure water dispensed through MilliPore, Sigma. Glacial Acetic Acid (certified American Chemical Society, ≥99.7%, A38C-212) obtained through Fisher. Ethyl alcohol (anhydrous, 200 proof) sourced from Warner Graham Company. pHLIP ligand V7 obtained from CSBio.

5.3.2 Cell Lines

The two malignant human pancreatic adenocarcinoma (PDAC) cell lines utilized herein were S2VP10L and MiaPaca-2. S2PV10 originates from University of Nebraska, under care of M. Hollingsworth, and a variant, S2VP10L, which constitutively expresses firefly luciferase for *in vivo* tumor growth tracking, was generated. MiaPaca-2, THLE-2 (normal liver), and NK-2 (normal kidney) were purchased from the American Type Culture Collection. All cancer cells were grown in Dulbecco's Modified Eagle Medium (DMEM) with 10% fetal bovine serum (FBS) and 1% L-glutamine. For evaluation of potential

toxicity of TROS and V7-TROS on non-malignant cells, THLE-2 cells and NK-2 cells were grown in standard DMEM with 10% FBS was supplemented with the Lonza Bullet Kit (CC3170) without the addition of gentamycin, amphotericin, and epinephrine. Cells were grown and maintained in a humified incubator at 37 °C and 5% CO_2 until treated with pH-specific media.

5.3.3 pH-Specific Media Preparation for the *In Vitro* Nanoparticle Assays

For evaluation of pH-specificity of particle uptake and cell viability of tumor cells, pH specific media was utilized. Briefly, phosphate buffer (25 mM) at the desired pH (7.4, 6.6) was prepared by dissolving sodium phosphate monobasic and dibasic solution dissolved in distilled water (Sigma-Aldrich, St. Louis, MO, USA). 13.6 g of DMEM powder was dissolved in the autoclaved phosphate buffer (25mM) at the desired pH (7.4 or 6.6). The solution was enriched with 10% FBS and 1% L-glutamine and filtered through grade-1 Whatman qualitative filter paper (Sigma-Aldrich, St. Louis, MO, USA). The pH of the solution was determined by pH meter (Denver Instrument Ultrabasic, Bohemia, NY, USA). The acidity and basicity adjustments of the pH solutions were performed with sterilized sodium hydroxide (1 M) or hydrochloric acid (1 M).

5.3.4 Nanoparticle Synthesis and Characterization

5.3.4a Core Particle Synthesis

The three prepared colloidal mesoporous silica core particles were prepared by identical methods with the only exception being substitution of analogous TROS and corresponding R(OH). Briefly, 2.00 g CTAB, 240 mL MQ water, 0.420 g TEA, and 88.0 mmol ROH are combined into a flask, with moderate to vigorous stirring, under reflux and slowly heated to 80°C (approx. 30 m). At temperature, 11.0 mmol of TROS is added

dropwise at a rate of approximately 0.5 mL/m and reflux is continued at 80 °C for 12–16 h. At completion, the reaction vessel is removed from heat and cooled to room temperature. A 0.5–1.0 mL aliquot of the resultant solution is reserved for dynamic light scattering (DLS) analysis of polydispersity (PDI) and hydrodynamic diameter.

5.3.4b Dynamic Light Scattering Analysis

A Zetasizer Nano ZS was used for analysis of colloid particle diameter and PDI following synthesis and dialysis processes. The instrument is equipped with a 5 mW HeNe laser exciting at 633 nm wavelength and detects scattered light at 1730 nm. Based on synthesis procedure, solvent refractive index and viscosity of 1.33 and 0.89 cP, respectively, were chosen. Measurements were collected in single angle backscatter (173°).

A Zetasizer Ultra was used for analyzing chitosan coated TROS. Measurements for the size parameter were collected in triplicate in multi-angle DLS (MADLS) mode (173°, 90°, 7°). Particle concentration measurements were collected in triplicate and preceded by a single MADLS size measurement for comparison between reported size distributions in both measurement types. General purpose data analysis settings, a dispersant refractive index and viscosity of 1.43 and 16.1118 (ethylene glycol), and material refractive index and absorbance of 1.33 and 0.01 were used for all particle concentration and MADLS measurements to optimize collected correlograms. An input of 145 kcps for dispersant mean count rate was used exclusively for particle concentration measurements.

5.3.4c Removal of Core MSN Surfactant Scaffold

A 1:1 (v/v) solution of 2 M glacial acetic acid and ethyl alcohol was prepared, in quantity 1 L, into which was placed dialysis tubing containing one of the three synthesized particles. The dialysis vessel was sealed to prevent evaporation and stirring of the

external solution was set to between 300–500 rpm with a 39 mm or 50 mm stir bar. The external solution was replaced every 12 h for a period of 3–4 days. Particle solutions were then removed from the acid and alcohol solution, rinsed (externally) with MQ water, and submerged in 1 L of MQ water for two periods of 12 h with continued stirring. Particle solutions were then removed from their tubing and stored in 1 L glass media bottles.

Briefly, 50 mL of each particle solution was separately heated to 60 °C in a 500 mL flask under reflux to which was added, dropwise, an equivalent volume of 74.95 mM ammonium nitrate in MQ water. The reaction was run for 1 h with moderate stirring and then allowed to cool to room temperature without stirring. These particle solutions were removed again to dialysis tubing, dialyzed twice for 12 h in MQ water, and again stored in 1 L glass vessels.

5.3.4d Particle Lyophilization, Brunauer-Emmett-Teller and Nitrogen Adsorption/ Desorption Analyses

Fully processed TROS colloids were vacuum centrifuged to lyophilized powders using an Eppendorf Vacufuge 5301. 1.6–1.8 mL of fully processed TROS colloid was pipetted into each of 48 2 mL Eppendorf micro centrifuge tubes all of which were placed, open capped, into an F-45–48-11 rotor. Internal chamber temperature was set to ambient (i.e., no temperature selected). Rate of sample evaporation was in the range 0.15 to 0.22 mL/h. Maximum vacuum achieved was 9 mbar and maximum rotor speed was 1400 rpm.

Using a TriStar analyzer, powders were vacuum dried at 120 °C overnight, were submerged in a liquid nitrogen bath using pure nitrogen gas, and a subsequent seven-point (Brauner, Emmett, Teller) BET isotherm and 50-point adsorption/desorption isotherm were collected. For specific surface area, pore diameter and pore volume

measurements, the BET and Barrett–Joyner–Halenda (BJH) methods, respectively, of calculation were used.

5.3.4e Sample Preparation and Transmission Electron Microscopy Analysis

To prepare samples for transmission electron microscopy (TEM) analysis, fully processed TROS colloids were diluted to 1:100 in MQ water. 20 µL of this solution was then pipetted onto 200 mesh copper formvar and, separately, lacey carbon electron micrograph grids. Grids were incubated for 30 m, had liquid wicked off with filter paper, and were allowed to air dry for 30 m. Grids were stored in stock grid holders. TEM analysis was performed on a Tecnai-F20 transmission electron microscope.

5.3.4f Surface Cross-Linking Functionalization and Chitosan Capping of Core MSNs

To apply GPTMS surface functionalization and attach chitosan polymer, the following steps were taken. Post-processed MSN colloids were diluted 4:1 in 100% Ethyl alcohol and ultrasonicated for 3 m at room temperature. pH of the colloidal solution at this stage was between 4 and 4.5. 0.1 mL GPTMS was added to the colloidal solution which was then shaken vigorously (2500 rpm) for 3 h on a vortex.

To derive the pH-responsive capping solution of chitosan, a 1% w/v chitosan solution in 5% nitric acid was prepared and stirred w/ 33 mm stir bar at room temp for 2 h. 90 mL of total chitosan solution was homogenized by swirling and quantitatively transferred into 6 15 mL falcon tubes in 15 mL aliquots. Tubes were centrifuged at room temp at 200 rpm (8×g) for 30 m. Light gold-colored pellet was apparent, with transparent solution above, in each tube. The top 3.33 mL of each of the six tubes (cumulatively, top 22% of total volume) was drawn off and combined 6:5 with the TROS fully processed colloid. This

MSN-Chitosan mixture was shaken vigorously (2500 rpm) for 12–16 h (i.e., overnight). MSN-Chitosan was isolated by centrifuging a 50 mL volume of solution at 24 °C and 17,000 rpm for 30 m. Pellet volume of approximately 50–100 µL, was not gelled or solid and not adherent to tube.

5.3.4g Loading of IR780 Contrast Agent, Retention and Release Assay, Dye per Particle Analysis

To load chitosan capped TROS with IR780, the following steps were performed. Total volume of MSN-Chitosan pellet was combined with 80 µL (3-aminopropyl) trimethoxysilane (ATPES) and 100 µL 1 mM IR780 contrast agent, pH of solution was lowered to 4–4.5 using 1 M HCl, and the solution was shaken for 5–6 h. Solution pH was then increased to 7.4. Dye loaded particles were isolated by centrifugation at 10,000 rpm for 5 m, dispersed in 500 µL pH 7.4 PBS, and shaken for 30 m for a total of 3 iterations. Maximum solution absorbance was measured by ultraviolet (UV)-visible light (VIS) for dispersed dye-loaded particles which were then diluted to 1 optical density (OD)/mL of IR780 signal measured at 653 nm wavelength. For retention and release assays, dye loaded particle solutions were pH adjusted between 7.4 to 6.6 and absorbance of the supernatant at 653 nm was reported for various time intervals following pH change.

Fluorescence OD per particle was determined by centrifugal isolation of dye-loaded MSNs followed by measurement of fluorescent signal in the solution supernatant and calculation of dye concentration in the isolated particles. Dye molecules per particle are reported as 101 million for TMOS, 338 million for TEOS, and 562 million for TPOS (**Supporting Figure S5.2**). Measurements taken for a particle concentration in sample solution of 8 million particles/mL.

5.3.4h Preparation of pHLIP V7 Ligand and Conjugation to Particle

V7 pH-low insertion peptide (pHLIP) (V7 pHLIP sequence ACEEQNPWARY LEWLFPTETLLLEL, CS Bio, Menlo Park, CA, USA) was added as an active targeting ligand. To prepare a pHLIP V7 solution for particle attachment, 5 mg of lyophilized pHLIP V7 powder was thawed from −80 °C and combined with 2.44 mL of pH 7.4 PBS and swirled by hand for 15 m until reasonably dissolved. This solution was aliquoted and stored at −80°C until it was used. Briefly, 75 µL of SMCC NH2-malemide linker and 100 µL of pHLIP V7 solution was added to the previous dye-loaded and chitosan capped TROS solution. Total solution was then shaken at room temp in the dark for 3–5 h and subsequently stored at −4 °C for use in targeted particle applications. V7-TROS was washed in in PBS and centrifuged at 10,000 g for 10 min. The supernatant was collected to determine the binding efficiency of V7 to TROS with a protein assay. Results corresponded to an approximate conjugation density of 2000 V7 molecules/particle for TMOS, 2000 V7 molecules/particle for TEOS, and 200 million V7 molecules/particle for TPOS.

5.3.5 *In Vitro* Experiments

5.3.5a Cell Viability

PDAC cells, S2VP10L and MiaPaca-2, along with non-malignant hepatocytes THLE-2 and non-malignant proximal tubule kidney cells were plated into 96 well plates at 5×10^3 cells per well for 24 h in standard DMEM media with 10% FBS and 1% L-glutamine. Both THLE-2 and NK-2 cells received extra supplements from the Lonza Bullet kit as indicated above. The cells were treated with 2.5 µL of TROS or V7-TROS particles in a 96 well plate for 24 and 48 h at 37 °C with 5% CO_2. Cell viability was measured using ATPlite™ according to the manufacturer's instructions (Perkin Elmer, Waltham, MA, USA).

Adenosine triphosphate (ATP) levels were measured using a plate reader (Packard TopCount NXT, Meriden, CT, USA) and normalized to phosphate buffered saline (PBS) treated control. To avoid potential interactions with other dye-based viability assays (MTT and MTS assays) ATPLite^{TM} was utilized.

5.3.5b *In Vitro* Evaluation of TROS Particles

Evaluation of pancreatic cancer cell uptake of TROS and V7-TROS containing IR780 was conducted using NIR fluorescent imaging and tissue mimicking phantoms. 5×10^5 pancreatic cancer cells (S2VP10 and MiaPaca-2) were grown in 6 well plates with the pH media 7.4 or 6.6 respectively. The cells were incubated for 2 h with TMOS, TEOS, and TPOS with and without V7 peptide, respectively. Particles contained encapsulated IR780 at a concentration of 2.7 mM (0.1 OD/mL) and a particle concentration in particle sample of 8×10^6 particles/mL. The cells were washed (3×) with the pH specific PBS containing 10% FBS. The uptake of IR780 dye from the particles was measured in two ways: 1) by analyzing the fluorescence intensity using an Odyssey Infrared System (LI-COR) in both the cell lines with dosimetry performed using LI-COR software; 2) Tissue mimicking phantoms were prepared for MSOT analysis. Cell pellets were added to the agar gel-based tissue mimicking phantoms. Tissue mimicking phantoms were prepared from 1.3% w/w of agar and 6% v/v intralipid was added to DI water which results in creating a gel with a reduced light scattering coefficient of $\mu = 10\ cm^{-1}$. S2VP10 cells treated with TMOS, TEOS, and TPOS with and without V7 peptide at pH 7.4 and 6.6 containing IR780 were added to the 3 mm diameter cylindrical opening in the tissue phantoms. All samples were evaluated at multiple wavelengths by utilization of a tunable laser source (680, 710, 730,

740, 760, 760, 770, 780, 800, 850 and 900 nm). At least 20 average readings were taken during the analysis at each wavelength.

5.3.5c Cell Internalization of TROS with Propidium Iodide

Propidium iodide was used in place of IR780 to evaluate cell internalization prior to dye release. PI usually emits green fluorescence, but when bound to nucleic acid, red fluorescence is instead emitted. Propidium iodide is impermeable to the cell membrane, but can be allowed entry into the cell by encapsulation within TROS. S2VP10 cells were grown to confluency in a 6 well plate containing 12 mm cover glasses in wells. Cells were grown overnight in DMEM with 10% FBS and 1% L-glutamine. pH-specific DMEM (pH 7.4 or 6.6) was used to mimic benign and malignant conditions for pH-specific internalization and release. 80 µL of PBS (control) or V7-TROS with propidium iodide was added to the plate for 1.5 h. Plates with then fixed with 4% formaldehyde for 10 m at room temperature. Cells were washed with PBS to remove free TROS and propidium iodide. The cover glasses were removed and mounted with VectaShield Vibrance Antifade Mounting Medium with DAPI (Vector Laboratories, Burlingame, CA). The samples were dried in the darkness for 2 h. Images were taken at 400X magnification using a Leica SP8 Confocal Microscope. Fluorescence counts of images were determined through channel splitting and thresholding via ImageJ.

5.3.6 *In Vivo* Experiments

5.3.6a Human Pancreatic Cancer Xenograft Mouse Models

Athymic female mice aged 4 wk were used for this study in strict adherence to the OUHSC/Wake Forest University Institutional Animal Care and Use Committee approved protocol. Athymic mice were utilized to eliminate the possibility of obscured signal as a

result of hair. Hair can disrupt the otherwise smooth surface between skin and ultrasound gel/ultrasonic transducer, thus acting as a confounding factor. **Chapter 4** suggests that chitosan mesoporous silica nanoparticles do not elicit an immune response. Mice were placed on a 2920X alfalfa free-rodent diet (Harlan Laboratories, Indianapolis, IN) to reduce background signal during imaging. An established model for orthotopic cell implantation into the mouse pancreas was followed as previously described.[217] Briefly, 10 mice were anesthetized with isoflurane, and the abdomen was then prepped with betadine. A 1 cm incision was made in the left upper quadrant, with the pancreas exposed by retraction of the spleen. Luciferase-cloned S2VP10 cells (S2VP10L) were suspended in serum-free DMEM medium at 4 °C in a sterile tube. A solution of 1.5×10^5 cells per 30 µL was drawn up using a 28-gauge needle and injected into the pancreas. A sterile cotton-tipped applicator was held over the injection site for 30 s to prevent peritoneal leakage. The organs were returned to the abdomen with the skin, and peritoneum closed in a single layer using 5–0 prolene sutures. Mice recovered underneath a warming blanket and were returned to their cages with food and water ad libitum after regaining full mobility.

The raw data of the multispectral analyzed samples were reconstructed with the ViewMSOT software version 3.8 (Ithera Medical, Munich, Germany). Using ViewMSOT software wavelengths corresponding to the IR780 dye were reconstructed at a resolution of 75 µm. The multispectral processing was conducted using linear regression with ViewMSOT 3.8 (Ithera Medical, Munich, Germany). Image stacks were imported into orthogonal views. The region of interest (ROI) was plotted over the tumor site, and the settings were kept constant for all the image slices obtained throughout the experiment. The signal intensity obtained from TROS nanoparticles containing IR780 at the tumor site

was represented in MSOT a.u units. The MSOT a.u. values for the TROS nanoparticles were compared using SAS 9.3 Cary, NC, USA.

5.3.6b Evaluation of Nanoparticles using MSOT

Mice were intravenously (IV) injected, at the tail vein, with actively (V7) and passively (no peptide) targeted TMOS, TEOS, and TPOS. Injected MSN probe contained encapsulated IR780 at a concentration of 2.7 mM (0.1 OD/mL) and an MSN concentration in solution of 8×10^6 particles/mL. After intravenous injection of probe, mice were imaged at 8 h using InVision 512 TF MSOT (iThera Medical, Munich, Germany). Mice were imaged ventral side up within the animal holder and positioned in a nose cone for anesthesia delivery. Anesthesia was maintained at 1.5% isoflurane in 0.8 L medical air and 0.1 L O_2 throughout imaging. Imaging was performed using axial slices with a 0.2 mm step through the liver-tumor-kidney region, at wavelengths of 680, 710, 730, 740, 750, 760, 770, 780, 800, 850, and 900 nm for each position. For each wavelength, 25 frames were obtained and averaged. To minimize the influence of animal movement in the images, an acquisition time of 10 μs per frame was used.[189] Respiration rate and signs of distress were monitored through all stages of the imaging procedure. After the last imaging time point of 24 h, animals were euthanized via carbon dioxide overdose and cervical dislocation. Pancreas tumor, liver, spleen, and kidney were removed and imaged using the advanced molecular imager (AMI) (Spectral Imaging Instruments, Tucson, AZ, USA).

5.3.6c Pharmacokinetics and Biodistribution of TROS with MSOT

Pharmacokinetics of TROS particles were evaluated using orthotopically implanted xenograft mice. Mice were tail-vein injected with V7-TROS or passively targeted TROS particles loaded with IR780 cargo at 2.7 mM (0.1 OD/mL). Mice were imaged ventral side

up while under a 1.5% isoflurane anesthesia using MSOT at 0 h, 4 h, 8 h, and 24 h post injection. Axial slices were recorded at 0.2 mm-steps throughout regions that contain the liver, tumor, kidney, and spleen. Aortic slices were required to measure the blood retention time for V7-TROS and TROS (**Figure S5.5**). Images were acquired analogously to the tumor, liver, kidney, and spleen, as a single snapshot kinetically at 0, 4, 8, and 24 h[226,227]. Multiwavelength illumination between 680 nm and 900 nm was utilized for spectral enrichment. 10 μs acquisition time and 25 acquisitions per wavelength were used for image capture. Mice were continuously monitored to ensure distress minimization.

5.3.7 *Ex Vivo* Organ Analysis

After the 8 h imaging time point, several control and V7-TROS treated mice were euthanized, and evaluation of signal accumulation within the tumor was compared with off-target organs using fluorescence imaging by the AMI. ROI analysis of IR780 cargo accumulation was used to verify MSOT data in the liver, kidney, and pancreas tumor. Liver and kidney were also evaluated for off-target toxicity using hematoxylin and eosin (H&E) staining.

5.3.8 Statistical Analysis

Statistical evaluation of the *in vitro* studies was performed using analysis of variance (ANOVA) and Tukey multiple comparison test with significance defined at $p<0.05$. *In vivo* pharmacokinetics were analyzed with repeated measures ANOVA at significance of $p<0.05$. The *in vivo* biodistribution and accumulation of the IR780 loaded V7-TROS and TROS nanoparticles containing IR780 in the pancreatic tumor, liver, and kidney were statistically analyzed using ANOVA with significance at $p<0.05$.

5.4 Results and Discussion:

5.4.1 Physical Characteristics of TROS Nanoparticles

Defining the optimum size range of nanoparticles is necessary for their successful theranostic use in cancer. This study evaluated the combined effect of nanoparticle active targeting and size on tumor specificity in an orthotopic *in vivo* mouse model. Particle size was controlled by a modified Stöber synthesis approach[228]. The synthesis procedure is graphically outlined in **Figure 5.1**. Three size-distinct MSNs, TMOS, TEOS, and TPOS, were successfully synthesized in a narrow size range with low batch-to-batch variability.

Average core particle diameters were 26 ± 3.1, 45 ± 3.8, and 73 ± 4.2 nm (TMOS, TEOS, and TPOS) with corresponding average pore sizes of 1.3 ± 0.2, 1.5 ± 0.2, and 1.7 ± 0.2 nm for TMOS, TEOS, and TPOS, respectively, as measured by transmission electron microscopy (TEM) (n= 25 particles/pore) (**Figure 5.2A−C**). The hydrodynamic diameters for the particles were slightly larger as measured with DLS (**Figure 5.2D**). Full DLS distributions are included (**Figure 5.2H**). DLS measurements of hydrodynamic diameters are reportedly slightly larger than core MSN diameters due to inclusion of nanoparticle-related hydration shells[228]. The PDI showed that MSNs were prepared as a monodisperse distribution (**Figure 5.2E**). The mean PDI of core TMOS, TEOS, and TPOS was low and stable over several months[229,230]. BJH analysis was used to interpret BET results[153] to determine the surface area and pore volume (**Figure 5.2F-G**). The pore volume as determined in **Figure 5.2F** represents a surface-level measurement, rather than a complete measure of the total pore volume throughout the nanoparticles, resulting in similar measures for differently sized particles. TMOS particles may have larger pore volumes due to pore overlap as a result of small particle size. Decreases in the surface

area dependent upon size are a result of differences in hydrolysis rates[228]. Precursor selection determines preferential nucleation of new particles and outward growth of existing particles in the synthesis mixture[228].

TROS synthesis was followed by conjugation with a natural polysaccharide, chitosan, as a gatekeeping molecule for encapsulation of the contrast agent IR780 within pores. IR780 is a hydrophobic nonaggregate cargo and was selected in this study due to its ability to generate optoacoustic signals[22,125]. TROS were dialyzed, conjugated with the (3-glycidyloxypropyl) trimethoxysilane (GPTMS) linker (TROS-GPTMS), and conjugated with chitosan (TROS-C), each confirmed by zeta potential changes. TROS were then conjugated with APTES (TROS-C-APTES) and the V7 (TROS-C-V7) peptide, again confirmed with zeta potential changes (**Figure 5.3A**). IR780 encapsulation increased with increases in particle size: 1.01×10^8 dye molecules/TMOS particle, 3.38×10^8 dye molecules/TEOS particle, and 5.62×10^8 dye molecules/TPOS particle (**Figure 5.3B** and **Supporting Figure S5.2**). Following dye encapsulation, TROS particles were functionalized with the V7 ligand for active tumor targeting, confirmed by zeta potential measurement (**Figure 5.3A**). Differences in the conjugation density of V7 peptide were observed according to TROS size: 2.0×10^3 V7 molecules/particle for TMOS, 2.0×10^3 V7 molecules/particle for TEOS, and 2.0×10^8 V7 molecules/particle for TPOS. Steric hindrance may inhibit optimal binding to TMOS and TEOS in this assay. In addition, the small size of V7 coupled with large nanoparticles carries considerable error with measurement of bound protein concentration.

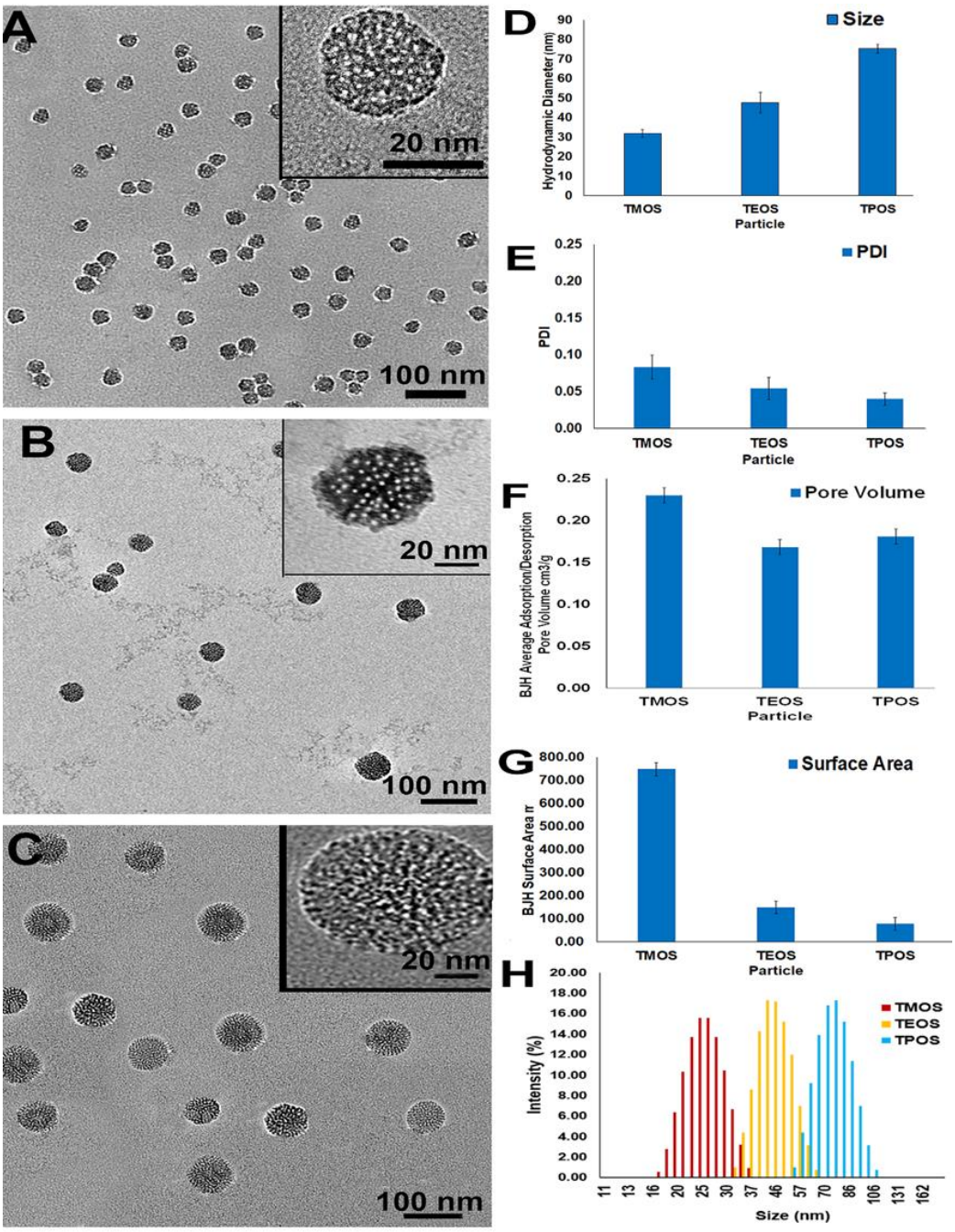

Figure 5.2: Characterization of TROS MSN size, pore volume, and surface area. Low magnification transmission electron micrograph (TEM) images, with high magnification insets of A) TMOS, B) TEOS, and C) TPOS demonstrate average particle diameters of 26 ± 3.1 nm, 45 ± 3.8 nm, and 73 ± 4.2 nm. D) Corresponding DLS data of 32 ± 3 nm for TMOS, 48 ± 5 nm for TEOS, and 75 ± 2 nm for TPOS. E) Polydispersity index of TROS MSNs. F) BJH method-computed adsorption/desorption pore volume and G) surface area of TROS MSNs following BET analysis. H) Full DLS distribution of TMOS, TEOS, and TPOS. No p-values to report.

5.4.2 V7-TROS Toxicity Evaluated in Pancreatic Tumor Cells and Nonmalignant Cells

Due to limited data on toxicity of chitosan-capped MSNs, S2VP10 and MiaPaca-2 human pancreatic cancer cells and nonmalignant liver (THLE-2) and kidney (NK-2) cells were treated with V7-TROS and passively targeted TROS. Kidney and liver cells were chosen due to being the two organs responsible of clearance of V7-TMOS from plasma. 24 h following treatment, cell viability was evaluated. No statistically significant differences in cell viability were observed in any cell line as a result of active targeting or size ($p > 0.05$) (**Supporting Figure S5.3**).

5.4.3 pH-Specific Release of TROS

The distinctive spectroscopic feature of IR780 (**Figure 5.3C**) allows for studying dye release from TROS. The efficacy of chitosan for contrast agent release was assessed by a dye release assay that simulates acidic conditions[22] (**Figure 5.3D−F**). The release characteristics of TMOS, TEOS, and TPOS nanoparticles were all similar for *in vitro* pH-controlled cargo release. TMOS, TEOS, and TPOS particles released the highest amount, 90−94%, of the encapsulated IR780 dye at pH 6.6, with lower release, 62−72%, at pH 6.8 (TMOS $p=0.0043$, TEOS $p=0.0490$, and TPOS $p=0.1271$) and 10−17% at pH 7.4 (TMOS $p=0.0010$, TEOS $p=0.0010$, and TPOS $p=0.0010$).

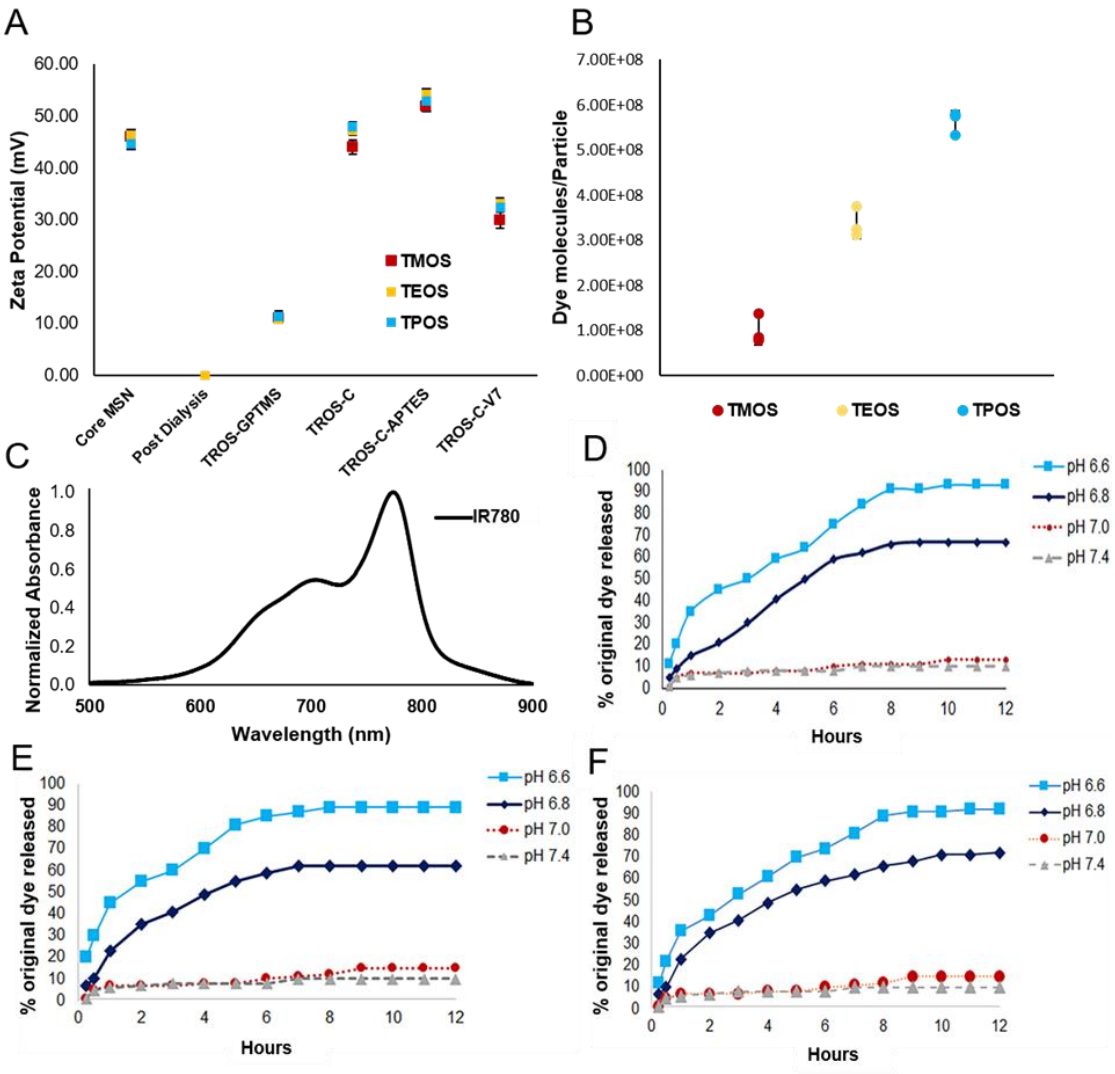

Figure 5.3: Characterization of TROS MSN charge, cargo encapsulation, and pH-specific release via chitosan. A) Zeta potential measurements confirm removal of surfactant from TROS and conjugation of additions to TROS. B) Dye molecules per particle for three TROS particle sizes. C) Absorbance spectra of optoacoustic contrast agent IR780. D) IR780 release, as facilitated by chitosan from TMOS particles at pH 7.4-6.6. E) IR780 release from TEOS particles at pH 7.4-6.6. F) IR780 release from TPOS particles at pH 7.4-6.6. No p-values to report.

5.4.4 pH-Specific Cell Uptake of V7-TROS Evaluated *in Vitro*

Pancreatic cancer is characterized as a highly acidic micro-environment due to rapid metabolism and the resulting acidosis. Acidosis is strongly correlated with aggressive

tumor progression, thus present surrounding the microenvironment and tumor cells in early stages, serving as an intriguing PDAC marker[231,232]. The acidic targeting properties of the pH-responsive V7 targeting peptide are mediated by the acidosis inherent to solid tumors and exacerbated by the increased Warburg effect in pancreatic cancer[233]. During the transition from physiological pH to extracellular tumor pH, V7 undergoes a conformational change into a transmembrane alpha helical structure, leading to binding to and uptake by tumor cells[194,234]. To visualize this uptake, S2VP10 cells were treated with passively targeted TROS and V7-TROS particles, each with encapsulated IR780 cargo, for 2 h under pH 7.4, 6.8, or 6.6 conditions. After washing cells, NIR fluorescence showed that uptake of V7-TROS with the IR780 cargo was pH-specific (**Figure 5.4A-B**), and passively targeted TROS had minimal cell uptake due to the lack of the tumor-targeting peptide V7. No passively targeted TROS, irrespective of size, exhibited any significant pH sensitivity. V7-TROS had significantly greater specificity at acidic pH than passively targeted particles at any acidic pH (**Figure 5.4A-B**). Specifically, V7-TMOS exhibited the greatest enhancement of *in vitro* uptake in response to acidic pH; uptake increased by 8.5-fold at pH 6.8 and 19.2-fold at pH 6.6 ($p=0.002$ and $p=0.0001$, respectively), compared to V7-TMOS at pH 7.4. V7-TEOS and V7-TPOS experienced similar, but less dramatic trends; V7-TEOS increased by 7.8-fold at pH 6.8 and 16.5-fold at pH 6.6, and V7-TPOS increased by 6.2-fold at pH 6.8 and 15.8-fold at pH 6.6 ($p< 0.005$).

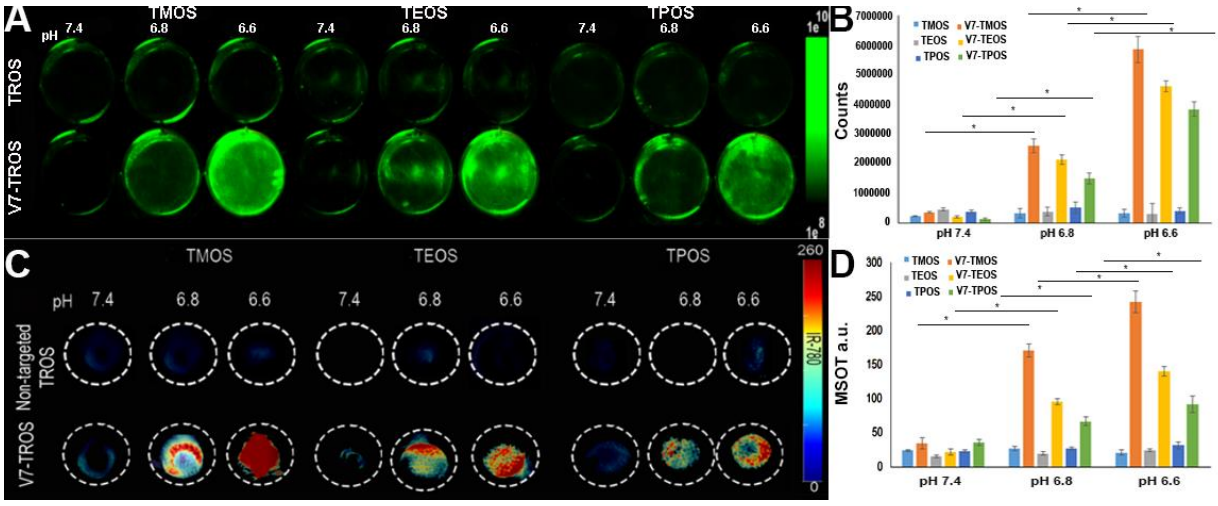

Figure 5.4: NIR fluorescence and MSOT confirmation of V7-TROS MSNs pH-specific cell uptake and cargo release. A) Plated S2VP10 pancreatic cancer cells were treated with V7-TROS or TROS and evaluated with NIR fluorescence. B) Quantification of NIR fluorescence signal in (A). C) Tissue mimicking phantoms containing S2VP10 pancreatic cancer cells treated with V7-TROS or TROS and evaluated with optoacoustic imaging. D) Quantification of optoacoustic signal in (C). *p<0.01.

Using tissue-mimicking phantoms, cell uptake of TROS particles was confirmed using MSOT (**Figure 5.4C-D**). Tissue phantoms simulate human tissues using cross-linked agar and intralipids for a gel-like vessel with a reduced scattering coefficient of 10 cm^{-1}. The optoacoustic signal observed in the tissue phantoms using MSOT confirmed increasing cellular uptake of the particles corresponding to V7 targeting and decreasing particle size. The results were consistent with NIR fluorescence data reported above; V7 targeting was the strongest influence on uptake, with smaller particles having a significant, but secondary, impact (**Figure 5.4A−D**). Passively targeted TROS particles were detected at levels of <35 a.u. in all samples, and variations in size did not result in significant changes in uptake. V7-TMOS samples contained 35, 171, and 243 a.u. for the pH 7.4, 6.8, and 6.6 samples, respectively. V7-TEOS and V7-TPOS exhibited similar

trends but attained lower maximal values: 141 and 92 a.u., respectively, at pH 6.6. Overall, for each V7-TROS, the signals at pH 6.6 were significantly higher than at either pH 7.4 or 6.8 ($p < 0.005$), indicating pH sensitivity (**Figure 5.4B−D**). The increased signal in TMOS is quite significant when considering that a single TPOS particle has a substantially greater cargo capacity than a smaller TMOS particle (**Figure 5.2**), indicating the enhanced uptake as a result of smaller nanoparticle size. Comparison of the proportion of the fluorescence signal in **Figure 5.4A-B**, for V7-TROS from pH 7.4 to 6.6 to the analogous signal measured by MSOT in **Figure 5.4C-D** shows that V7-TEOS and V7-TPOS produce a higher magnitude (V7-TEOS < V7-TPOS) of the fluorescence signal per unit of the MSOT signal than V7-TMOS does ($p < 0.00127$).

5.4.5 Cell Internalization of TROS with Propidium Iodide

To further substantiate the internalization and release mechanism of TROS nanoparticles, propidium iodide was encapsulated within TROS in place of IR780. PI is a cell membrane-impermeable dye that exhibits differential fluorescence depending on the intracellular or extracellular presence[235]. Most often, propidium iodide binds to nucleic acids in dead cells and shows red fluorescence. However, when propidium iodide is not bound to nucleic acids, fluorescence is green-shifted by approximately 15 nm[235]. When encapsulated within TROS, the mechanism of entry into live cells can be confirmed through intracellular red fluorescence, while extracellular PI is impermeable and is removed via post-treatment washes, or, if remaining present, detected via green-shifted fluorescence[127,235]. **Figure 5.5** indicates that red fluorescence is observed significantly in actively targeted pH 6.6 samples only (TMOS $p=5\times10^{-14}$, TEOS $p=5\times10^{-14}$, and TPOS $p=4\times10^{-10}$). Specifically, at pH 6.6, V7-TMOS images showed an average red fluorescence count of 8943, V7-

TEOS at 9072, and V7-TPOS at 2310 (**Figure 5.5B**). Small amounts (<60 counts) of red fluorescence were observed in V7-TROS at pH 7.4. Negligible red and green fluorescence was observed in all other treatments (**Figure 5.5B**). This implies that not only is V7 crucial for internalization of MSNs but also that V7 is active in a cancerous pH of 6.6 but minimally active in a physiological pH of 7.4. Low levels of green fluorescence in passively targeted treatments and pH 7.4 media are suspectedly a result of washing following treatment; because TROS and PI are not bound to cells due to inactive V7, PI is removed due to PBS washing. In addition, S2VP10 cells in the presence of acidic media at pH 6.6 did not undergo cell death, evident through the absence of intracellular PI and red fluorescence. Actively targeting for the acidity of pancreatic cancer may represent a more efficient option than targeting for an extracellular protein or receptor due to the high heterogeneity of pancreatic cancer[189]. While these tumors do not uniformly express receptors or other proteins, the entire pancreatic tumor is highly acidic[188,190].

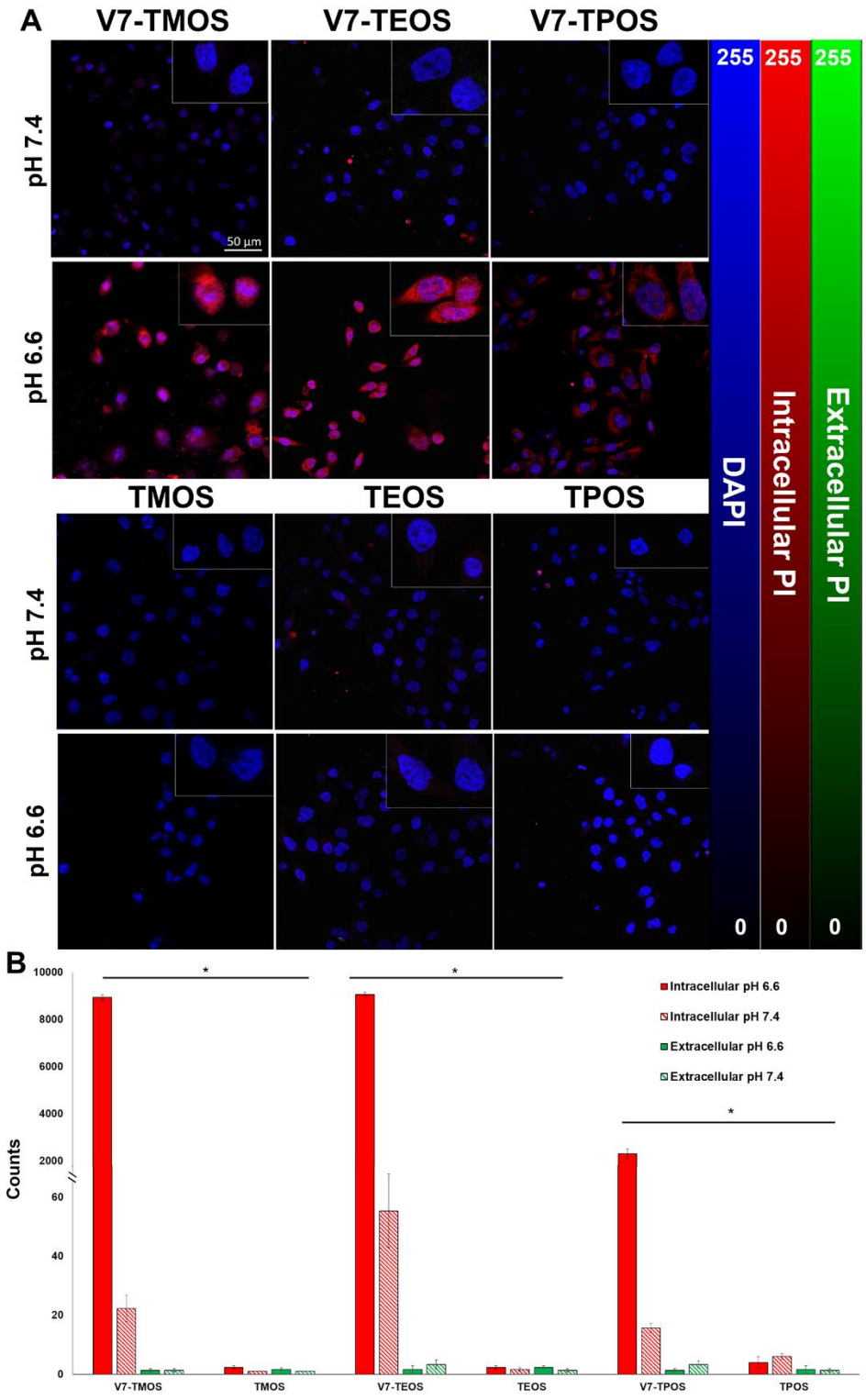

Figure 5.5: Cell internalization of V7-TROS and TROS in acidic, cancerous environments through detection of propidium iodide in pancreatic cancer cell line S2VP10. A) Fluorescence confocal microscopy images displaying cell internalization facilitated by V7, and agent release, facilitated by chitosan. Rows are characterized by the pH of the media

(7.4 vs. 6.6). Columns are characterized by treatment type (V7-TROS vs. TROS). B) Quantification of red vs. green fluorescence observed for reach treatment for pH 7.4 and pH 6.6. *$p<3x10^{-10}$.

5.4.6 *In Vivo* Kinetics of TROS

Defining the characteristics of nanoparticles is critical for successful translation to the clinic. Active targeting and size have been identified as potential influencers on tumor specificity, but to date, studies evaluating these features rarely used clinically relevant *in vivo* models. Here, an orthotopic *in vivo* mouse model is used to evaluate the effects of active targeting and particle size on tumor specificity using MSOT imaging. Specifically, athymic mice were utilized to eliminate signal absorption by hair of mice, particularly following the lack of immune response observed with chitosan coated MSNs in **Chapter 4**. TROS exhibit the potential to carry and deliver high amounts of the contrast agent to tumors compared to conventional techniques such as antibody targeting. MSOT was chosen to measure TROS kinetics and biodistribution in this study due to its high resolution, sensitivity, and deeper penetration into tissues[2]. The use of MSOT also has the benefit of its prior application in clinical trials[1,3]. MSOT and active targeting of nanoparticles show excellent synergy, as rapid tumor accumulation is visualized, without longer exposure, which is often required for significant tumor accumulation[236,237]. Effects of active targeting vs passive targeting and size on tumor-specific uptake were compared following IV of V7-TROS or TROS into mice orthotopically implanted with pancreatic cancer cells[217]. Mice were IV injected with 100 µL of solution containing $8×10^6$ V7-TROS or passively targeted TROS particles, each loaded with the IR780 cargo at 2.7 mM (0.1 OD 600/100µL). Concentrations were selected based upon previous evaluations to heighten efficacy[238]. To evaluate the pharmacokinetic properties of V7-TROS and TROS,

mice were imaged at 0, 4, 8, and 24 h post injection (**Figure 5.6A**). While some accumulation of V7-TROS in tumors was observed 4 h post injection for V7-TMOS, V7-TEOS, and V7-TPOS (29.2, 8.2, and 5.7 a.u., respectively), peak tumor signals were attained at 8 h post injection (65.3, 29.1, and 14.5 a.u.) with $p = 0.0008$, $p = 0.0007$, and $p = 0.005$. The signal of the V7-TROS decreased significantly after 24 h (17.6, 3.6, and 1.6a.u.) with $p<0.00001$, which indicates 8 h as the optimal time point for evaluation of biodistribution (**Figure 5.6A**). Among the V7-TROS treatments, nanoparticle size impacted tumor accumulation and off-target uptake, in which the smaller V7-TMOS particles had significantly greater tumor accumulation than either the V7-TEOS ($p = 0.0003$) or V7-TPOS ($p = 0.0001$) 8 h post injection. In contrast, no significant differences of the signal in tumors treated with any passively targeted TROS were observed: 2.9−1.0 a.u. with $p = 0.672$.

5.4.7 *In Vivo* Biodistribution of TROS

Figure 5.6B-C shows MSOT data comparing pancreatic tumor accumulation of both actively and passively targeted TROS particles loaded with the IR780 dye 8 h post injection. Active targeting of V7-TROS caused significantly greater tumor accumulation than passively targeted TROS. Specifically, MSOT recorded 65.3 a.u. for V7-TMOS and only 2.9 a.u. for TMOS ($p = 0.00001$). Similarly, for the actively and passively targeted V7-TEOS/TEOS and V7-TPOS/TPOS, the MSOT signals were 29.2 a.u. vs 2.8 a.u. ($p = 0.00002$) and 14.5 a.u. vs 2.8 a.u. ($p = 0.00023$), respectively. These results suggest that active targeting leads to greater accumulation of nanoparticles in the tumor than passive targeting. In addition, TROS size has a secondary effect on tumor accumulation but only in the context of actively targeted V7-TROS and not passively targeted TROS. The

smaller size of TMOS suggests that particles are more efficient in extravasating into the tumor space due to the enhanced EPR effect in pancreatic cancer[239]. In addition, smaller particles are less likely to be rapidly cleared from blood by macrophage uptake, as expected with larger TPOS particles, creating a longer period of time that TMOS may accumulate in the tumor[181]. As particles accumulate within the tumor space, concentration gradients would suggest diffusion of particles away from the tumor[240], resulting in similar uptake, independent of size, as observed herein with passively targeted TROS. However, inclusion of V7 provides additional anchoring of TROS to the tumor cells, resisting diffusion for maintaining high tumor accumulation[193,194]. Specifically, the V7-TMOS signal (65.3 a.u.) within the tumor was significantly higher than either V7-TEOS at 29.2 a.u. ($p = 0.000002$) or V7-TPOS at 14.5 a.u. ($p = 0.000001$). As the amount of the signal/particle is proportional to particle size, i.e.,1.01×10^8 dye molecules/TMOS particle, 3.38×10^8 dye molecules/TEOS particle, and 5.62×10^8 dye molecules/TPOS particle (**Figure S5.2**), substantially more V7-TMOS particles accumulated within the tumor than direct comparison of the a.u. values would suggest. In contrast to the actively targeted V7-TROS, differences in tumor accumulation for passively targeted TROS were not significant ($p > 0.05$). These results reinforce the notion that while nanoparticle size can influence tumor accumulation, utilization of active targeting over passive targeting should be prioritized.

Figure 5.6B also shows off-target accumulation and delivery of actively and passively targeted V7-TROS/TROS to vital organs at the same time point (8 h) as tumor accumulation. V7-TROS accumulated in off-target organs at lower levels than the passively targeted TROS. V7-TMOS off-target delivery was recorded at 2.8, 1.2, and 1.3

a.u. for the kidney, liver, and spleen, respectively, while passively targeted TMOS delivery was recorded at values of 6.1, 8.2, and 8.3 a.u. for the same organs. The values for passively targeted TMOS were significantly higher than those for V7-TMOS in the case of both the liver ($p = 0.0001$) and spleen ($p = 0.0131$). The data for V7-TEOS vs TEOS and V7-TPOS vs TPOS followed similar trends, i.e., for both, accumulation of the passively targeted TROS was higher in the liver and spleen. Overall, V7-TROS not only showed significantly higher accumulation within the tumor but also significantly lower off-target delivery than passively targeted TROS. The impact of TROS size on tumor accumulation and off-target delivery is shown, although the effect of size is minor compared to active vs passive targeting. Specifically, an increase in nanoparticle size led to higher accumulation in the liver, for V7-TMOS compared to V7-TEOS ($p = 0.0166$) and V7-TPOS ($p = 0.0006$). The signal from the liver trended to be higher in passively targeted TEOS and was significantly higher in TPOS ($p = 0.008$) compared to TMOS. This increased liver uptake may be attributed to increased Kupffer cell sequestration, which has been previously reported as a result of larger nanoparticle size[222]. While a size increase did not significantly affect splenic uptake of actively targeted TROS ($p = 0.219$), passively targeted TEOS and TPOS had increased splenic uptake compared to TMOS ($p = 0.042$ and $p = 0.015$, respectively). Overall, the MSOT signal observed in the colon indicates that passively targeted particles are excreted via the biliary system[241]. No statistical differences were observed in kidney uptake of either actively or passively targeted TROS, likely due to the nanoparticles having a size larger than the kidney filtration boundary[223].

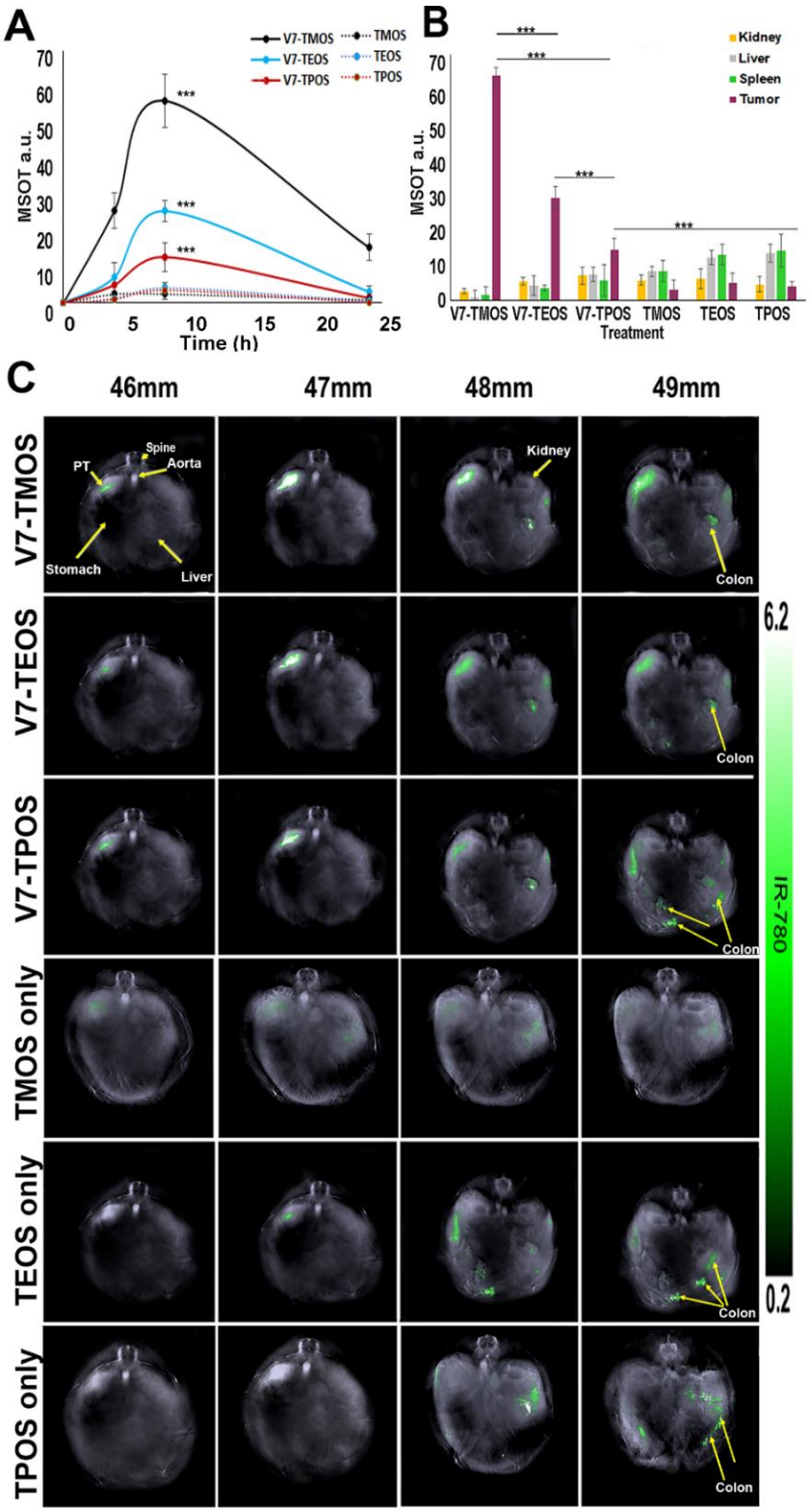

Figure 5.6: *In vivo* biodistribution measurements of V7-TROS and TROS MSNs with optoacoustic imaging in orthotopic tumor-bearing mice. A) Pharmacokinetic assessment of optoacoustic signal within the tumor at timepoints of 0 h, 4 h, 8 h, and 24 h post

intravenous injection. B) After 8 h, biodistribution was quantified within the tumor, kidney, liver, and spleen. C) Biodistribution of TROS in axial slices showing accumulation within the tumor, kidney, liver, and spleen. Refer to **Figure S1.1** for organ locations for tomographic cross sections. *p<0.05, **p<0.01, ***p<0.0001.

5.4.8 Secondary Confirmation of TROS Biodistribution

The *in vivo* MSOT biodistribution results were confirmed *in vivo* using NIR fluorescence (**Figure 5.7A-B**). While 2D fluorescence has benefits relating to topical applications in real time, limited tissue penetration hinders whole-body imaging. Therefore, MSOT was primarily used in this study for real-time imaging without organ removal. NIR fluorescence is a strong secondary confirmation option. The pancreas region of the mice treated with V7-TROS showed the highest accumulation and NIR signal (**Figure 5.7A**). *In vivo*, the V7-TROS particles had significantly higher accumulation compared to passively targeted TROS with $p = 3\times10^{-7}$. V7-TMOS had the highest tumor accumulation with 4.3×10^{6} photons/s followed by V7-TEOS with 4.5×10^{5} photons/s and V7-TPOS with 5.4×10^{4} photons/s (V7-TMOS vs V7-TEOS, p = 0.00001; V7-TMOS vs V7-TPOS, p = 0.000001; V7-TEOS vs V7-TPOS, p = 0.000002). The comparable passively targeted TMOS, TEOS, and TPOS contained 1.7×10^{3}, 1.5×10^{3}, and 1.1×10^{3} photons/s, respectively, and did not significantly vary based on size (p = 0.43). NIR fluorescence imaging confirmed the trends of accumulation observed with MSOT in our *in vivo* orthotopic mouse model. After euthanasia, mouse organs were excised, and accumulation was confirmed *ex vivo* using NIR fluorescence (**Figure 5.7C**). The *ex vivo* results confirmed the measurements recorded with MSOT in terms of biodistribution and tumor specificity. The *ex vivo* maximum signal and accumulation within the tumor of actively targeted V7-TMOS (2.8×10^{5} photons/s), V7-TEOS (9.1×10^{4} photons/s), and V7-TPOS (7.7×10^{3} photons/s),

compared to their passively targeted counterparts TMOS (8.8×10^2 photons/s), TEOS (7.2×10^2 photons/s), and TPOS (4.8×10^2 photons/s), were significant with p = 0.000004. Further post hoc analysis also demonstrated significant differences between V7-TMOS vs TMOS (p = 0.0080), V7-TEOS vs TEOS (p = 0.00035), and V7-TPOS vs TPOS (p = 0.0088). However, accumulation solely based upon nanoparticle size demonstrated significant differences between the smallest and largest sizes tested for TMOS vs TPOS (p = 0.0432) but not significantly different between TMOS vs TEOS (p = 0.3111). These results confirm and emphasize the critical importance of active targeting for tumor accumulation, with size, <50 nm, as a secondary influencing factor in particle accumulation within tumors, particularly in the case of actively targeted particles.

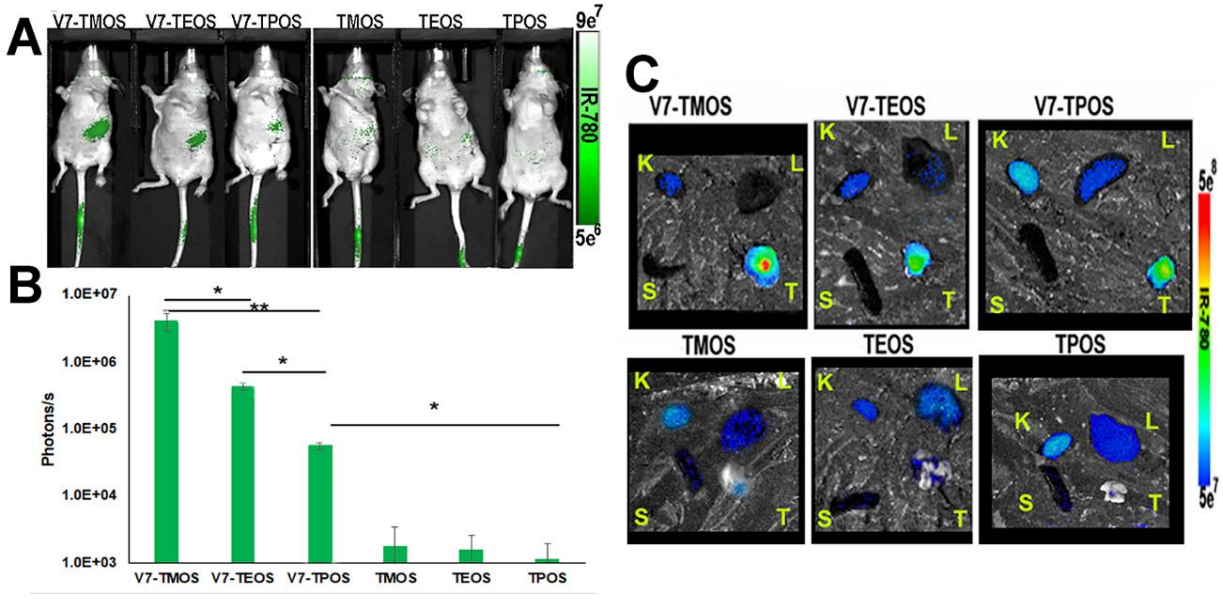

Figure 5.7: A) *In vivo* biodistribution measurements of V7-TROS and TROS MSNs with NIR fluorescence in orthotopic tumor-bearing mice. B) Quantification of (A). C) *Ex vivo* confirmation of NIR fluorescence signal in organs. *p<0.05, **p<0.01, ***p<0.0001.

5.4.9 Detection of Submillimeter Tumors Using V7-TROS

Following determination of V7-TMOS as the optimal treatment for detection in this study, small, submillimeter tumors were imaged with the same *in vivo* model to investigate the sensitivity limits of MSOT imaging, both with and without V7-TMOS, compared to fluorescence (**Supporting Figure S5.4**). While resolution/sensitivity is important for optoacoustic imaging, submillimeter tumor detection was outside the major scope of this study. **Supporting Figure S5.4A and S5.4C** show that while V7-TMOS and oxy/deoxyhemoglobin were capable of detecting a 0.72 mm PDAC tumor, V7-TMOS was able to detect a 0.23 mm PDAC tumor (**Supporting Figure S5.4B)** while oxy/deoxyhemoglobin was not (**Supporting Figure S5.4D**). Whole-body NIR fluorescence in **Supporting Figure S5.4E-F** shows that detection was achieved with the 0.72 mm tumor, but the signal was insufficient to confirm the presence of the smaller, 0.23 mm tumor. **Supporting Figure S5.4G** confirms that the excised tumor shows an NIR fluorescence signal *ex vivo*. These results show that MSOT has capabilities to synergize with contrast-carrying nanoparticles for the detection of small tumors.

5.4.10 Evaluation of TROS Toxicity

Histological evaluation of the liver and kidney was performed by a board-certified pathologist (W.E.G.) and showed no change in the tissue outside of the normal range (**Figure 5.8A−G**). These results support cellular viability conclusions in **Supporting Figure S5.3** that TROS and V7-TROS are nontoxic. The nanoparticle system used avoids the use of PEG as a nanoparticle coating as PEGylated nanoparticles give rise to toxicity concerns based on inhibition of cellular uptake and extended circulation time[141,142,242-244]; in contrast, our data indicates no toxicity associated with the use of V7-TROS for acidosis targeting (**Figures 5.6−5.8** and **Supporting Figure S5.3**). The lack of cytotoxicity in V7-

TROS nanoparticles was likely due to the nearly complete removal of the surfactant used in TROS synthesis, visually evident in TEM images (**Figure 5.2**). While the toxicity of each of the TROS particle types was insignificant, it should be noted that larger TPOS particles tended toward greater toxicity than TMOS or TEOS particles (**Supporting Figure S5.3**). While each TROS particle is relatively small (<75 nm), there are subtle changes among the particles in viability that may influence particle behavior *in vivo*. Chitosan has previously been shown to encourage protein corona formation, potentially leading to toxicity and hindered targeting efficacy[245], although the addition of V7 in this system largely counteracts that effect. The dense conjugation of V7 on the MSN surface creates an extended chain conformation similar to PEG that restricts surface interactions with proteins[195-197,246]. It not only increases efficacy of specific targeting but decreases off-target accumulation and toxicity[177,247]. It obviates any need to PEGylate the MSN, which itself raises concerns of toxicity, especially potential anaphylactic shock or hypersensitivity[141,177,243,248].

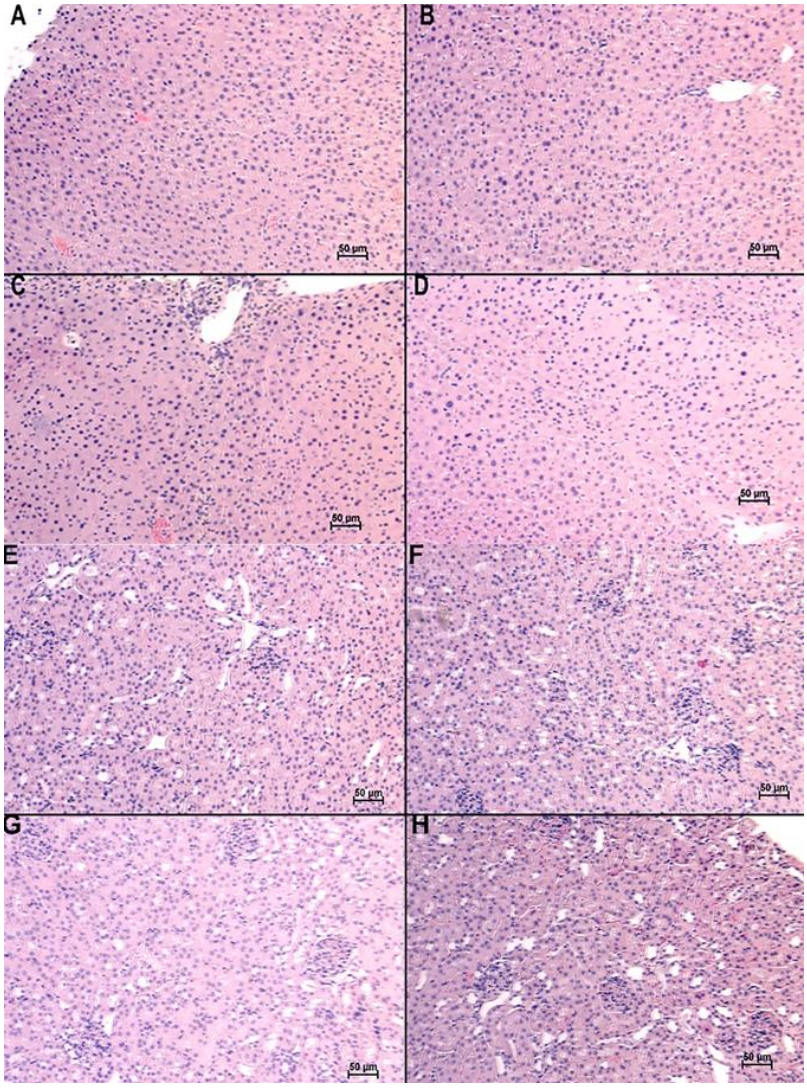

Figure 5.8: Histological evaluation of liver and kidney of mice treated with V7-TROS MSNs. (A-D) Livers and (E-H) kidneys of untreated mice (A, E), and mice treated with V7-TMOS (B, F), V7-TEOS (C, G), and V7-TPOS (D, H). All livers and kidneys appear to be normal/non-diseased.

5.5 Conclusions:

In summary, nanobiotechnologies have universally seen suboptimal clinical outcomes in cancer-related applications due to a poor understanding of how to reliably improve tumor specificity. Numerous structural features of nanoparticles have been previously manipulated to achieve high tumor uptake paired with low off-target accumulation.

However, the resulting data remains controversial due to the lack of clinically appropriate *in vivo* models. This study examines the influence of active targeting vs passive targeting simultaneously with changes in particle size to determine combinations that produce high tumor-specific uptake in a clinically relevant orthotopic model of pancreatic cancer *in vivo*. Nanoparticles were prepared as TMOS (26 nm), TEOS (45 nm), and TPOS (73 nm) and either actively targeted with the V7 peptide or passively targeted without peptide addition. Our results show a strong, primary influence of active targeting, with a secondary influence of particle size, on tumor uptake. Ultimately, V7-targeted 26 nm TMOS particles resulted in the greatest tumor specificity *in vivo*. The superior influence of active targeting was further shown as the actively targeted largest particle (V7-TPOS-73 nm) had higher uptake than the passively targeted smallest particle (TMOS-26 nm). Particle size had a secondary, but important, influence, with particles <50 nm having the best uptake profile among the tested particles. In addition, MSOT showed the capability to outperform many clinical imaging modalities through detection of 0.23 mm PDAC tumors with V7-TMOS and 0.72 mm PDAC tumors without any exogenous contrast. Our study provides valuable insight for the future development of similar nonaggregate nanoparticles for cancer theranostics using powerful imaging modalities such as MSOT.

5.6 Acknowledgements and Funding:

The authors acknowledge funding sources: National Institute of Health grant R01CA205941, National Institute of Health grant R01CA212350, National Institute of Health grant R01EB020125, National Institute of Health grant P30CA225520.

Chapter 6 – Conclusions and Future Directions

The work described in this thesis focuses on expanding the relevance of optoacoustic tomography through improving optoacoustic signature and the delivery of contrast agents. To recap, optoacoustic imaging has emerged as an imaging modality that holds high potential in the clinic due to inherent advantages of the photoacoustic effect. Due to the utilization of low energy near-infrared (NIR) light and the detection of ultrasonic waves rather than re-emitted light, the imaging depth/spatial resolution tradeoff is less relevant; thus, allowing high resolution at increased depths. Multi-wavelength illumination allows for spectral processing (MSOT) and therefore the determination of location and concentration of individual optoacoustic contrast agents in a complex sample. This has been shown clinically with oxygenated and deoxygenated hemoglobin. A major limitation of optoacoustic imaging currently is the small library of dedicated optoacoustic contrast agents; most are primary fluorescence agents that happen to provide optoacoustic signal as well. Chapters 2 and 3 of this document describe studies that create a framework for the production of optoacoustic contrast agents.

Specifically, chapter 2 details the utilization of squaraine dyes as simple, symmetrical, and tunable compounds for determination of how different structural features impact optoacoustic signal generation. As shown, heavy halogenation and increasing the rotatable bond amount through hydrocarbon chain extension, both in tandem and individually, improved optoacoustic signal. However, such changes had no impact on the optoacoustic spectral signatures of the compounds, only the magnitude of optoacoustic signal. As spectral processing software necessitates unique spectral signatures for proper multiplexing, a more complicated dye structure was utilized in chapter 3. Indeed, through

addition of asymmetrical amino groups with increased rotatable bonds, a shift of approximately 50 nm was observed in the peak optoacoustic signal. The studies in chapters 2 and 3 describe a framework for the development of unique optoacoustic contrast agents. As unique and targeting agents for optoacoustic imaging become available, the applications will increase proportionally.

The addition of targeting and improved delivery of contrast agents may vastly improve the applications of optoacoustic imaging. Tracking of a specific protein/antigen, long term imaging through agent retention, and uptake directly into cells are a few methods to increase applications for imaging modalities such as optoacoustic imaging. Utilization of nanoparticles is one technique to potentially include all mentioned benefits. There is no shortage in types of nanoparticles being developed currently, but silica nanoparticles are an intriguing option that are focused on in this document. Specifically, mesoporous silica nanoparticles (MSNs) are a viable nanoparticle system that have been extensively studied recently due to ease of synthesis, tunability, and potential for conjugation. While the potential of MSNs remains high, the lack of standardization and differences in synthesis have raised concerns of toxicity. Autoimmune diseases, fibrosis, and renal/hepatic injury are just a few of the potential complications of administration of MSNs. However, since such issues are likely to be a result of MSN size, coating, cargo, functionalization, etc. toxicity needs to be assessed on a case-by-case basis. Chapter 4 of this thesis describes a study that evaluates toxicity of MSNs, without a coating, and with three common coatings, low molecular weight polyethylene glycol (PEG), high molecular weight PEG, and chitosan. Results concluded that low molecular weight PEG may cause or worsen vascular injury, and low molecular weight PEG specifically may

result in minor kidney dysfunction. Of all treatment groups, MSNs coated with chitosan resulted in no observable toxicity.

Chapter 5 expands on the use of chitosan coated MSNs, this time loaded with optoacoustic contrast agent and targeted for cancer. Using V7 peptide with the chitosan coating, both of which are targeted for the acidic microenvironment of cancer, MSNs specifically accumulated in a pancreatic tumor *in vivo*. In this chapter, MSNs were constructed in three different sizes, all with and without V7 active targeting, to find the optimal construction of MSNs for targeting pancreatic cancer in an orthotopic murine model. V7 active targeting massively outperformed passive targeting, that is, relying only on the enhanced permeability and retention effect. Size of the nanoparticle had a secondary, but strong effect on tumor accumulation in which the smallest of the MSNs (26 nm diameter) had maximum accumulation, followed by 45 nm and 73 nm MSNs.

The work detailed in this document has many future routes and studies to be performed. In relevance to chapters 2 and 3, improved understanding of how to control optoacoustic signal through structural enhancement may be performed similarly to the studies detailed. This will only further enhance and expand the library of optoacoustic contrast agents, allowing for improved sensitivity of agents and multiplexing studies. In addition, such optoacoustic contrast agents may be incorporated with nanoparticles such as the formation outlined in chapters 4 and 5. These may improve signal generation with more controlled release or specific accumulation of contrast agents.

Longer term future directions would include the use of optimized contrast agents in a clinical setting. Through standardization and optimization of both the optoacoustic contrast agent and the nanoparticle system, targeting studies may visualize disease such

as cancer in humans. This could occur simultaneously with optoacoustic imaging to view multiple agents, for example, targeted tumor cells and oxygenation. In addition to cancer, other diseases that have antigens that are targetable through small peptides may be visualized with optoacoustic imaging.

References:

1. Stoffels, I., Morscher, S., Helfrich, I., Hillen, U., Leyh, J., Burton, N.C., Sardella, T.C., Claussen, J., Poeppel, T.D., and Bachmann, H.S. (2015). Metastatic status of sentinel lymph nodes in melanoma determined noninvasively with multispectral optoacoustic imaging. Science translational medicine *7*, 317ra199-317ra199.
2. Bhutiani, N., Kimbrough, C., Burton, N., Morscher, S., Egger, M., McMasters, K., Woloszynska-Read, A., El-Baz, A., and McNally, L. (2017). Detection of microspheres in vivo using multispectral optoacoustic tomography. Biotechnic & histochemistry *92*, 1-6.
3. Knieling, F., Neufert, C., Hartmann, A., Claussen, J., Urich, A., Egger, C., Vetter, M., Fischer, S., Pfeifer, L., and Hagel, A. (2017). Multispectral Optoacoustic Tomography for Assessment of Crohn's Disease Activity. The New England journal of medicine *376*, 1292.
4. Becker, A., Masthoff, M., Claussen, J., Ford, S.J., Roll, W., Burg, M., Barth, P.J., Heindel, W., Schaefers, M., and Eisenblaetter, M. (2018). Multispectral optoacoustic tomography of the human breast: characterisation of healthy tissue and malignant lesions using a hybrid ultrasound-optoacoustic approach. European radiology *28*, 602-609.
5. Ntziachristos, V., and Razansky, D. (2010). Molecular imaging by means of multispectral optoacoustic tomography (MSOT). Chemical reviews *110*, 2783-2794.
6. McNally, L.R., Mezera, M., Morgan, D.E., Frederick, P.J., Yang, E.S., Eltoum, I.-E., and Grizzle, W.E. (2016). Current and emerging clinical applications of multispectral optoacoustic tomography (MSOT) in oncology. Clinical cancer research *22*, 3432-3439.
7. Tzoumas, S., Deliolanis, N.C., Morscher, S., and Ntziachristos, V. (2013). Unmixing molecular agents from absorbing tissue in multispectral optoacoustic tomography. IEEE transactions on medical imaging *33*, 48-60.
8. Razansky, D., Baeten, J., and Ntziachristos, V. (2009). Sensitivity of molecular target detection by multispectral optoacoustic tomography (MSOT). Medical physics *36*, 939-945.
9. Xia, J., Yao, J., and Wang, L.V. (2014). Photoacoustic tomography: principles and advances. Electromagnetic waves (Cambridge, Mass.) *147*, 1.
10. Wissmeyer, G., Pleitez, M.A., Rosenthal, A., and Ntziachristos, V. (2018). Looking at sound: optoacoustics with all-optical ultrasound detection. Light: Science & Applications *7*, 53.
11. Schellenberg, M.W., and Hunt, H.K. (2018). Hand-held optoacoustic imaging: A review. Photoacoustics *11*, 14-27.
12. Dean-Ben, X.L., Buehler, A., Ntziachristos, V., and Razansky, D. (2012). Accurate model-based reconstruction algorithm for three-dimensional optoacoustic tomography. IEEE transactions on medical imaging *31*, 1922-1928.
13. Tzoumas, S., and Ntziachristos, V. (2017). Spectral unmixing techniques for optoacoustic imaging of tissue pathophysiology. Philosophical Transactions of

the Royal Society A: Mathematical, Physical and Engineering Sciences *375*, 20170262.
14. Cox, B., Laufer, J., and Beard, P. (2009). The challenges for quantitative photoacoustic imaging. (International Society for Optics and Photonics), pp. 717713.
15. Chen, Z., Deán-Ben, X.L., Liu, N., Gujrati, V., Gottschalk, S., Ntziachristos, V., and Razansky, D. (2019). Concurrent fluorescence and volumetric optoacoustic tomography of nanoagent perfusion and bio-distribution in solid tumors. Biomedical Optics Express *10*, 5093-5102.
16. Diot, G., Metz, S., Noske, A., Liapis, E., Schroeder, B., Ovsepian, S.V., Meier, R., Rummeny, E., and Ntziachristos, V. (2017). Multispectral optoacoustic tomography (MSOT) of human breast cancer. Clinical Cancer Research *23*, 6912-6922.
17. Zackrisson, S., Van De Ven, S., and Gambhir, S. (2014). Light in and sound out: emerging translational strategies for photoacoustic imaging. Cancer research *74*, 979-1004.
18. Li, M., Tang, Y., and Yao, J. (2018). Photoacoustic tomography of blood oxygenation: A mini review. Photoacoustics *10*, 65-73.
19. Kim, H., and Chang, J.H. (2018). Multimodal photoacoustic imaging as a tool for sentinel lymph node identification and biopsy guidance. Biomedical Engineering Letters *8*, 183-191.
20. Anani, T., Brannen, A., Panizzi, P., Duin, E.C., and David, A.E. (2020). Quantitative, real-time in vivo tracking of magnetic nanoparticles using multispectral optoacoustic tomography (MSOT) imaging. Journal of pharmaceutical and biomedical analysis *178*, 112951.
21. Hashem, F., Nasr, M., and Ahmed, Y. (2018). Preparation and evaluation of iron oxide nanoparticles for treatment of iron deficiency anemia. Int J Pharm Pharm Sci *10*, 142.
22. Zeiderman, M.R., Morgan, D.E., Christein, J.D., Grizzle, W.E., McMasters, K.M., and McNally, L.R. (2016). Acidic pH-targeted chitosan-capped mesoporous silica coated gold nanorods facilitate detection of pancreatic tumors via multispectral optoacoustic tomography. ACS biomaterials science & engineering *2*, 1108-1120.
23. Deán-Ben, X.L., Fehm, T.F., Gostic, M., and Razansky, D. (2016). Volumetric hand-held optoacoustic angiography as a tool for real-time screening of dense breast. Journal of biophotonics *9*, 253-259.
24. Toi, M., Asao, Y., Matsumoto, Y., Sekiguchi, H., Yoshikawa, A., Takada, M., Kataoka, M., Endo, T., Kawaguchi-Sakita, N., and Kawashima, M. (2017). Visualization of tumor-related blood vessels in human breast by photoacoustic imaging system with a hemispherical detector array. Scientific reports *7*, 41970.
25. Abeyakoon, O., Woitek, R.A., Wallis, M., Moyle, P.L., Morscher, S., Malchus, N., Manavaki, R., Mendichovsky, I.A., Joseph, J., Quiros-Gonzalez, I., et al. (2018). Optoacoustic imaging increases the sensitivity of mammography and specificity of US: implications for practice (Abstract). Insights Imaging *9*, 415.
26. Neuschler, E.I., Butler, R., Young, C.A., Barke, L.D., Bertrand, M.L., Böhm-Vélez, M., Destounis, S., Donlan, P., Grobmyer, S.R., and Katzen, J. (2018). A pivotal

study of optoacoustic imaging to diagnose benign and malignant breast masses: a new evaluation tool for radiologists. Radiology *287*, 398-412.
27. Menezes, G.L., Pijnappel, R.M., Meeuwis, C., Bisschops, R., Veltman, J., Lavin, P.T., Van De Vijver, M.J., and Mann, R.M. (2018). Downgrading of breast masses suspicious for cancer by using optoacoustic breast imaging. Radiology *288*, 355-365.
28. Kothapalli, S.-R., Sonn, G.A., Choe, J.W., Nikoozadeh, A., Bhuyan, A., Park, K.K., Cristman, P., Fan, R., Moini, A., and Lee, B.C. (2019). Simultaneous transrectal ultrasound and photoacoustic human prostate imaging. Science translational medicine *11*, eaav2169.
29. Peng, K., He, L., Wang, B., and Xiao, J. (2015). Detection of cervical cancer based on photoacoustic imaging—the in-vitro results. Biomedical optics express *6*, 135-143.
30. Nandy, S., Mostafa, A., Hagemann, I.S., Powell, M.A., Amidi, E., Robinson, K., Mutch, D.G., Siegel, C., and Zhu, Q. (2018). Evaluation of ovarian cancer: initial application of coregistered photoacoustic tomography and US. Radiology *289*, 740-747.
31. Qu, Y., Li, C., Shi, J., Chen, R., Xu, S., Rafsanjani, H., Maslov, K., Krigman, H., Garvey, L., and Hu, P. (2018). Transvaginal fast-scanning optical-resolution photoacoustic endoscopy. Journal of biomedical optics *23*, 121617-121617.
32. Knieling, F., Hartmann, A., Claussen, J., Urich, A., Atreya, R., Rascher, W., and Waldner, M. (2017). Multispectral Optoacoustic Tomography in Ulcerative Colitis-A First-in-human Diagnostic Clinical Trial. Journal of Nuclear Medicine *58*, 1196-1196.
33. Schwarz, M., Buehler, A., Aguirre, J., and Ntziachristos, V. (2016). Three-dimensional multispectral optoacoustic mesoscopy reveals melanin and blood oxygenation in human skin in vivo. Journal of biophotonics *9*, 55-60.
34. Chuah, S., Attia, A., Long, V., Ho, C., Malempati, P., Fu, C., Ford, S., Lee, J., Tan, W., and Razansky, D. (2017). Structural and functional 3D mapping of skin tumours with non-invasive multispectral optoacoustic tomography. Skin Research and Technology *23*, 221-226.
35. Langhout, G.C., Grootendorst, D.J., Nieweg, O.E., Wouters, M.W.J.M., Hage, J.A.v.d., Jose, J., Boven, H.v., Steenbergen, W., Manohar, S., and Ruers, T.J.M. (2014). Detection of melanoma metastases in resected human lymph nodes by noninvasive multispectral photoacoustic imaging. Journal of Biomedical Imaging *2014*, 5-5.
36. Krönke, M., Karlas, A., Fasoula, N., Markwardt, N., Kallmayer, M., Eckstein, H., Scheidhauer, K., Weber, W., and Ntziachristos, V. (2019). Multispectral Optoacoustic Tomography (MSOT): A Novel Label-Free Imaging Technique for Thyroid Imaging. Nuklearmedizin *58*, V89.
37. Roll, W., Markwardt, N.A., Masthoff, M., Helfen, A., Claussen, J., Eisenblätter, M., Hasenbach, A., Hermann, S., Karlas, A., and Wildgruber, M. (2019). Multispectral Optoacoustic Tomography of Benign and Malignant Thyroid Disorders: A Pilot Study. Journal of Nuclear Medicine *60*, 1461-1466.
38. Ivankovic, I., and Razansky, D. (2019). non-invasive 3d imaging of the human carotid artery with volumetric multispectral optoacoustic tomography (vMsOt).

THE ROLE OF CORONARY CT ANGIOGRAPHY IN SUSPECTED CORONARY HEART DISEASE *15*, 34.
39. Masthoff, M., Helfen, A., Claussen, J., Roll, W., Karlas, A., Becker, H., Gabriëls, G., Riess, J., Heindel, W., and Schäfers, M. (2018). Multispectral optoacoustic tomography of systemic sclerosis. Journal of biophotonics *11*, e201800155.
40. Reber, J., Willershäuser, M., Karlas, A., Paul-Yuan, K., Diot, G., Franz, D., Fromme, T., Ovsepian, S.V., Bézière, N., and Dubikovskaya, E. (2018). Non-invasive measurement of brown fat metabolism based on optoacoustic imaging of hemoglobin gradients. Cell metabolism *27*, 689-701. e684.
41. Shao, Q., and Ashkenazi, S. (2015). Photoacoustic lifetime imaging for direct in vivo tissue oxygen monitoring. Journal of biomedical optics *20*, 036004.
42. Shcherbakova, D.M., and Verkhusha, V.V. (2013). Near-infrared fluorescent proteins for multicolor in vivo imaging. Nature methods *10*, 751-754.
43. Joseph, J., Tomaszewski, M.R., Quiros-Gonzalez, I., Weber, J., Brunker, J., and Bohndiek, S.E. (2017). Evaluation of precision in optoacoustic tomography for preclinical imaging in living subjects. Journal of Nuclear Medicine *58*, 807-814.
44. Luo, S., Zhang, E., Su, Y., Cheng, T., and Shi, C. (2011). A review of NIR dyes in cancer targeting and imaging. Biomaterials *32*, 7127-7138.
45. Ilina, K., MacCuaig, W.M., Laramie, M., Jeouty, J.N., McNally, L.R., and Henary, M. (2019). Squaraine Dyes: Molecular Design for Different Applications and Remaining Challenges. Bioconjugate chemistry.
46. Zha, Z., Deng, Z., Li, Y., Li, C., Wang, J., Wang, S., Qu, E., and Dai, Z. (2013). Biocompatible polypyrrole nanoparticles as a novel organic photoacoustic contrast agent for deep tissue imaging. Nanoscale *5*, 4462-4467.
47. Treibs, A., and Jacob, K. (1965). Cyclotrimethine dyes derived from squaric acid. Angewandte Chemie International Edition in English *4*, 694-694.
48. Podgorski, K., Terpetschnig, E., Klochko, O.P., Obukhova, O.M., and Haas, K. (2012). Ultra-bright and-stable red and near-infrared squaraine fluorophores for in vivo two-photon imaging. PLoS One *7*, e51980.
49. Shimi, M., Sankar, V., Rahim, M.A., Nitha, P., Das, S., Radhakrishnan, K., and Raghu, K. (2017). Novel glycoconjugated squaraine dyes for selective optical imaging of cancer cells. Chemical Communications *53*, 5433-5436.
50. Oswald, B., Lehmann, F., Simon, L., Terpetschnig, E., and Wolfbeis, O.S. (2000). Red laser-induced fluorescence energy transfer in an immunosystem. Analytical biochemistry *280*, 272-277.
51. Gross, S., and Piwnica-Worms, D. (2006). Molecular imaging strategies for drug discovery and development. Current opinion in chemical biology *10*, 334-342.
52. Keller, P.J., Pampaloni, F., and Stelzer, E.H. (2006). Life sciences require the third dimension. Current opinion in cell biology *18*, 117-124.
53. Devi, D.G., Cibin, T., Ramaiah, D., and Abraham, A. (2008). Bis (3, 5-diiodo-2, 4, 6-trihydroxyphenyl) squaraine: A novel candidate in photodynamic therapy for skin cancer models in vivo. Journal of photochemistry and photobiology B: Biology *92*, 153-159.
54. Wang, B., Fan, J., Sun, S., Wang, L., Song, B., and Peng, X. (2010). 1-(Carbamoylmethyl)-3H-indolium squaraine dyes: synthesis, spectra, photo-stability and association with BSA. Dyes and Pigments *85*, 43-50.

55. Terpetsching, E., Szmacinski, H., and Lakowicz, J.R. (1993). Synthesis, spectral properties and photostabilities of symmetrical and unsymmetrical squarines; a new class of flourophores with long-wavelength exiciation and emmision. Analytica chimica acta *282*, 633-641.
56. Arunkumar, E., Fu, N., and Smith, B.D. (2006). Squaraine-derived rotaxanes: Highly stable, fluorescent near-IR dyes. Chemistry–A European Journal *12*, 4684-4690.
57. Law, K.Y. (1993). Organic photoconductive materials: recent trends and developments. Chemical Reviews *93*, 449-486.
58. Li, L., Liu, T., Fu, C., Tan, L., Meng, X., and Liu, H. (2015). Biodistribution, excretion, and toxicity of mesoporous silica nanoparticles after oral administration depend on their shape. Nanomedicine: Nanotechnology, Biology and Medicine *11*, 1915-1924.
59. He, Y.Q., Liu, S.P., Kong, L., and Liu, Z.F. (2005). A study on the sizes and concentrations of gold nanoparticles by spectra of absorption, resonance Rayleigh scattering and resonance non-linear scattering. Spectrochimica Acta Part A: Molecular and Biomolecular Spectroscopy *61*, 2861-2866.
60. Shrivastava, R., Kushwaha, P., Bhutia, Y.C., and Flora, S. (2016). Oxidative stress following exposure to silver and gold nanoparticles in mice. Toxicology and industrial health *32*, 1391-1404.
61. Paramelle, D., Sadovoy, A., Gorelik, S., Free, P., Hobley, J., and Fernig, D.G. (2014). A rapid method to estimate the concentration of citrate capped silver nanoparticles from UV-visible light spectra. Analyst *139*, 4855-4861.
62. Pfohl, M., Tune, D.D., Graf, A., Zaumseil, J., Krupke, R., and Flavel, B.S. (2017). Fitting single-walled carbon nanotube optical spectra. ACS omega *2*, 1163-1171.
63. Cheng, X., Zhong, J., Meng, J., Yang, M., Jia, F., Xu, Z., Kong, H., and Xu, H. (2011). Characterization of multiwalled carbon nanotubes dispersing in water and association with biological effects. Journal of Nanomaterials *2011*.
64. Weber, J., Beard, P.C., and Bohndiek, S.E. (2016). Contrast agents for molecular photoacoustic imaging. Nature methods *13*, 639-650.
65. MacCuaig, W.M., Jones, M.A., Abeyakoon, O., and McNally, L.R. (2020). Development of Multispectral Optoacoustic Tomography as a Clinically Translatable Modality for Cancer Imaging. Radiology: Imaging Cancer *2*.
66. Wang, L.V., and Hu, S. (2012). Photoacoustic tomography: in vivo imaging from organelles to organs. science *335*, 1458-1462.
67. Attia, A.B.E., Balasundaram, G., Moothanchery, M., Dinish, U., Bi, R., Ntziachristos, V., and Olivo, M. (2019). A review of clinical photoacoustic imaging: Current and future trends. Photoacoustics *16*, 100144.
68. Regensburger, A.P., Brown, E., Krönke, G., Waldner, M.J., and Knieling, F. (2021). Optoacoustic Imaging in Inflammation. Biomedicines *9*, 483.
69. Regensburger, A.P., Wagner, A.L., Claussen, J., Waldner, M.J., and Knieling, F. (2020). Shedding light on pediatric diseases: multispectral optoacoustic tomography at the doorway to clinical applications. Molecular and cellular pediatrics *7*, 1-6.
70. Manohar, S., and Gambhir, S. (2020). Clinical photoacoustic imaging. Photoacoustics *19*.

71. Regensburger, A.P., Fonteyne, L.M., Jüngert, J., Wagner, A.L., Gerhalter, T., Nagel, A.M., Heiss, R., Flenkenthaler, F., Qurashi, M., and Neurath, M.F. (2019). Detection of collagens by multispectral optoacoustic tomography as an imaging biomarker for Duchenne muscular dystrophy. Nature Medicine *25*, 1905-1915.
72. Zhang, H.F., Maslov, K., Sivaramakrishnan, M., Stoica, G., and Wang, L.V. (2007). Imaging of hemoglobin oxygen saturation variations in single vessels in vivo using photoacoustic microscopy. Applied physics letters *90*, 053901.
73. Upputuri, P.K., and Pramanik, M. (2020). Recent advances in photoacoustic contrast agents for in vivo imaging. Wiley Interdisciplinary Reviews: Nanomedicine and Nanobiotechnology, e1618.
74. Knieling, F., Hartmann, A., Uter, W., Urich, A., Claussen, J., Atreya, R., Rascher, W., and Waldner, M. (2017). Multispectral Optoacoustic Tomography in Crohn's disease-A First-in-human Diagnostic Clinical Trial. Journal of Nuclear Medicine *58*, 379-379.
75. Attia, A.B.E., Chuah, S.Y., Razansky, D., Ho, C.J.H., Malempati, P., Dinish, U., Bi, R., Fu, C.Y., Ford, S.J., and Lee, J.S.-S. (2017). Noninvasive real-time characterization of non-melanoma skin cancers with handheld optoacoustic probes. Photoacoustics *7*, 20-26.
76. Zhang, Y., He, S., Chen, W., Liu, Y., Zhang, X., Miao, Q., and Pu, K. (2021). Activatable Polymeric Nanoprobe for Near-Infrared Fluorescence and Photoacoustic Imaging of T Lymphocytes. Angewandte Chemie *133*, 5986-5992.
77. Beziere, N., Lozano, N., Nunes, A., Salichs, J., Queiros, D., Kostarelos, K., and Ntziachristos, V. (2015). Dynamic imaging of PEGylated indocyanine green (ICG) liposomes within the tumor microenvironment using multi-spectral optoacoustic tomography (MSOT). Biomaterials *37*, 415-424.
78. Laramie, M., Smith, M., Marmarchi, F., McNally, L., and Henary, M. (2018). Small Molecule Optoacoustic Contrast Agents: An Unexplored Avenue for Enhancing In Vivo Imaging. Molecules *23*, 2766.
79. Song, K.H., Stein, E.W., Margenthaler, J.A., and Wang, L.V. (2008). Noninvasive photoacoustic identification of sentinel lymph nodes containing methylene blue in vivo in a rat model. Journal of biomedical optics *13*, 054033.
80. Chen, J., Liu, C., Zeng, G., You, Y., Wang, H., Gong, X., Zheng, R., Kim, J., Kim, C., and Song, L. (2016). Indocyanine green loaded reduced graphene oxide for in vivo photoacoustic/fluorescence dual-modality tumor imaging. Nanoscale research letters *11*, 1-11.
81. Li, W., Peng, J., Yang, Q., Chen, L., Zhang, L., Chen, X., and Qian, Z. (2018). α-Lipoic acid stabilized DTX/IR780 micelles for photoacoustic/fluorescence imaging guided photothermal therapy/chemotherapy of breast cancer. Biomaterials science *6*, 1201-1216.
82. Hui, J., Li, R., Phillips, E.H., Goergen, C.J., Sturek, M., and Cheng, J.-X. (2016). Bond-selective photoacoustic imaging by converting molecular vibration into acoustic waves. Photoacoustics *4*, 11-21.
83. Weng, X.-L., and Liu, J.-Y. (2021). Strategies for maximizing photothermal conversion efficiency based on organic dyes. Drug Discovery Today *26*, 2045-2052.

84. Yadav, Y., Owens, E., Nomura, S., Fukuda, T., Baek, Y., Kashiwagi, S., Choi, H.S., and Henary, M. (2020). Ultrabright and Serum-Stable Squaraine Dyes. Journal of medicinal chemistry *63*, 9436-9445.
85. Liu, Y., Teng, L., Yin, B., Meng, H., Yin, X., Huan, S., Song, G., and Zhang, X.-B. (2022). Chemical design of activatable photoacoustic probes for precise biomedical applications. Chemical Reviews *122*, 6850-6918.
86. Koziar, J.C., and Cowan, D.O. (1978). Photochemical heavy-atom effects. Accounts of chemical research *11*, 334-341.
87. Chatterjee, M., Ben-Josef, E., Robb, R., Vedaie, M., Seum, S., Thirumoorthy, K., Palanichamy, K., Harbrecht, M., Chakravarti, A., and Williams, T.M. (2017). Caveolae-mediated endocytosis is critical for albumin cellular uptake and response to albumin-bound chemotherapy. Cancer research *77*, 5925-5937.
88. Wang, T.H., Wang, H.S., and Soong, Y.K. (2000). Paclitaxel-induced cell death: where the cell cycle and apoptosis come together. Cancer: Interdisciplinary International Journal of the American Cancer Society *88*, 2619-2628.
89. St. Lorenz, A., Buabeng, E.R., Taratula, O., Taratula, O., and Henary, M. (2021). Near-infrared heptamethine cyanine dyes for nanoparticle-based photoacoustic imaging and photothermal therapy. Journal of Medicinal Chemistry *64*, 8798-8805.
90. Al-Otaibi, J.S., and Al-Wabli, R.I. (2015). Vibrational spectroscopic investigation (FT-IR and FT-Raman) using ab initio (HF) and DFT (B3LYP) calculations of 3-ethoxymethyl-1, 4-dihydroquinolin-4-one. Spectrochimica Acta Part A: Molecular and Biomolecular Spectroscopy *137*, 7-15.
91. An, X.-X., Liu, C., Chen, Z.-Z., Xie, K.-F., and Zhang, Y. (2019). Fluorescence properties and density functional theory calculation of a structurally characterized heterotetranuclear [ZnII2–SmIII2] 4, 4′-bipy-salamo-constructed complex. Crystals *9*, 602.
92. Essam, Z.M., Ozmen, G.E., Setiawan, D., Hamid, R.R., Abd El-Aal, R.M., Aneja, R., Hamelberg, D., and Henary, M. (2021). Donor acceptor fluorophores: synthesis, optical properties, TD-DFT and cytotoxicity studies. Organic & biomolecular chemistry *19*, 1835-1846.
93. Furche, F., and Ahlrichs, R. (2002). Adiabatic time-dependent density functional methods for excited state properties. The Journal of chemical physics *117*, 7433-7447.
94. Epifanovsky, E., Gilbert, A.T., Feng, X., Lee, J., Mao, Y., Mardirossian, N., Pokhilko, P., White, A.F., Coons, M.P., and Dempwolff, A.L. (2021). Software for the frontiers of quantum chemistry: An overview of developments in the Q-Chem 5 package. The Journal of chemical physics *155*, 084801.
95. Perdew, J.P., Burke, K., and Ernzerhof, M. (1996). Generalized gradient approximation made simple. Physical review letters *77*, 3865.
96. Hehre, W.J., Ditchfield, R., and Pople, J.A. (1972). Self—consistent molecular orbital methods. XII. Further extensions of Gaussian—type basis sets for use in molecular orbital studies of organic molecules. The Journal of Chemical Physics *56*, 2257-2261.

97. Gao, F., Kishor, R., Feng, X., Liu, S., Ding, R., Zhang, R., and Zheng, Y. (2017). An analytical study of photoacoustic and thermoacoustic generation efficiency towards contrast agent and film design optimization. Photoacoustics *7*, 1-11.
98. Roncali, J. (2007). Molecular engineering of the band gap of π-conjugated systems: Facing technological applications. Macromolecular Rapid Communications *28*, 1761-1775.
99. Yanagisawa, S., Yasuda, T., Inagaki, K., Morikawa, Y., Manseki, K., and Yanagida, S. (2013). Intermolecular interaction as the origin of red shifts in absorption spectra of zinc-phthalocyanine from first-principles. The Journal of Physical Chemistry A *117*, 11246-11253.
100. Toutain, P.-L., and Bousquet-mélou, A. (2004). Plasma clearance. Journal of veterinary pharmacology and therapeutics *27*, 415-425.
101. Lau, S., Gossen, M., Lendlein, A., and Jung, F. (2021). Venous and arterial endothelial cells from human umbilical cords: potential cell sources for cardiovascular research. International Journal of Molecular Sciences *22*, 978.
102. Bell, A.G. (1881). On the production and reproduction of sound by light. pp. 115-136.
103. Beard, P. (2011). Biomedical photoacoustic imaging. Interface focus *1*, 602-631.
104. Rajapaksha, A.A., Fu, Y.-X., Guo, W.Y., Liu, S.-Y., Li, Z.-W., Xiong, C.-Q., Yang, W.-C., and Yang, G.-F. (2021). Review on the recent progress in the development of fluorescent probes targeting enzymes. Methods and Applications in Fluorescence *9*, 032001.
105. Sun, W., Guo, S., Hu, C., Fan, J., and Peng, X. (2016). Recent development of chemosensors based on cyanine platforms. Chemical reviews *116*, 7768-7817.
106. Li, H., Kim, H., Xu, F., Han, J., Yao, Q., Wang, J., Pu, K., Peng, X., and Yoon, J. (2022). Activity-based NIR fluorescent probes based on the versatile hemicyanine scaffold: design strategy, biomedical applications, and outlook. Chemical Society Reviews *51*, 1795-1835.
107. Zeng, Z., Liew, S.S., Wei, X., and Pu, K. (2021). Hemicyanine-based near-infrared activatable probes for imaging and diagnosis of diseases. Angewandte Chemie *133*, 26658-26679.
108. Gardner, S.H., Brady, C.J., Keeton, C., Yadav, A.K., Mallojjala, S.C., Lucero, M.Y., Su, S., Yu, Z., Hirschi, J.S., and Mirica, L.M. (2021). A general approach to convert hemicyanine dyes into highly optimized photoacoustic scaffolds for analyte sensing. Angewandte Chemie International Edition *60*, 18860-18866.
109. Knox, H.J., and Chan, J. (2018). Acoustogenic probes: a new frontier in photoacoustic imaging. Accounts of chemical research *51*, 2897-2905.
110. He, X., Li, L., Fang, Y., Shi, W., Li, X., and Ma, H. (2017). In vivo imaging of leucine aminopeptidase activity in drug-induced liver injury and liver cancer via a near-infrared fluorescent probe. Chemical Science *8*, 3479-3483.
111. Wang, C., Chi, W., Qiao, Q., Tan, D., Xu, Z., and Liu, X. (2021). Twisted intramolecular charge transfer (TICT) and twists beyond TICT: From mechanisms to rational designs of bright and sensitive fluorophores. Chemical Society Reviews *50*, 12656-12678.
112. Hu, R., Lager, E., Aguilar-Aguilar, A., Liu, J., Lam, J.W., Sung, H.H., Williams, I.D., Zhong, Y., Wong, K.S., and Pena-Cabrera, E. (2009). Twisted intramolecular

charge transfer and aggregation-induced emission of BODIPY derivatives. The Journal of Physical Chemistry C *113*, 15845-15853.
113. Tanaka, H., Shizu, K., Nakanotani, H., and Adachi, C. (2013). Twisted intramolecular charge transfer state for long-wavelength thermally activated delayed fluorescence. Chemistry of Materials *25*, 3766-3771.
114. Chen, C., and Fang, C. (2023). Fluorescence Modulation by Amines: Mechanistic Insights into Twisted Intramolecular Charge Transfer (TICT) and Beyond. Chemosensors *11*, 87.
115. Sasaki, S., Drummen, G.P., and Konishi, G.-i. (2016). Recent advances in twisted intramolecular charge transfer (TICT) fluorescence and related phenomena in materials chemistry. Journal of Materials Chemistry C *4*, 2731-2743.
116. Owens, E.A., Hyun, H., Tawney, J.G., Choi, H.S., and Henary, M.J.J.o.m.c. (2015). Correlating molecular character of NIR imaging agents with tissue-specific uptake. *58*, 4348-4356.
117. Yuan, L., Lin, W., Zhao, S., Gao, W., Chen, B., He, L., and Zhu, S. (2012). A unique approach to development of near-infrared fluorescent sensors for in vivo imaging. Journal of the American Chemical Society *134*, 13510-13523.
118. Levitz, A., Marmarchi, F., and Henary, M. (2018). Introduction of various substitutions to the methine bridge of heptamethine cyanine dyes Via substituted dianil linkers. Photochemical & Photobiological Sciences *17*, 1409-1416.
119. Hecht, M., and Wurthner, F. (2020). Supramolecularly engineered J-aggregates based on perylene bisimide dyes. Accounts of Chemical Research *54*, 642-653.
120. Pelaz, B., Alexiou, C., Alvarez-Puebla, R.A., Alves, F., Andrews, A.M., Ashraf, S., Balogh, L.P., Ballerini, L., Bestetti, A., and Brendel, C. (2017). Diverse applications of nanomedicine. ACS nano *11*, 2313-2381.
121. Manzano, M., and Vallet-Regí, M. (2020). Mesoporous silica nanoparticles for drug delivery. Advanced Functional Materials *30*, 1902634.
122. Jeelani, P.G., Mulay, P., Venkat, R., and Ramalingam, C. (2020). Multifaceted application of silica nanoparticles. A review. Silicon *12*, 1337-1354.
123. Carniato, F., Tei, L., and Botta, M. (2018). Gd-Based Mesoporous Silica Nanoparticles as MRI Probes. European Journal of Inorganic Chemistry *2018*, 4936-4954.
124. Nakamura, T., Sugihara, F., Matsushita, H., Yoshioka, Y., Mizukami, S., and Kikuchi, K. (2015). Mesoporous silica nanoparticles for 19 F magnetic resonance imaging, fluorescence imaging, and drug delivery. Chemical science *6*, 1986-1990.
125. Gurka, M.K., Pender, D., Chuong, P., Fouts, B.L., Sobelov, A., McNally, M.W., Mezera, M., Woo, S.Y., and McNally, L.R. (2016). Identification of pancreatic tumors in vivo with ligand-targeted, pH responsive mesoporous silica nanoparticles by multispectral optoacoustic tomography. Journal of controlled release *231*, 60-67.
126. Khanal, A., Ullum, C., Kimbrough, C.W., Garbett, N.C., Burlison, J.A., McNally, M.W., Chuong, P., El-Baz, A.S., Jasinski, J.B., and McNally, L.R. (2015). Tumor targeted mesoporous silica-coated gold nanorods facilitate detection of pancreatic tumors using Multispectral optoacoustic tomography. Nano Research *8*, 3864-3877.

127. Samykutty, A., Grizzle, W.E., Fouts, B.L., McNally, M.W., Chuong, P., Thomas, A., Chiba, A., Otali, D., Woloszynska, A., Said, N., et al. (2018). Optoacoustic imaging identifies ovarian cancer using a microenvironment targeted theranostic wormhole mesoporous silica nanoparticle. Biomaterials *182*, 114-126.
128. Rimal, B., Greenberg, A.K., and Rom, W.N. (2005). Basic pathogenetic mechanisms in silicosis: current understanding. Current opinion in pulmonary medicine *11*, 169-173.
129. Mahmoud, A.M., Desouky, E.M., Hozayen, W.G., Bin-Jumah, M., El-Nahass, E.-S., Soliman, H.A., and Farghali, A.A. (2019). Mesoporous Silica Nanoparticles Trigger Liver and Kidney Injury and Fibrosis Via Altering TLR4/NF-κB, JAK2/STAT3 and Nrf2/HO-1 Signaling in Rats. Biomolecules *9*, 528.
130. Yu, Y., Li, Y., Wang, W., Jin, M., Du, Z., Li, Y., Duan, J., Yu, Y., and Sun, Z. (2013). Acute toxicity of amorphous silica nanoparticles in intravenously exposed ICR mice. PloS one *8*, e61346.
131. Waegeneers, N., Brasseur, A., Van Doren, E., Van der Heyden, S., Serreyn, P.-J., Pussemier, L., Mast, J., Schneider, Y.-J., Ruttens, A., and Roels, S. (2018). Short-term biodistribution and clearance of intravenously administered silica nanoparticles. Toxicology reports *5*, 632-638.
132. Tarn, D., Ashley, C.E., Xue, M., Carnes, E.C., Zink, J.I., and Brinker, C.J. (2013). Mesoporous silica nanoparticle nanocarriers: biofunctionality and biocompatibility. Accounts of chemical research *46*, 792-801.
133. Li, X., Xie, C., Xia, H., and Wang, Z. (2018). pH and ultrasound dual-responsive polydopamine-coated mesoporous silica nanoparticles for controlled drug delivery. Langmuir *34*, 9974-9981.
134. Li, Z., Zhang, Y., and Feng, N. (2019). Mesoporous silica nanoparticles: Synthesis, classification, drug loading, pharmacokinetics, biocompatibility, and application in drug delivery. Expert opinion on drug delivery *16*, 219-237.
135. Tian, Z., Yu, X., Ruan, Z., Zhu, M., Zhu, Y., and Hanagata, N. (2018). Magnetic mesoporous silica nanoparticles coated with thermo-responsive copolymer for potential chemo-and magnetic hyperthermia therapy. Microporous and Mesoporous Materials *256*, 1-9.
136. Amoozgar, Z., and Yeo, Y. (2012). Recent advances in stealth coating of nanoparticle drug delivery systems. Wiley Interdisciplinary Reviews: Nanomedicine and Nanobiotechnology *4*, 219-233.
137. He, X., Nie, H., Wang, K., Tan, W., Wu, X., and Zhang, P. (2008). In vivo study of biodistribution and urinary excretion of surface-modified silica nanoparticles. Analytical chemistry *80*, 9597-9603.
138. Cui, J., Björnmalm, M., Ju, Y., and Caruso, F. (2018). Nanoengineering of poly (ethylene glycol) particles for stealth and targeting. Langmuir *34*, 10817-10827.
139. Dai, Q., Bertleff-Zieschang, N., Braunger, J.A., Björnmalm, M., Cortez-Jugo, C., and Caruso, F. (2018). Particle targeting in complex biological media. Advanced healthcare materials *7*, 1700575.
140. Han, X., Li, Z., Sun, J., Luo, C., Li, L., Liu, Y., Du, Y., Qiu, S., Ai, X., and Wu, C. (2015). Stealth CD44-targeted hyaluronic acid supramolecular nanoassemblies for doxorubicin delivery: probing the effect of uncovalent pegylation degree on

cellular uptake and blood long circulation. Journal of Controlled Release *197*, 29-40.
141. Zhang, X.-D., Di Wu, X.S., Liu, P.-X., Yang, N., Zhao, B., Zhang, H., Sun, Y.-M., Zhang, L.-A., and Fan, F.-Y. (2011). Size-dependent in vivo toxicity of PEG-coated gold nanoparticles. International journal of nanomedicine *6*, 2071.
142. Cerdá, V.J., Pacheco, R.R., Witek, J.D., de la Calle, F.M.M., and de la Sen Fernández, M.L. (2019). Immediate hypersensitivity to polyethylene glycols in unrelated products: when standardization in the nomenclature of the components of drugs, cosmetics, and food becomes necessary. Allergy, Asthma & Clinical Immunology *15*, 1-5.
143. Laramie, M.D., Fouts, B.L., MacCuaig, W.M., Buabeng, E., Jones, M.A., Mukherjee, P., Behkam, B., McNally, L.R., and Henary, M. (2021). Improved pentamethine cyanine nanosensors for optoacoustic imaging of pancreatic cancer. Scientific reports *11*, 1-12.
144. Mohammed, M.A., Syeda, J., Wasan, K.M., and Wasan, E.K. (2017). An overview of chitosan nanoparticles and its application in non-parenteral drug delivery. Pharmaceutics *9*, 53.
145. Li, J., Cai, C., Li, J., Li, J., Li, J., Sun, T., Wang, L., Wu, H., and Yu, G. (2018). Chitosan-based nanomaterials for drug delivery. Molecules *23*, 2661.
146. Gerweck, L.E., and Seetharaman, K. (1996). Cellular pH gradient in tumor versus normal tissue: potential exploitation for the treatment of cancer. Cancer research *56*, 1194-1198.
147. Garg, U., Chauhan, S., Nagaich, U., and Jain, N. (2019). Current advances in chitosan nanoparticles based drug delivery and targeting. Advanced pharmaceutical bulletin *9*, 195.
148. Rizeq, B.R., Younes, N.N., Rasool, K., and Nasrallah, G.K. (2019). Synthesis, bioapplications, and toxicity evaluation of chitosan-based nanoparticles. International journal of molecular sciences *20*, 5776.
149. Zubareva, A., Shagdarova, B., Varlamov, V., Kashirina, E., and Svirshchevskaya, E. (2017). Penetration and toxicity of chitosan and its derivatives. European Polymer Journal *93*, 743-749.
150. Moghaddam, S.P.H., Mohammadpour, R., and Ghandehari, H. (2019). In vitro and in vivo evaluation of degradation, toxicity, biodistribution, and clearance of silica nanoparticles as a function of size, porosity, density, and composition. Journal of Controlled Release *311*, 1-15.
151. Bhavsar, D., Patel, V., and Sawant, K. (2019). Systematic investigation of in vitro and in vivo safety, toxicity and degradation of mesoporous silica nanoparticles synthesized using commercial sodium silicate. Microporous and Mesoporous Materials *284*, 343-352.
152. Ullman-Culleré, M.H., and Foltz, C.J. (1999). Body condition scoring: a rapid and accurate method for assessing health status in mice. Comparative Medicine *49*, 319-323.
153. Lehman, S.E., Morris, A.S., Mueller, P.S., Salem, A.K., Grassian, V.H., and Larsen, S.C. (2016). Silica nanoparticle-generated ROS as a predictor of cellular toxicity: mechanistic insights and safety by design. Environmental Science: Nano *3*, 56-66.

154. MacCuaig, W.M., Fouts, B.L., McNally, M.W., Grizzle, W.E., Chuong, P., Samykutty, A., Mukherjee, P., Li, M., Jasinski, J.B., and Behkam, B. (2021). Active Targeting Significantly Outperforms Nanoparticle Size in Facilitating Tumor-Specific Uptake in Orthotopic Pancreatic Cancer. ACS Applied Materials & Interfaces.
155. Qian, Q., Zhu, L., Zhu, X., Sun, M., and Yan, D. (2019). Drug-polymer hybrid macromolecular engineering: degradable PEG integrated by platinum (IV) for cancer therapy. Matter *1*, 1618-1630.
156. Andreani, T., de Souza, A.L.R., Kiill, C.P., Lorenzón, E.N., Fangueiro, J.F., Calpena, A.C., Chaud, M.V., Garcia, M.L., Gremião, M.P.D., and Silva, A.M. (2014). Preparation and characterization of PEG-coated silica nanoparticles for oral insulin delivery. International journal of pharmaceutics *473*, 627-635.
157. Xu, H., Yan, F., Monson, E.E., and Kopelman, R. (2003). Room-temperature preparation and characterization of poly (ethylene glycol)-coated silica nanoparticles for biomedical applications. Journal of Biomedical Materials Research Part A: An Official Journal of The Society for Biomaterials, The Japanese Society for Biomaterials, and The Australian Society for Biomaterials and the Korean Society for Biomaterials *66*, 870-879.
158. Berridge, B.R., Van Vleet, J.F., and Herman, E. (2013). Cardiac, vascular, and skeletal muscle systems. Haschek and Rousseaux's Handbook of Toxicologic Pathology, 1567-1665.
159. Babcock, M.B., and Cardell Jr, R.R. (1975). Fine structure of hepatocytes from fasted and fed rats. American Journal of Anatomy *143*, 399-437.
160. Babcock, M.B., and Cardell Jr, R.R. (1974). Hepatic glycogen patterns in fasted and fed rats. American Journal of Anatomy *140*, 299-337.
161. Bradley, A., Mukaratirwa, S., and Petersen-Jones, M. (2012). Incidences and range of spontaneous findings in the lymphoid and haemopoietic system of control Charles River CD-1 mice (Crl: CD-1 (ICR) BR) used in chronic toxicity studies. Toxicologic pathology *40*, 375-381.
162. Elangbam, C.S., Colman, K.A., Lightfoot, R.M., Tyler, R.D., and Wall, H.G. (2002). Endocardial Myxomatous Change in Harlan Sprague-Dawley Rats (Hsd: S—D) and CD-1 Mice: Its Microscopic Resemblance to Drug-Induced Valvulopathy in Humans. Toxicologic pathology *30*, 483-491.
163. Ruben, Z., Arceo, R., Bishop, S., Elwell, M., Kerns, W., Mesfin, G., Sandusky, G., and Van Vleet, J. (2000). Non-proliferative lesions of the heart and vasculature in rats. Guides for toxicologic pathology, 1-10.
164. Berridge, B.R., Mowat, V., Nagai, H., Nyska, A., Okazaki, Y., Clements, P.J., Rinke, M., Snyder, P.W., Boyle, M.C., and Wells, M.Y. (2016). Non-proliferative and proliferative lesions of the cardiovascular system of the rat and mouse. Journal of toxicologic pathology *29*, 1S-47S.
165. Vervloet, M.G., Sezer, S., Massy, Z.A., Johansson, L., Cozzolino, M., and Fouque, D. (2017). The role of phosphate in kidney disease. Nature Reviews Nephrology *13*, 27-38.
166. Webster, R., Elliott, V., Park, B.K., Walker, D., Hankin, M., and Taupin, P. (2009). PEG and PEG conjugates toxicity: towards an understanding of the toxicity of

PEG and its relevance to PEGylated biologicals. PEGylated protein drugs: Basic science and clinical applications, 127-146.
167. Choi, N., Lee, J., Chang, Y., Jung, S., Kim, Y., Lee, S., Lee, J., Kim, J., Song, H., and Park, B. (2013). Polyethylene glycol bowel preparation does not eliminate the risk of acute renal failure: a population-based case-crossover study. Endoscopy *45*, 208-213.
168. Malta, D., Petersen, K.S., Johnson, C., Trieu, K., Rae, S., Jefferson, K., Santos, J.A., Wong, M.M., Raj, T.S., and Webster, J. (2018). High sodium intake increases blood pressure and risk of kidney disease. From the Science of Salt: A regularly updated systematic review of salt and health outcomes (August 2016 to March 2017). The Journal of Clinical Hypertension *20*, 1654-1665.
169. Turecek, P.L., Bossard, M.J., Schoetens, F., and Ivens, I.A. (2016). PEGylation of biopharmaceuticals: a review of chemistry and nonclinical safety information of approved drugs. Journal of pharmaceutical sciences *105*, 460-475.
170. Ivens, I.A., Achanzar, W., Baumann, A., Brändli-Baiocco, A., Cavagnaro, J., Dempster, M., Depelchin, B.O., Irizarry Rovira, A.R., Dill-Morton, L., and Lane, J.H. (2015). PEGylated biopharmaceuticals: current experience and considerations for nonclinical development. Toxicologic pathology *43*, 959-983.
171. Chiu, H.-Y., Gößl, D.e., Haddick, L., Engelke, H., and Bein, T. (2018). Clickable multifunctional large-pore mesoporous silica nanoparticles as nanocarriers. Chemistry of Materials *30*, 644-654.
172. Wu, S.-H., Hung, Y., and Mou, C.-Y. (2011). Mesoporous silica nanoparticles as nanocarriers. Chemical Communications *47*, 9972-9985. 10.1039/C1CC11760B.
173. Huang, D.-M., Hung, Y., Ko, B.-S., Hsu, S.-C., Chen, W.-H., Chien, C.-L., Tsai, C.-P., Kuo, C.-T., Kang, J.-C., and Yang, C.-S.J.T.F.j. (2005). Highly efficient cellular labeling of mesoporous nanoparticles in human mesenchymal stem cells: implication for stem cell tracking. *19*, 2014-2016.
174. Song, Y., Li, Y., Xu, Q., and Liu, Z. (2017). Mesoporous silica nanoparticles for stimuli-responsive controlled drug delivery: advances, challenges, and outlook. International journal of nanomedicine *12*, 87.
175. How, K.N., Yap, W.H., Lim, C.L.H., Goh, B.H., and Lai, Z.W. (2020). Hyaluronic acid-mediated drug delivery system targeting for inflammatory skin diseases: A mini review. Frontiers in Pharmacology *11*, 1105.
176. Castillo, R.R., Lozano, D., González, B., Manzano, M., Izquierdo-Barba, I., and Vallet-Regí, M. (2019). Advances in mesoporous silica nanoparticles for targeted stimuli-responsive drug delivery: An update. Expert opinion on drug delivery *16*, 415-439.
177. Frickenstein, A.N., Hagood, J.M., Britten, C.N., Abbott, B.S., McNally, M.W., Vopat, C.A., Patterson, E.G., MacCuaig, W.M., Jain, A., and Walters, K.B. (2021). Mesoporous Silica Nanoparticles: Properties and Strategies for Enhancing Clinical Effect. Pharmaceutics *13*, 570.
178. Zhang, G., Li, X., Liao, Q., Liu, Y., Xi, K., Huang, W., and Jia, X. (2018). Water-dispersible PEG-curcumin/amine-functionalized covalent organic framework nanocomposites as smart carriers for in vivo drug delivery. Nature communications *9*, 1-11.

179. Reboredo, C., González-Navarro, C.J., Martínez-López, A.L., Martínez-Ohárriz, C., Sarmento, B., and Irache, J.M. (2021). Zein-Based Nanoparticles as Oral Carriers for Insulin Delivery. Pharmaceutics *14*, 39.
180. Poon, W., Kingston, B.R., Ouyang, B., Ngo, W., and Chan, W.C. (2020). A framework for designing delivery systems. Nature Nanotechnology, 1-11.
181. Sykes, E.A., Chen, J., Zheng, G., and Chan, W.C. (2014). Investigating the impact of nanoparticle size on active and passive tumor targeting efficiency. ACS nano *8*, 5696-5706.
182. Frieboes, H.B., Wu, M., Lowengrub, J., Decuzzi, P., and Cristini, V. (2013). A computational model for predicting nanoparticle accumulation in tumor vasculature. PloS one *8*, e56876.
183. Bertrand, N., Wu, J., Xu, X., Kamaly, N., and Farokhzad, O.C. (2014). Cancer nanotechnology: the impact of passive and active targeting in the era of modern cancer biology. Advanced drug delivery reviews *66*, 2-25.
184. Perry, J.L., Reuter, K.G., Luft, J.C., Pecot, C.V., Zamboni, W., and DeSimone, J.M. (2017). Mediating passive tumor accumulation through particle size, tumor type, and location. Nano letters *17*, 2879-2886.
185. Korangath, P., Barnett, J.D., Sharma, A., Henderson, E.T., Stewart, J., Yu, S.-H., Kandala, S.K., Yang, C.-T., Caserto, J.S., and Hedayati, M. (2020). Nanoparticle interactions with immune cells dominate tumor retention and induce T cell–mediated tumor suppression in models of breast cancer. Science Advances *6*, eaay1601.
186. Haubner, R., Wester, H.-J., Burkhart, F., Senekowitsch-Schmidtke, R., Weber, W., Goodman, S.L., Kessler, H., and Schwaiger, M. (2001). Glycosylated RGD-containing peptides: tracer for tumor targeting and angiogenesis imaging with improved biokinetics. Journal of Nuclear Medicine *42*, 326-336.
187. Gao, W., Xiang, B., Meng, T.-T., Liu, F., and Qi, X.-R. (2013). Chemotherapeutic drug delivery to cancer cells using a combination of folate targeting and tumor microenvironment-sensitive polypeptides. Biomaterials *34*, 4137-4149.
188. Du, W., and Elemento, O. (2015). Cancer systems biology: embracing complexity to develop better anticancer therapeutic strategies. Oncogene *34*, 3215-3225.
189. Kimbrough, C.W., Khanal, A., Zeiderman, M., Khanal, B.R., Burton, N.C., McMasters, K.M., Vickers, S.M., Grizzle, W.E., and McNally, L.R. (2015). Targeting acidity in pancreatic adenocarcinoma: multispectral optoacoustic tomography detects pH-low insertion peptide probes in vivo. Clinical cancer research *21*, 4576-4585.
190. Gillies, R.J., Verduzco, D., and Gatenby, R.A. (2012). Evolutionary dynamics of carcinogenesis and why targeted therapy does not work. Nature Reviews Cancer *12*, 487-493.
191. Weerakkody, D., Moshnikova, A., Thakur, M.S., Moshnikova, V., Daniels, J., Engelman, D.M., Andreev, O.A., and Reshetnyak, Y.K. (2013). Family of pH (low) insertion peptides for tumor targeting. Proceedings of the National Academy of Sciences *110*, 5834-5839.
192. Andreev, O.A., Engelman, D.M., and Reshetnyak, Y.K. (2014). Targeting diseased tissues by pHLIP insertion at low cell surface pH. Frontiers in physiology *5*, 97.

193. Andreev, O.A., Engelman, D.M., and Reshetnyak, Y.K. (2010). pH-sensitive membrane peptides (pHLIPs) as a novel class of delivery agents. Molecular membrane biology *27*, 341-352.
194. Reshetnyak, Y.K., Andreev, O.A., Segala, M., Markin, V.S., and Engelman, D.M. (2008). Energetics of peptide (pHLIP) binding to and folding across a lipid bilayer membrane. Proceedings of the National Academy of Sciences *105*, 15340-15345.
195. Singh, P., Szigyártó, I.C., Ricci, M., Zsila, F., Juhász, T., Mihály, J., Bősze, S., Bulyáki, É., Kardos, J., and Kitka, D. (2020). Membrane active peptides remove surface adsorbed protein corona from extracellular vesicles of red blood cells. Frontiers in chemistry *8*, 703.
196. Natte, K., Friedrich, J.F., Wohlrab, S., Lutzki, J., von Klitzing, R., Österle, W., and Orts-Gil, G. (2013). Impact of polymer shell on the formation and time evolution of nanoparticle–protein corona. Colloids and Surfaces B: Biointerfaces *104*, 213-220.
197. Xiao, W., and Gao, H. (2018). The impact of protein corona on the behavior and targeting capability of nanoparticle-based delivery system. International Journal of Pharmaceutics *552*, 328-339.
198. Blanco, E., Shen, H., and Ferrari, M. (2015). Principles of nanoparticle design for overcoming biological barriers to drug delivery. Nature biotechnology *33*, 941.
199. Oh, N., and Park, J.-H. (2014). Endocytosis and exocytosis of nanoparticles in mammalian cells. International journal of nanomedicine *9*, 51.
200. Cabral, H., Matsumoto, Y., Mizuno, K., Chen, Q., Murakami, M., Kimura, M., Terada, Y., Kano, M., Miyazono, K., and Uesaka, M. (2011). Accumulation of sub-100 nm polymeric micelles in poorly permeable tumours depends on size. Nature nanotechnology *6*, 815.
201. Bharti, C., Nagaich, U., Pal, A.K., and Gulati, N. (2015). Mesoporous silica nanoparticles in target drug delivery system: A review. International journal of pharmaceutical investigation *5*, 124.
202. Narayan, R., Nayak, U.Y., Raichur, A.M., and Garg, S. (2018). Mesoporous silica nanoparticles: A comprehensive review on synthesis and recent advances. Pharmaceutics *10*, 118.
203. Wu, Y., Cain-Hom, C., Choy, L., Hagenbeek, T.J., de Leon, G.P., Chen, Y., Finkle, D., Venook, R., Wu, X., and Ridgway, J. (2010). Therapeutic antibody targeting of individual Notch receptors. Nature *464*, 1052-1057.
204. Wang, T., Chai, F., Fu, Q., Zhang, L., Liu, H., Li, L., Liao, Y., Su, Z., Wang, C., and Duan, B. (2011). Uniform hollow mesoporous silica nanocages for drug delivery in vitro and in vivo for liver cancer therapy. Journal of Materials Chemistry *21*, 5299-5306.
205. Gary-Bobo, M., Mir, Y., Rouxel, C., Brevet, D., Basile, I., Maynadier, M., Vaillant, O., Mongin, O., Blanchard-Desce, M., and Morère, A. (2011). Mannose-functionalized mesoporous silica nanoparticles for efficient two-photon photodynamic therapy of solid tumors. Angewandte Chemie International Edition *50*, 11425-11429.
206. Shen, S.-C., Ng, W.K., Shi, Z., Chia, L., Neoh, K.G., and Tan, R.B.H. (2011). Mesoporous silica nanoparticle-functionalized poly (methyl methacrylate)-based

bone cement for effective antibiotics delivery. Journal of Materials Science: Materials in Medicine *22*, 2283.
207. Shang, L., Nienhaus, K., and Nienhaus, G.U. (2014). Engineered nanoparticles interacting with cells: size matters. Journal of nanobiotechnology *12*, 5.
208. Daum, N., Tscheka, C., Neumeyer, A., and Schneider, M. (2012). Novel approaches for drug delivery systems in nanomedicine: effects of particle design and shape. Wiley Interdisciplinary Reviews: Nanomedicine and Nanobiotechnology *4*, 52-65.
209. Yanes, R.E., and Tamanoi, F. (2012). Development of mesoporous silica nanomaterials as a vehicle for anticancer drug delivery. Therapeutic delivery *3*, 389-404.
210. Moreira, A.F., Dias, D.R., and Correia, I.J. (2016). Stimuli-responsive mesoporous silica nanoparticles for cancer therapy: A review. Microporous and Mesoporous Materials *236*, 141-157.
211. Mamaeva, V., Sahlgren, C., and Lindén, M. (2013). Mesoporous silica nanoparticles in medicine—Recent advances. Advanced drug delivery reviews *65*, 689-702.
212. Wen, J., Yang, K., Liu, F., Li, H., Xu, Y., and Sun, S. (2017). Diverse gatekeepers for mesoporous silica nanoparticle based drug delivery systems. Chemical Society Reviews *46*, 6024-6045.
213. Kaasalainen, M., Aseyev, V., von Haartman, E., Karaman, D.Ş., Mäkilä, E., Tenhu, H., Rosenholm, J., and Salonen, J. (2017). Size, stability, and porosity of mesoporous nanoparticles characterized with light scattering. Nanoscale research letters *12*, 74.
214. Christian, D.A., Cai, S., Garbuzenko, O.B., Harada, T., Zajac, A.L., Minko, T., and Discher, D.E. (2009). Flexible filaments for in vivo imaging and delivery: persistent circulation of filomicelles opens the dosage window for sustained tumor shrinkage. Molecular pharmaceutics *6*, 1343-1352.
215. Bhutiani, N., Samykutty, A., McMasters, K.M., Egilmez, N.K., and McNally, L.R. (2019). In vivo tracking of orally-administered particles within the gastrointestinal tract of murine models using multispectral optoacoustic tomography. Photoacoustics *13*, 46-52.
216. Kalyane, D., Raval, N., Maheshwari, R., Tambe, V., Kalia, K., and Tekade, R.K. (2019). Employment of enhanced permeability and retention effect (EPR): Nanoparticle-based precision tools for targeting of therapeutic and diagnostic agent in cancer. Materials Science and Engineering: C.
217. Kimbrough, C.W., Hudson, S., Khanal, A., Egger, M.E., and McNally, L.R. (2015). Orthotopic pancreatic tumors detected by optoacoustic tomography using Syndecan-1. Journal of surgical research *193*, 246-254.
218. Tallury, P., Payton, K., and Santra, S. (2008). Silica-based multimodal/multifunctional nanoparticles for bioimaging and biosensing applications. *3*, 579-592. 10.2217/17435889.3.4.579.
219. Lutzweiler, C., Meier, R., Rummeny, E., Ntziachristos, V., and Razansky, D. (2014). Real-time optoacoustic tomography of indocyanine green perfusion and oxygenation parameters in human finger vasculature. Optics letters *39*, 4061-4064.

220. Lu, F., Wu, S.H., Hung, Y., and Mou, C.Y. (2009). Size effect on cell uptake in well-suspended, uniform mesoporous silica nanoparticles. small *5*, 1408-1413.
221. Chauhan, V.P., Stylianopoulos, T., Martin, J.D., Popović, Z., Chen, O., Kamoun, W.S., Bawendi, M.G., Fukumura, D., and Jain, R.K. (2012). Normalization of tumour blood vessels improves the delivery of nanomedicines in a size-dependent manner. Nature nanotechnology *7*, 383.
222. Sadauskas, E., Wallin, H., Stoltenberg, M., Vogel, U., Doering, P., Larsen, A., and Danscher, G. (2007). Kupffer cells are central in the removal of nanoparticles from the organism. Particle and fibre toxicology *4*, 10.
223. Chan, K.W.-Y., and Wong, W.-T. (2007). Small molecular gadolinium (III) complexes as MRI contrast agents for diagnostic imaging. Coordination Chemistry Reviews *251*, 2428-2451.
224. Takakura, Y., Mahato, R.I., and Hashida, M. (1998). Extravasation of macromolecules. Advanced drug delivery reviews *34*, 93-108.
225. Gaumet, M., Vargas, A., Gurny, R., and Delie, F. (2008). Nanoparticles for drug delivery: the need for precision in reporting particle size parameters. European journal of pharmaceutics and biopharmaceutics *69*, 1-9.
226. Morscher, S., Driessen, W.H., Claussen, J., and Burton, N.C. (2014). Semi-quantitative Multispectral Optoacoustic Tomography (MSOT) for volumetric PK imaging of gastric emptying. Photoacoustics *2*, 103-110.
227. Xiao, T.G., Weis, J.A., Gayzik, F.S., Thomas, A., Chiba, A., Gurcan, M.N., Topaloglu, U., Samykutty, A., and McNally, L.R. (2018). Applying dynamic contrast enhanced MSOT imaging to intratumoral pharmacokinetic modeling. Photoacoustics *11*, 28-35.
228. Yamada, H., Urata, C., Aoyama, Y., Osada, S., Yamauchi, Y., and Kuroda, K. (2012). Preparation of colloidal mesoporous silica nanoparticles with different diameters and their unique degradation behavior in static aqueous systems. Chemistry of Materials *24*, 1462-1471.
229. Urata, C., Aoyama, Y., Tonegawa, A., Yamauchi, Y., and Kuroda, K.J.C.C. (2009). Dialysis process for the removal of surfactants to form colloidal mesoporous silica nanoparticles. 5094-5096.
230. Kobayashi, M., Juillerat, F., Galletto, P., Bowen, P., and Borkovec, M. (2005). Aggregation and charging of colloidal silica particles: effect of particle size. Langmuir *21*, 5761-5769.
231. Swietach, P., Vaughan-Jones, R.D., and Harris, A.L. (2007). Regulation of tumor pH and the role of carbonic anhydrase 9. Cancer and Metastasis Reviews *26*, 299-310.
232. Cruz-Monserrate, Z., Roland, C.L., Deng, D., Arumugam, T., Moshnikova, A., Andreev, O.A., Reshetnyak, Y.K., and Logsdon, C.D. (2014). Targeting pancreatic ductal adenocarcinoma acidic microenvironment. Scientific reports *4*, 4410.
233. Zhang, X., Lin, Y., and Gillies, R.J. (2010). Tumor pH and its measurement. Journal of Nuclear Medicine *51*, 1167-1170.
234. Andreev, O.A., Dupuy, A.D., Segala, M., Sandugu, S., Serra, D.A., Chichester, C.O., Engelman, D.M., and Reshetnyak, Y.K. (2007). Mechanism and uses of a membrane peptide that targets tumors and other acidic tissues in vivo. Proceedings of the National Academy of Sciences *104*, 7893-7898.

235. Yin, W., Kimbrough, C.W., Gomez-Gutierrez, J.G., Burns, C.T., Chuong, P., Grizzle, W.E., and McNally, L.R. (2015). Tumor specific liposomes improve detection of pancreatic adenocarcinoma in vivo using optoacoustic tomography. Journal of nanobiotechnology *13*, 90.
236. Ernsting, M.J., Murakami, M., Roy, A., and Li, S.-D. (2013). Factors controlling the pharmacokinetics, biodistribution and intratumoral penetration of nanoparticles. Journal of controlled release *172*, 782-794.
237. Li, S.-D., and Huang, L. (2008). Pharmacokinetics and biodistribution of nanoparticles. Molecular pharmaceutics *5*, 496-504.
238. Ouyang, B., Poon, W., Zhang, Y.-N., Lin, Z.P., Kingston, B.R., Tavares, A.J., Zhang, Y., Chen, J., Valic, M.S., and Syed, A.M. (2020). The dose threshold for nanoparticle tumour delivery. Nature Materials, 1-10.
239. Torchilin, V. (2011). Tumor delivery of macromolecular drugs based on the EPR effect. Advanced Drug Delivery Reviews *63*, 131-135. https://doi.org/10.1016/j.addr.2010.03.011.
240. Baxter, L.T., and Jain, R.K. (1989). Transport of fluid and macromolecules in tumors. I. Role of interstitial pressure and convection. Microvascular research *37*, 77-104.
241. Longmire, M., Choyke, P.L., and Kobayashi, H. (2008). Clearance properties of nano-sized particles and molecules as imaging agents: considerations and caveats.
242. Gachoka, D. (2015). Polyethylene glycol (PEG)-induced anaphylactic reaction during bowel preparation. ACG Case Reports Journal *2*, 216.
243. Wylon, K., Dölle, S., and Worm, M. (2016). Polyethylene glycol as a cause of anaphylaxis. Allergy, Asthma & Clinical Immunology *12*, 67.
244. Hatakeyama, H., Akita, H., and Harashima, H. (2011). A multifunctional envelope type nano device (MEND) for gene delivery to tumours based on the EPR effect: a strategy for overcoming the PEG dilemma. Advanced drug delivery reviews *63*, 152-160.
245. Almalik, A., Benabdelkamel, H., Masood, A., Alanazi, I.O., Alradwan, I., Majrashi, M.A., Alfadda, A.A., Alghamdi, W.M., Alrabiah, H., and Tirelli, N. (2017). Hyaluronic acid coated chitosan nanoparticles reduced the immunogenicity of the formed protein corona. Scientific reports *7*, 1-9.
246. Sloan-Dennison, S., Bevins, M.R., Scarpitti, B.T., Sauvé, V.K., and Schultz, Z.D. (2019). Protein corona-resistant SERS tags for live cell detection of integrin receptors. Analyst *144*, 5538-5546.
247. Lynch, I., and Dawson, K.A. (2008). Protein-nanoparticle interactions. Nano today *3*, 40-47.
248. Liu, J., Yu, M., Ning, X., Zhou, C., Yang, S., and Zheng, J.J.A.C.I.E. (2013). PEGylation and zwitterionization: pros and cons in the renal clearance and tumor targeting of near-IR-emitting gold nanoparticles. *52*, 12572-12576.

Appendix A – Abbreviations:

Chapter 1:

NIR-near infrared, US-ultrasound, MSOT-multispectral optoacoustic tomography, ICG-indocyanine green.

Chapter 2:

MSOT-multispectral optoacoustic tomography, ICG-indocyanine green, MB-methylene blue, HPLC-high performance liquid chromatography, UV-ultraviolet, VIS-visible light, NIR-near infrared, NMR-nuclear magnetic resonance, HRMS-high resolution mass spectroscopy, DFT-density functional theory, TD-DFT-time dependent density functional theory, PBE-Perdew/Burke/Ernzerhof, HUVEC-human umbilical vein endothelial cells, DMEM-Dulbecco's modified eagle medium, FBS- fetal bovine serum, PBS-phosphate buffer saline, AMI-advanced molecular imager, H&E-hematoxylin and eosin, ANOVA-analysis of variance, Br-bromine, Cl-chlorine, F-fluorine, H-hydrogen, TMAB-trimethylpropylammonium, SQ-squaraine, HOMO-highest occupied molecular orbital, LUMO-lowest unoccupied molecular orbital, CY-cyanine.

Chapter 3:

ICG-indocyanine green, HC-hemicyanine, NIR-near infrared, ICT-intramolecular charge transfer, TICT-twisted intramolecular charge transfer, TGS-twisted ground state, HPLC-high performance liquid chromatography, NMR-nuclear magnetic resonance, TMS-tetramethylsilane, UV-ultraviolet, VIS-visible light, HUVEC-human umbilical vein endothelial cells, DMEM-Dulbecco's modified eagle medium, FBS- fetal bovine serum, AMI-advanced molecular imager, H&E-hematoxylin and eosin, ANOVA-analysis of variance, MSOT-multispectral optoacoustic tomography.

Chapter 4:

MSN-mesoporous silica nanoparticle, MRI-magnetic resonance imaging, PEG-polyethylene glycol, CTAB-cetyltrimethylammonium bromide, 2KPEG-2000Molecular weight PEG, 35KPEG-35000Molecular weight PEG, GPTMS-glycidyloxypropyltrimethoxysilane, TMOS-trimethyl orthosilicate, TEA-triethanolamine, DMEM-Dulbecco's modified eagle medium, FBS-fetal bovine serum, PDI-polydispersity index, DLS-dynamic light scattering, MADLS-multi angle dynamic light scattering, BET-Brunauer-Emmett-Teller, BJH-Barrett-Joyner-Halenda, C-MSN-chitosan coated-MSN, CBC-complete blood count, BC-blood chemistry, H&E-hematoxylin and eosin, EDTA-ethylenediaminetetraacetic acid, LH-lithium heparin, ANOVA-analysis of variance, ALB-albumin, ALP-alkaline phosphatase, ALT-alanine transaminase, AMY-amylase, TBIL-total bilirubin, BUN-blood urea nitrogen, CA-calcium, PHOS-phosphorus, CRE-creatinine, GLU-glucose, NA+-sodium, K+-potassium, TP-total protein, GLOB-globulin, RBC-red

blood cell, HGB-hemoglobin, HCT-hematocrit, MCV-mean corpuscular volume, MCH-mean corpuscular hemoglobin, MCHC-mean corpuscular hemoglobin concentration, RDW-red cell distribution width, RET-reticulocyte, PLT-platelets, PDW-platelet distribution width, MPV-mean platelet volume, P-LCR-platelet/large cell ratio, PCT-procalcitonin, WBC-white blood cell, NEUT-neutrophils, LYMPH-lymphocytes, MONO-monocytes, EO-eosinophils, BASO-basophils.

Chapter 5:

SMCC-succinimidyl 4-n-maleimidomethylcyclohexane-1-carboxylate, PEG-polyethylene glycol, EPR-enhanced permeability and retention, MSN-mesoporous silica nanoparticle, MSOT-multispectral optoacoustic tomography, NIR-near infrared, PET-positron emission tomography, MRI-magnetic resonance imaging, ICG-indocyanine green, TMOS-trimethyl orthosilicate, TEOS-triethyl orthosilicate, TPOS-tripropyl orthosilicate, CTAB-cetyltrimethylammonium bromide, GPTMS-glycidyloxypropyltrimethoxysilane, TEA-triethanolamine, PI-propidium iodide, PDAC-pancreatic ductal adenocarcinoma, DMEM-Dulbecco's modified eagle medium, FBS-fetal bovine serum, DLS-dynamic light scattering, PDI-polydispersity index, MADLS-multi angle dynamic light scattering, BET-Brunauer-Emmett-Teller, BJH-Barrett-Joyner-Halenda, TEM-transmission electron microscopy, ATPES-3-aminopropyltriethoxysilane, UV-ultraviolet, VIS-visible light, OD-optical density, pHLIP-pH low insertion peptide, ATP-adenosine triphosphate, PBS-phosphate buffered saline, ROI-region of interest, IV-intravenous, AMI-advanced molecular imager, H&E-hematoxylin and eosin, ANOVA- analysis of variance.

Chapter 6:

NIR-near infrared, MSOT-multispectral optoacoustic tomography, MSN-mesoporous silica nanoparticle, PEG-polyethylene glycol

Appendix B – Supporting Information:

Chapter 1:

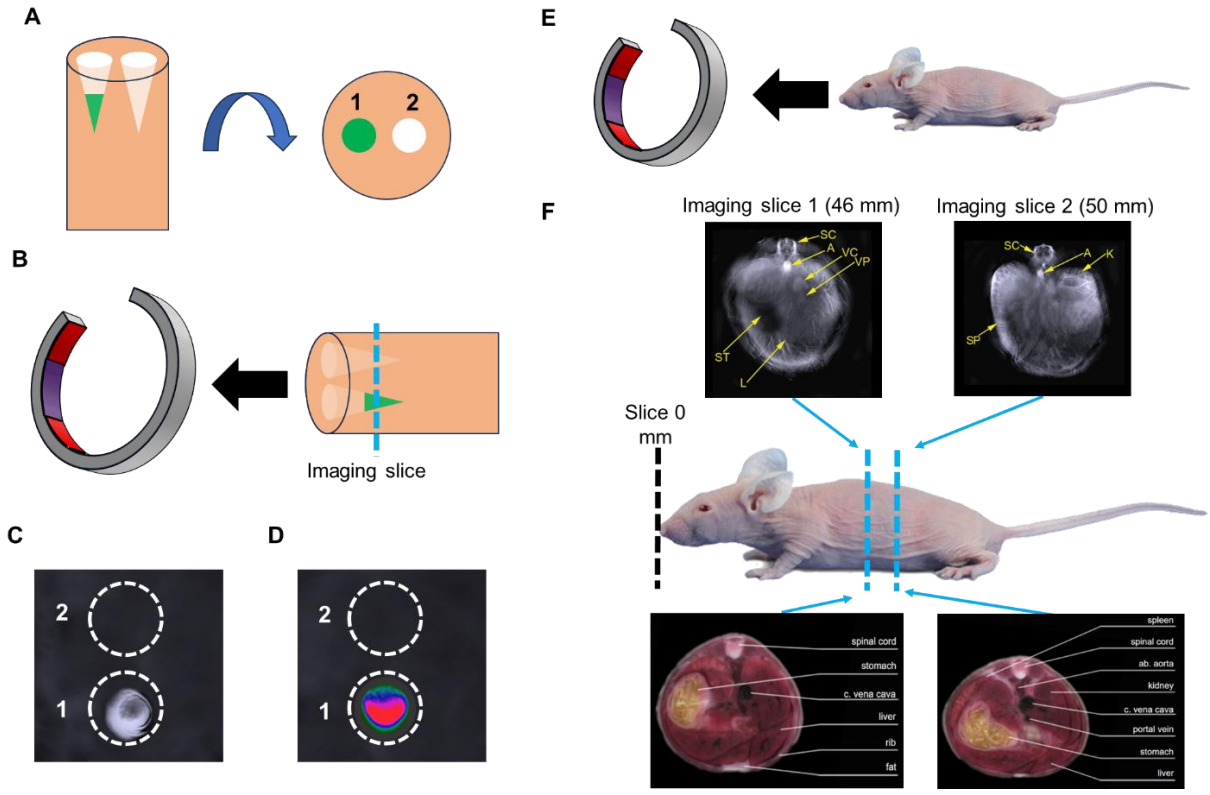

Figure S1.1: Optoacoustic imaging setups for *in vitro* (A-D) and *in vivo* (E-F) evaluation. A) Loading of contrast agent (1: green) within cylindrical opening of an agar-based tissue mimicking phantom from a frontal perspective (left) and a top-down perspective (right). A second cylindrical well is prepared and used as a blank (2: white). B) Encapsulation of contrast agent, rotation of phantom, and insertion into imaging setup perpendicular to system. C) Reconstructed optoacoustic image of sample at imaging slice shown in B. D) Spectrally unmixed optoacoustic agent of sample at imaging slice shown in B. E) Perspective of a mouse prior to optoacoustic evaluation. F) Insertion of a mouse into the imaging system with two imaging slices shown. Top images show optoacoustic images acquired at corresponding imaging slices. Bottom images show cross sections of mouse anatomy in color corresponding to imaging slices for reference. The following structures are labeled: spinal cord (SC); aorta (A); vena cava (VC); vena porta (VP); liver (L); stomach (ST); kidney (K); spleen (SP). Panels F and G are adapted from reference 6.

Chapter 2:

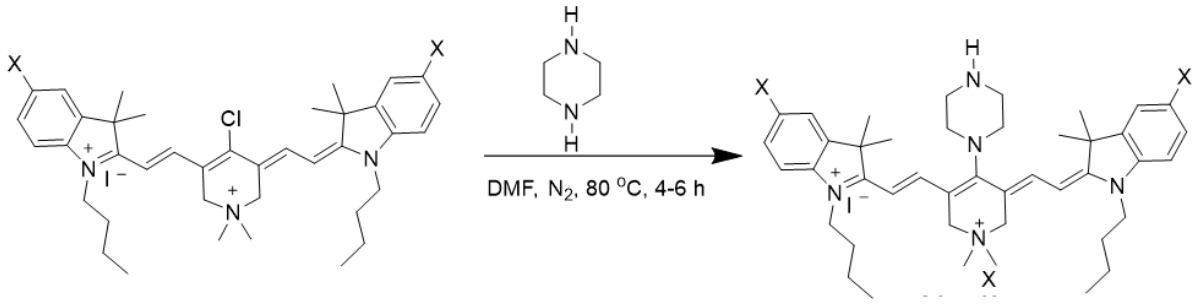

Molecule	X
CY H	H
CY Cl	Cl
CY Br	Br

Figure S2.1: Synthetic step for cyanine optoacoustic probes.

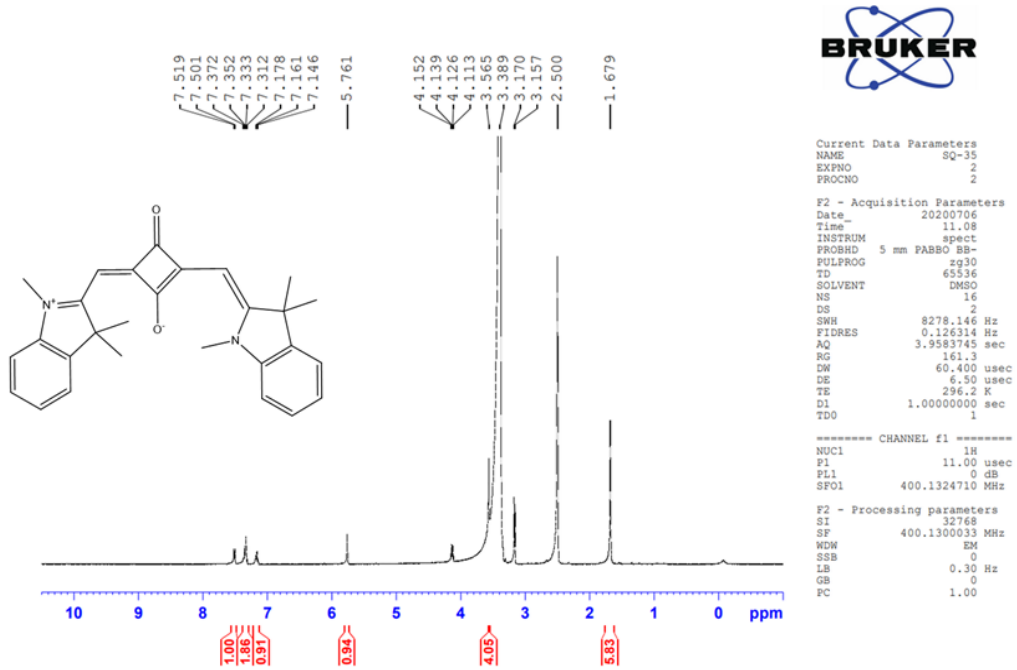

Figure S2.2: ^{1}H NMR spectrum of **SQ H no TMAB**.

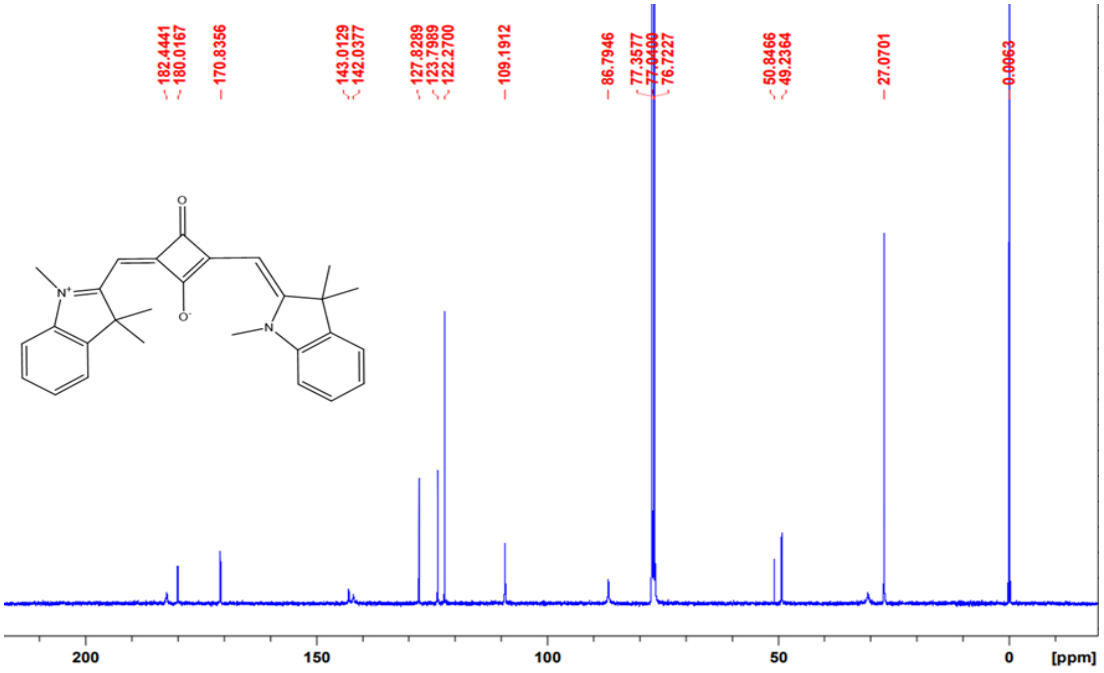

Figure S2.3: ^{13}C NMR spectrum of **SQ H no TMAB**.

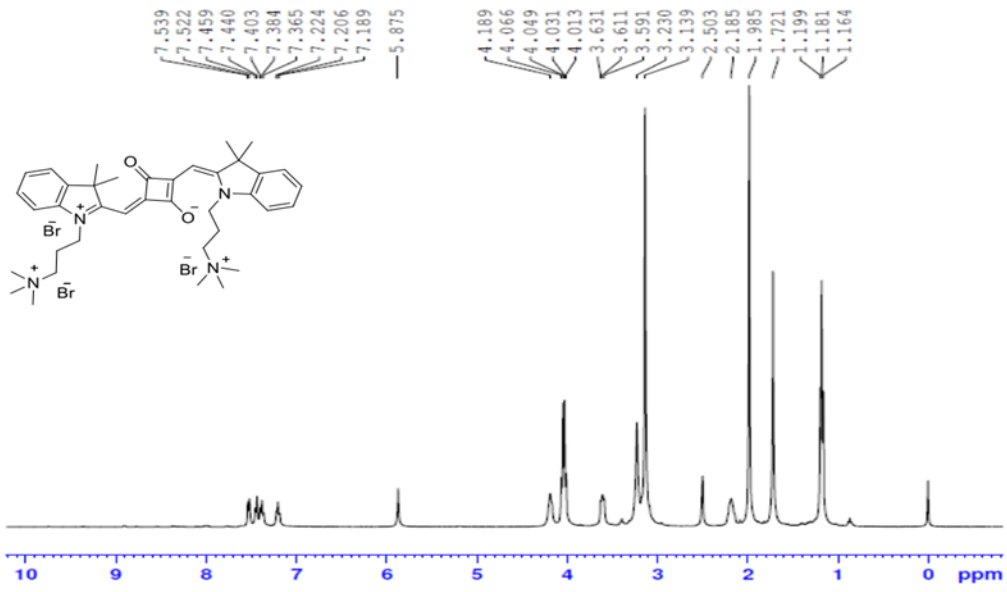

Figure S2.4: ^{1}H NMR spectrum of **SQ H**.

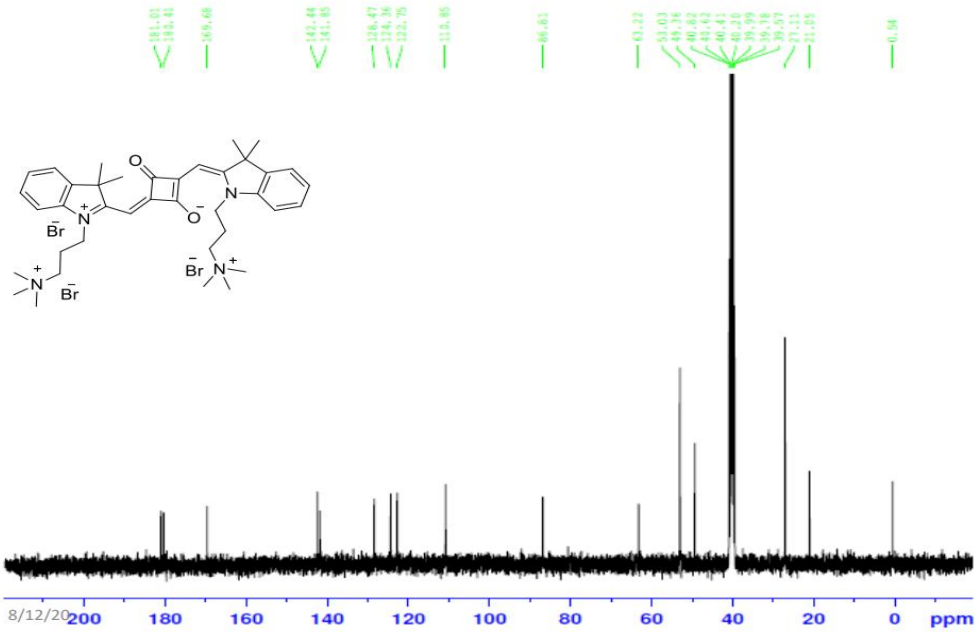

Figure S2.5: ^{13}C NMR spectrum of **SQ H**.

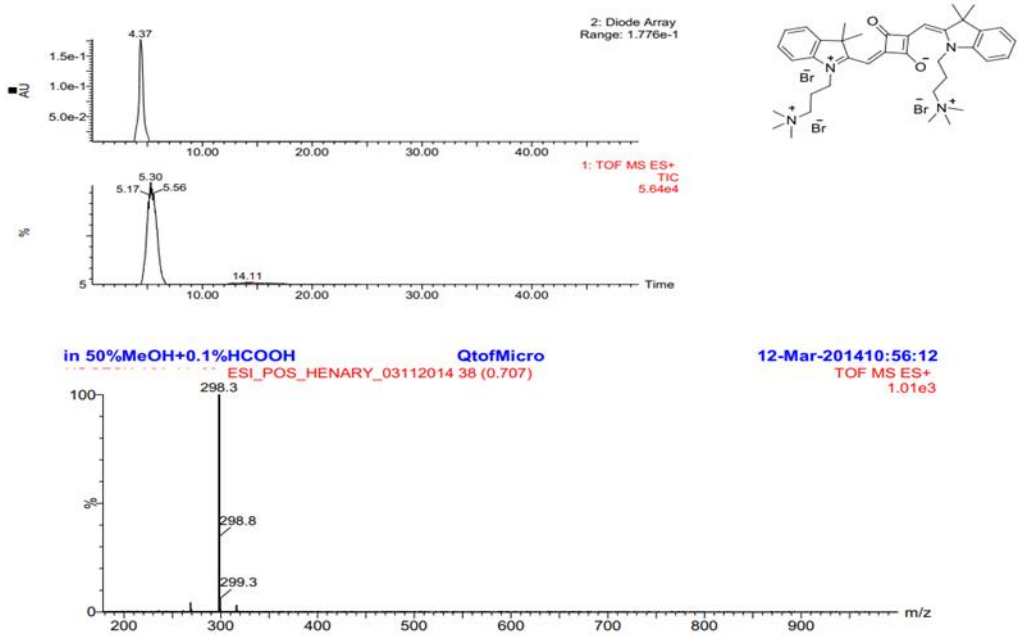

Figure S2.6: Mass spectrum of **SQ H**.

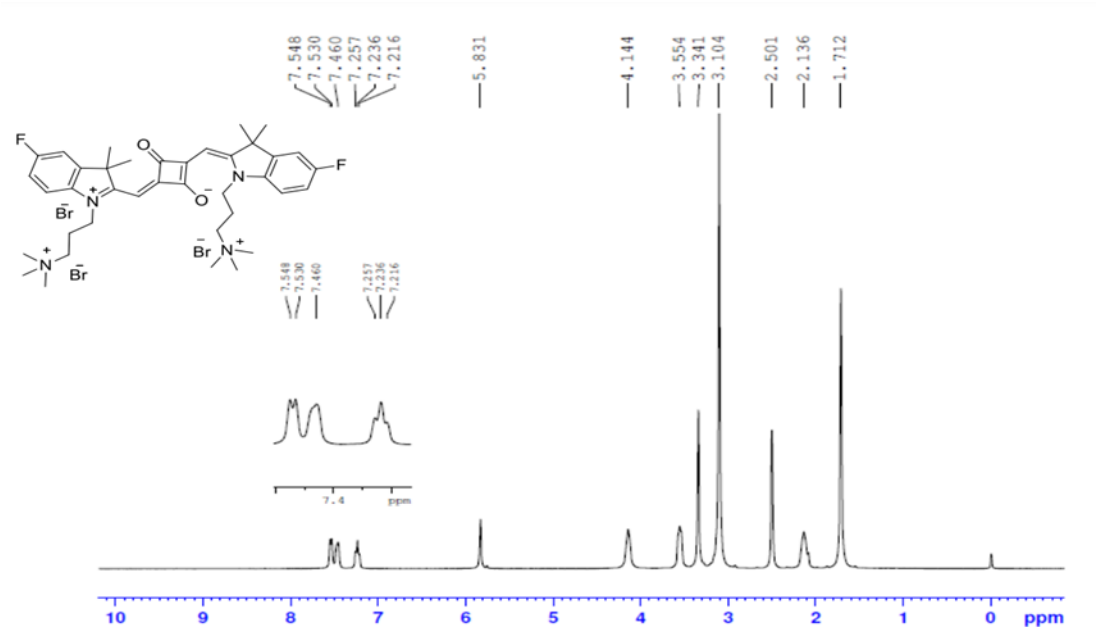

Figure S2.7: ^{1}H NMR spectrum of **SQ F**.

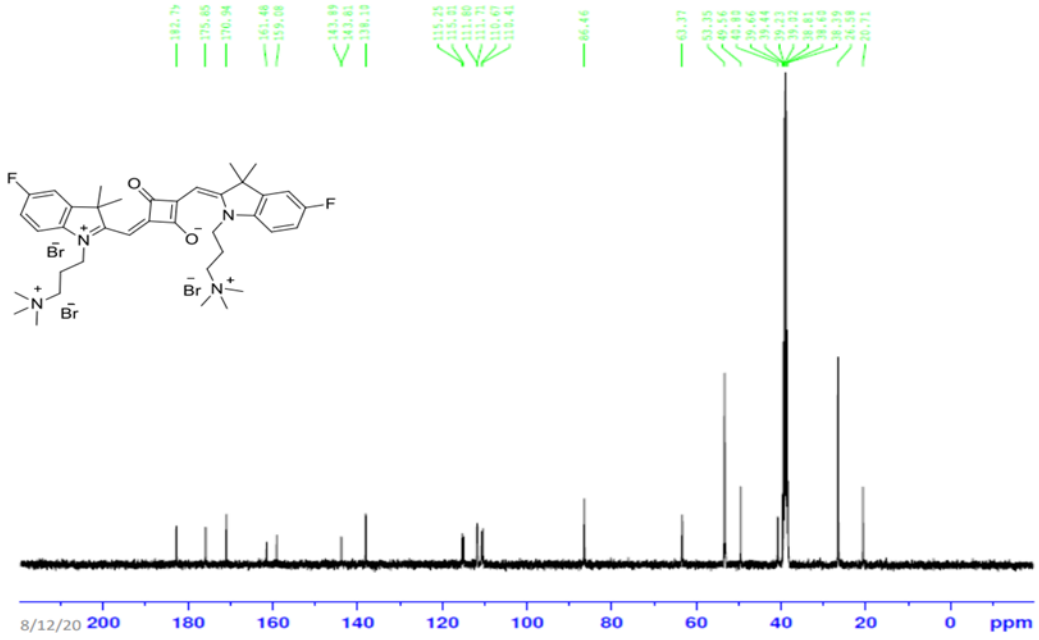

Figure S2.8: ^{13}C NMR spectrum of **SQ F**.

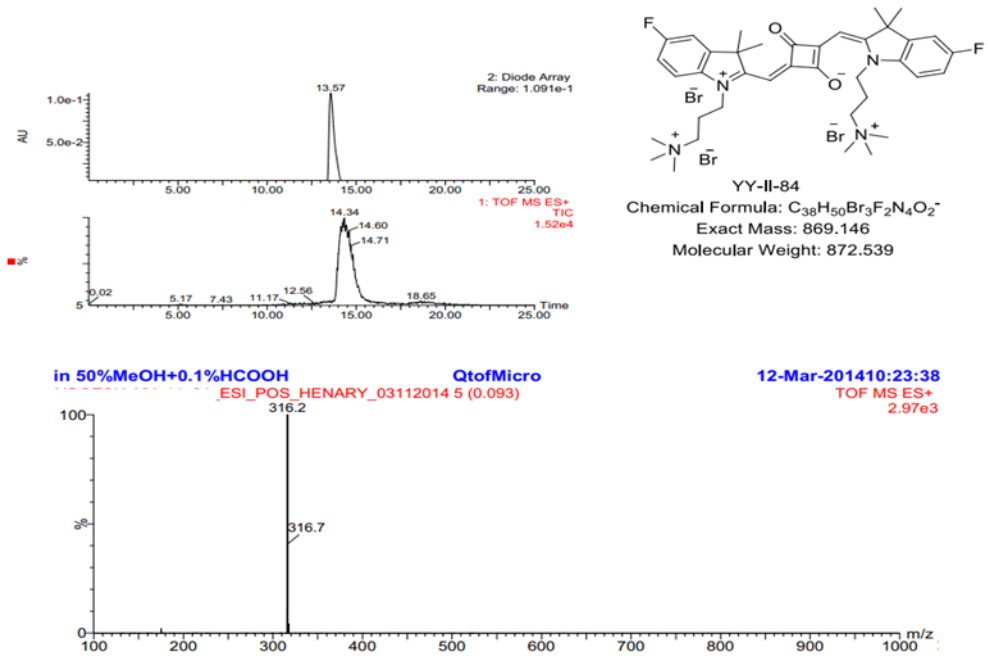

Figure S2.9: Mass spectrum of **SQ F**.

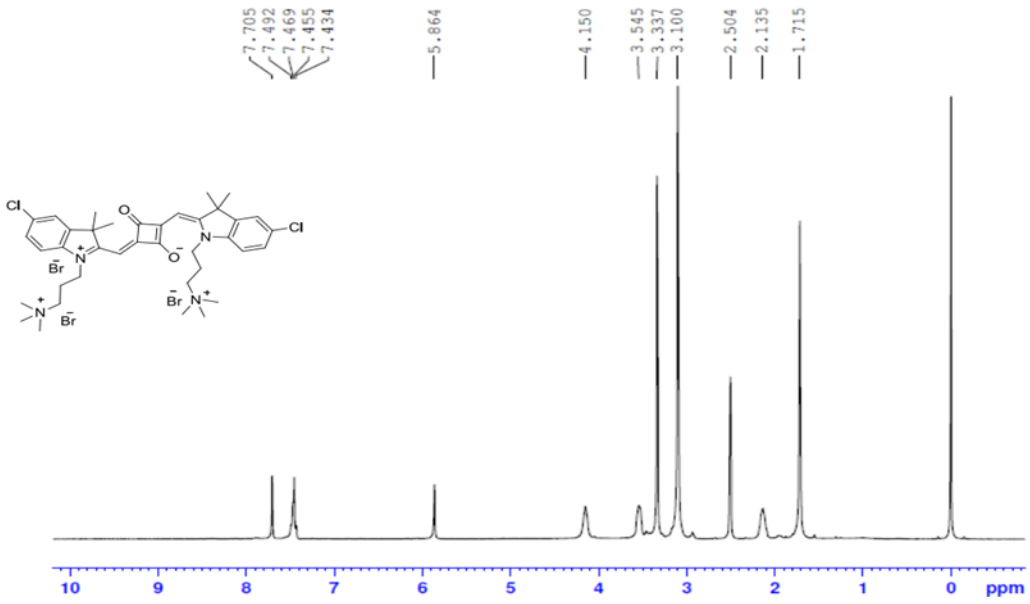

Figure S2.10: ^{1}H NMR spectrum of **SQ Cl**.

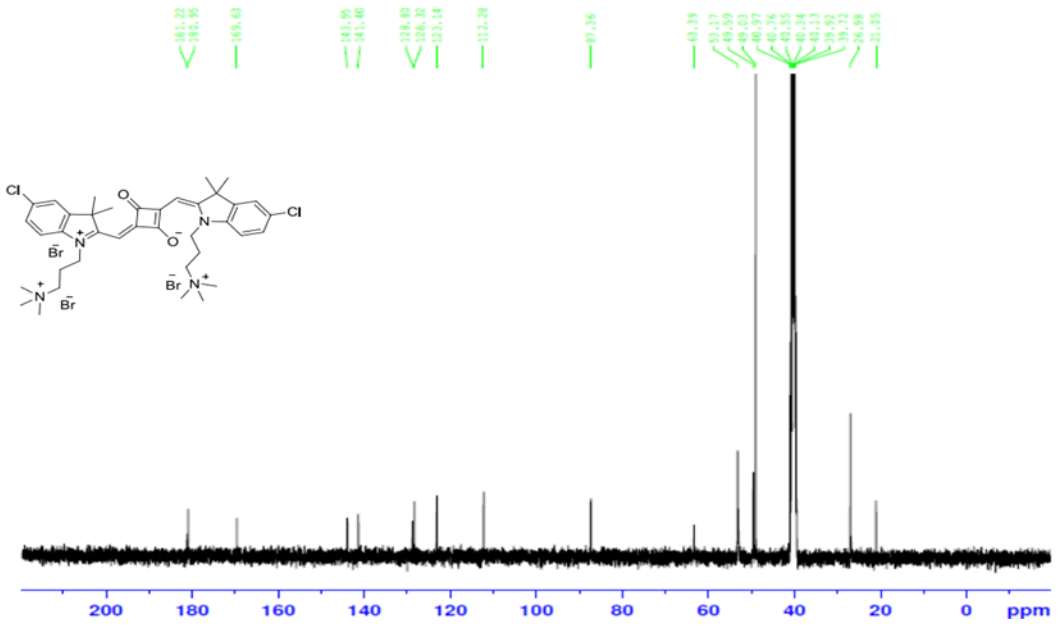

Figure S2.11: ^{13}C NMR spectrum of **SQ Cl**.

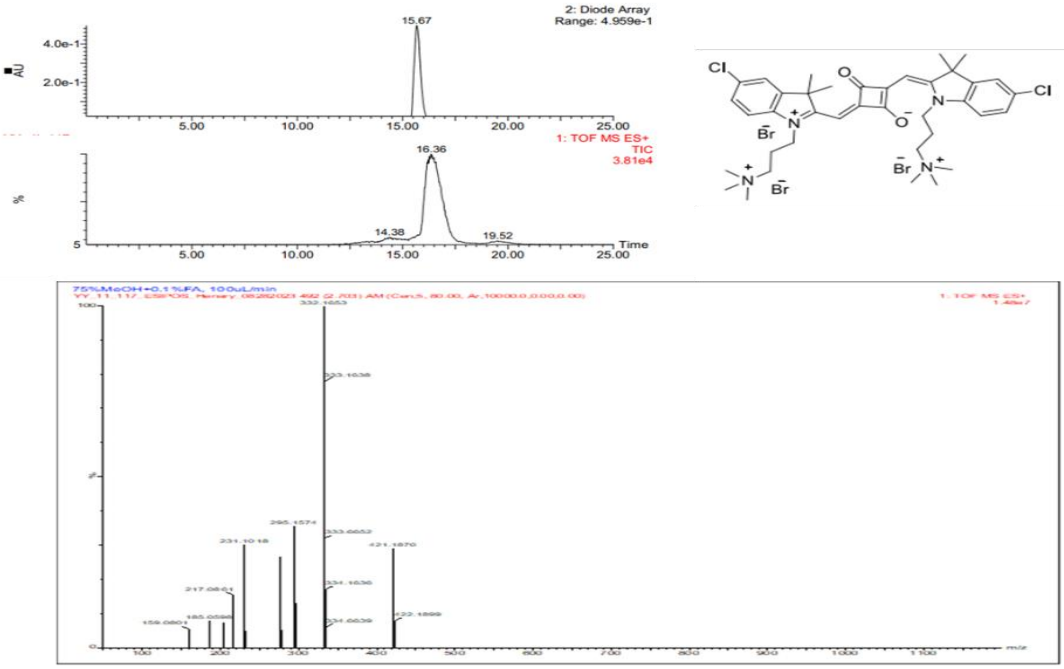

Figure S2.12: Mass spectrum of **SQ Cl**.

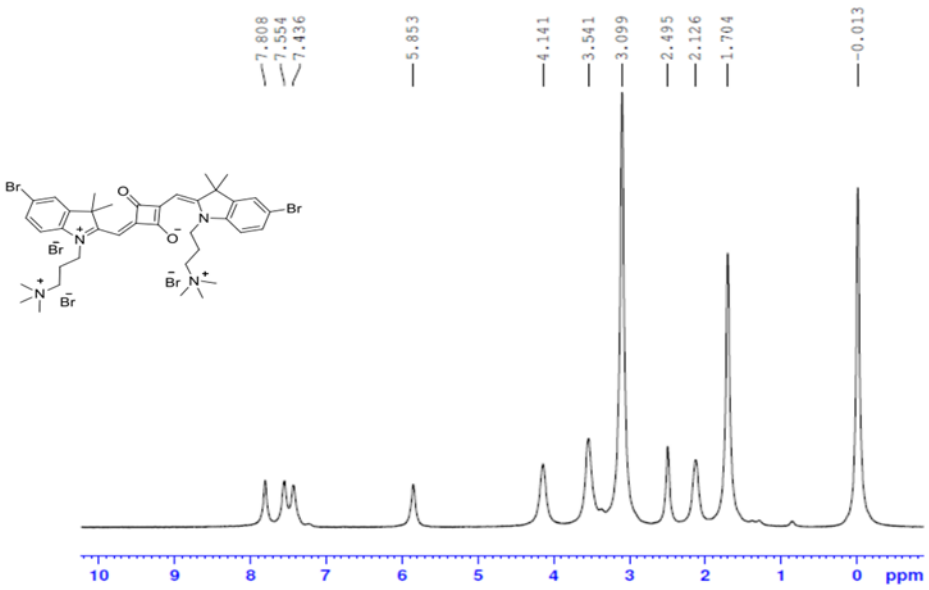

Figure S2.13: ^{1}H NMR spectrum of **SQ Br**.

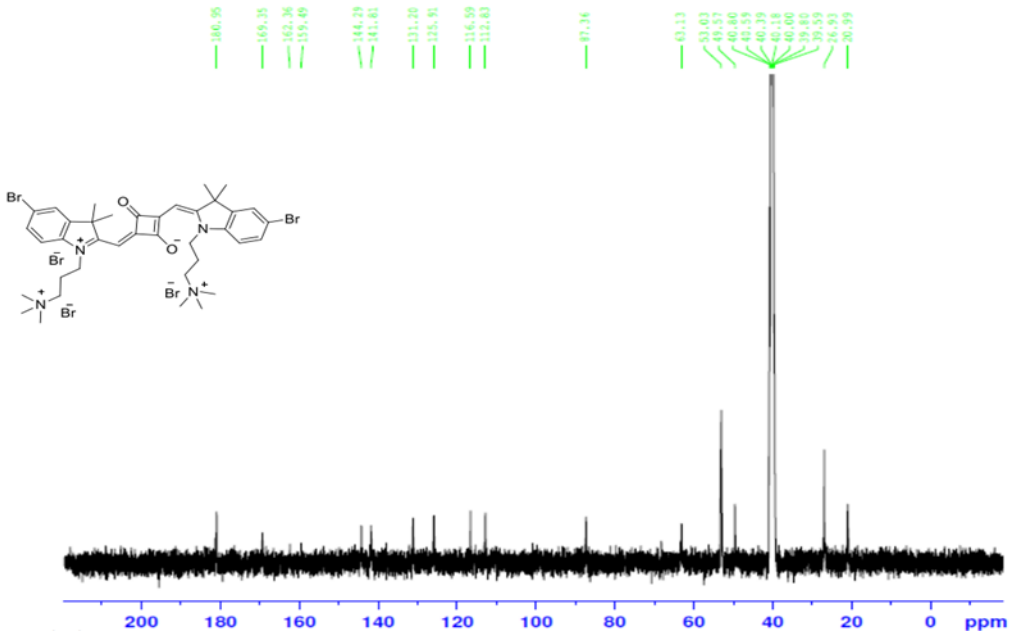

Figure S2.14: ^{13}C NMR spectrum of **SQ Br**.

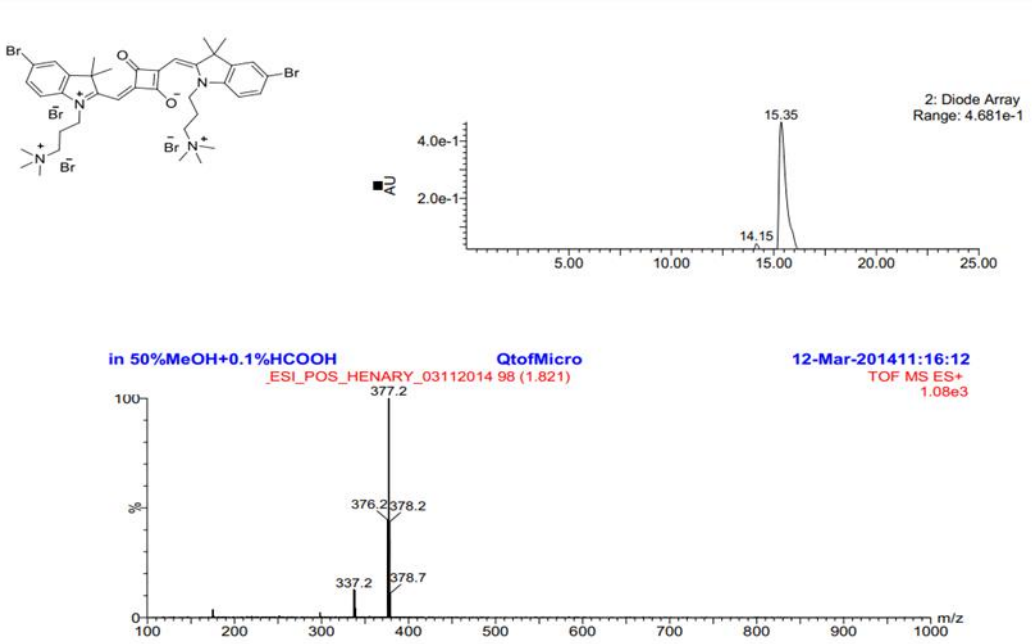

Figure S2.15: Mass spectrum of **SQ Br**.

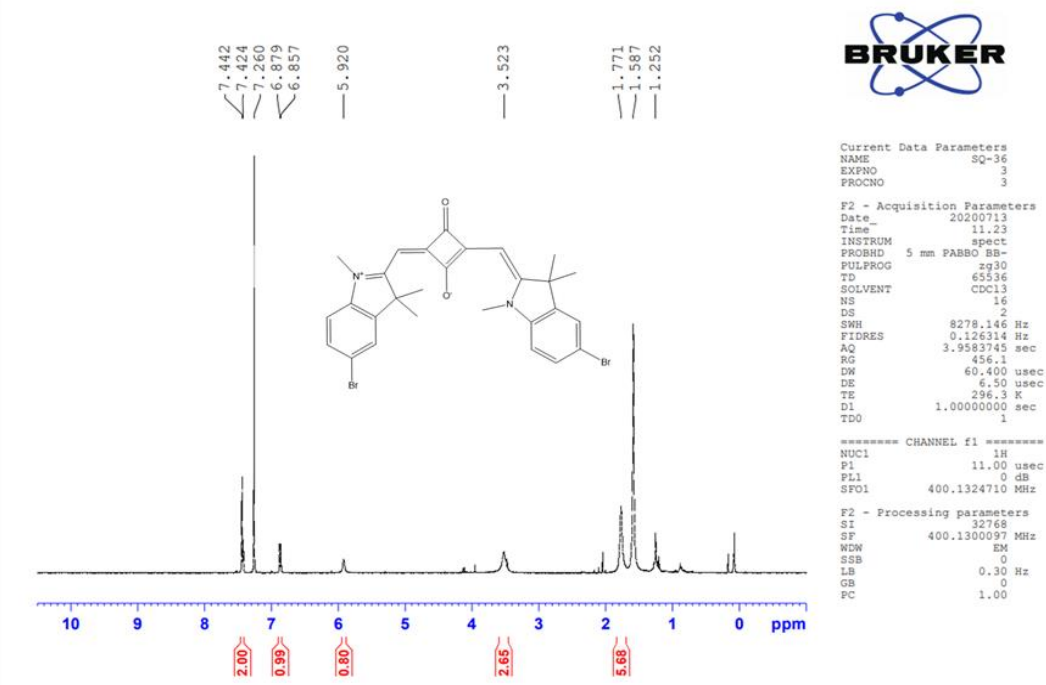

Figure S2.16: ^{1}H NMR spectrum of **SQ Br no TMAB**.

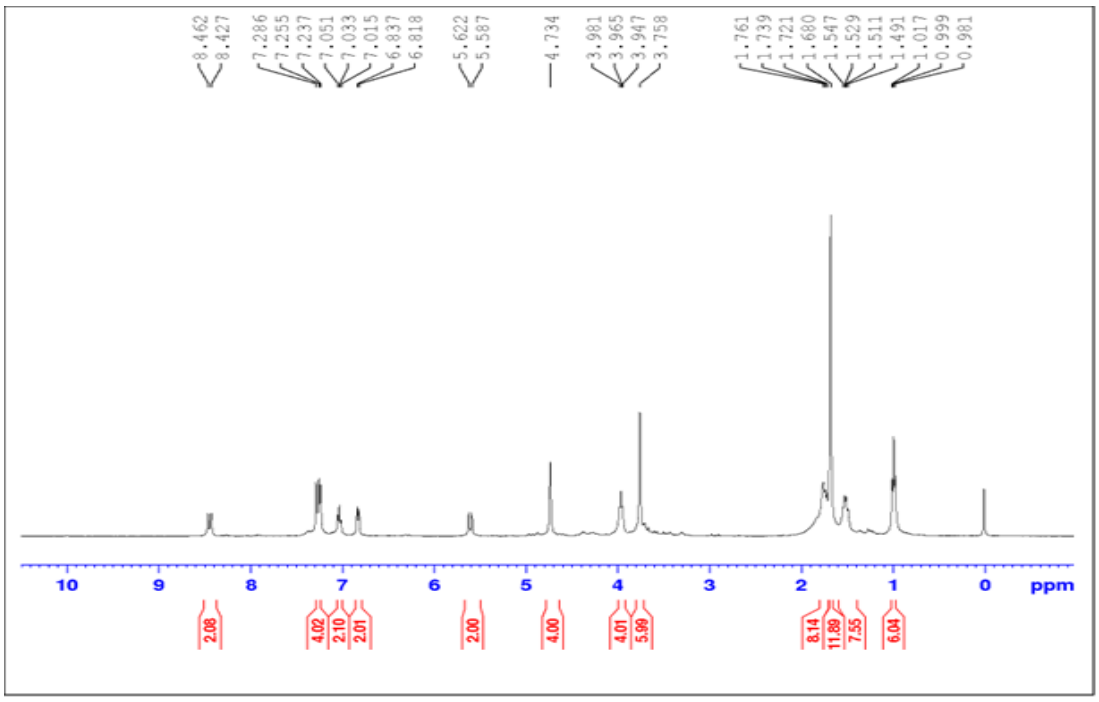

Figure S2.17: ^{1}H NMR spectrum of **CY H**.

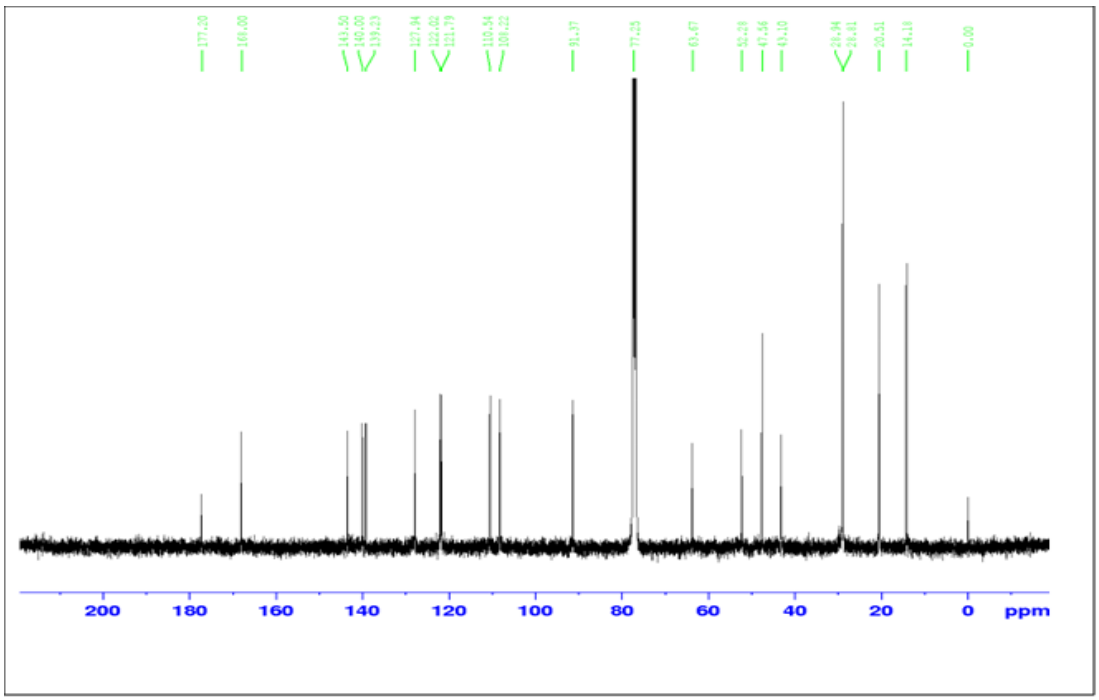

Figure S2.18: ^{13}C NMR spectrum of **CY H**.

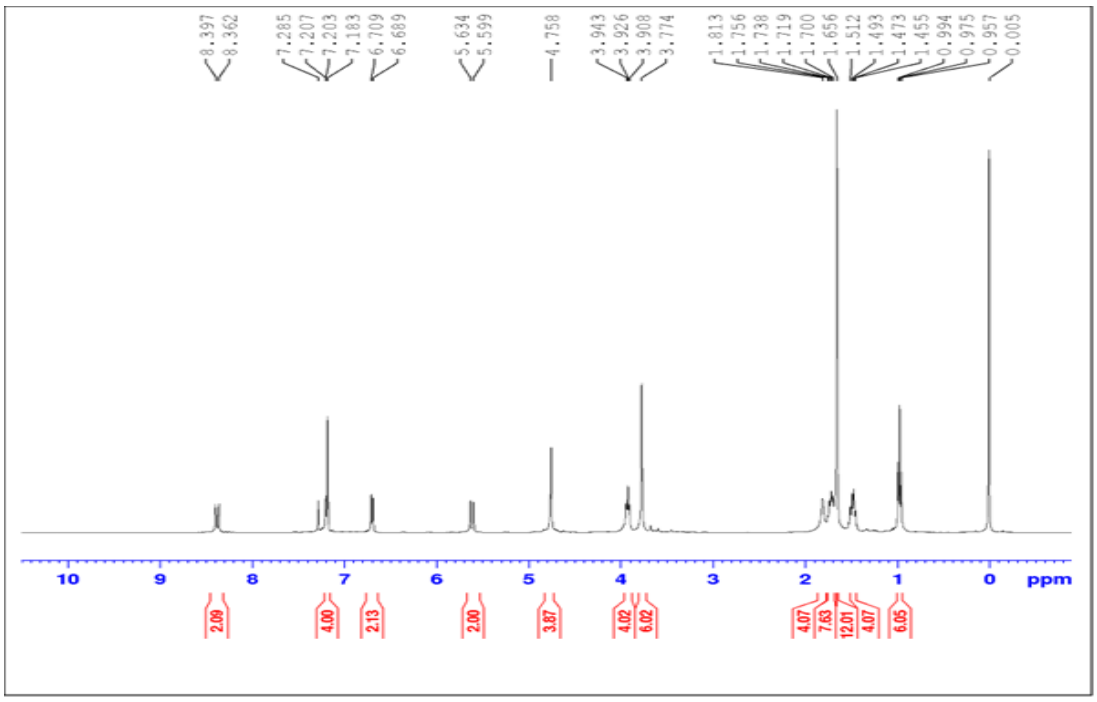

Figure S2.19: ^{1}H NMR spectrum of **CY CI**.

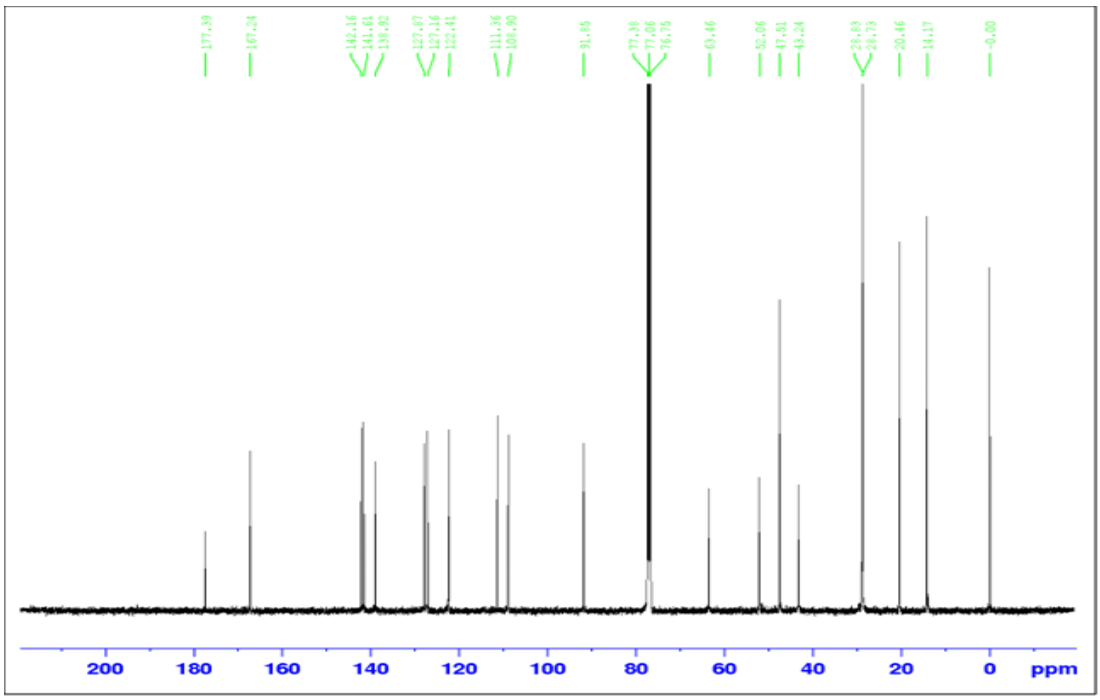

Figure S2.20: ^{13}C NMR spectrum of **CY CI**.

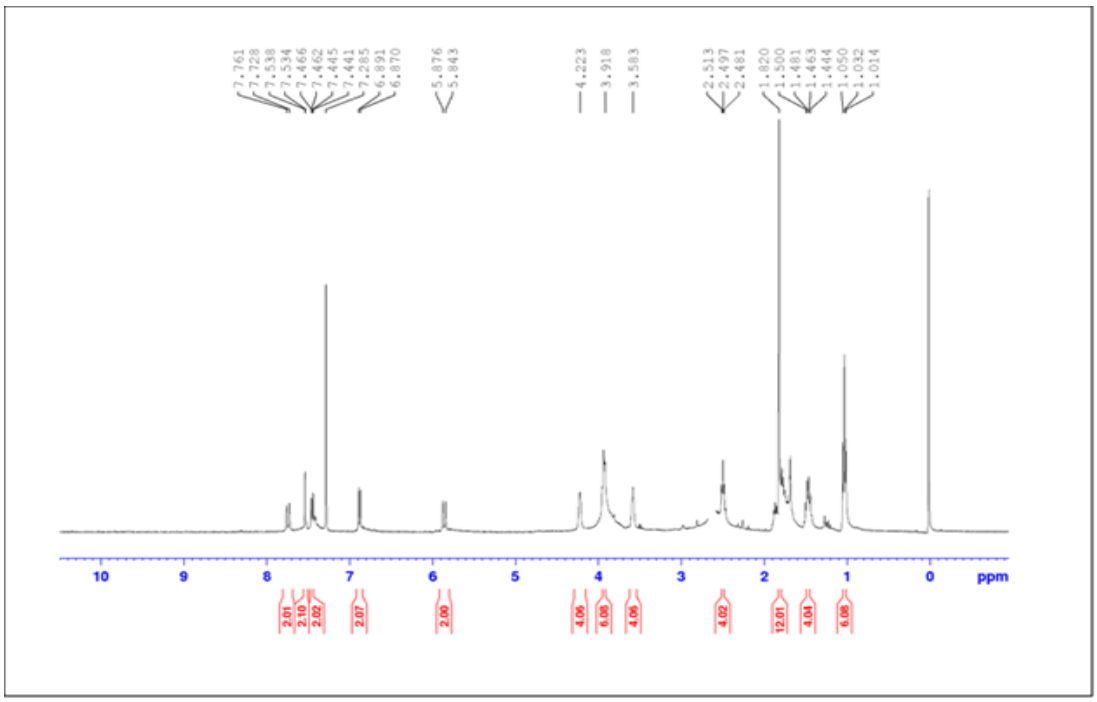

Figure S2.21: ^{1}H NMR spectrum of **CY Br**.

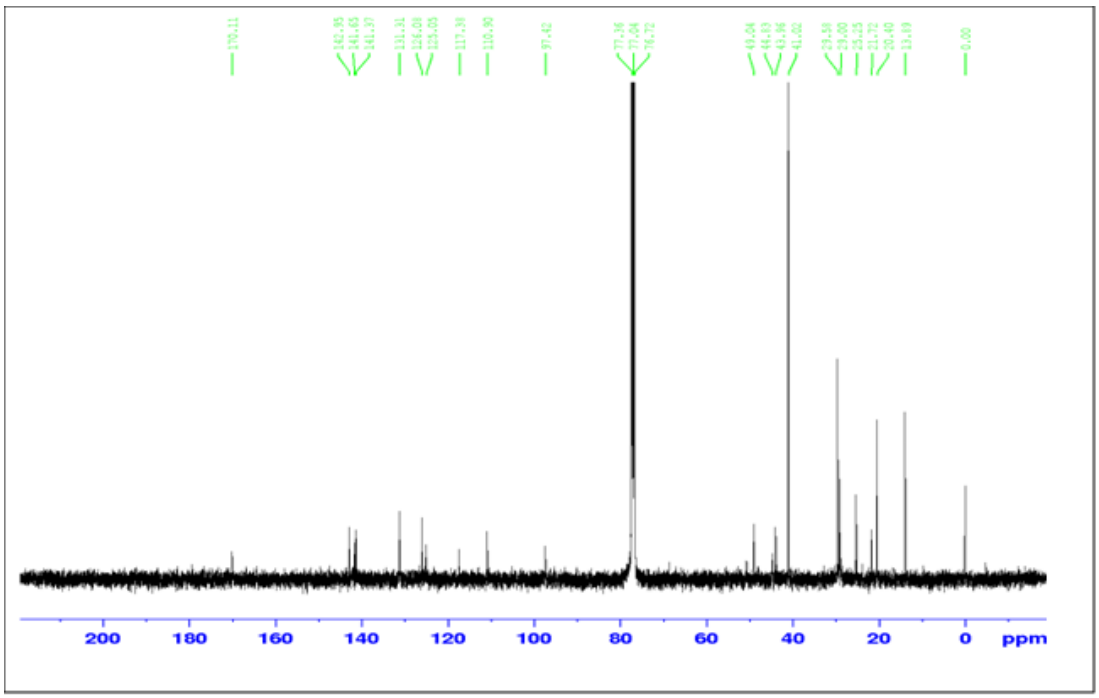

Figure S2.22: ^{13}C NMR spectrum of **CY Br**.

Molecule		Ground State Energy (a.u.)	Polarizability (kcal/mol)	Vibrational Entropy (cal/ mol K)	Dipole moment (x)	Dipole moment (y)	Dipole moment (z)	Dipole moment (Total)
SQ H no TMAB	cis	-1342.1409	3.492E+05	115.088	0.0796	-0.4077	0.7908	0.8932
	trans	-1342.1396	3.578E+05	108.848	0.1907	0.4925	-1.2875	1.3916
SQ H	cis	-1845.9627	4.301E+05	183.585	7.5529	-20.1652	3.2564	21.7781
	trans	-1845.966	4.302E+05	183.813	1.0094	-0.9427	1.2848	1.8864
SQ F	cis	-2044.2722	4.370E+05	190.944	8.0782	-23.6666	3.0972	25.1984
	trans	-2044.2761	4.371E+05	192.859	1.5396	-1.8041	1.1275	2.6261
SQ Cl	cis	-2764.7623	4.739E+05	194.192	8.1801	-25.0910	3.1361	26.5765
	trans	-2764.7665	4.733E+05	192.380	-0.0798	-0.5787	-0.0716	0.5886
SQ Br	cis	-6991.7141	4.937E+05	197.317	8.0505	-28.2397	3.0325	29.5209
	trans	-6991.7176	4.934E+05	203.903	3.1749	-4.1023	0.5364	5.215
SQ Br no TMAB	cis	-6487.8988	3.986E+05	129.835	-0.0960	0.8132	-2.0692	2.2254
	trans	-6487.8977	4.136E+05	128.677	0.8218	1.3156	-2.3504	2.8161

Figure S2.23: Properties of squaraines from DFT/TD-DFT calculations with PBE/6-31+G*.

Molecule		Wavelength (nm)	Strength	Wavelength (nm)	Strength
SQ H no TMAB	cis	741.449	2.235E-03	586.261	1.222E+00
	trans	787.002	3.014E-05	578.331	1.189E+00
SQ H	cis	700.689	5.140E-02	582.449	1.212E+00
	trans	698.440	3.990E-08	586.888	1.249E+00
SQ F	cis	698.715	5.967E-02	592.525	1.213E+00
	trans	700.492	2.040E-08	598.272	1.259E+00
SQ Cl	cis	704.192	7.987E-02	610.679	1.250E+00
	trans	710.528	1.300E-09	617.215	1.318E+00
SQ Br	cis	701.482	1.027E-01	626.225	1.178E+00
	trans	699.78	2.988E-06	634.331	1.275E+00
SQ Br no TMAB	cis	752.473	2.282E-03	600.892	1.411E+00
	trans	800.733	3.227E-04	595.010	1.298E+00

Figure S2.24: First two absorption peaks of squaraines from DFT/TD-DFT calculations with PBE/6-31+G*.

Molecule	Δ E (λ)	f	μ (Debye)	HOMO→LUMO	HOMO-1→LUMO
SQ H no TMAB	1.672 eV (741.4 nm)	2.235e-03	0.594	0.0000	0.9961
SQ H	1.769 eV (700.7 nm)	5.14e-02	2.768	0.4044	0.9155
SQ F	1.774 eV (698.7 nm)	5.967e-02	2.978	0.4021	0.9164
SQ Cl	1.761 eV (704.2 nm)	7.987e-02	3.458	0.4216	0.9067
SQ Br	1.767 eV (701.5 nm)	1.027e-01	3.915	0.4383	0.8981
SQ Br no TMAB	1.648 eV (752.5 nm)	2.282e-03	0.604	0.0000	0.9967

Figure S2.25: Molecular properties of squaraine analogs calculated using PBE functional and 6-31+G* basis set. f represents the oscillator strength of the lowest-energy absorption, μ represents the transition dipole moment of the lowest-energy absorption.

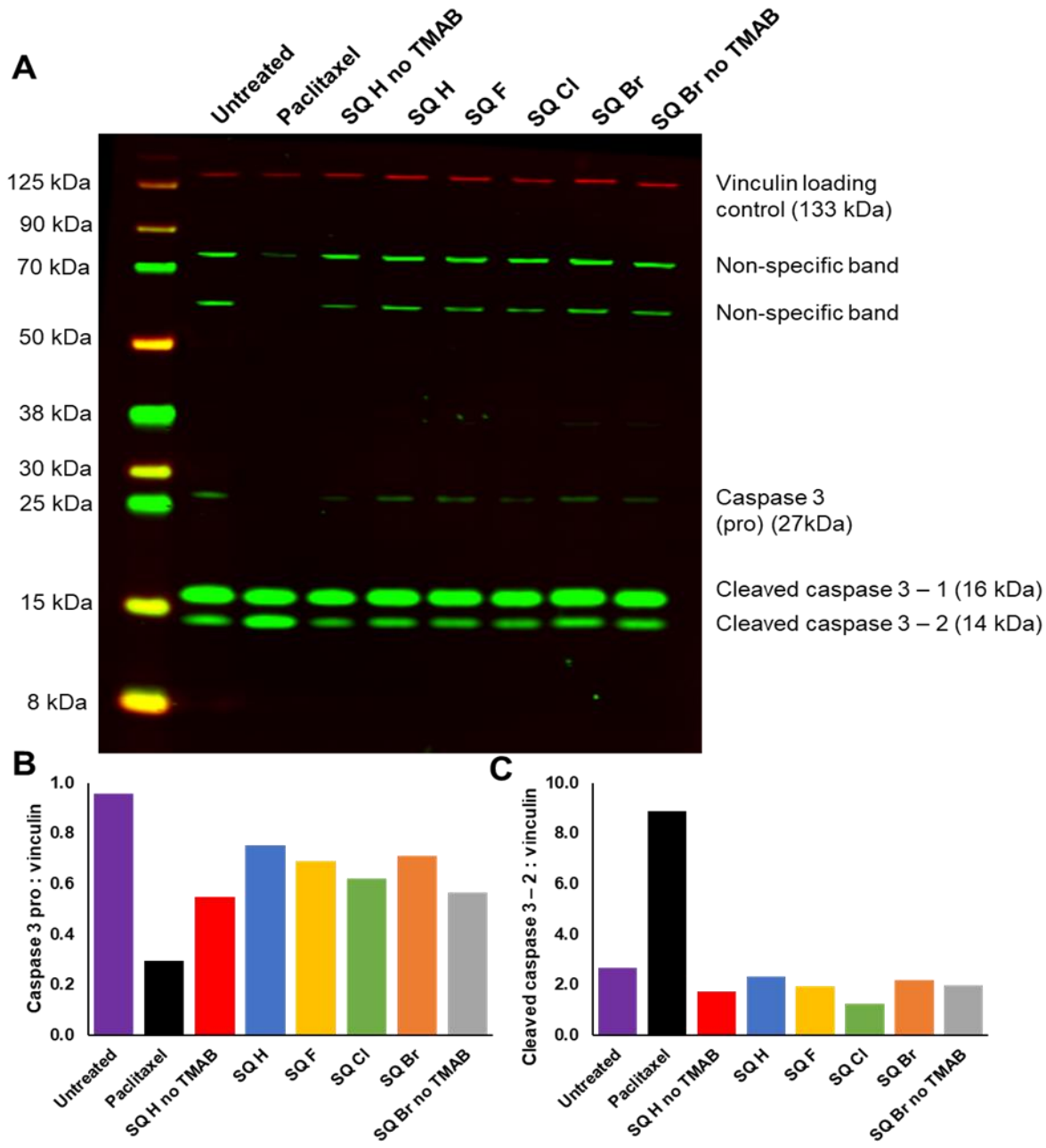

Figure S2.26: Western blot analysis of apoptosis in COLO205 colon cells treated with squaraine compounds using apoptosis marker caspase 3. A) Visualization of NIR fluorescence western blot. B) Pro caspase 3 quantification in all treatments (adjusted with loading control). C) Cleaved caspase 3 – 2 quantifications in all treatments (adjusted with loading control).

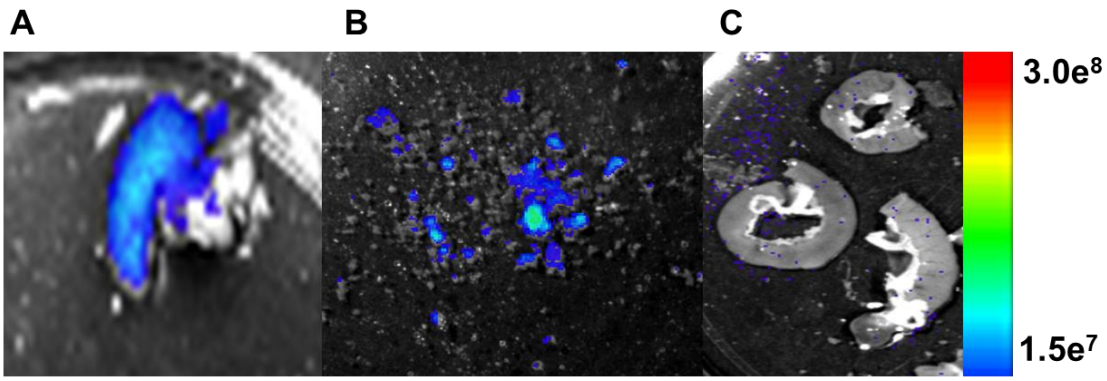

Figure S2.27: *Ex vivo* NIR fluorescence squaraine compounds in animal colon A) Colon prior to flushing with saline B) Contents flushed from the colon with saline C) Colon after being flushed with saline.

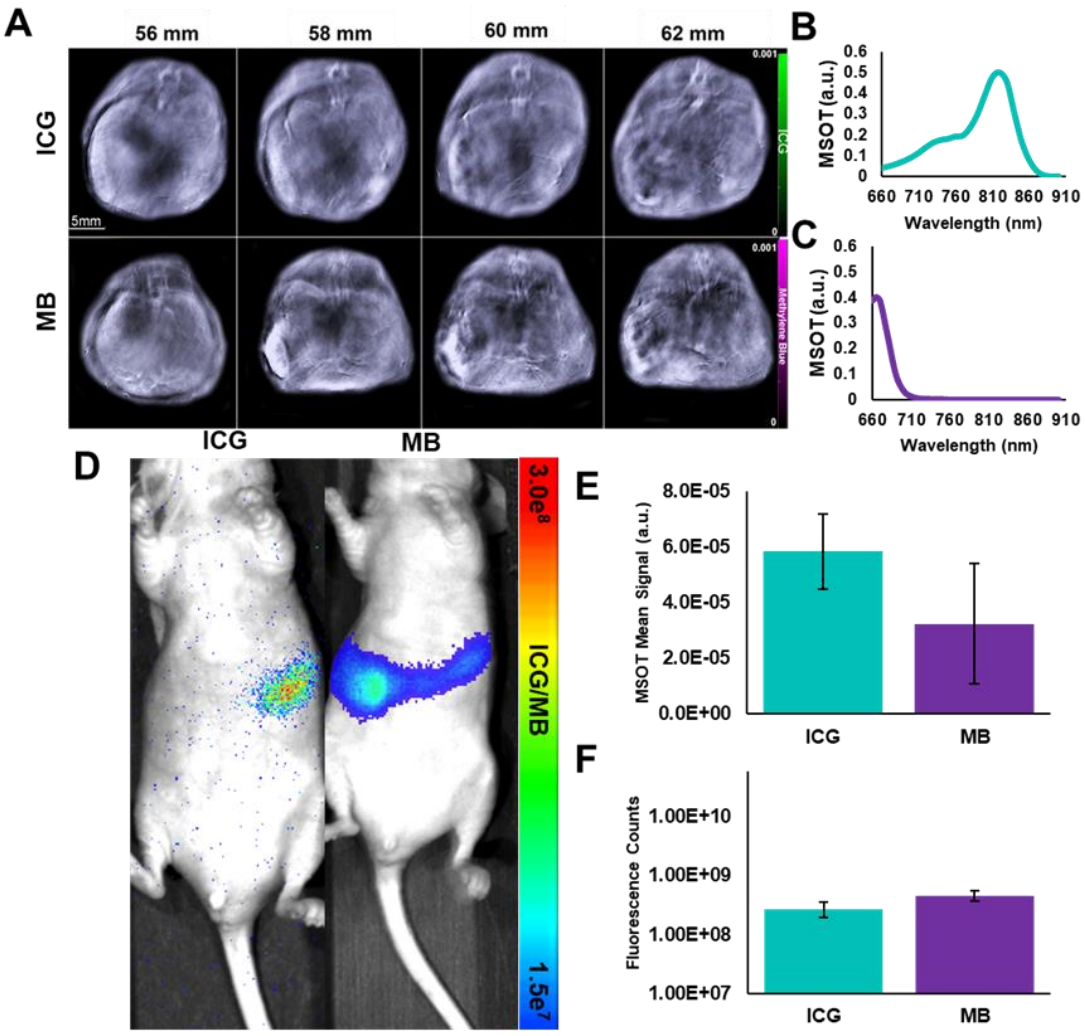

Figure S2.28: A) *In vivo* visualization of optoacoustic signal generated from ICG and MB subsequent to oral administration. Columns represent slightly different tomographic slices within the mouse. B) Quantification of optoacoustic signal observed in A) (n=3). C) *In vivo* visualization of NIR fluorescence signal generated from ICG and MB. D) Quantification of NIR fluorescence signal observed in C).

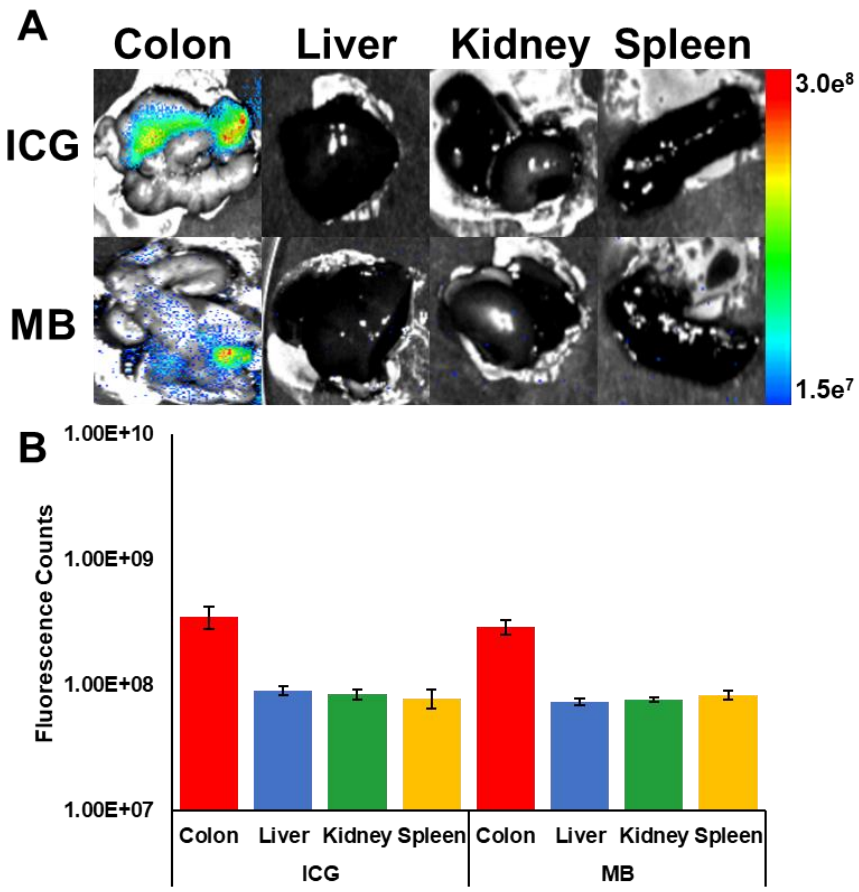

Figure S2.29: A) *Ex vivo* visualization of NIR fluorescence signal generated from ICG and MB in animal colons, livers, kidneys, and spleens subsequent to oral administration. B) Quantification of NIR fluorescence signal observed in A).

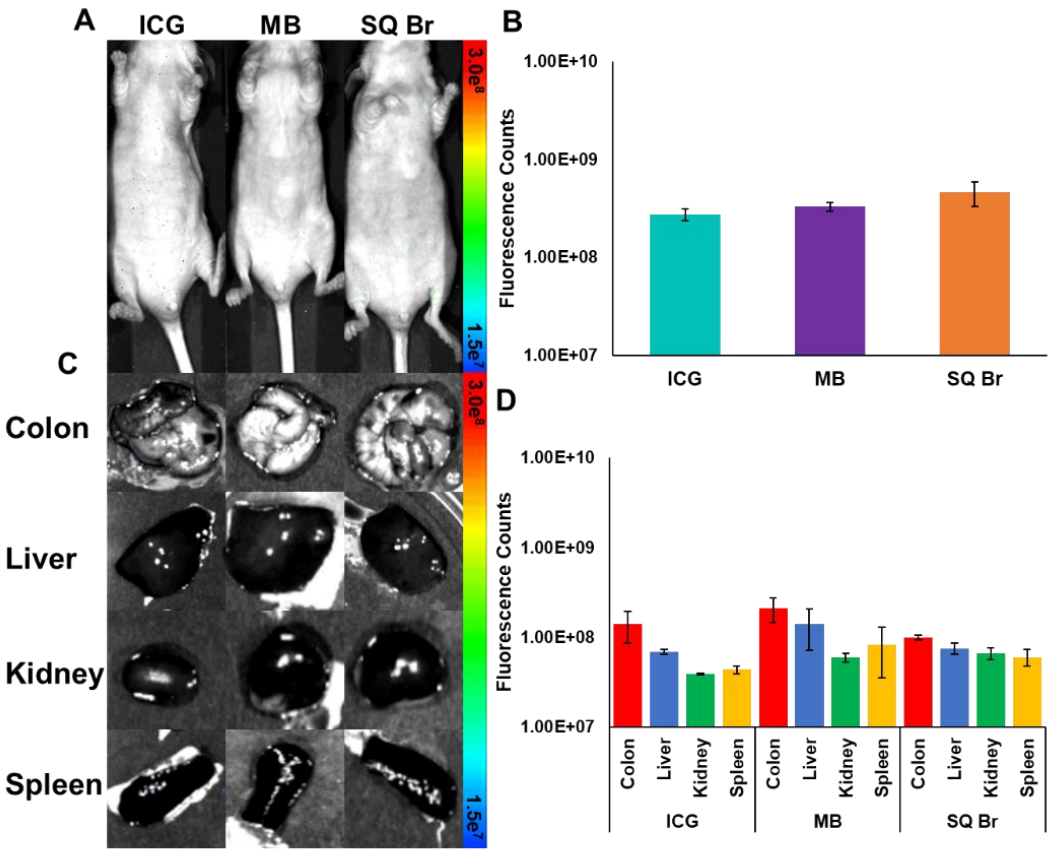

Figure S2.30: A) NIR fluorescence images of mice 6 h post-oral administration of ICG, MB, or SQ Br. B) Quantification of NIR fluorescence signal in A). C) NIR fluorescence images of excised organs of mice 6 h post-oral administration of ICG, MB, or SQ Br. D) Quantification of NIR fluorescence signal observed in C).

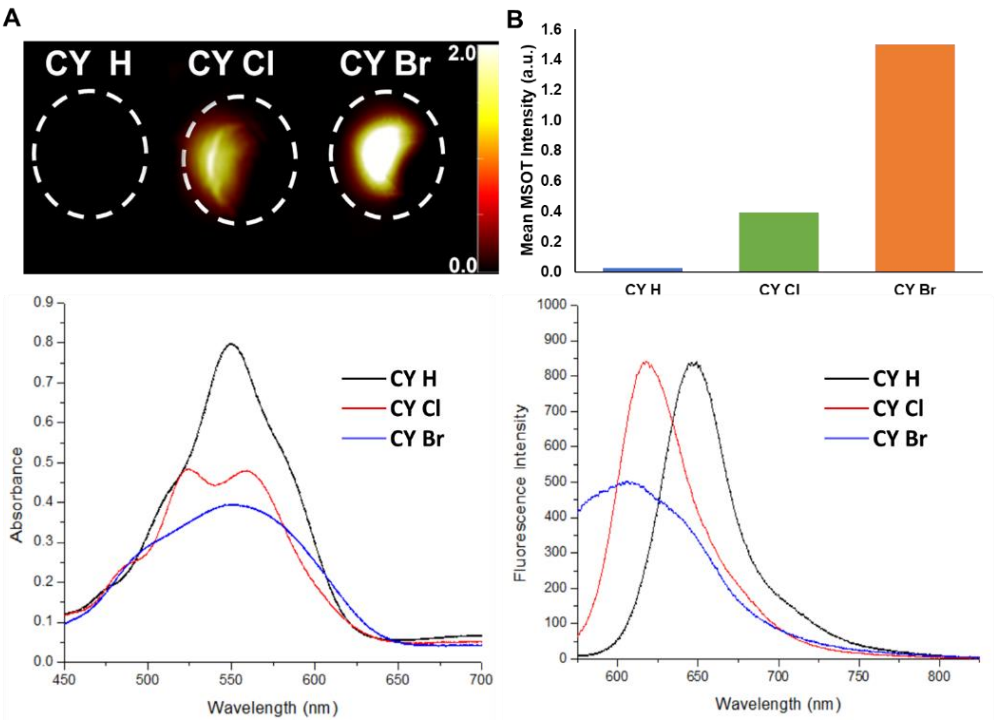

Figure S2.31: Optoacoustic evaluation of halogenated cyanine compounds. A) Optoacoustic images of compounds in tissue mimicking phantoms. B) Peak optoacoustic intensity of compounds. C) Absorption spectra for **CY H, CY Cl,** and **CY Br.** D) Absorption spectra for **CY H, CY Cl,** and **CY Br.**

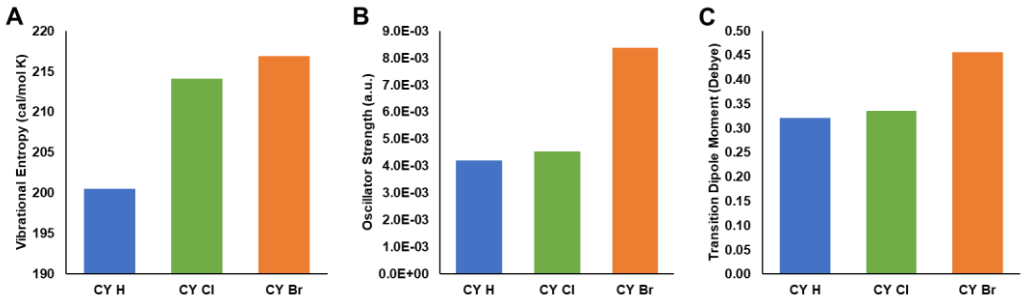

Figure S2.32: Computational modeling of cyanine compounds. A) Vibrational entropy of cyanine compounds from DFT frequency calculations. B) Oscillator strength of the lowest-energy absorptions of cyanine compounds from TD-DFT calculations. C) Transition dipole moment of the lowest-energy absorptions of cyanine compounds from TD-DFT calculations.

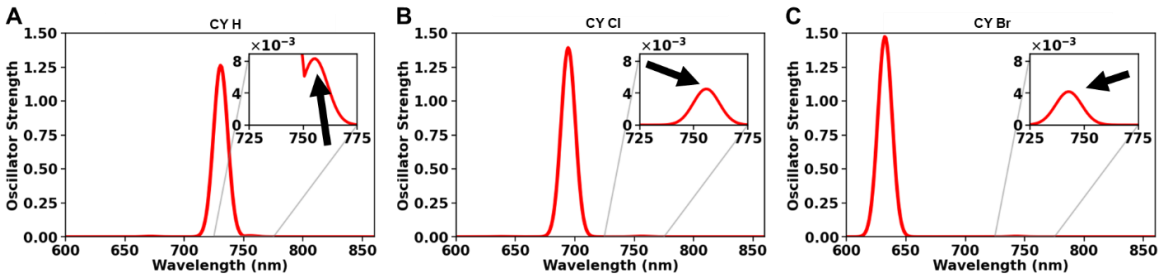

Figure S2.33: Full TD-DFT derived absorption peaks of cyanine compounds A) **CY H**, B) **CY Cl**, C) **CY Br**. Arrows in panels A-C indicate the absorption peak that is responsible for optoacoustic signal generation.

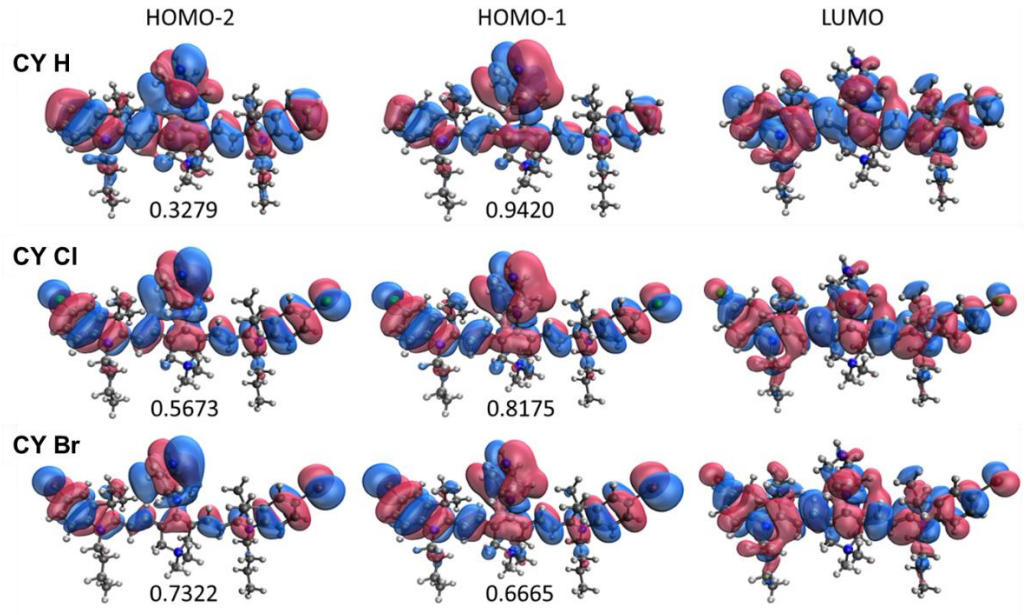

Figure S2.34: HOMO-2, HOMO-1, and LUMO of cyanine compounds from DFT calculations using PBE functional and 6-31+G* basis set. Amplitudes for HOMO-2 to LUMO and HOMO-1 to LUMO electronic transitions for the lowest energy absorption are listed below the respective orbitals.

Molecule	Λ_{abs} (nm)	Λ_{ems} (nm)	Extinction Coefficient ($M^{-1}cm^{-1}$)	Quantum Yield (Φ, %)
CY H	550	652	42,560	25
CY Cl	550	615	41,680	25
CY Br	550	612	37,897	15

Figure S2.35: Optical properties for cyanine compounds in FBS supplemented with HEPES buffer at pH 7.4 and warmed to physiological temperature (37°C)

Molecule	Ground State Energy (a.u.)	Polarizability (kcal/mol)	Vibrational Entropy (cal/mol K)	Dipole moment (x)	Dipole moment (y)	Dipole moment (z)	Dipole moment (Total)
CY H	-1946.0698	5.353e+05	200.534	76.741	-42.466	4.140	87.805
CY Cl	-2864.8692	5.976e+05	214.102	75.590	-43.086	4.490	87.123
CY Br	-7091.8211	6.264e+05	216.925	75.845	-42.981	4.446	87.290

Figure S2.36: Properties of cyanine compounds from TD-DFT calculations with PBE/6-31+G*.

Molecule	Wavelength (nm)	Strength	Wavelength (nm)	Strength
CY H	742.751	4.202e-03	632.357	1.475e+00
CY Cl	755.791	4.551e-03	694.449	1.393e+00
CY Br	755.239	8.375e-03	730.583	1.263e+00

Figure S2.37: First absorption peaks of cyanines from TD-DFT calculations with PBE/6-31+G*.

Molecule	Rotatable Bonds	Surface Area (Å^2)	Volume (Å^3)	LogD
CY H	17	884	661	-2.1
CY Cl	17	892	692	-1.1
CY Br	17	911	700	-0.51

Figure S2.38: Molecular properties of cyanine compounds. Rotatable bonds, surface area, and volume were computed with RDkit. LogD (pH 7.4) computed with ChemAxon.

Molecule	ΔE (λ)	f	μ (Debye)	HOMO-1→LUMO	HOMO-2→LUMO
CY H	1.669 eV (742.8 nm)	4.202e-03	0.321	0.9420	0.3279
CY Cl	1.640 eV (755.8 nm)	4.551e-03	0.336	0.8175	0.5673
CY Br	1.642 eV (755.2 nm)	8.375e-03	0.456	0.6665	0.7322

Figure S2.39: Molecular properties of cyanine dyes calculated using PBE functional and 6-31+G* basis set. f represents the oscillator strength of the lowest-energy absorption, μ represents the transition dipole moment of the lowest-energy absorption.

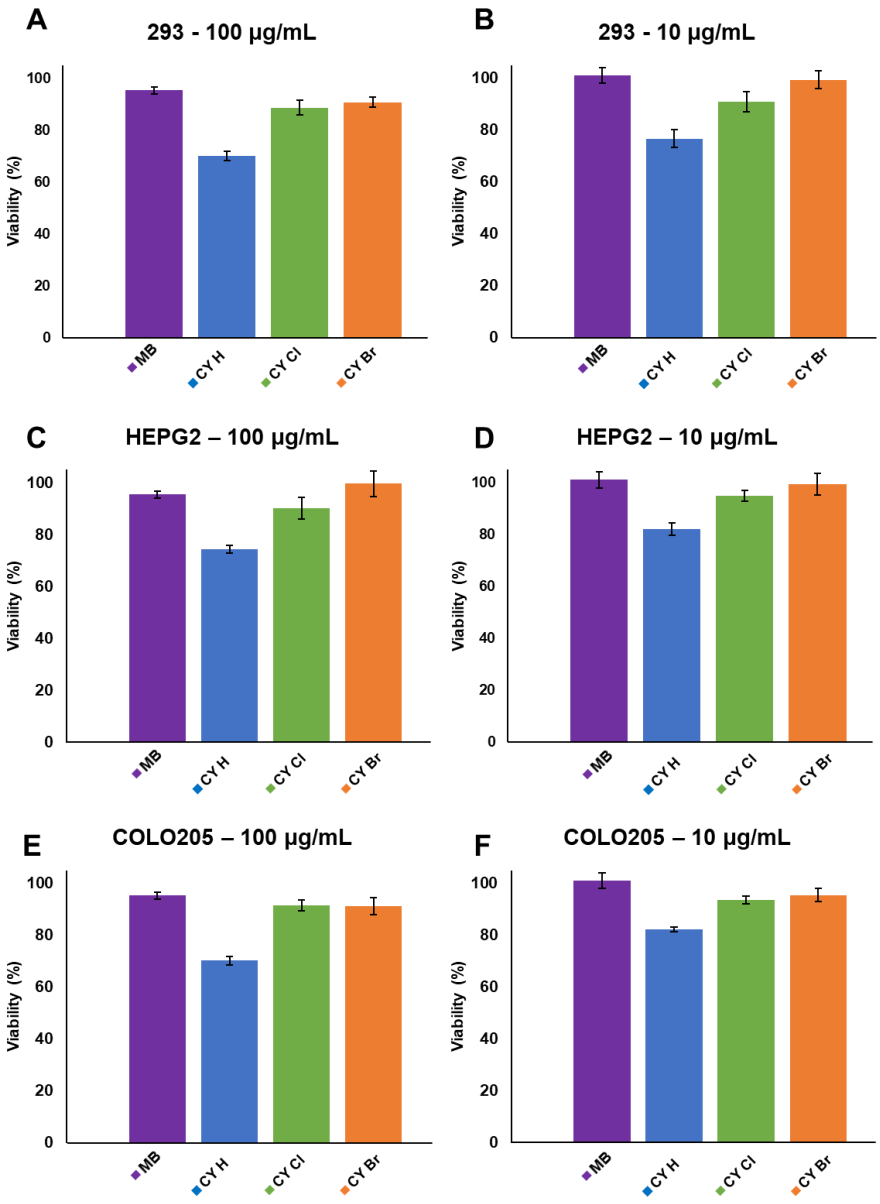

Figure S2.40: Cellular viability of cells following treatment with cyanine compounds. A) 293 kidney cells at 100 µg/mL, B) 293 kidney cells at 10 µg/mL, C) HEPG2 liver cells at 100 µg/mL, D) HEPG2 liver cells at 10 µg/mL, E) COLO205 colon cells at 100 µg/mL, F) COLO205 colon cells at 10 µg/mL. MB is commercially available dye methylene blue.

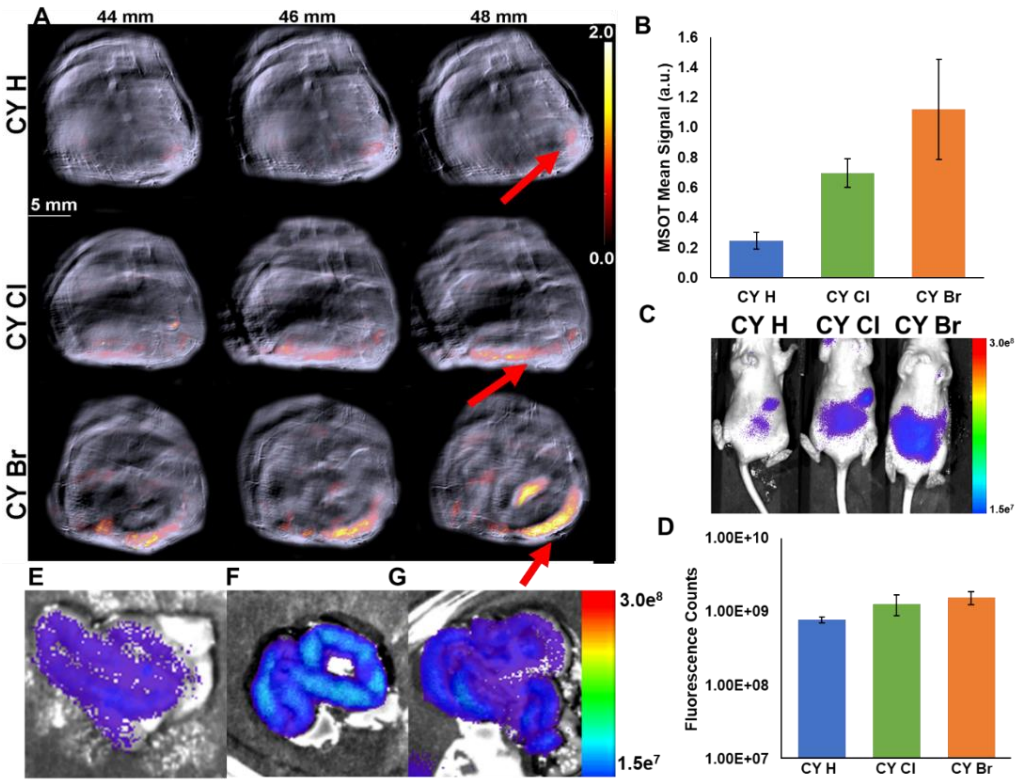

Figure S2.41: A) *In vivo* visualization of optoacoustic signal generated from cyanine compounds subsequent to oral administration. Columns represent slightly different tomographic slices within the mouse. Red arrows show optoacoustic signal as a result of cyanine compounds in the body. B) Quantification of optoacoustic signal observed in A). C) *In vivo* visualization of NIR fluorescence signal generated from cyanine compounds. D) Quantification of NIR fluorescence signal observed in C). E) *Ex vivo* visualization of NIR fluorescence signal in the colon of a mouse treated with **CY H**. F) *Ex vivo* visualization of NIR fluorescence signal in the colon of a mouse treated with **CY Cl**. G) *Ex vivo* visualization of NIR fluorescence signal in the colon of a mouse treated with **CY Br**.

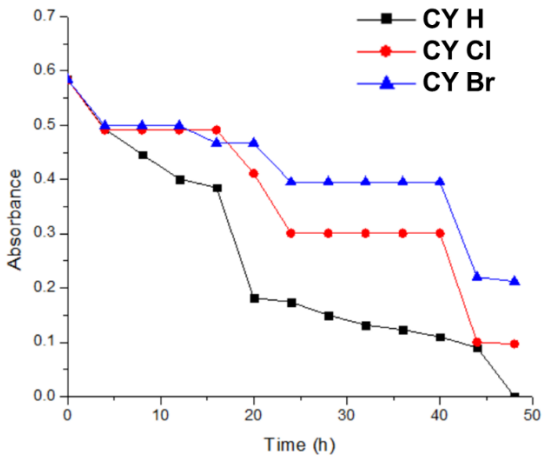

Figure S2.42: Thermal stability study of cyanine compounds. Compounds were placed under continuous irradiation with UV lamp for 48 h. The rate of photobleaching of compounds were determined based on the reduced absorbance as a result of continuous irradiation.

SQ H no TMAB			
-1342.13958938745 a.u.			
C	1.204656	0.149036	0.027879
C	0.481828	-0.86877	0.83144
C	-0.55717	-0.98	-0.2213
C	0.161921	0.053982	-1.02061
C	-1.72654	-1.74883	-0.09708
C	-2.8211	-2.04468	-0.90983
C	-4.09468	-2.70508	-0.35119
C	-4.95431	-2.81959	-1.59616
C	-4.23969	-2.30403	-2.69505
N	-2.97386	-1.85635	-2.25883
O	0.008103	0.649168	-2.10186
O	0.617757	-1.4261	1.934447
C	-4.75794	-1.79886	0.714698

C	-3.78837	-4.09812	0.251188
C	-6.23893	-3.32994	-1.77414
C	-4.78687	-2.28285	-3.98592
C	-6.08413	-2.80084	-4.15091
C	-6.80737	-3.31894	-3.06396
C	2.323886	0.997381	-0.00696
C	3.376789	1.182173	0.887699
C	3.6764	0.5029	2.231995
N	4.382902	2.092253	0.621834
C	5.347692	2.114792	1.647533
C	4.976628	1.180638	2.632794
C	2.565574	0.787198	3.276072
C	3.881614	-1.02389	2.060111
C	4.442317	2.916281	-0.57424
C	5.77603	1.004697	3.760831
C	6.510296	2.891158	1.761451
C	7.306526	2.702562	2.905674
C	6.950328	1.772262	3.896312
H	7.587118	1.644614	4.777647
H	-7.8168	-3.71346	-3.21877
H	-1.80834	-2.1803	0.912735
H	-4.97842	-0.79896	0.305174
H	-4.09589	-1.67705	1.589031
H	-5.70588	-2.2507	1.056802
H	-3.30635	-4.75774	-0.48959
H	-4.72607	-4.57779	0.583728
H	-3.12177	-4.01063	1.126294

H	-6.80278	-3.73575	-0.92606
H	-4.24334	-1.87604	-4.84358
H	-6.53521	-2.79416	-5.14887
H	2.344145	1.609524	-0.91952
H	2.385305	1.871045	3.37879
H	2.883722	0.396293	4.2588
H	1.634016	0.272555	2.991104
H	4.652649	-1.23606	1.299984
H	2.933065	-1.50877	1.781558
H	4.21393	-1.4558	3.020466
H	5.373394	3.49851	-0.56902
H	3.58626	3.613497	-0.614
H	5.498177	0.278989	4.533911
H	6.803396	3.622448	1.001611
H	8.219917	3.295869	3.02043
H	4.426423	2.2842	-1.47934
C	-1.91715	-1.40295	-3.15386
H	-2.28037	-1.43822	-4.18938
H	-1.04392	-2.07357	-3.05736
H	-1.57919	-0.38153	-2.90628

Figure S2.43: Coordinates (Angstroms) and energy (a.u.) of **SQ H no TMAB.** Geometries were optimized using PBE functional and 6-31+G* basis set.

SQ H			
-1845.96271711902 a.u.			
C	0.611534	0.152722	-0.22712
C	0.074687	1.262868	0.604871

C	-1.31453	0.788773	0.351167
C	-0.75464	-0.38817	-0.35653
C	-2.46802	1.424972	0.830231
C	-3.84758	1.392675	0.58962
C	-4.82358	2.166005	1.496945
C	-6.15606	1.905238	0.821446
C	-5.94461	1.12629	-0.32899
N	-4.56196	0.806175	-0.42572
O	-1.21837	-1.44711	-0.8494
O	0.524718	2.204687	1.267244
C	-4.50243	3.683659	1.502955
C	-4.77885	1.61045	2.942907
C	-7.44308	2.342068	1.137031
C	-6.98313	0.792062	-1.20842
C	-8.27493	1.243051	-0.88069
C	-8.50718	1.9984	0.281031
C	-4.01155	0.091818	-1.57559
C	-4.40316	-1.40386	-1.64521
C	-4.12872	-2.08963	-0.30902
N	-4.12906	-3.62256	-0.34916
C	-5.47683	-4.16194	-0.75196
C	-3.80327	-4.10928	1.042244
C	-3.06419	-4.13276	-1.297
C	1.802275	-0.3707	-0.77087
C	3.061697	0.202113	-0.94521
C	3.52847	1.651612	-0.70196
N	4.127846	-0.50447	-1.49829

C	5.214319	0.353601	-1.79702
C	4.912287	1.644256	-1.33248
C	2.613585	2.691669	-1.39043
C	3.636208	1.945465	0.820602
C	4.234973	-1.95118	-1.6218
C	5.306183	-2.5541	-0.67026
C	5.032515	-2.18496	0.789737
N	6.249512	-2.24992	1.726128
C	7.259786	-1.17986	1.376885
C	5.764613	-2.00464	3.137636
C	6.90258	-3.60793	1.659409
C	5.836709	2.676053	-1.50397
C	6.410678	0.059008	-2.4686
C	7.331173	1.110203	-2.63859
C	7.055026	2.400691	-2.15598
H	7.782927	3.203415	-2.30832
H	-9.52166	2.335638	0.514222
H	-2.20033	2.193444	1.57142
H	-4.49445	4.097986	0.481665
H	-3.52274	3.880501	1.970182
H	-5.26954	4.218906	2.087358
H	-5.02113	0.534135	2.972041
H	-5.51362	2.142525	3.570686
H	-3.77928	1.755997	3.38592
H	-7.62856	2.95436	2.026242
H	-6.81581	0.229246	-2.13103
H	-9.10826	1.006576	-1.54971

H	-2.91777	0.172909	-1.53344
H	-4.35963	0.596531	-2.49543
H	-3.77242	-1.83052	-2.44338
H	-5.45847	-1.51912	-1.9442
H	-4.88162	-1.81206	0.447453
H	-3.11633	-1.81192	0.031426
H	-6.23451	-3.79387	-0.04457
H	-5.44124	-5.26116	-0.72847
H	-5.715	-3.82229	-1.76911
H	-4.55125	-3.71341	1.744669
H	-2.80118	-3.7472	1.314189
H	-3.82698	-5.20883	1.051525
H	-3.40306	-3.98802	-2.33107
H	-2.92233	-5.2075	-1.10976
H	-2.13815	-3.56405	-1.12074
H	1.647588	-1.36623	-1.21231
H	2.508972	2.477832	-2.46697
H	3.056831	3.695995	-1.28098
H	1.619388	2.713031	-0.92133
H	4.278236	1.198632	1.32616
H	2.636379	1.9586	1.285764
H	4.099409	2.936277	0.970156
H	4.495886	-2.22016	-2.66113
H	3.252212	-2.39656	-1.41219
H	6.29796	-2.19367	-0.99111
H	5.299567	-3.64903	-0.81033
H	4.279081	-2.85431	1.237242

H	4.661303	-1.14957	0.872949
H	6.761811	-0.19962	1.39404
H	7.670779	-1.36738	0.376747
H	8.068394	-1.20894	2.121664
H	5.292865	-1.01221	3.184385
H	6.624921	-2.04533	3.82157
H	5.035005	-2.78277	3.405394
H	7.296082	-3.76954	0.646763
H	6.152552	-4.375	1.902221
H	7.724581	-3.64111	2.388828
H	5.616328	3.691451	-1.1565
H	6.617593	-0.92904	-2.89384
H	8.266859	0.919797	-3.17396

Figure S2.44: Coordinates (Angstroms) and energy (a.u.) of **SQ H**. Geometries were optimized using PBE functional and 6-31+G* basis set.

SQ F			
-2044.27223196399 a.u.			
C	0.637614	-0.03342	-0.26236
C	0.113666	1.072113	0.582026
C	-1.28159	0.625644	0.313889
C	-0.73671	-0.55051	-0.40775
C	-2.41873	1.288705	0.795073
C	-3.79948	1.303033	0.56177
C	-4.73467	2.137494	1.460015
C	-6.0817	1.919411	0.799808
C	-5.91366	1.105249	-0.33381

N	-4.54677	0.724736	-0.43404
O	-1.21376	-1.59514	-0.91831
O	0.573808	1.99791	1.260256
C	-4.34946	3.639903	1.42506
C	-4.70583	1.614168	2.918213
C	-7.34002	2.423086	1.125707
C	-6.9766	0.799913	-1.19514
C	-8.24699	1.307743	-0.87397
C	-8.40563	2.091798	0.275139
C	-4.0415	-0.03333	-1.57709
C	-4.48627	-1.5146	-1.61092
C	-4.11381	-2.21908	-0.3084
N	-4.12752	-3.75174	-0.36222
C	-5.51434	-4.28128	-0.62134
C	-3.65128	-4.24924	0.981301
C	-3.17334	-4.25804	-1.42276
C	1.826147	-0.56429	-0.80375
C	3.094602	-0.00502	-0.95597
C	3.574715	1.436791	-0.68854
N	4.158934	-0.71643	-1.50602
C	5.255753	0.134185	-1.78792
C	4.961995	1.422707	-1.31039
C	2.677556	2.498024	-1.36747
C	3.680767	1.706869	0.838685
C	4.251451	-2.16263	-1.64698
C	5.318988	-2.78965	-0.70703
C	5.053834	-2.43958	0.759206

N	6.268943	-2.54909	1.693639
C	7.296721	-1.48809	1.370072
C	5.788739	-2.33121	3.111277
C	6.898842	-3.91638	1.593416
C	5.888196	2.454977	-1.45778
C	6.452974	-0.15799	-2.4594
C	7.388663	0.8806	-2.61425
C	7.095564	2.151874	-2.10616
F	8.012697	3.13886	-2.26003
F	-9.6408	2.561093	0.574616
H	-2.12498	2.050687	1.533323
H	-4.32577	4.025836	0.392889
H	-3.3608	3.806516	1.884692
H	-5.09129	4.223762	1.995362
H	-5.01242	0.555667	2.976055
H	-5.39805	2.204511	3.542143
H	-3.69358	1.708959	3.345492
H	-7.51635	3.065349	1.993936
H	-6.84822	0.21109	-2.10739
H	-9.11268	1.108195	-1.51124
H	-2.94404	0.012434	-1.56018
H	-4.39119	0.463957	-2.50055
H	-3.94587	-1.95638	-2.46525
H	-5.56698	-1.59386	-1.81685
H	-4.79974	-1.94567	0.510297
H	-3.07346	-1.95446	-0.0495
H	-6.18687	-3.92744	0.174142

H	-5.48282	-5.38116	-0.6244
H	-5.86447	-3.92093	-1.59816
H	-4.31379	-3.85257	1.764223
H	-2.62356	-3.8913	1.137313
H	-3.68037	-5.34854	0.986063
H	-3.61081	-4.09191	-2.41621
H	-3.02708	-5.33719	-1.26828
H	-2.22546	-3.70606	-1.32798
H	1.66407	-1.55093	-1.26199
H	2.574706	2.299974	-2.44714
H	3.132223	3.495364	-1.24212
H	1.682069	2.525582	-0.90187
H	4.311719	0.944635	1.334714
H	2.678734	1.724487	1.298739
H	4.154112	2.690154	1.00534
H	4.504168	-2.42318	-2.69066
H	3.264609	-2.59885	-1.43743
H	6.31479	-2.43797	-1.02493
H	5.298854	-3.88218	-0.86267
H	4.285104	-3.09999	1.193824
H	4.705024	-1.39807	0.860819
H	6.823129	-0.49823	1.442126
H	7.681459	-1.64016	0.353454
H	8.120416	-1.56724	2.094476
H	5.321542	-1.33794	3.180614
H	6.650749	-2.38998	3.791713
H	5.056743	-3.11183	3.364838

H	7.302706	-4.05579	0.581544
H	6.131892	-4.67608	1.804376
H	7.710144	-3.98723	2.331993
H	5.699004	3.475162	-1.10958
H	6.656809	-1.13966	-2.89955
H	8.331587	0.718824	-3.14376

Figure S2.45: Coordinates (Angstroms) and energy (a.u.) of **SQ F**. Geometries were optimized using PBE functional and 6-31+G* basis set.

SQ Cl			
-2764.76229746764 a.u.			
C	0.677866	-0.20481	-0.2453
C	0.165828	0.896808	0.61144
C	-1.234	0.464689	0.342671
C	-0.70115	-0.70916	-0.39166
C	-2.36392	1.13483	0.83115
C	-3.74426	1.167428	0.598813
C	-4.66832	2.01175	1.499496
C	-6.01824	1.81295	0.838138
C	-5.86022	0.998745	-0.29589
N	-4.50006	0.600927	-0.39814
O	-1.18852	-1.74516	-0.90972
O	0.635708	1.811462	1.297802
C	-4.2629	3.508818	1.468254
C	-4.64693	1.48376	2.956111
C	-7.26875	2.333421	1.163476
C	-6.92928	0.711152	-1.15456

C	-8.19051	1.238219	-0.8301
C	-8.35654	2.028074	0.32125
C	-4.00762	-0.16487	-1.54202
C	-4.46914	-1.64075	-1.57042
C	-4.08934	-2.35048	-0.27272
N	-4.11502	-3.8828	-0.32981
C	-5.50833	-4.40118	-0.57665
C	-3.62993	-4.38693	1.008108
C	-3.17505	-4.39386	-1.40077
C	1.860459	-0.73963	-0.79593
C	3.132531	-0.18877	-0.9467
C	3.625291	1.246566	-0.66826
N	4.189496	-0.90388	-1.50808
C	5.290625	-0.06018	-1.78537
C	5.010223	1.226222	-1.29626
C	2.733491	2.320483	-1.33401
C	3.740134	1.502233	0.860823
C	4.269444	-2.34966	-1.66526
C	5.334935	-2.99385	-0.73498
C	5.0751	-2.6594	0.735943
N	6.294362	-2.77539	1.66406
C	7.317091	-1.7069	1.348856
C	5.819006	-2.57598	3.085947
C	6.928652	-4.13928	1.54545
C	5.94459	2.250636	-1.43751
C	6.484627	-0.35287	-2.4612
C	7.425683	0.681226	-2.60819

C	7.159713	1.961431	-2.09121
Cl	8.346321	3.226011	-2.28377
Cl	-9.93529	2.658816	0.706984
H	-2.06119	1.888181	1.57472
H	-4.23662	3.897627	0.437166
H	-3.27095	3.661843	1.925624
H	-4.99597	4.100629	2.041632
H	-4.96961	0.429858	3.010962
H	-5.33046	2.082428	3.581674
H	-3.63364	1.56162	3.384437
H	-7.41754	2.975705	2.036965
H	-6.8137	0.121519	-2.06837
H	-9.04885	1.041788	-1.47849
H	-2.90959	-0.13047	-1.53122
H	-4.3569	0.334452	-2.46441
H	-3.94459	-2.08863	-2.43145
H	-5.55319	-1.70689	-1.76294
H	-4.76529	-2.07385	0.553154
H	-3.04485	-2.09432	-0.02271
H	-6.17045	-4.04418	0.226113
H	-5.4851	-5.50126	-0.5825
H	-5.865	-4.03597	-1.54931
H	-4.28106	-3.98575	1.798297
H	-2.59752	-4.03856	1.154768
H	-3.66888	-5.48594	1.01127
H	-3.62147	-4.22324	-2.38947
H	-3.03448	-5.47417	-1.24936

H	-2.22252	-3.84857	-1.31483
H	1.689209	-1.72054	-1.26297
H	2.625595	2.133233	-2.41511
H	3.196175	3.313112	-1.20129
H	1.73984	2.351384	-0.86465
H	4.369235	0.731994	1.346863
H	2.740791	1.522057	1.326674
H	4.220578	2.480987	1.033553
H	4.51714	-2.60032	-2.71249
H	3.279727	-2.78009	-1.45747
H	6.331752	-2.6438	-1.05144
H	5.308875	-4.08436	-0.90328
H	4.309902	-3.32619	1.167035
H	4.724225	-1.61987	0.849543
H	6.844493	-0.71904	1.44953
H	7.687471	-1.83657	0.32375
H	8.151024	-1.80104	2.059661
H	5.343866	-1.58739	3.167555
H	6.684713	-2.63437	3.761667
H	5.094836	-3.36534	3.334914
H	7.332457	-4.26435	0.531685
H	6.164261	-4.90414	1.746946
H	7.740587	-4.21727	2.282621
H	5.748183	3.263622	-1.07217
H	6.68263	-1.33112	-2.91187
H	8.361778	0.499135	-3.14363

Figure S2.46: Coordinates (Angstroms) and energy (a.u.) of **SQ Cl**. Geometries were optimized using PBE functional and 6-31+G* basis set.

SQ Br			
-6991.71406768331 a.u.			
C	0.761226	-0.53212	-0.18521
C	0.264818	0.578136	0.670301
C	-1.14104	0.164822	0.40015
C	-0.62344	-1.02335	-0.32112
C	-2.26252	0.870472	0.858817
C	-3.63596	0.937862	0.594804
C	-4.55282	1.843957	1.441069
C	-5.89109	1.670947	0.749489
C	-5.73484	0.805388	-0.3459
N	-4.38773	0.358044	-0.39788
O	-1.12283	-2.05863	-0.82927
O	0.747226	1.490052	1.351127
C	-4.09233	3.323615	1.374439
C	-4.59329	1.363085	2.913572
C	-7.12768	2.25634	1.013943
C	-6.79072	0.521288	-1.22166
C	-8.03724	1.114688	-0.95894
C	-8.20227	1.962277	0.150793
C	-3.89737	-0.46476	-1.5018
C	-4.3911	-1.93005	-1.47894
C	-4.03512	-2.60152	-0.15338
N	-4.08995	-4.13331	-0.15345
C	-5.48961	-4.63457	-0.40146

C	-3.63391	-4.59545	1.209591
C	-3.14533	-4.70277	-1.18992
C	1.926878	-1.07322	-0.76522
C	3.202724	-0.5376	-0.937
C	3.727409	0.877632	-0.61929
N	4.22958	-1.24834	-1.55691
C	5.350371	-0.42193	-1.80445
C	5.109258	0.846562	-1.25232
C	2.857274	1.984979	-1.26159
C	3.846765	1.095672	0.914258
C	4.276438	-2.68565	-1.79043
C	5.305751	-3.40002	-0.87079
C	5.018919	-3.13934	0.610624
N	6.225617	-3.28592	1.551108
C	7.249382	-2.20246	1.293975
C	5.729782	-3.14335	2.972551
C	6.866647	-4.64215	1.388298
C	6.074633	1.847934	-1.34484
C	6.534	-0.71677	-2.49741
C	7.505885	0.295196	-2.59685
C	7.280528	1.554247	-2.01324
Br	8.626895	2.895853	-2.12774
Br	-9.89709	2.753659	0.476669
H	-1.95305	1.631643	1.591366
H	-4.02856	3.679758	0.333074
H	-3.10614	3.456367	1.850209
H	-4.81655	3.959282	1.911012

H	-4.94742	0.320762	2.990722
H	-5.28029	2.000075	3.496077
H	-3.59347	1.426464	3.37511
H	-7.26972	2.941463	1.855185
H	-6.67356	-0.11254	-2.10514
H	-8.88104	0.922393	-1.62691
H	-2.79911	-0.45313	-1.47947
H	-4.22457	0.003657	-2.44809
H	-3.87212	-2.41882	-2.32114
H	-5.47552	-1.97856	-1.67523
H	-4.70988	-2.28153	0.657623
H	-2.98798	-2.35724	0.095653
H	-6.15731	-4.2321	0.37471
H	-5.48799	-5.73414	-0.36169
H	-5.82353	-4.30322	-1.39419
H	-4.29286	-4.15928	1.974224
H	-2.59981	-4.25493	1.362302
H	-3.68693	-5.69305	1.249874
H	-3.57567	-4.56273	-2.19019
H	-3.02669	-5.77874	-0.9944
H	-2.18393	-4.17195	-1.113
H	1.7296	-2.04262	-1.24497
H	2.744545	1.822262	-2.34622
H	3.341981	2.964162	-1.10974
H	1.865233	2.027975	-0.78975
H	4.462944	0.304084	1.382135
H	2.848821	1.124626	1.382416

H	4.344371	2.061725	1.1082
H	4.549161	-2.88077	-2.84286
H	3.271882	-3.10446	-1.63843
H	6.313429	-3.04594	-1.14571
H	5.270083	-4.47931	-1.09988
H	4.255118	-3.83383	0.998423
H	4.653844	-2.1102	0.765888
H	6.77658	-1.22126	1.446079
H	7.624432	-2.27892	0.265102
H	8.08104	-2.33285	2.001926
H	5.242917	-2.16334	3.083478
H	6.586708	-3.21751	3.657983
H	5.011214	-3.94872	3.183084
H	7.287576	-4.72494	0.377333
H	6.101798	-5.41676	1.546396
H	7.666666	-4.74787	2.13506
H	5.908155	2.843977	-0.92263
H	6.703561	-1.67844	-2.99315
H	8.435025	0.105557	-3.14153

Figure S2.47: Coordinates (Angstroms) and energy (a.u.) of **SQ Br**. Geometries were optimized using PBE functional and 6-31+G* basis set.

SQ Br no TMAB			
-6487.89765783118 a.u.			
C	1.211363	0.200423	0.004303
C	0.46697	-0.79695	0.814386
C	-0.56456	-0.9063	-0.24581
C	0.174906	0.109057	-1.05014

C	-1.73404	-1.67467	-0.12345
C	-2.82697	-1.98913	-0.93082
C	-4.06989	-2.69914	-0.36072
C	-4.93222	-2.84975	-1.59946
C	-4.25357	-2.2944	-2.70102
N	-3.01136	-1.78142	-2.27478
O	0.035477	0.693365	-2.13904
O	0.586449	-1.34414	1.923724
C	-4.762	-1.81232	0.704154
C	-3.71098	-4.07799	0.244078
C	-6.18848	-3.42876	-1.7586
C	-4.81544	-2.30287	-3.98544
C	-6.08483	-2.88576	-4.14814
C	-6.75582	-3.43883	-3.04707
C	2.346385	1.027498	-0.03105
C	3.394914	1.200034	0.870393
C	3.667615	0.52872	2.225107
N	4.422975	2.086357	0.603336
C	5.376255	2.100852	1.637021
C	4.977282	1.18602	2.629213
C	2.554033	0.847882	3.25606
C	3.848501	-1.00307	2.07187
C	4.514423	2.891807	-0.60386
C	5.756182	0.996356	3.767775
C	6.554678	2.850942	1.759136
C	7.341335	2.660869	2.909171
C	6.942326	1.744306	3.893367

Br	8.033198	1.495761	5.446505
Br	-8.47126	-4.24295	-3.29411
H	-1.80981	-2.10575	0.887027
H	-5.01284	-0.8198	0.294237
H	-4.10381	-1.6697	1.578109
H	-5.69527	-2.29338	1.046172
H	-3.21678	-4.72566	-0.49912
H	-4.62746	-4.58659	0.592081
H	-3.03675	-3.96379	1.109433
H	-6.72554	-3.87031	-0.91377
H	-4.30292	-1.87705	-4.85263
H	-6.5485	-2.90824	-5.13826
H	2.386101	1.630126	-0.94933
H	2.391823	1.93606	3.340738
H	2.855762	0.466273	4.247358
H	1.616548	0.34507	2.969556
H	4.619933	-1.237	1.318679
H	2.893372	-1.47439	1.792961
H	4.167393	-1.43081	3.038507
H	5.45964	3.450818	-0.59795
H	3.676484	3.609169	-0.66167
H	5.46297	0.285774	4.546747
H	6.876769	3.56994	0.999675
H	8.266435	3.230013	3.033611
H	4.491984	2.246455	-1.49923
C	-1.99729	-1.26518	-3.18561
H	-2.44434	-1.11437	-4.17728

H	-1.16785	-1.99127	-3.27071
H	-1.57436	-0.30979	-2.82935

Figure S2.48: Coordinates (Angstroms) and energy (a.u.) of **SQ Br no TMAB**. Geometries were optimized using PBE functional and 6-31+G* basis set.

CY H			
-1946.06983345369 a.u.			
C	7.606934	-1.78784	0.404386
C	7.862877	-3.15193	0.664722
C	8.791519	-5.35727	0.050152
C	9.904627	-6.21471	-0.08194
C	9.845745	-7.61959	-0.13074
C	10.92123	-8.5321	-0.06912
N	10.7365	-9.8773	-0.1793
C	9.463441	-10.5655	-0.42967
C	8.707747	-10.9309	0.858506
C	7.365932	-11.6206	0.565225
C	11.95003	-10.5896	0.011228
C	12.16445	-11.9731	-1.8E-05
C	13.48098	-12.4149	0.213739
C	14.5299	-11.5022	0.425709
C	14.2874	-10.1152	0.43062
C	12.98342	-9.66435	0.224396
C	12.41911	-8.2553	0.146232
C	12.69286	-7.47205	1.452773
C	13.02478	-7.53271	-1.08688
C	8.901448	-3.9223	0.026183
H	8.245711	-1.33434	-0.35511

H	10.87765	-5.71459	-0.11401
H	8.854233	-8.07657	-0.21638
H	9.696837	-11.4711	-1.01449
H	8.84976	-9.92577	-1.08663
H	8.539726	-10.0123	1.455225
H	9.342109	-11.5904	1.479907
H	6.74362	-10.9611	-0.07299
H	7.543985	-12.5376	-0.0289
H	11.35786	-12.6943	-0.15978
H	13.68908	-13.4891	0.215209
H	15.54563	-11.8748	0.58904
H	15.11234	-9.41286	0.593334
H	12.24342	-7.97896	2.322703
H	12.29895	-6.44343	1.404582
H	13.7809	-7.41047	1.621908
H	12.83826	-8.09867	-2.01459
H	14.11627	-7.44263	-0.95674
H	12.60962	-6.5198	-1.20766
C	2.283793	-0.43831	2.936853
C	3.229781	0.056594	1.830452
C	4.537181	0.633647	2.398259
N	5.44417	1.11976	1.349788
C	5.358557	2.44361	0.845399
C	4.501014	3.4754	1.245901
C	4.632368	4.705499	0.580279
C	5.584912	4.882311	-0.43924
C	6.435089	3.827648	-0.82327

C	6.312255	2.599428	-0.17203
C	7.073143	1.294921	-0.35173
C	6.878683	0.756803	-1.79249
C	8.57334	1.519192	-0.02878
C	6.393176	0.392416	0.696577
C	6.637499	-0.9639	0.998459
H	2.061886	0.394802	3.630881
H	2.797102	-1.21195	3.542798
H	2.726142	0.832852	1.224259
H	3.467846	-0.77341	1.135958
H	5.073901	-0.11012	3.010177
H	4.327092	1.484815	3.066907
H	3.755522	3.348265	2.036361
H	3.980381	5.537633	0.862569
H	5.665624	5.851652	-0.94029
H	7.173554	3.978706	-1.61815
H	7.286334	1.486129	-2.51233
H	5.810108	0.613888	-2.02416
H	7.400149	-0.2016	-1.95241
H	8.989105	2.258445	-0.73364
H	9.160683	0.59175	-0.12551
H	8.70901	1.909984	0.993327
H	6.013118	-1.39235	1.789068
C	6.596773	-11.9849	1.841044
C	0.972499	-1.00509	2.377278
H	6.370944	-11.0895	2.44914
H	7.177345	-12.679	2.473769

H	5.639456	-12.4767	1.600646
H	1.16394	-1.83116	1.667824
H	0.397264	-0.23115	1.839857
H	0.331037	-1.39589	3.184585
C	6.967908	-3.95286	1.557452
N	6.334789	-5.11328	0.757648
C	7.464725	-6.04178	0.3316
C	5.589756	-4.59325	-0.44608
C	5.372251	-5.86833	1.635253
H	6.129962	-3.37635	1.97429
H	7.503005	-4.44859	2.387029
H	7.073932	-6.60252	-0.53896
H	7.592015	-6.76464	1.157183
H	6.29779	-4.09405	-1.11954
H	4.826429	-3.87615	-0.10986
H	5.110383	-5.44436	-0.95237
H	5.878927	-6.14085	2.572729
H	5.041268	-6.77526	1.107643
H	4.505848	-5.2255	1.849843
N	10.00136	-3.3274	-0.56863
C	10.60023	-2.0743	-0.07283
C	12.12984	-2.14925	-0.1663
N	12.48818	-2.36642	-1.56517
C	11.99921	-3.66227	-2.02294
C	10.46974	-3.68693	-1.92633
H	10.27629	-1.90924	0.966501
H	10.2823	-1.2155	-0.69792

H	12.50064	-2.95242	0.515552
H	12.551	-1.18862	0.17614
H	13.49775	-2.27583	-1.71403
H	12.41638	-4.50731	-1.42414
H	12.29218	-3.81544	-3.07568
H	10.07397	-4.67564	-2.2003
H	10.06332	-2.93665	-2.63651

Figure S2.49: Coordinates (Angstroms) and energy (a.u.) of **CY H.** Geometries were optimized using PBE functional and 6-31+G* basis set.

CY Cl			
-2864.86924296899 a.u.			
C	7.606302	-1.78655	0.409547
C	7.861703	-3.15042	0.671239
C	8.792871	-5.35588	0.059185
C	9.90559	-6.2131	-0.07628
C	9.845262	-7.61823	-0.13005
C	10.9173	-8.53377	-0.07219
N	10.72894	-9.87881	-0.19318
C	9.454777	-10.5623	-0.45285
C	8.695379	-10.9388	0.82979
C	7.352732	-11.6226	0.526028
C	11.93682	-10.5945	-0.00322
C	12.15373	-11.9777	-0.02274
C	13.4636	-12.4303	0.192495
C	14.50863	-11.5131	0.415133
C	14.27632	-10.1224	0.430419
C	12.97399	-9.67592	0.221013

C	12.41616	-8.2631	0.149936
C	12.68847	-7.48982	1.462523
C	13.02965	-7.53626	-1.07658
C	8.901919	-3.92084	0.03507
H	8.244191	-1.3348	-0.35177
H	10.87878	-5.71322	-0.10879
H	8.852981	-8.07286	-0.21942
H	9.687157	-11.4621	-1.0471
H	8.844349	-9.91442	-1.10468
H	8.527796	-10.026	1.435397
H	9.32624	-11.6061	1.446502
H	6.733238	-10.9546	-0.10605
H	7.530121	-12.5332	-0.07802
H	11.35084	-12.7011	-0.19066
H	13.67912	-13.5019	0.189649
Cl	16.12271	-12.1077	0.679315
H	15.1079	-9.43189	0.602712
H	12.23408	-8.00033	2.327704
H	12.29743	-6.46006	1.418545
H	13.77599	-7.43158	1.636164
H	12.8454	-8.09616	-2.00838
H	14.12079	-7.4486	-0.94178
H	12.61665	-6.52204	-1.19274
C	2.289246	-0.42866	2.958119
C	3.231454	0.063165	1.847052
C	4.541042	0.640681	2.409191
N	5.445144	1.12411	1.356425

C	5.357569	2.443733	0.84956
C	4.505987	3.482126	1.24681
C	4.629377	4.709986	0.580566
C	5.579757	4.871741	-0.44593
C	6.430928	3.817506	-0.83535
C	6.304985	2.598047	-0.17403
C	7.067406	1.293819	-0.35412
C	6.867362	0.752127	-1.79249
C	8.568298	1.522216	-0.0376
C	6.391964	0.394008	0.70044
C	6.637807	-0.9608	1.004054
H	2.07008	0.406331	3.65077
H	2.804601	-1.20085	3.564085
H	2.725463	0.837967	1.240879
H	3.466702	-0.76847	1.153628
H	5.079862	-0.10232	3.020064
H	4.334122	1.492806	3.077814
H	3.763431	3.365778	2.041511
H	3.985655	5.549681	0.855791
Cl	5.707497	6.406756	-1.25578
H	7.16087	3.973842	-1.63533
H	7.273472	1.477986	-2.51673
H	5.798022	0.608628	-2.02005
H	7.387689	-0.2071	-1.9499
H	8.981541	2.258609	-0.74695
H	9.15537	0.594637	-0.13285
H	8.707561	1.916749	0.982553

H	6.015577	-1.38762	1.797284
C	6.580285	-11.9991	1.796293
C	0.975915	-0.99655	2.404434
H	6.356018	-11.1099	2.413939
H	7.157508	-12.702	2.422274
H	5.622021	-12.4852	1.548545
H	1.164313	-1.82677	1.699082
H	0.400401	-0.22467	1.864361
H	0.335975	-1.38195	3.215482
C	6.965527	-3.95084	1.563413
N	6.335013	-5.11252	0.763587
C	7.466198	-6.04081	0.340957
C	5.59236	-4.59415	-0.44237
C	5.370867	-5.86717	1.639961
H	6.12609	-3.37444	1.977408
H	7.499154	-4.4449	2.394919
H	7.076963	-6.60375	-0.52887
H	7.59324	-6.76177	1.16822
H	6.301713	-4.09594	-1.11516
H	4.828476	-3.87659	-0.10848
H	5.113838	-5.44587	-0.94844
H	5.875386	-6.13816	2.579039
H	5.041787	-6.77496	1.112656
H	4.50345	-5.22473	1.851578
N	10.00177	-3.32523	-0.55933
C	10.60075	-2.07264	-0.06223
C	12.13048	-2.14802	-0.15461

N	12.48962	-2.36483	-1.55324
C	12.00077	-3.66011	-2.01217
C	10.47119	-3.68428	-1.91674
H	10.27617	-1.90804	0.976957
H	10.28371	-1.21335	-0.68716
H	12.50056	-2.95149	0.527309
H	12.5517	-1.18766	0.188467
H	13.49909	-2.27337	-1.70214
H	12.41717	-4.50576	-1.41344
H	12.29456	-3.81286	-3.06472
H	10.07507	-4.67262	-2.19165
H	10.06587	-2.93344	-2.62695

Figure S2.50: Coordinates (Angstroms) and energy (a.u.) of **CY Cl.** Geometries were optimized using PBE functional and 6-31+G* basis set.

CY Br			
-7091.82109394151 a.u.			
C	7.604397	-1.78727	0.419696
C	7.860851	-3.15097	0.681026
C	8.792423	-5.35602	0.067184
C	9.904064	-6.21372	-0.07462
C	9.842434	-7.61885	-0.12687
C	10.91384	-8.53549	-0.07984
N	10.72077	-9.88098	-0.19125
C	9.442186	-10.5628	-0.43253
C	8.694022	-10.9294	0.859705
C	7.348321	-11.6139	0.572605
C	11.92967	-10.5982	-0.01725

C	12.14257	-11.982	-0.03186
C	13.45527	-12.4367	0.163642
C	14.50696	-11.5213	0.361504
C	14.27794	-10.1297	0.372699
C	12.97271	-9.68099	0.184444
C	12.41671	-8.26698	0.115917
C	12.71323	-7.48853	1.420178
C	13.01077	-7.54747	-1.12442
C	8.901223	-3.92095	0.04416
H	8.243916	-1.334	-0.33931
H	10.87744	-5.71482	-0.11238
H	8.848833	-8.07271	-0.20414
H	9.666714	-11.4671	-1.02295
H	8.826809	-9.91805	-1.08285
H	8.532787	-10.0122	1.46039
H	9.329742	-11.593	1.475345
H	6.723798	-10.9501	-0.05887
H	7.519793	-12.5291	-0.02639
H	11.33512	-12.7044	-0.18122
H	13.66264	-13.5099	0.163497
Br	16.2676	-12.1737	0.619406
H	15.11129	-9.43654	0.524594
H	12.26883	-7.99196	2.294668
H	12.3278	-6.45664	1.377032
H	13.80351	-7.43593	1.577435
H	12.81192	-8.11319	-2.04963
H	14.10388	-7.45934	-1.007

H	12.59628	-6.53382	-1.24061
C	2.26191	-0.44696	2.914473
C	3.214786	0.055423	1.817079
C	4.517216	0.631644	2.396836
N	5.433157	1.119533	1.356449
C	5.352582	2.441449	0.855157
C	4.496904	3.478557	1.24678
C	4.632109	4.711145	0.590259
C	5.597786	4.878755	-0.42075
C	6.450827	3.824575	-0.80627
C	6.313506	2.60058	-0.15506
C	7.076255	1.296321	-0.33354
C	6.892102	0.763401	-1.77735
C	8.573675	1.52066	0.001584
C	6.388102	0.392084	0.708723
C	6.632182	-0.96319	1.010753
H	2.032891	0.382013	3.611111
H	2.773025	-1.22237	3.519897
H	2.713257	0.833374	1.211302
H	3.458968	-0.77085	1.120282
H	5.049287	-0.11351	3.010968
H	4.302171	1.481156	3.066204
H	3.742956	3.358403	2.030265
H	3.983949	5.546984	0.865606
Br	5.760402	6.559728	-1.28434
H	7.193531	3.980298	-1.59427
H	7.307377	1.493387	-2.49222

H	5.82533	0.622711	-2.01842
H	7.412961	-0.19549	-1.93502
H	8.996308	2.259751	-0.69936
H	9.160291	0.592486	-0.09104
H	8.701643	1.910033	1.025189
H	6.005042	-1.39187	1.79912
C	6.586139	-11.9813	1.851756
C	0.956228	-1.01403	2.342304
H	6.364686	-11.0877	2.464137
H	7.169145	-12.6783	2.478977
H	5.626854	-12.471	1.615165
H	1.1546	-1.83788	1.632208
H	0.384313	-0.23941	1.802387
H	0.308733	-1.40794	3.143205
C	6.965571	-3.95167	1.573821
N	6.335232	-5.1139	0.774899
C	7.466852	-6.0416	0.353218
C	5.592449	-4.59679	-0.43149
C	5.371557	-5.86839	1.651851
H	6.1263	-3.37571	1.9887
H	7.500212	-4.44524	2.404975
H	7.077203	-6.60754	-0.51447
H	7.595889	-6.76011	1.182358
H	6.301673	-4.09895	-1.10469
H	4.828412	-3.87909	-0.09825
H	5.114148	-5.44909	-0.93681
H	5.87619	-6.13802	2.59126

H	5.043237	-6.77699	1.125451
H	4.503643	-5.22639	1.862744
N	10.00065	-3.32431	-0.55026
C	10.59938	-2.07221	-0.05187
C	12.12917	-2.14708	-0.14373
N	12.48897	-2.36301	-1.54235
C	12.00013	-3.658	-2.0022
C	10.47041	-3.68167	-1.90788
H	10.27456	-1.90864	0.987414
H	10.28234	-1.21239	-0.67615
H	12.49925	-2.95082	0.537848
H	12.54998	-1.18678	0.200007
H	13.49857	-2.2718	-1.69054
H	12.4159	-4.5039	-1.4033
H	12.29471	-3.81035	-3.0546
H	10.07394	-4.66937	-2.18457
H	10.06599	-2.92963	-2.61734

Figure S2.51: Coordinates (Angstroms) and energy (a.u.) of **CY Br.** Geometries were optimized using PBE functional and 6-31+G* basis set.

Chapter 3:

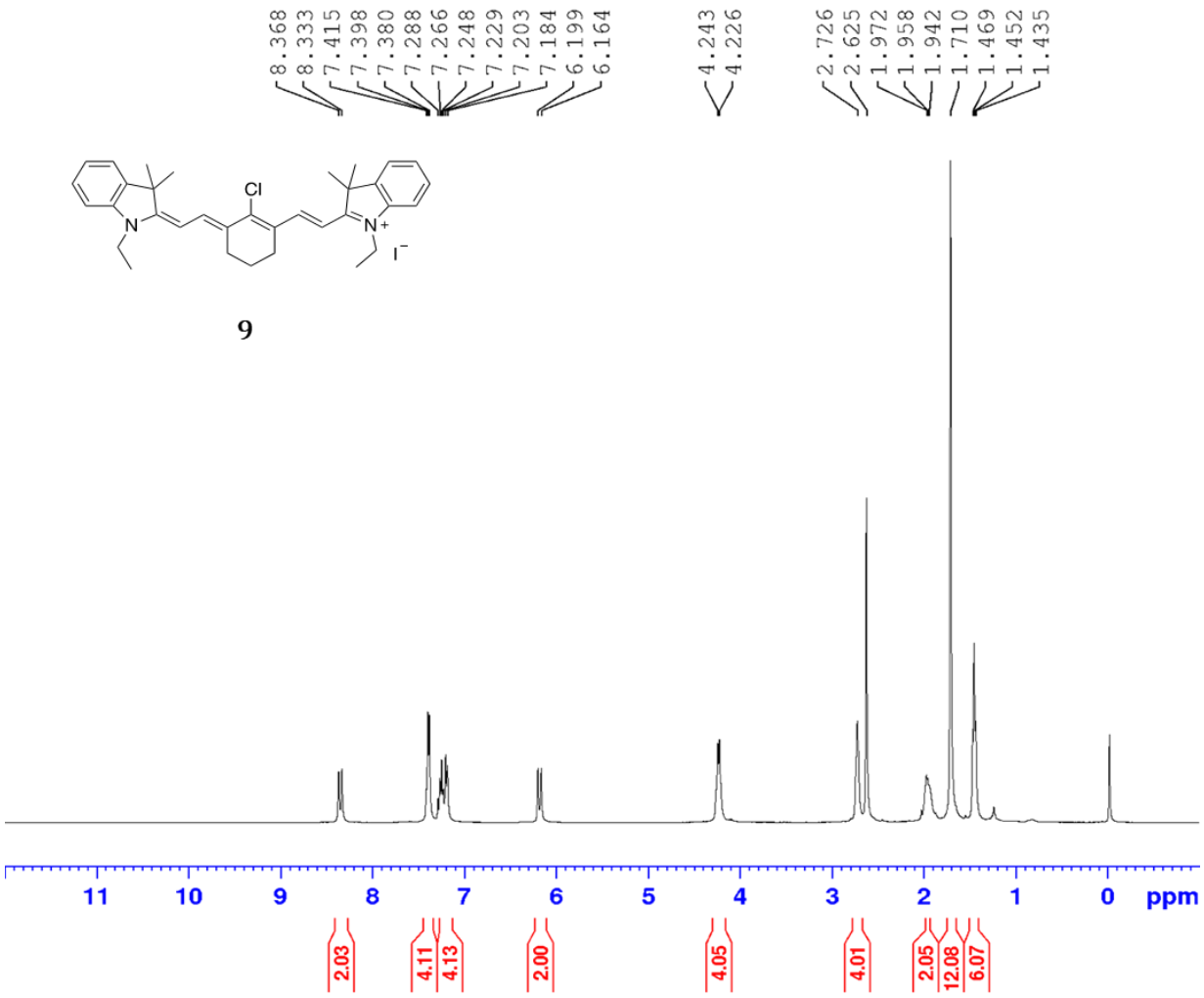

Figure S3.1: ^{1}H NMR spectrum of **compound 9.**

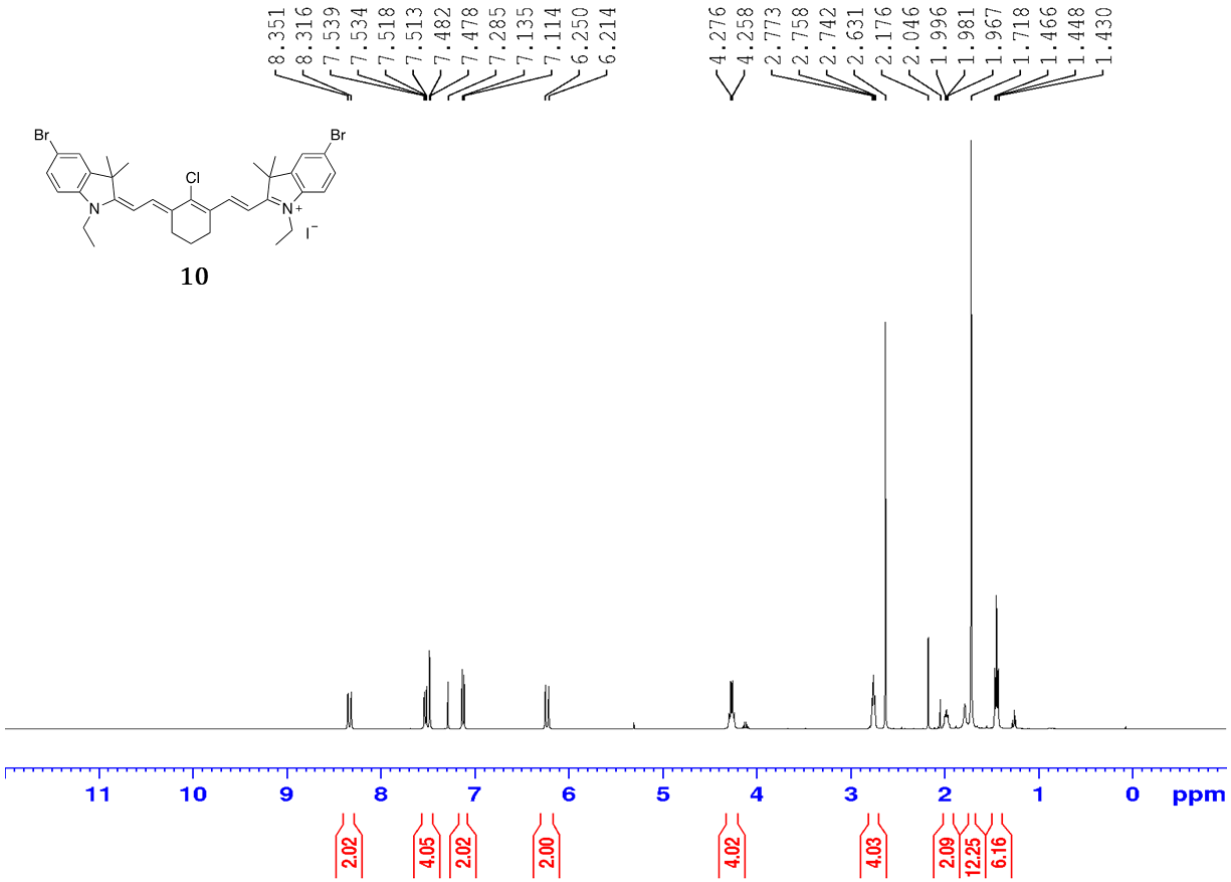

Figure S3.2: ^{1}H NMR spectrum of **compound 10.**

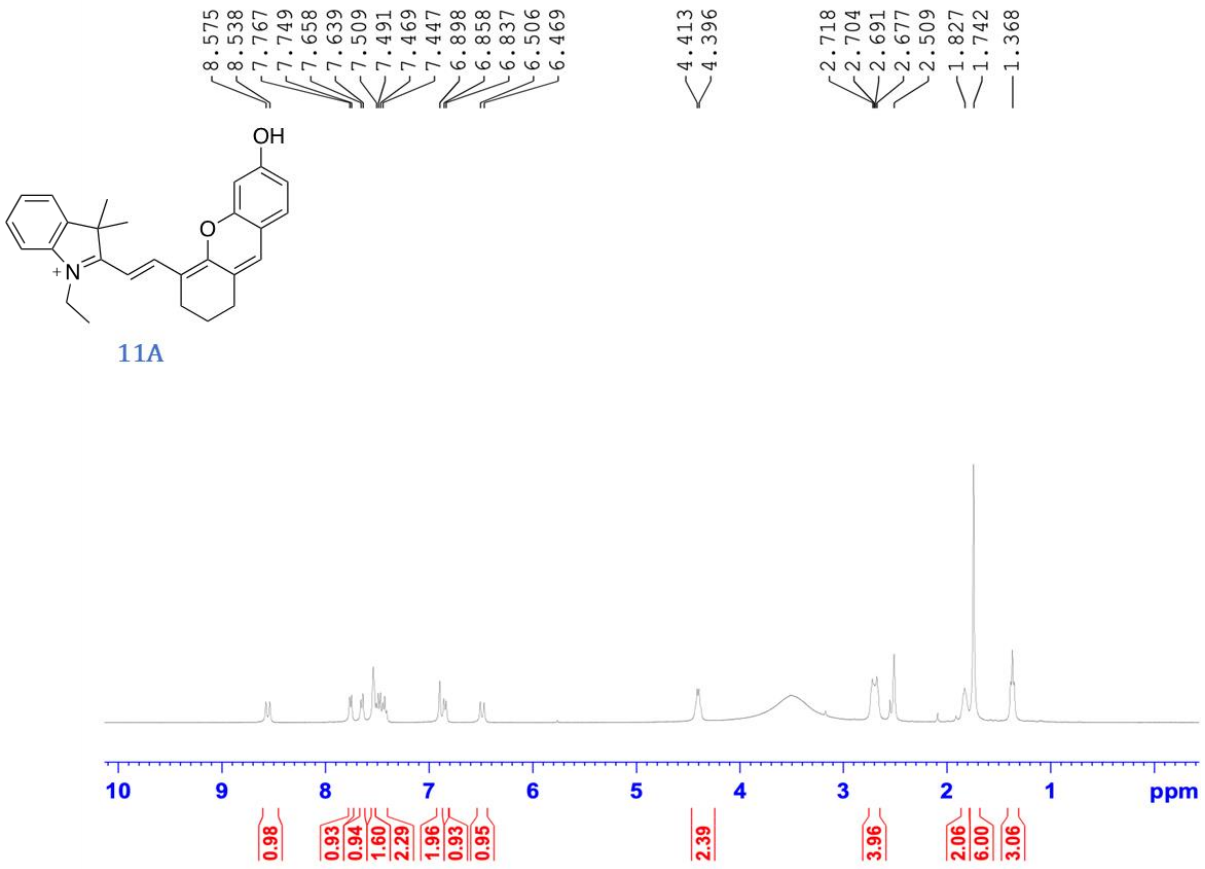

Figure S3.3: ^{1}H NMR spectrum of **compound 11A.**

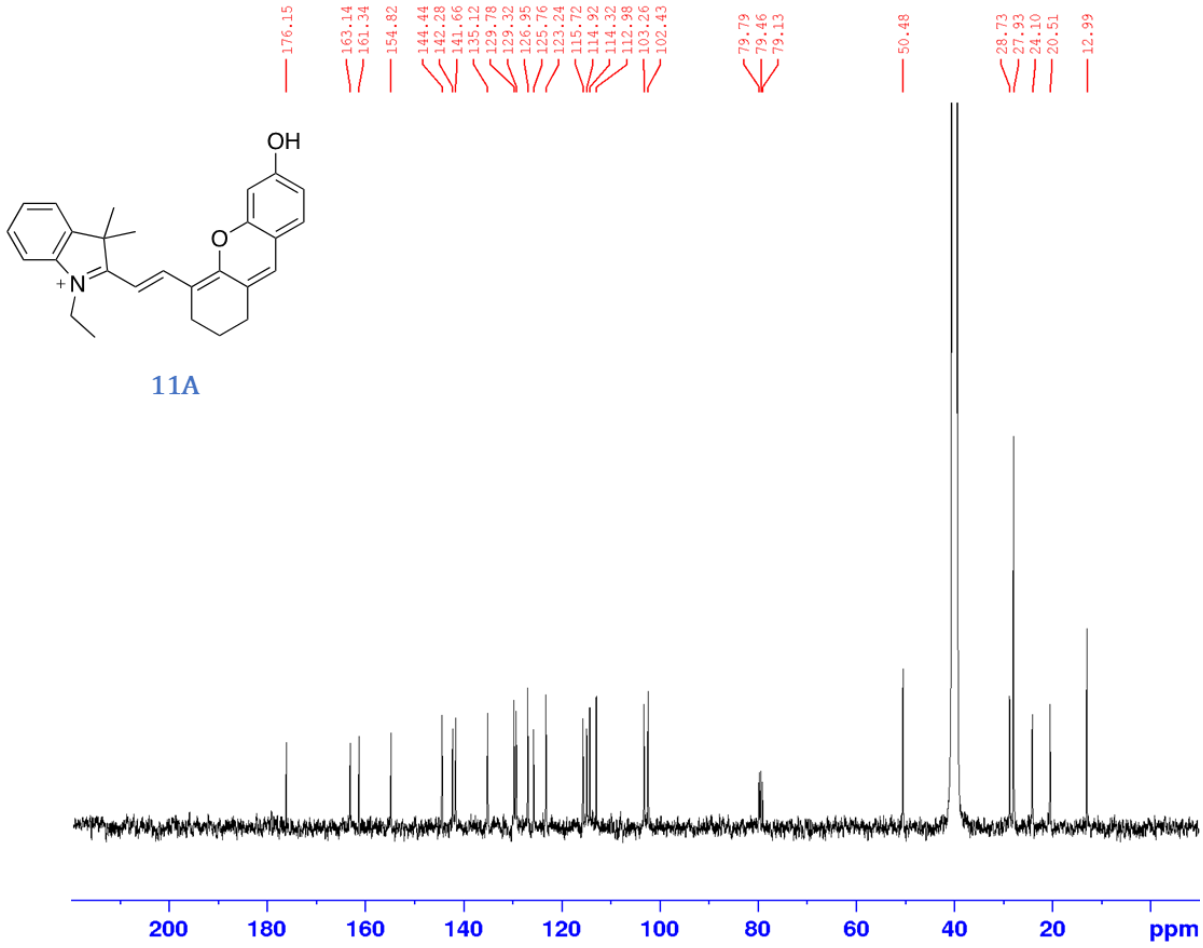

Figure S3.4: ^{13}C NMR spectrum of **compound 11A.**

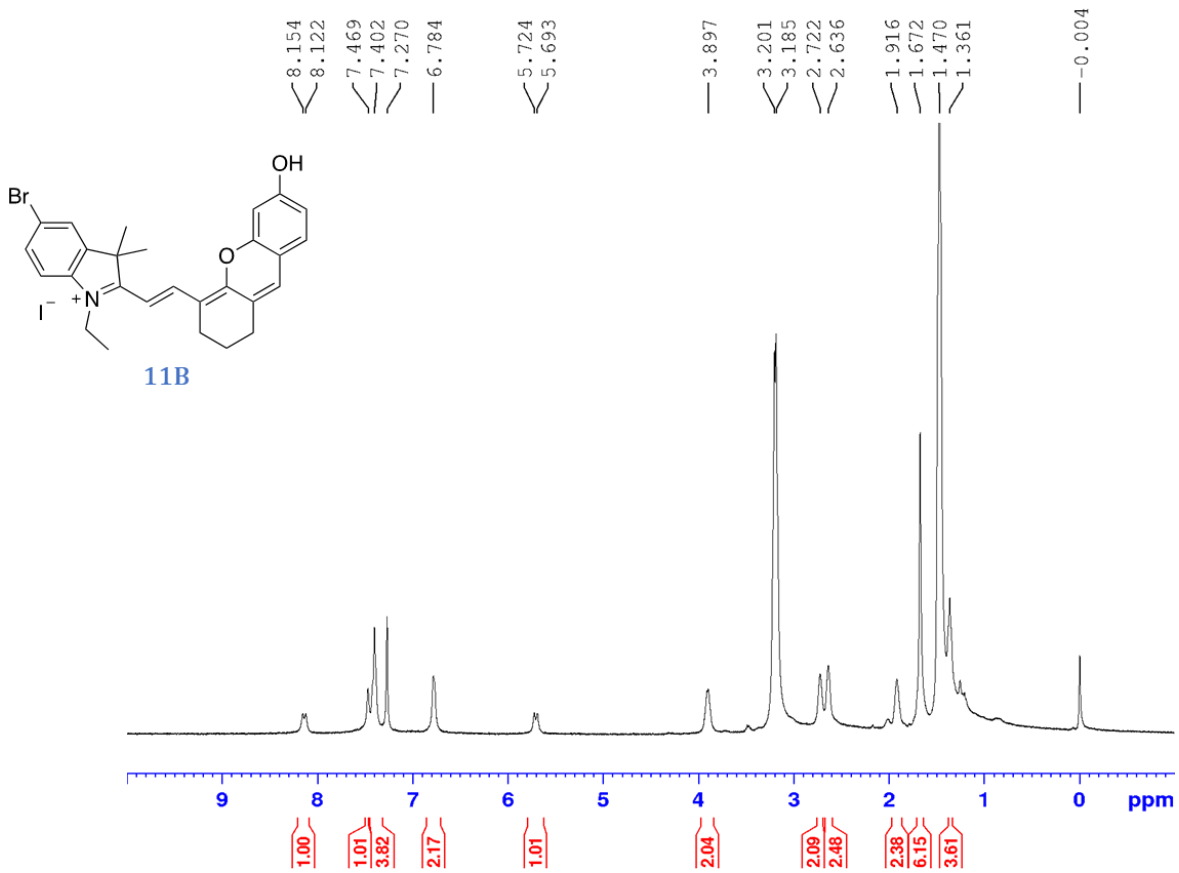

Figure S3.5: ^{1}H NMR spectrum of **compound 11B.**

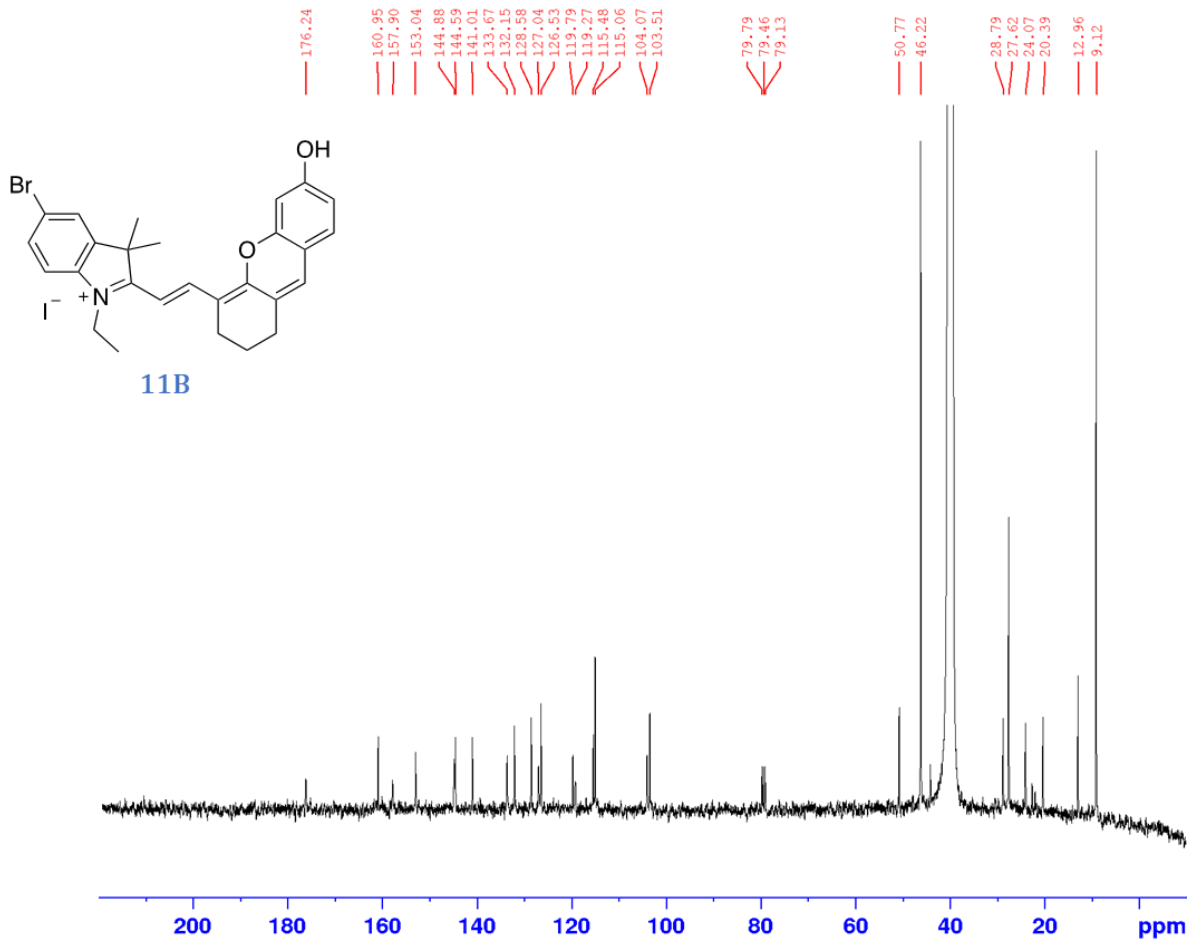

Figure S3.6: ^{13}C NMR spectrum of **compound 11B.**

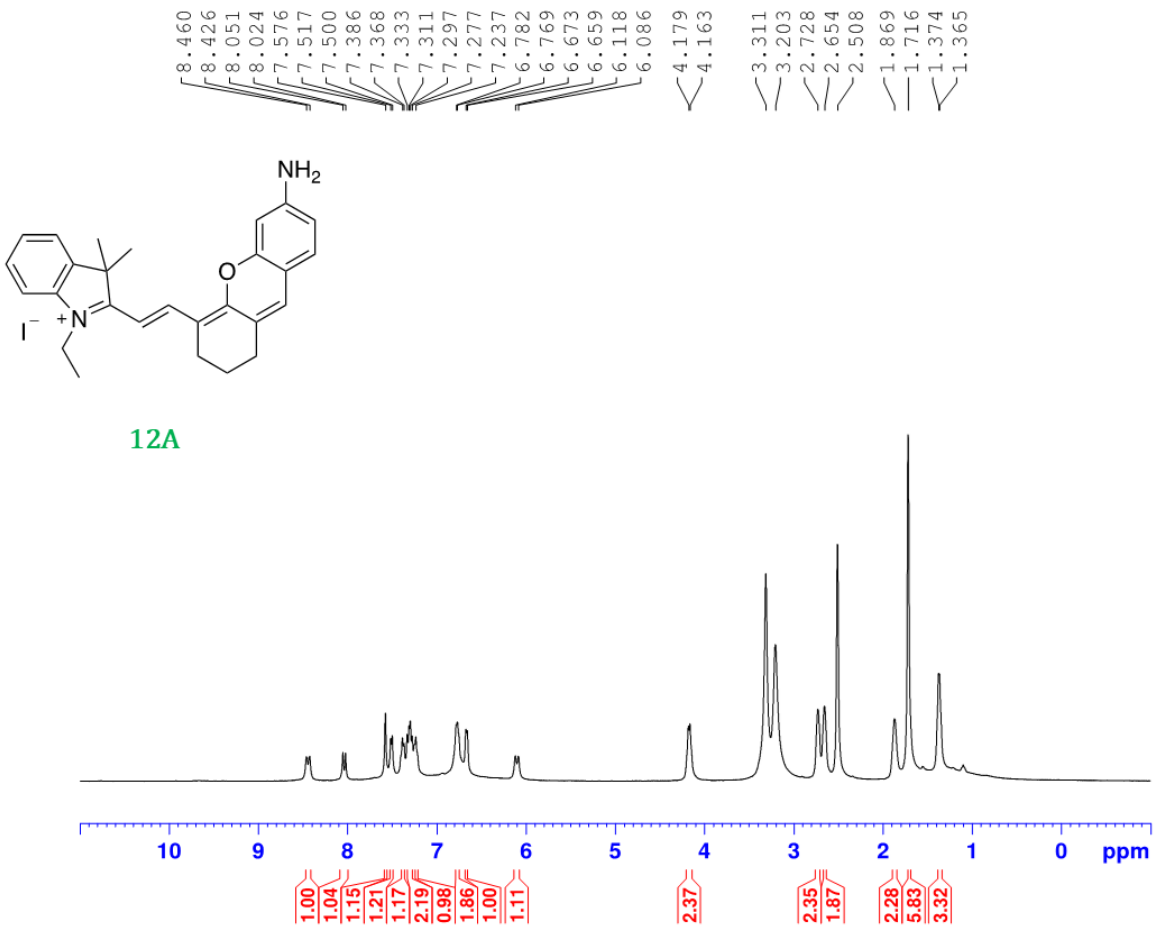

Figure S3.7: ^{1}H NMR spectrum of **compound 12A.**

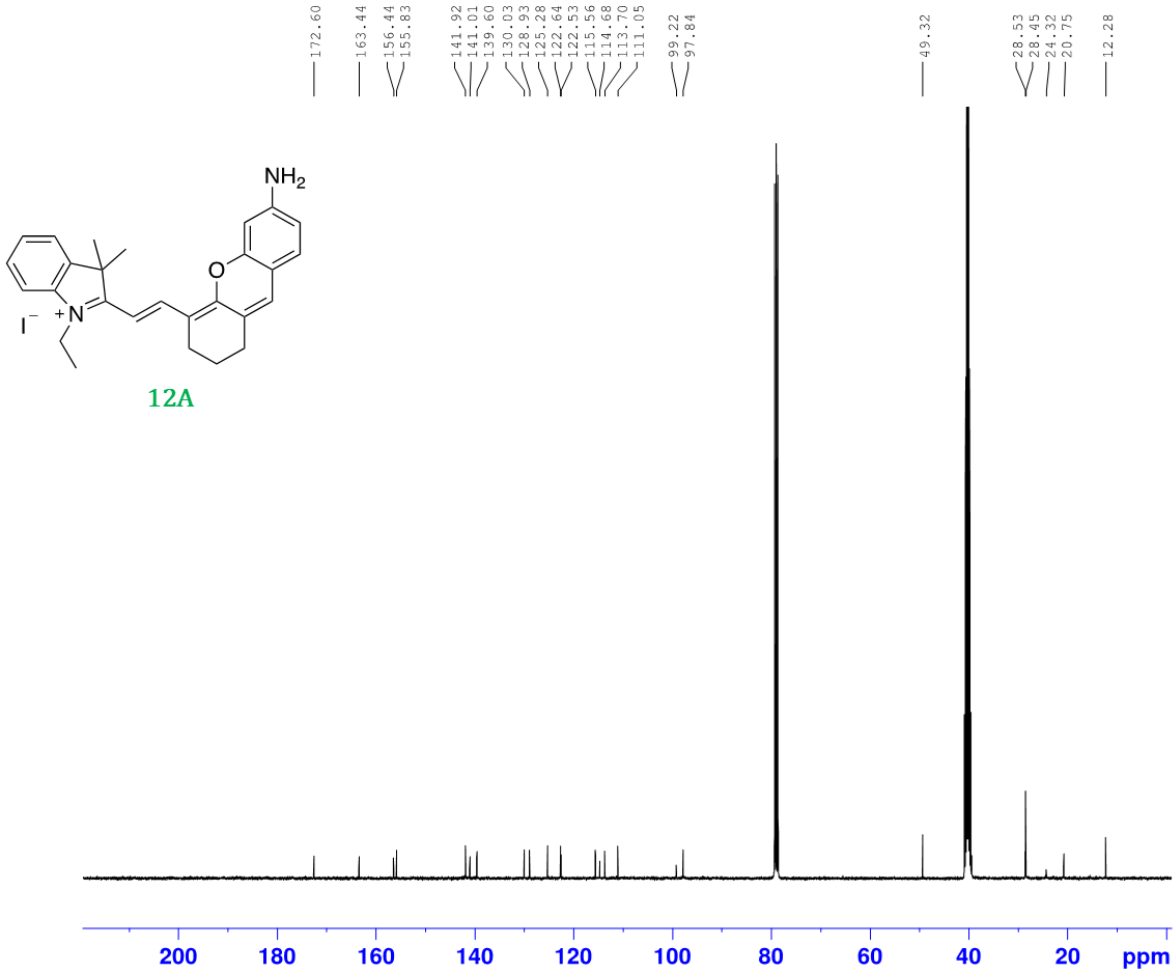

Figure S3.8: ^{13}C NMR spectrum of **compound 12A.**

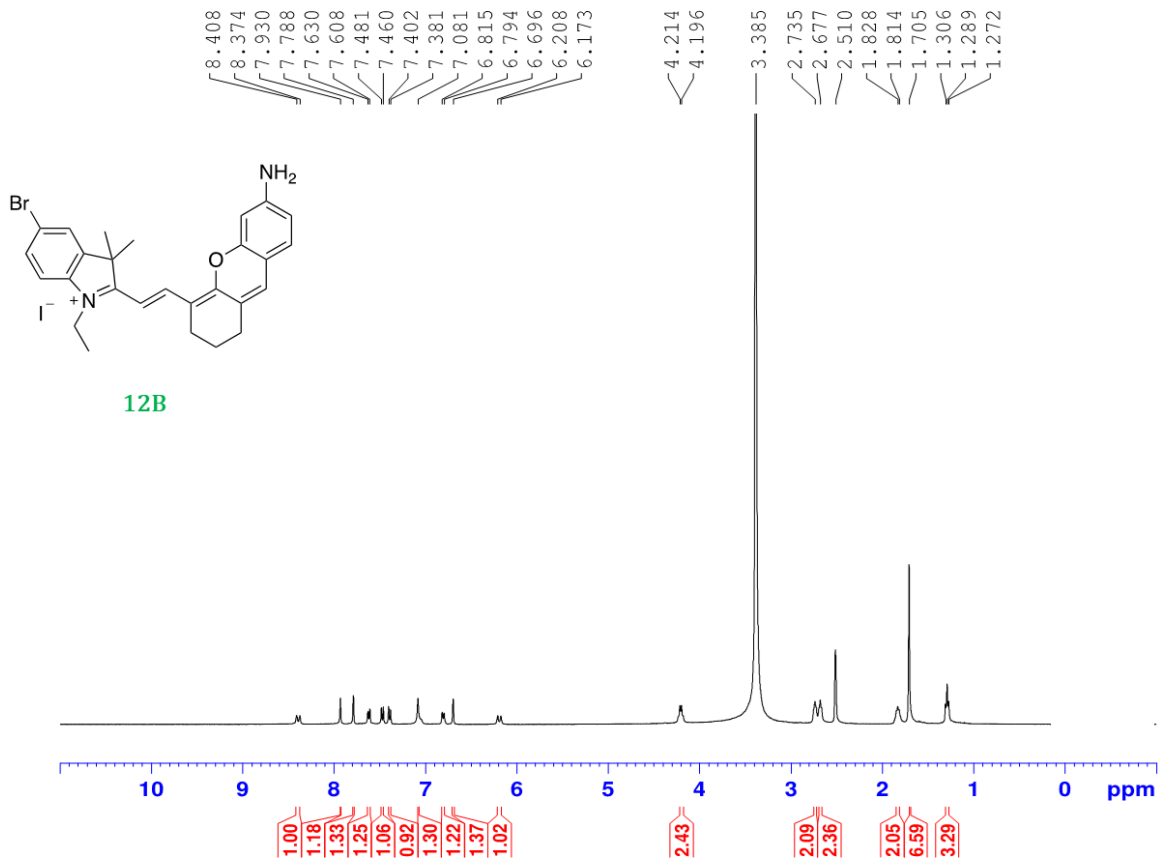

Figure S3.9: ^{1}H NMR spectrum of **compound 12B.**

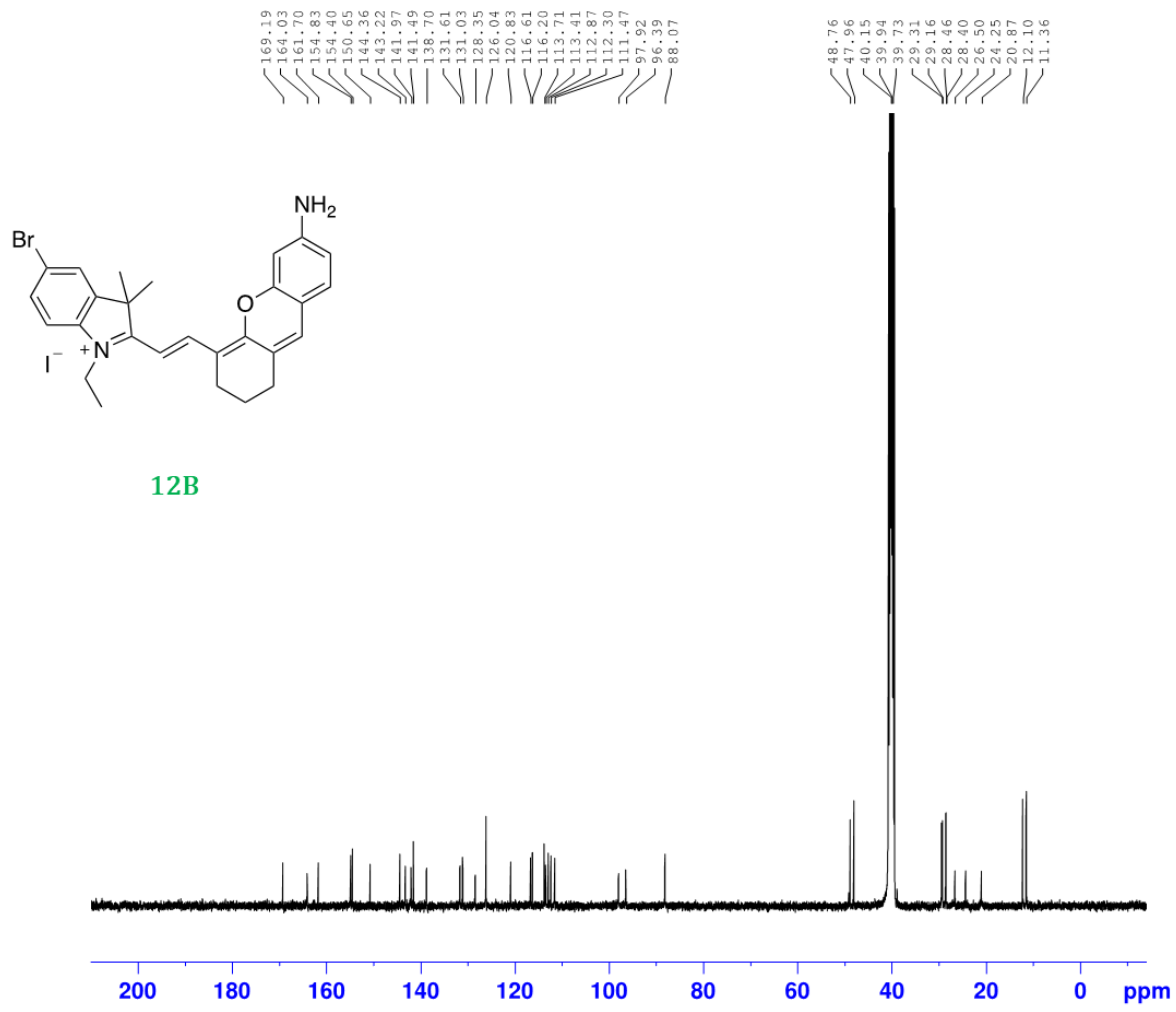

Figure S3.10: ^{13}C NMR spectrum of **compound 12B.**

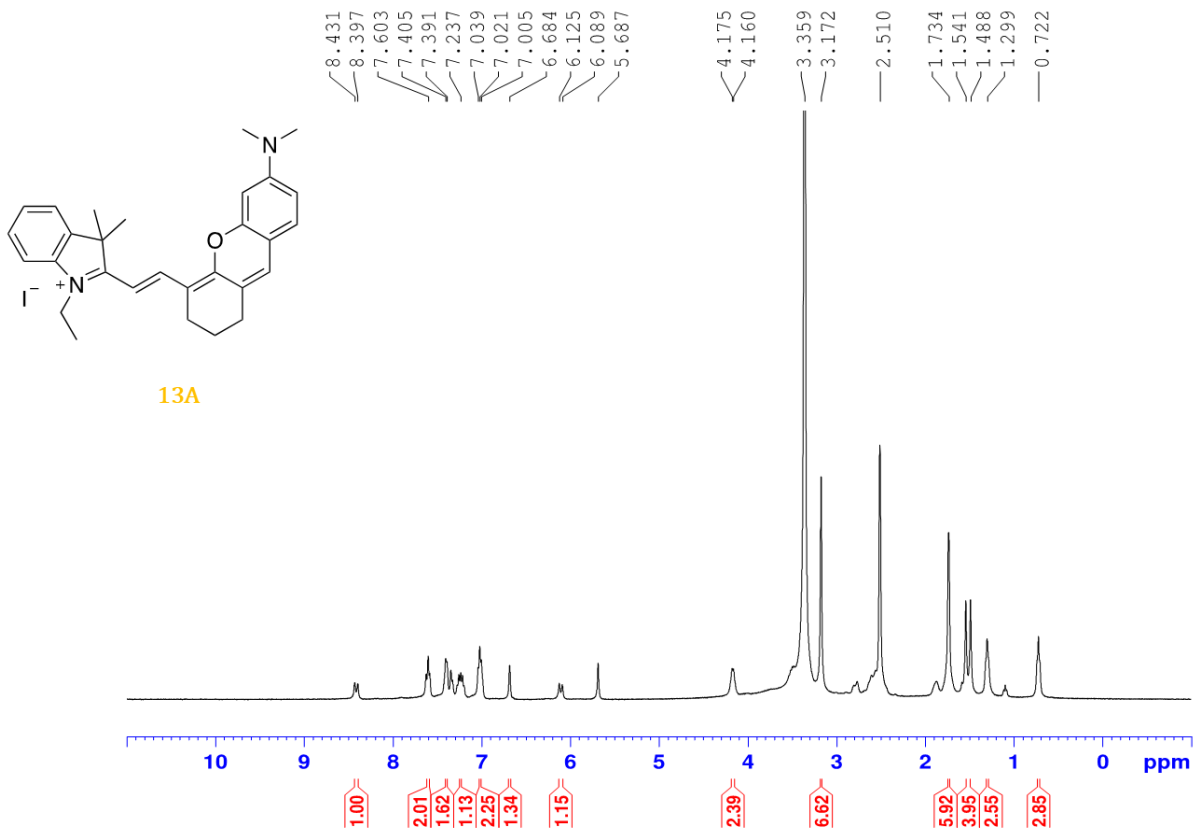

Figure S3.11: ^{1}H NMR spectrum of **compound 13A.**

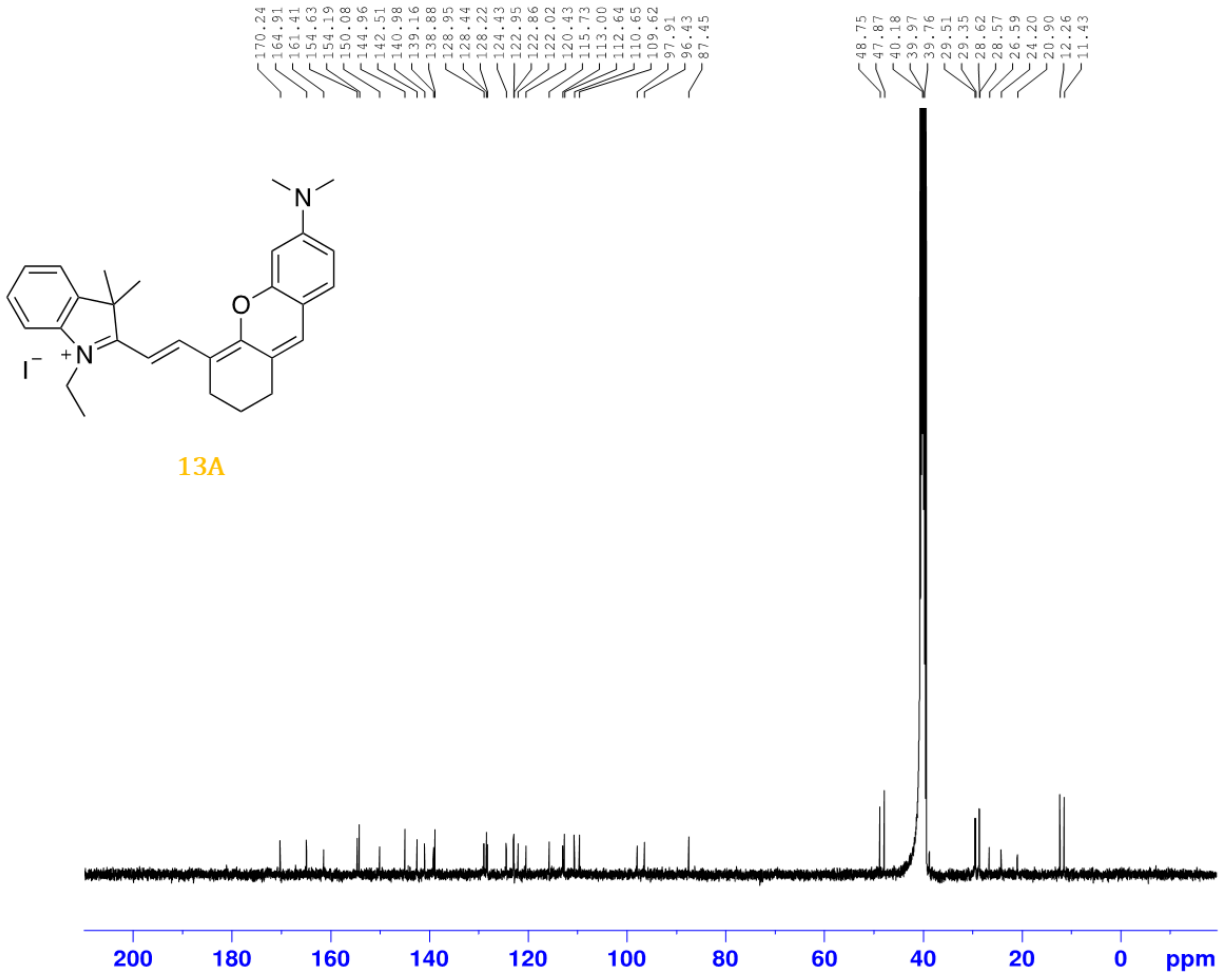

Figure S3.12: ^{13}C NMR spectrum of **compound 13A.**

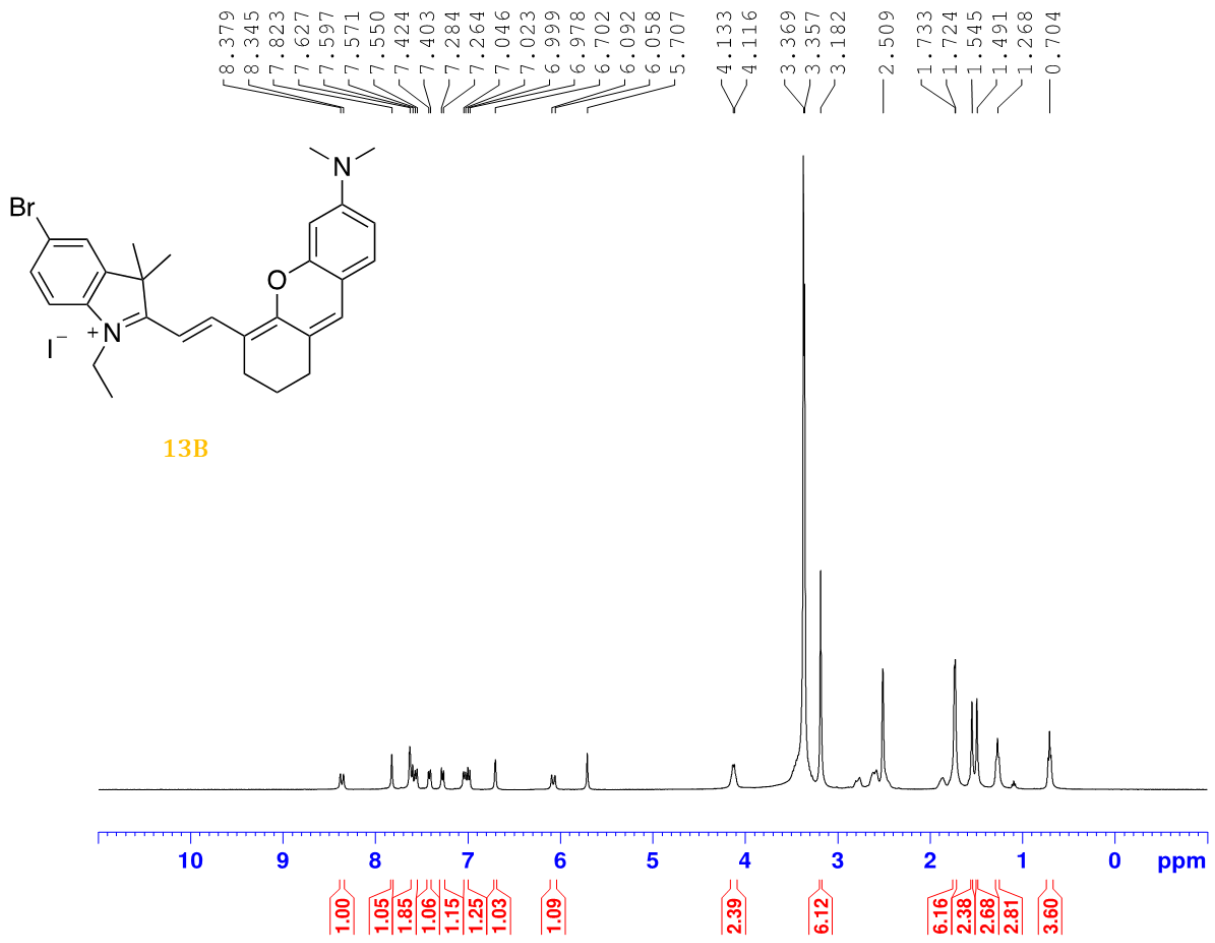

Figure S3.13: ^{1}H NMR spectrum of **compound 13B.**

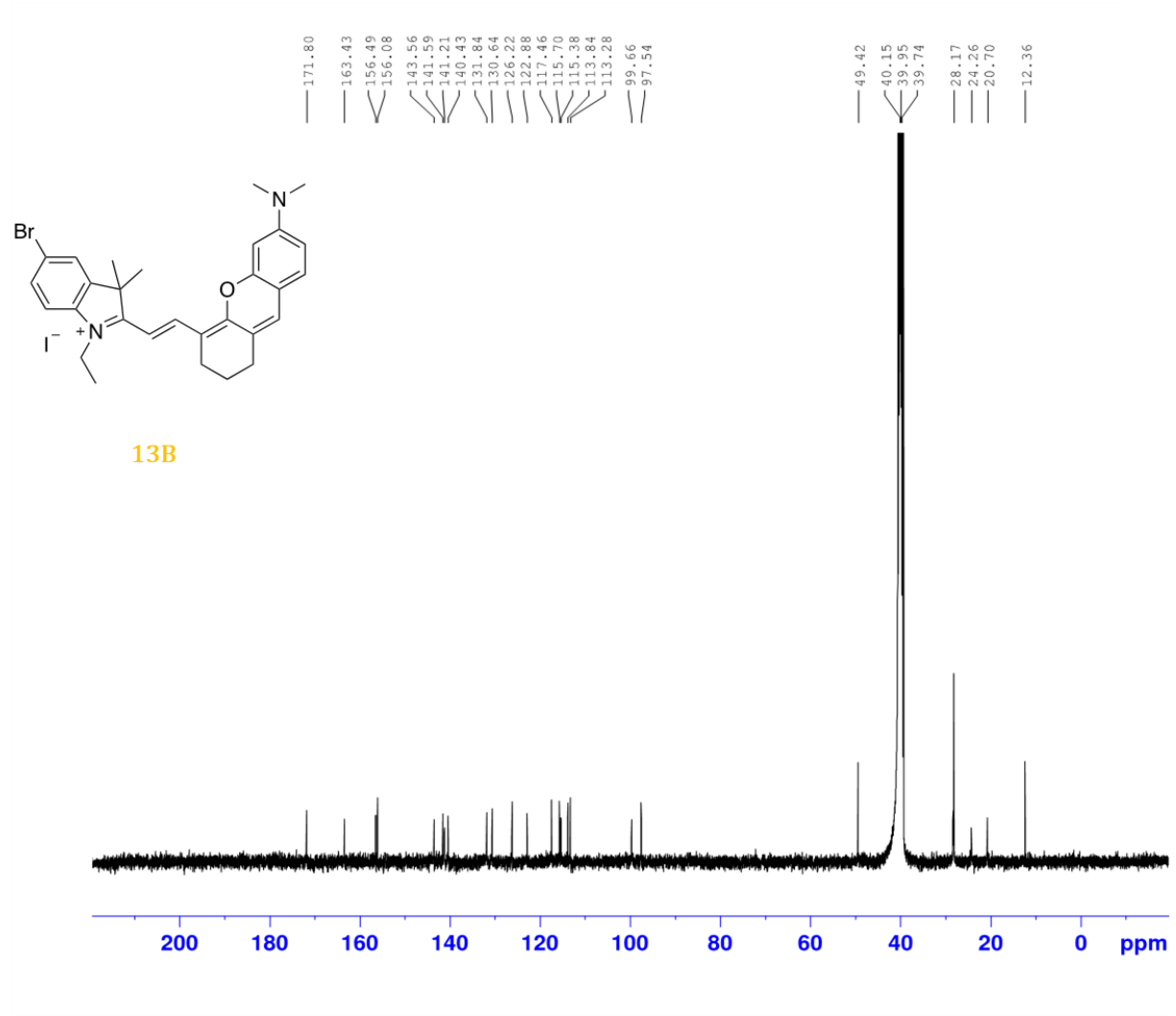

Figure S3.14: ^{13}C NMR spectrum of **compound 13B.**

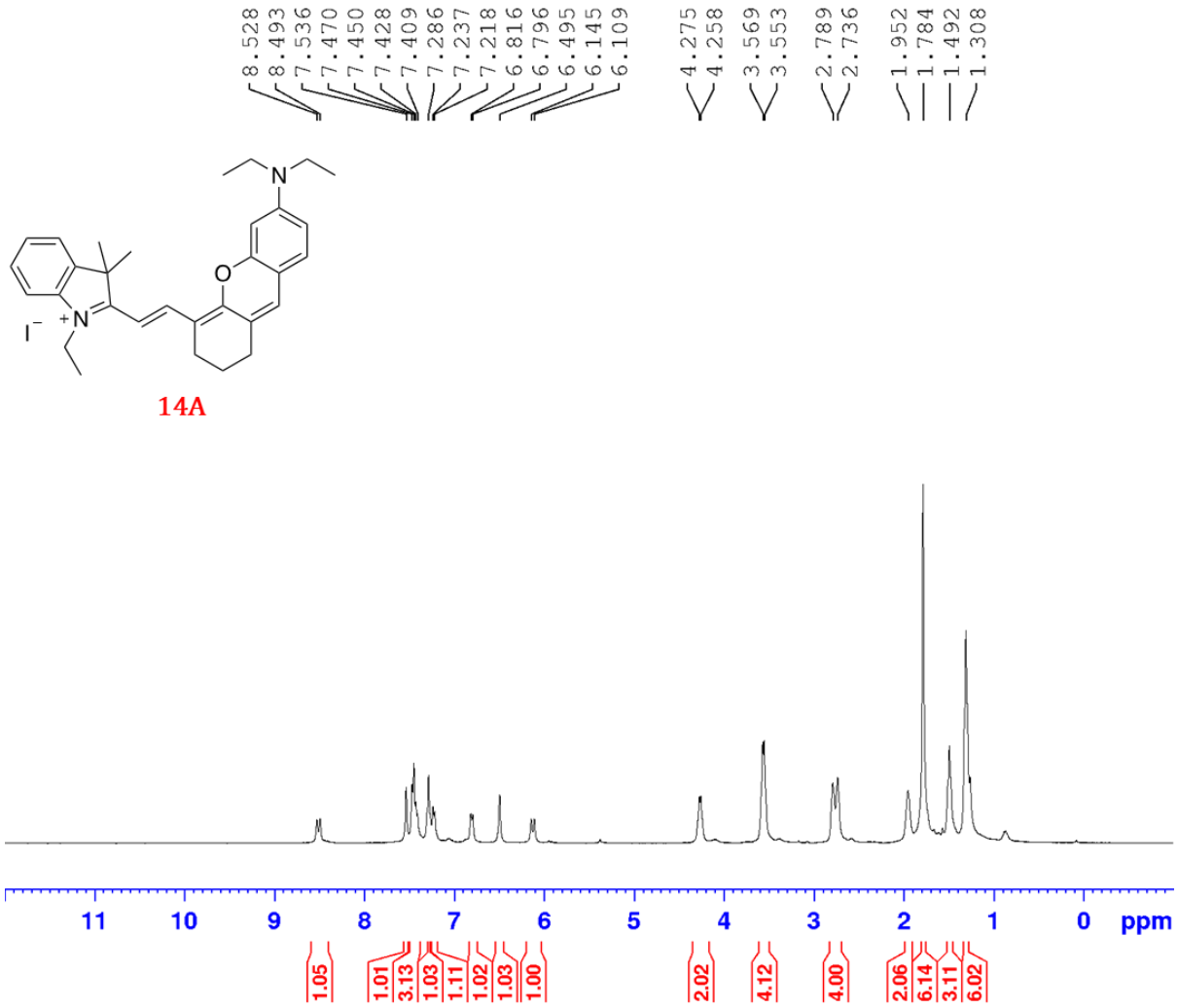

Figure S3.15: ^{1}H NMR spectrum of **compound 14A.**

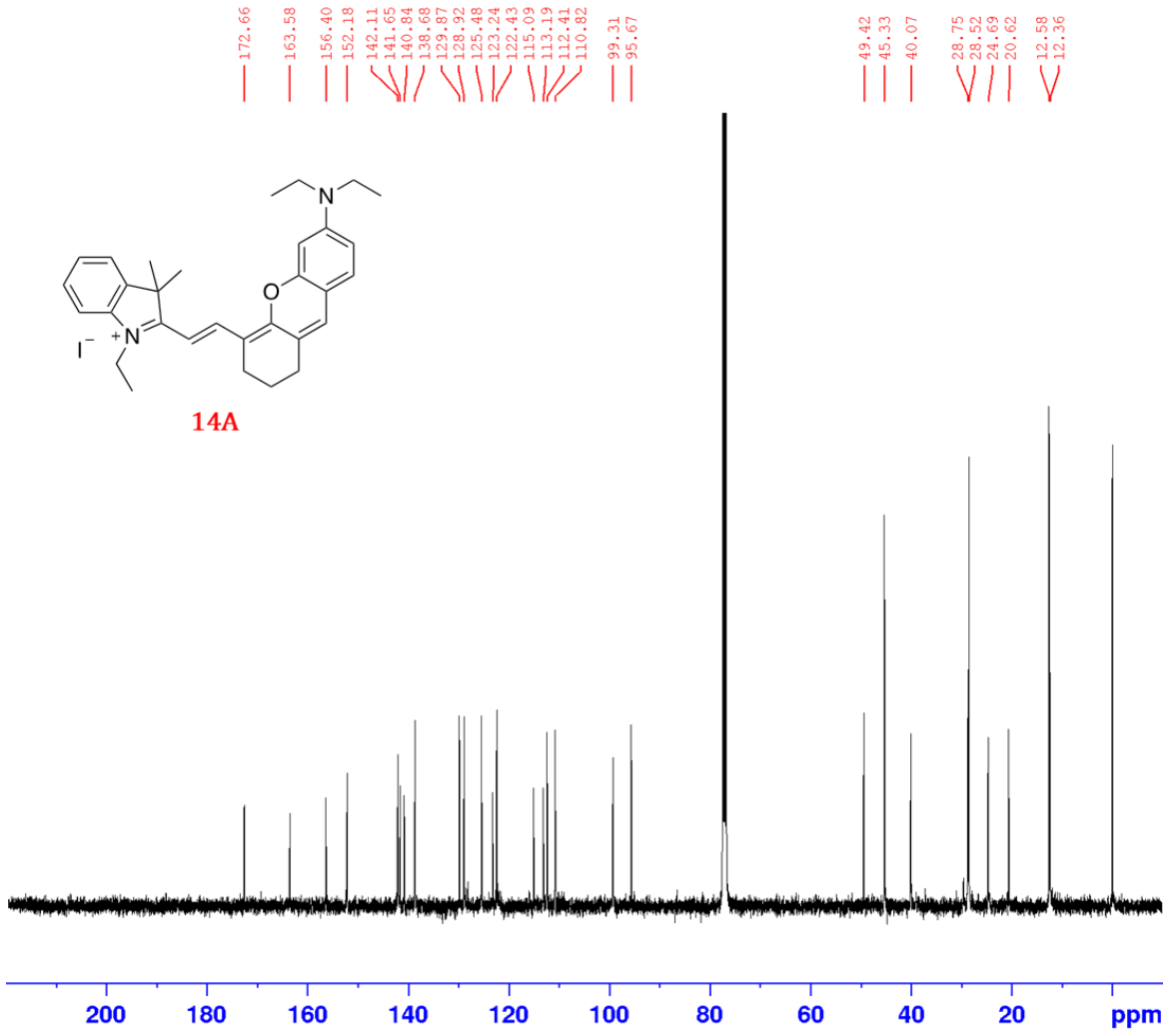

Figure S3.16: ^{13}C NMR spectrum of **compound 14A.**

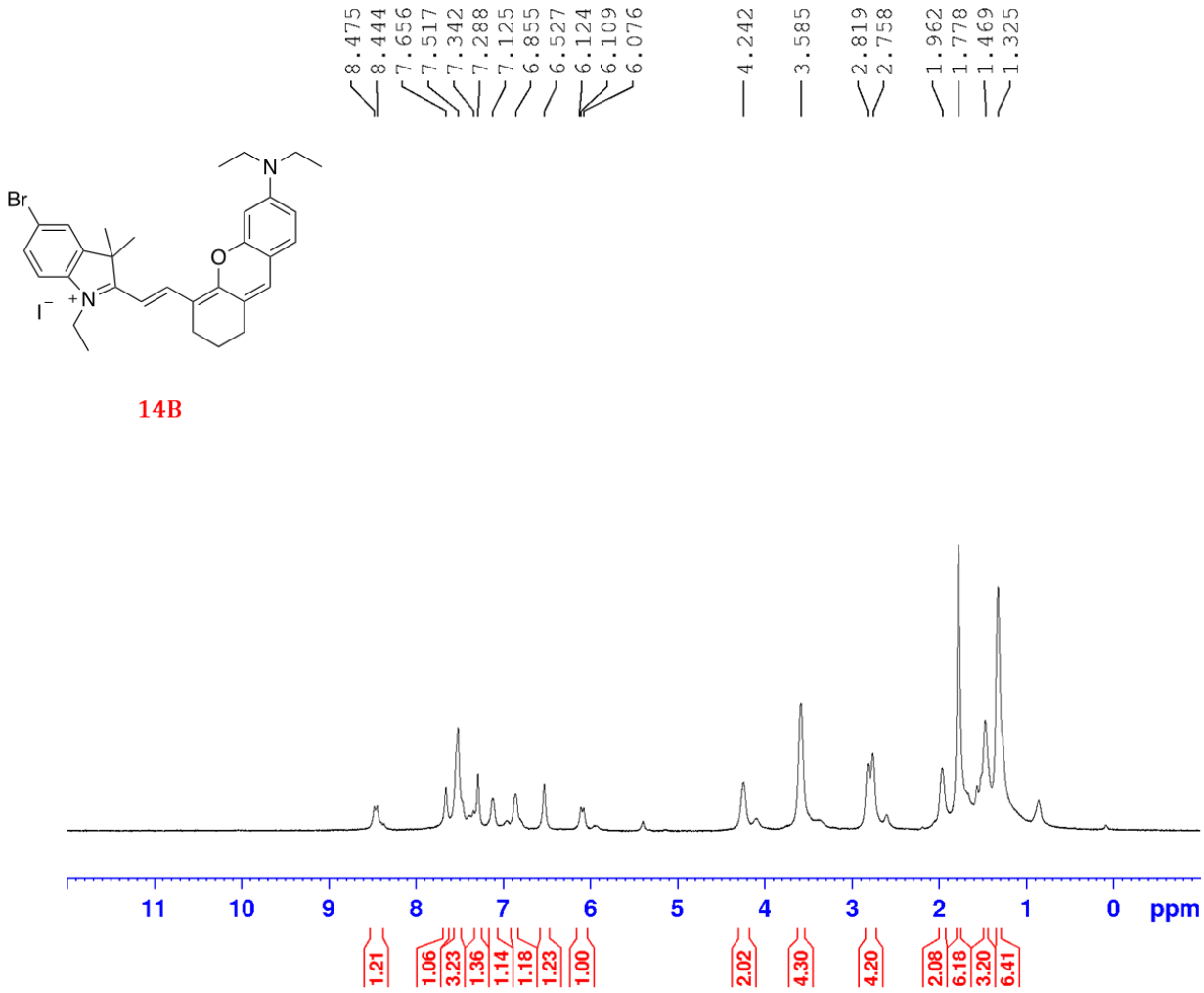

Figure S3.17: ^{1}H NMR spectrum of **compound 14B.**

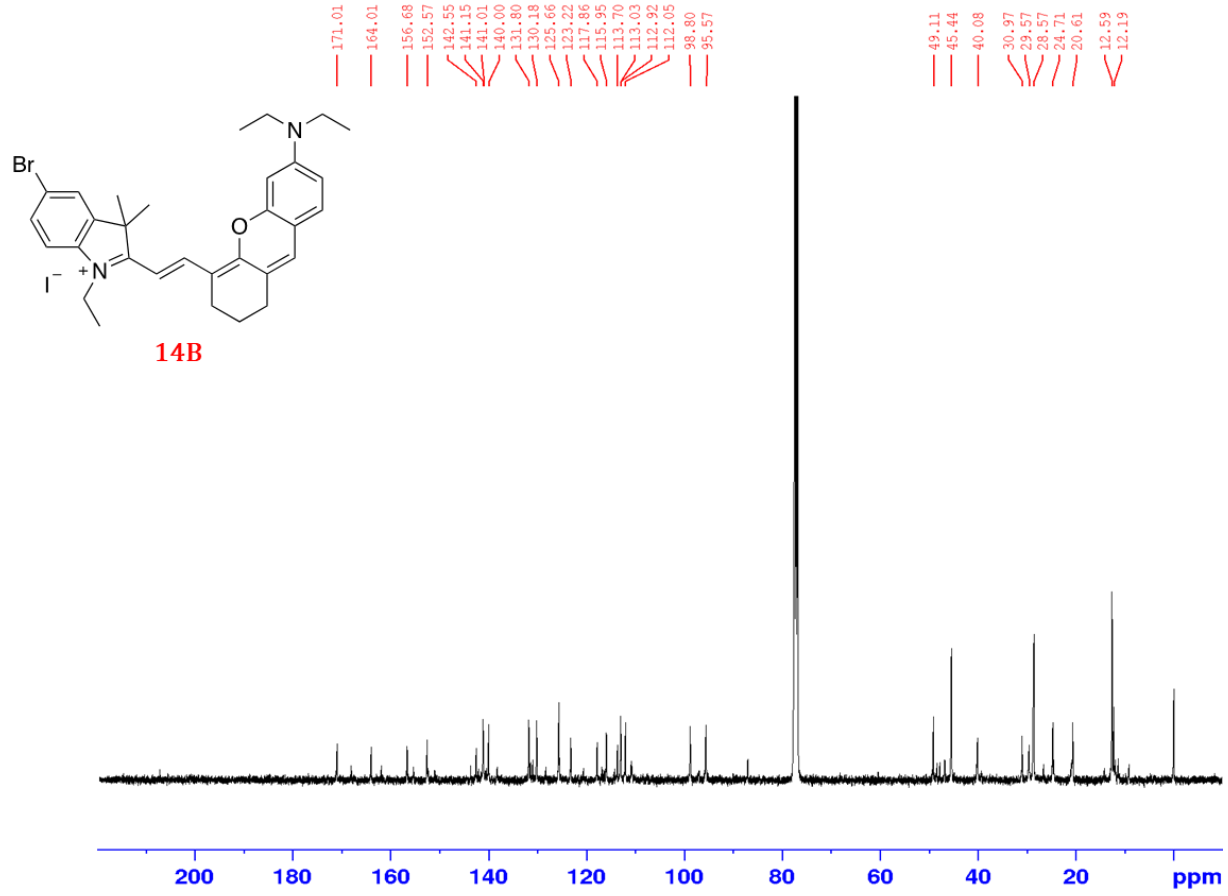

Figure S3.18: ^{13}C NMR spectrum of **compound 14B.**

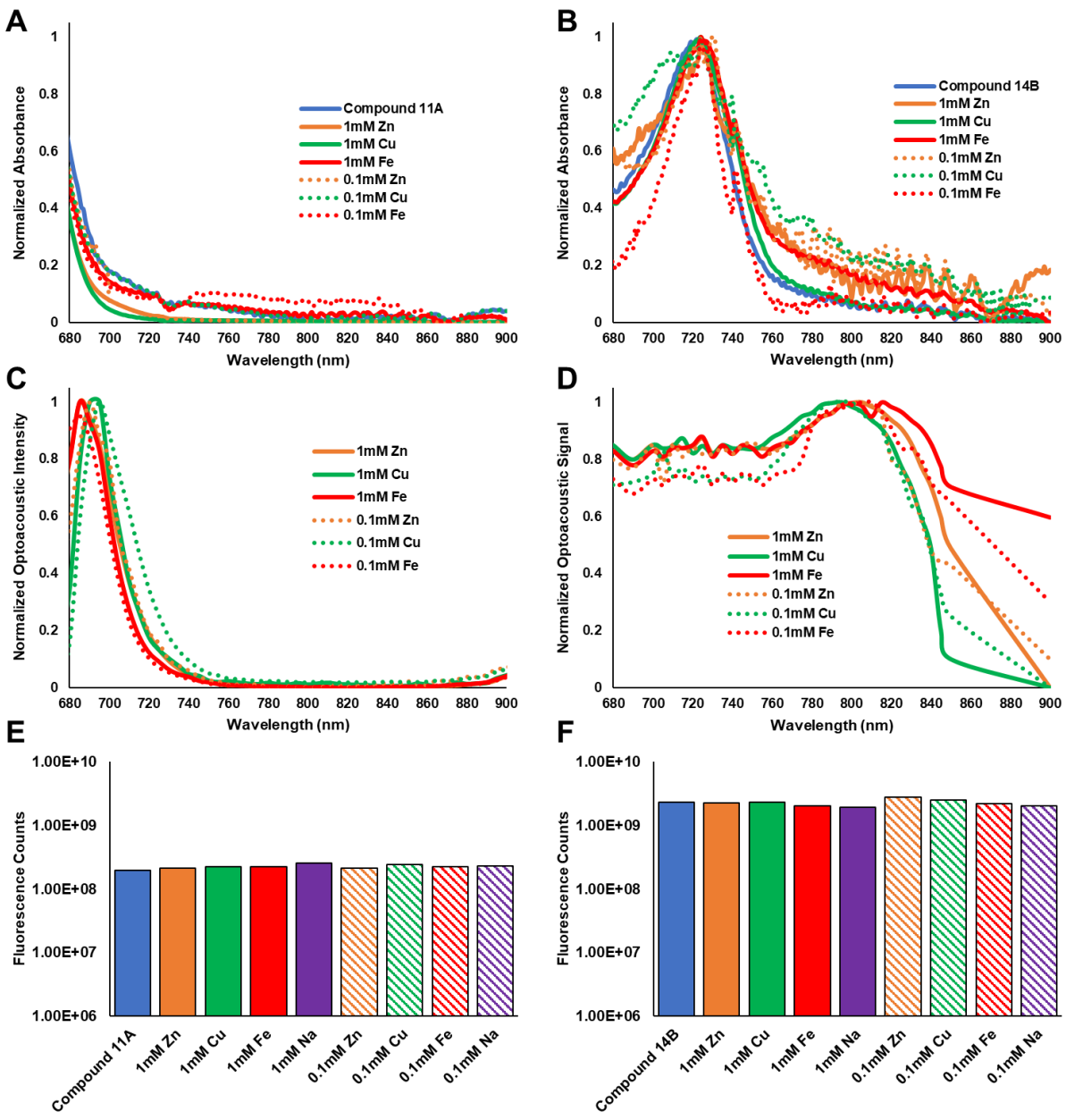

Figure S3.19: Metal sensitivity evaluation of **compound 11A** and **compound 14B** through absorbance (A, B), optoacoustic imaging (C, D), and fluorescence intensity (E, F). No p-values to report.

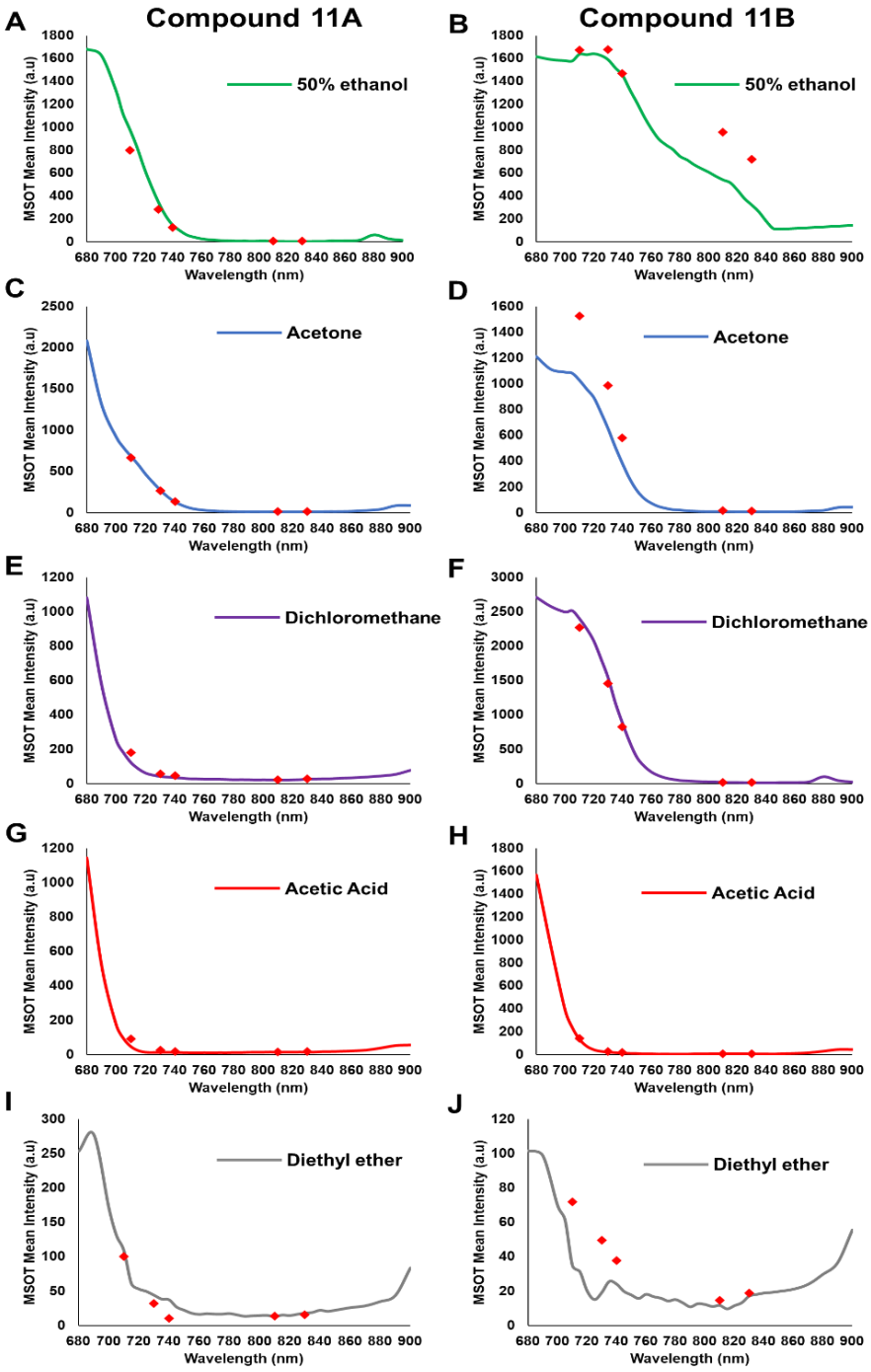

Figure S3.20: Single-wavelength measurements of compound 11A (A, C, E, G, I) and compound 11B (B, D, F, H, J). Single wavelength measurements (red diamonds) are compared to entire spectral measurements in 50% ethanol (green – A, B), acetone (blue – C, D), dichloromethane (purple – E, F), acetic acid (red – G, H), and diethyl ether (gray – I, J).

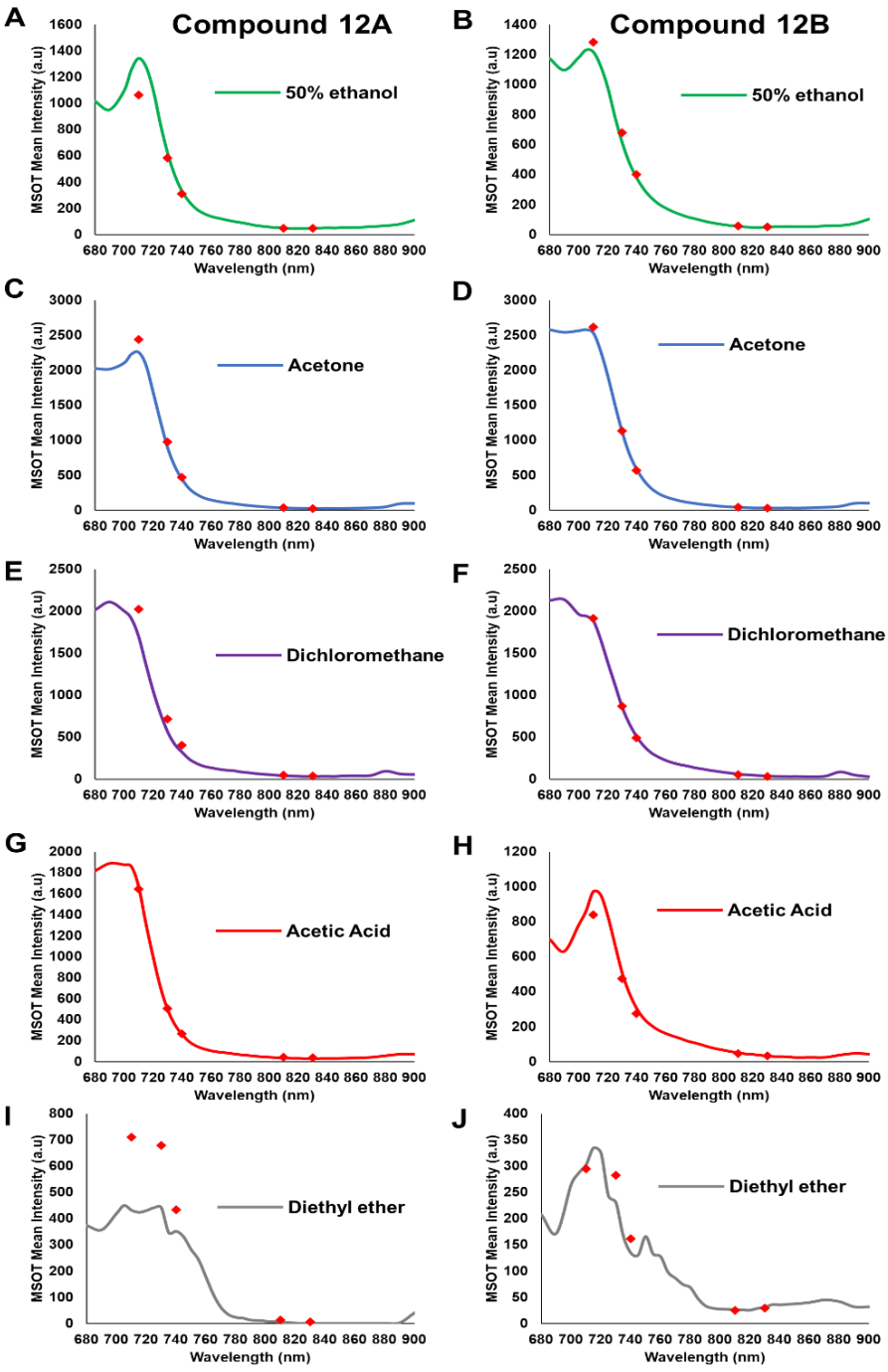

Figure S3.21: Single-wavelength measurements of compound 12A (A, C, E, G, I) and compound 12B (B, D, F, H, J). Single wavelength measurements (red diamonds) are compared to entire spectral measurements in 50% ethanol (green – A, B), acetone (blue – C, D), dichloromethane (purple – E, F), acetic acid (red – G, H), and diethyl ether (gray – I, J).

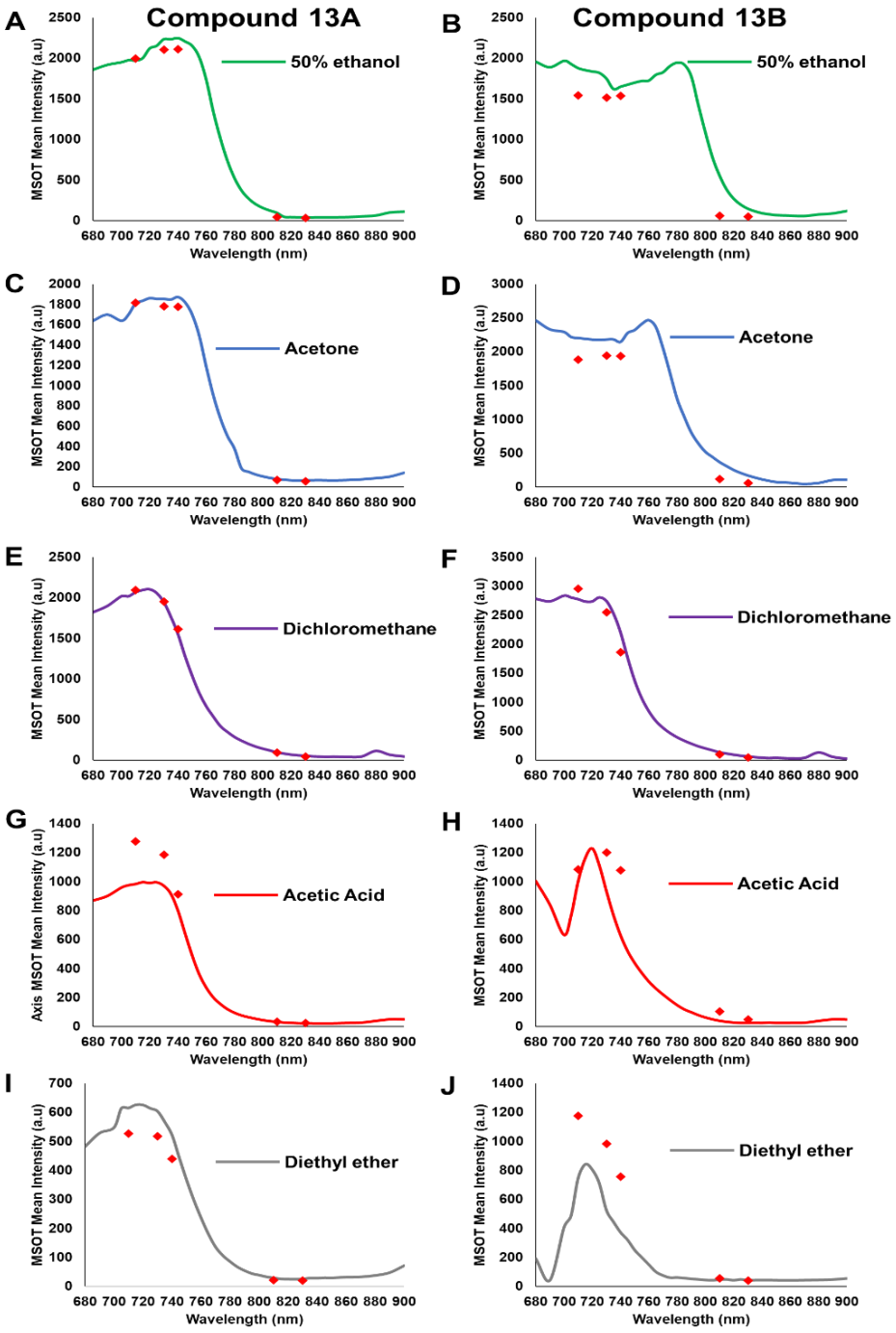

Figure S3.22: Single-wavelength measurements of compound 13A (A, C, E, G, I) and compound 13B (B, D, F, H, J). Single wavelength measurements (red diamonds) are compared to entire spectral measurements in 50% ethanol (green – A, B), acetone (blue – C, D), dichloromethane (purple – E, F), acetic acid (red – G, H), and diethyl ether (gray – I, J).

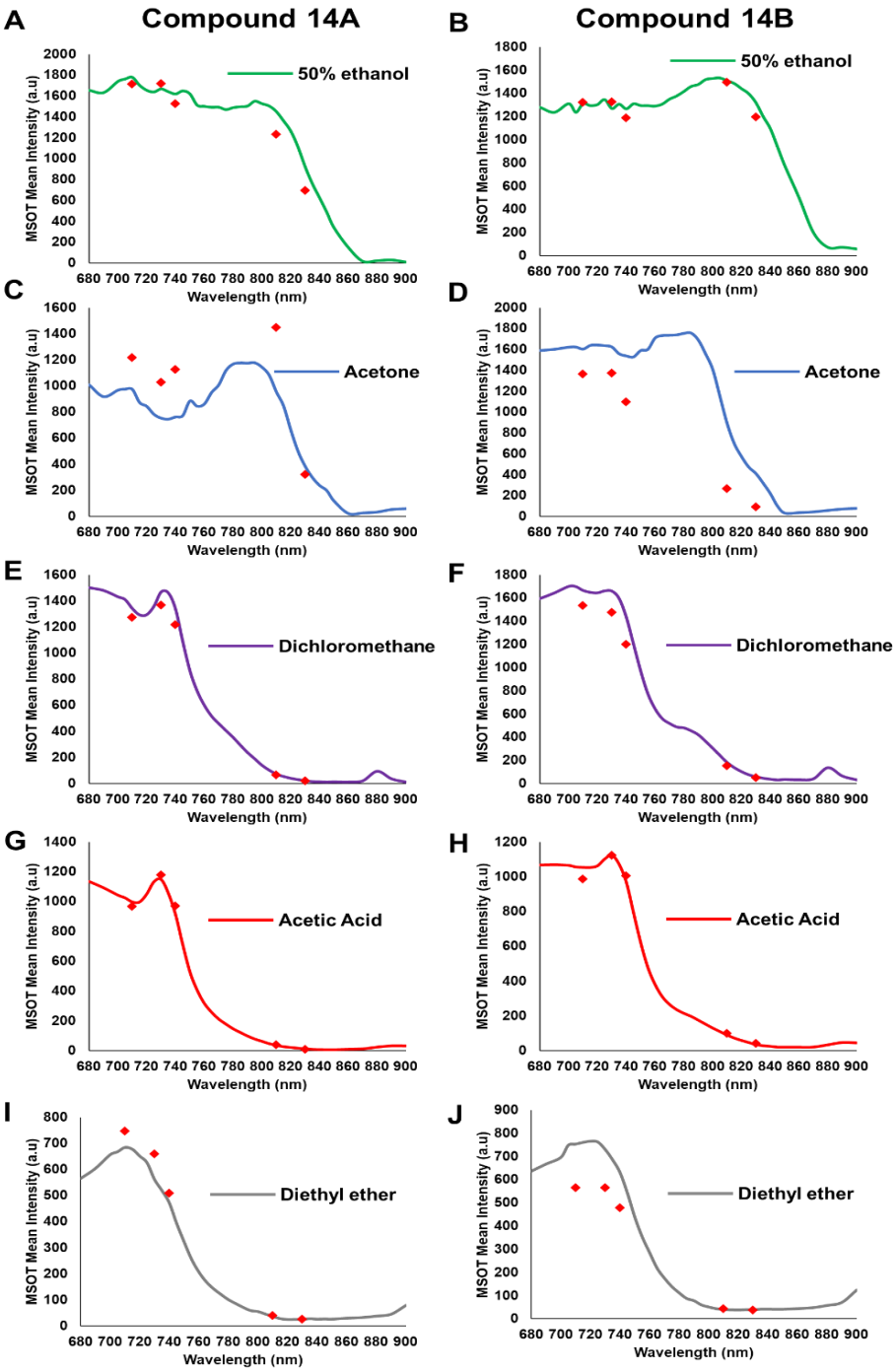

Figure S3.23: Single-wavelength measurements of compound 14A (A, C, E, G, I) and compound 14B (B, D, F, H, J). Single wavelength measurements (red diamonds) are compared to entire spectral measurements in 50% ethanol (green – A, B), acetone (blue – C, D), dichloromethane (purple – E, F), acetic acid (red – G, H), and diethyl ether (gray – I, J).

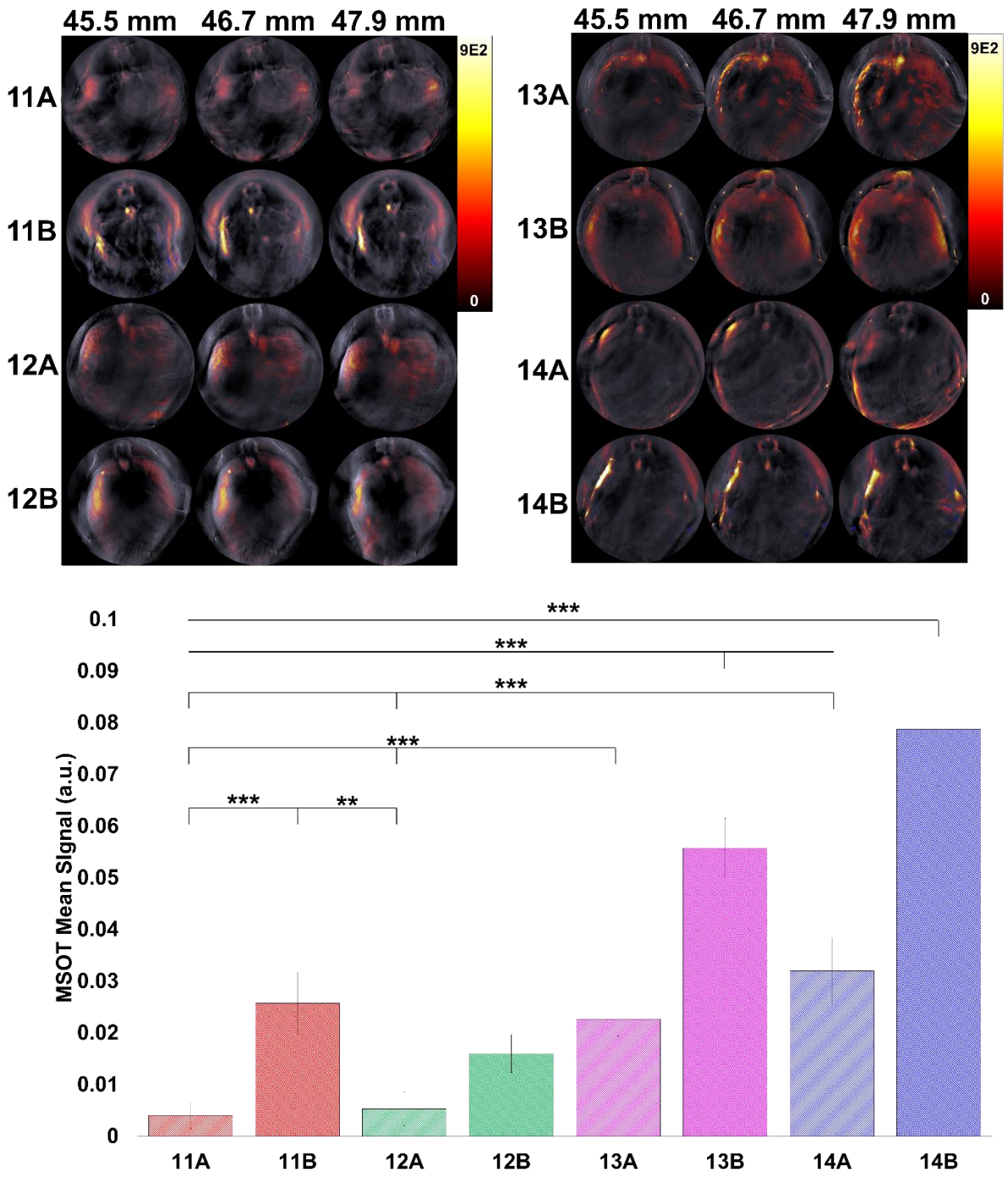

Figure S3.24: *In vivo* evaluation of compounds 11A-14B. A) Visualization of *in vivo* optoacoustic signal. B) Quantification of signal from A. Compound 14B spectra was utilized as the reference spectra for all quantification.

Chapter 4:

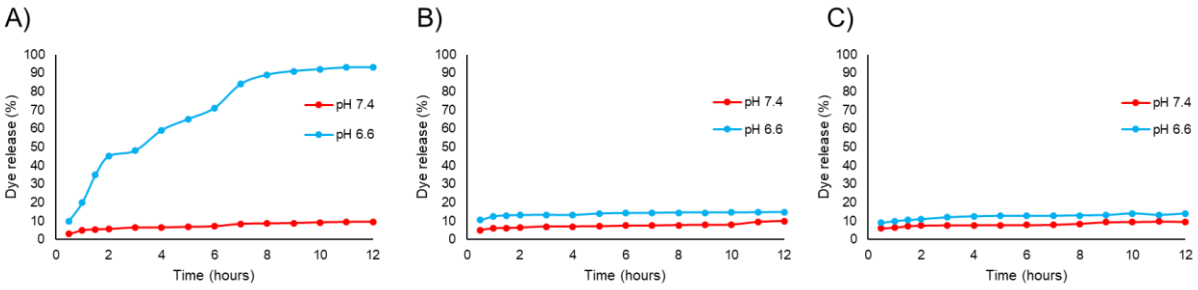

Figure S4.1: Simulation of contrast agent IR780 exfiltration from MSN pores while coated via A) Chitosan, B) 2KPEG, or C) 35KPEG. Samples were added to 10% phosphate buffered saline at a biological pH level of 7.4 or a hypoxic pH level of 6.6.

Chapter 5:

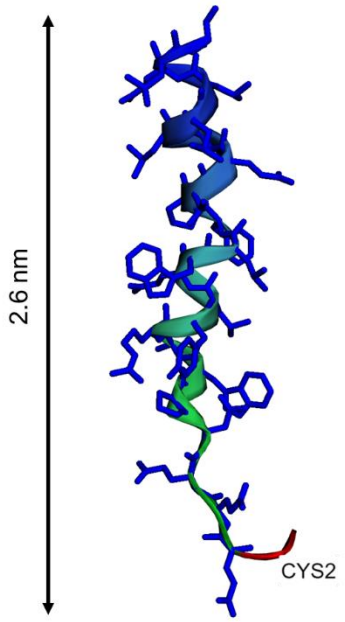

Figure S5.1: 3D model of V7 peptide using EzMol. V7 consists of 26 amino acids and is approximately 2.6 nm in length. The CYS residue utilized to attach the V7 peptide to the nanoparticle via SMCC is noted in red.

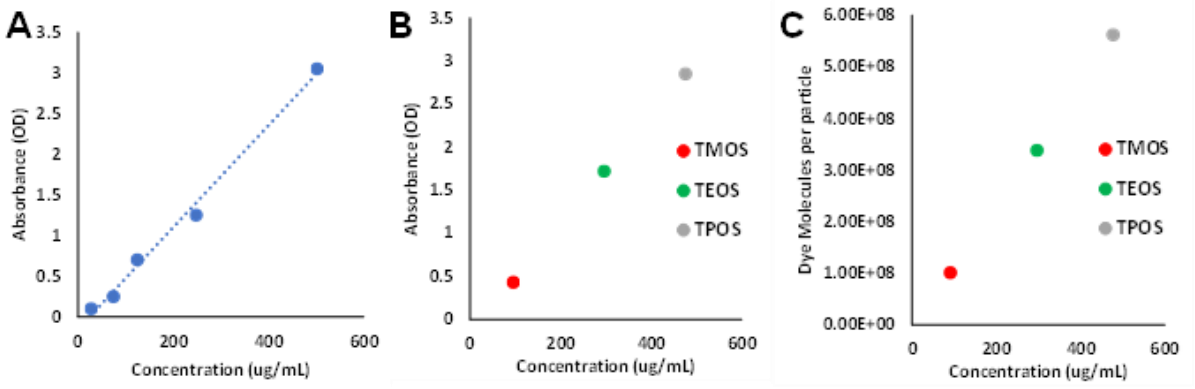

Figure S5.2: Characterization if IR780 dyes within TROS. Graphs depict A) IR780 standard curve, B) measurement of optical density compared to IR780 dye within TROS, and C) number of dye molecules per particle for given concentrations of IR780 in TROS.

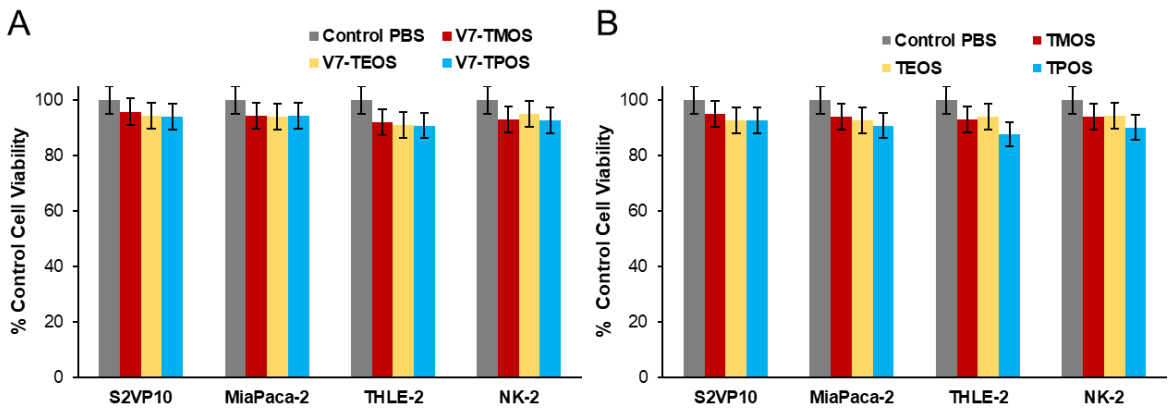

Figure S5.3: Evaluation of cell viability following TROS and V7-TROS treatment. (A) No significant toxicity was observed in malignant (S2VP10 and MiaPaca-2) or non-malignant (THLE-2 and NK-2) cells at any particle size for V7 actively targeted TROS ($p>0.05$). (B) No significant toxicity was observed in malignant (S2VP10 and MiaPaca-2) or non-malignant (THLE-2 and NK-2) cells at any particle size for passively targeted TROS $p>0.05$.

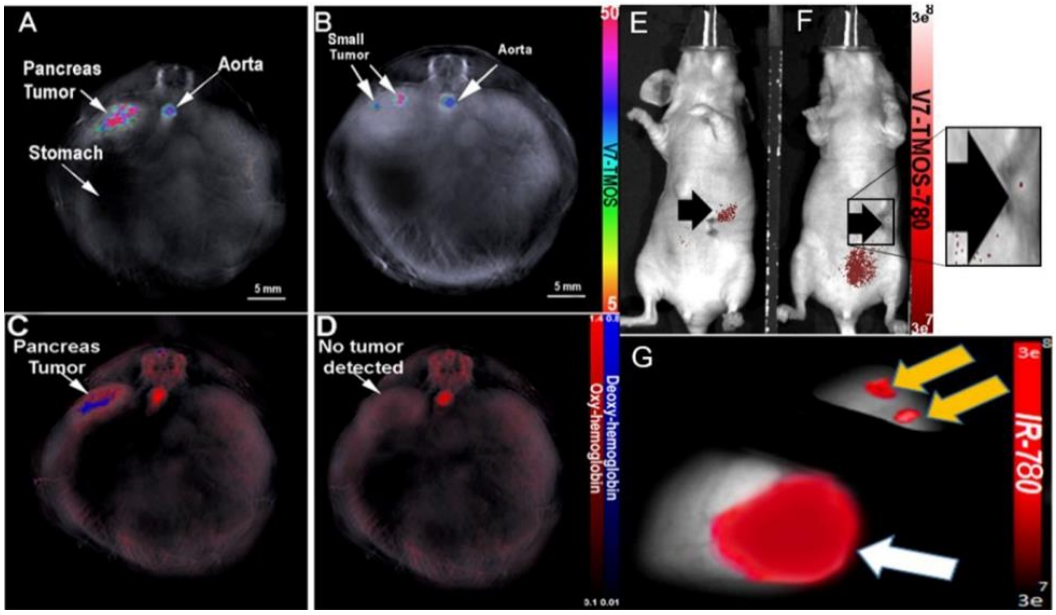

Figure S5.4: MSOT detection of sub-millimeter DPAC tumor via V7-TMOS *in vivo*. A) Orthotopic sub-millimeter (0.72 mm) PDAC tumor detected using V7-TMOS B) Orthotopic sub-millimeter (0.23 mm) PDAC tumor detected using V7-TMOS C) Orthotopic sub-millimeter (0.72 mm) PDAC tumor detected using oxy/deoxyhemoglobin D) Orthotopic sub-millimeter (0.23 mm) PDAC tumor not detected using oxy/deoxyhemoglobin. E) NIR

fluorescence was able to detect PDAC tumor of size 0.72 mm. F) NIR fluorescence was unable to detect PDAC tumor of size 0.23 mm. G) Confirmation of sub-millimeter tumor using NIR fluorescence *ex vivo*.

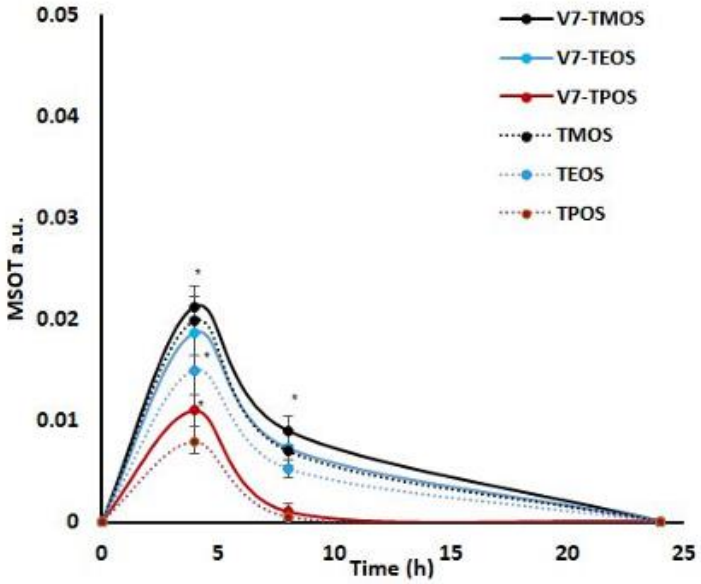

Figure S5.5: Assessment of blood retention of V7-TROS and TROS signal at timepoints of 0, 4h, 8h, and 24h post intravenous injection. Signal was measured using a region of interest analysis at a single snapshot at each timepoint in the aorta. The levels of V7-TMOS and V7-TEOS in the blood (represented by the aorta) were not statistically different ($p=0.57$), however both V7-TMOS and V7-TEOS were significantly higher than V7-TPOS ($p=0.046$).